# Membrane Remodelling Mediated by a Cyanobacterial Dynamin-like Protein

Max Peter Manley

Imperial College London

Department of Infectious Disease

*PhD Supervisor: Dr Harry Low*

Thesis Submitted for the Degree of:

Doctor of Philosophy

October 2024

## Abstract

Membrane remodelling is fundamental to cellular life, essential for processes ranging from cell division to organelle maintenance. While lipid bilayers are the predominant membrane structure, non-bilayer lipids and phases play crucial roles in cellular function and stress responses. Proteins are key mediators of membrane remodelling, with the dynamin superfamily representing an ancient and conserved class of membrane-remodelling GTPases found across all domains of life. Most eukaryotic dynamins and dynamin-related proteins have defined roles in fission or fusion, such as the mitofusins mediating outer mitochondrial membrane fusion. Bacterial dynamins generally have more diverse cellular roles, but often share conserved characteristics with eukaryotic dynamins, including their domain architecture and ability to self-assemble into helical polymers that constrict lipid membranes. Bacterial dynamin-like protein (BDLP) from the cyanobacterium *Nostoc punctiforme* serves as a valuable model for investigating bacterial dynamin function and the fundamental membrane remodelling principles of the dynamin superfamily, especially given its homology to the mitofusins. This thesis demonstrates BDLP's specific upregulation during development of motile *N. punctiforme* filaments, and its putative association with thylakoid membranes remodelled into non-bilayer phases. High-resolution cryo-electron microscopy structures of GMPPNP- and GDP-bound BDLP filaments provide a structural basis of GTP coordination and catalysis, and demonstrate a novel mechanism of membrane constriction. Cryo-electron tomography reveals how BDLP remodels lipids from a bilayer configuration into a non-bilayer arrangement *in vitro*, providing the first evidence of a dynamin family member mediating stable lipid phase transitions. These findings expand our understanding of bacterial DRP functions while demonstrating conserved DSF membrane remodelling principles. The identification of a conserved membrane displacement domain across mitofusin-like DRPs suggests a shared mechanism for bilayer disruption, potentially elucidating mitofusin-mediated fusion.

## Declaration of Originality

I, Max Manley, declare that this thesis is entirely my own original work. All the results detailed arise from my own research unless otherwise stated. Any information and conclusions derived from other works has been referenced appropriately.

## Copyright Declaration

‘The copyright of this thesis rests with the author. Unless otherwise indicated, its contents are licensed under a Creative Commons Attribution-Non Commercial 4.0 International Licence (CC BY-NC). Under this licence, you may copy and redistribute the material in any medium or format. You may also create and distribute modified versions of the work. This is on the condition that: you credit the author and do not use it, or any derivative works, for a commercial purpose. When reusing or sharing this work, ensure you make the licence terms clear to others by naming the licence and linking to the licence text. Where a work has been adapted, you should indicate that the work has been changed and describe those changes. Please seek permission from the copyright holder for uses of this work that are not included in this licence or permitted under UK Copyright Law.’

## Acknowledgement of Collaborations

The work of collaborators that contributes to this thesis has been acknowledged throughout within the figure legends. They also provided useful discussion over the past four years, for which I am immensely grateful. To summarise, Dr Douglas Risser (University of Colorado, Colorado Springs) conducted RNA-seq transcriptomic data analyses, generated *N. punctiforme* mutants, analysed them by Western blot and fluorescence microscopy, and provided the BDLP-GFP overexpression strain used for in-cell cryo-electron tomography. Cryo-correlative light-electron microscopy data was collected, and tomograms reconstructed and denoised by members of the Engel group (Biozentrum, University of Basel): Prof. Dr Ben Engel, Dr Annemarie Perez Boerema, Dr Wojciech Wietrzynski and Dr Ricardo Righetto. Prof. Dr Thomas Pucadyil and Keerti Singh (Indian Institute of Science Education and Research, Pune), performed and analysed PLiMAP membrane binding assays and GTP turnover assays.

# Acknowledgements

First and foremost, I extend my deepest thanks to Harry Low for his exceptional supervision, guidance, and innovative ideas. Despite the challenging COVID-related circumstances at the beginning of my time in his lab, he enabled me to hit the ground running. His supervision style, balancing hands-on and hands-off approaches at the right moments, allowed me to develop my own ideas and interests while maintaining focus when necessary. I'm also indebted to the members of the Low lab, both past and present, for their invaluable guidance, insightful discussions, meticulous proof-reading, and collaborative spirit: Alasdair Leeding, Jayanti Singh, Ioanna Stefani, Andrew Morrison, Souvik Naskar, Michael Hohl, and Matteo Tassinari. I'd particularly like to acknowledge Jayanti's ongoing collaboration on bacterial ESCRT-III projects, which, although not forming part of this thesis, significantly enhanced my understanding of bacterial membrane remodelling systems. My appreciation extends to the lab members and wider section colleagues who allowed me to distract them and accompanied me on numerous walks - special mentions go to Clare Robinson and Nina Short. I'm also grateful to the master's students I supervised - Yuqing Qi, Hanyue Gong, and Maximillian Mollenhauer-Starkl - who indirectly taught me a great deal about academia and worked diligently on projects on other dynamin systems. I owe a debt of gratitude to the CSB community, especially Paul Simpson, whose informative and entertaining guidance taught me so much about the intricacies of microscopes and their software. His patience and understanding when things went awry were invaluable; without his expertise, much of this work would not have been possible.

This thesis would also not have been possible without the unwavering support of Amy Hazelwood, who made the past four years a joy to navigate, provided emotional support, and showed remarkable understanding of the often antisocial hours involved. The support of my family was equally indispensable. In particular, my parents made pursuing research, which is never an easy choice, an obvious decision. Only now do I fully appreciate why they always stressed the importance of "reading around the subject". Lastly, I extend my thanks to all the friends, both old and new, who joined me in pursuing my passions outside research or simply helped me unwind when needed - they know who they are.

# Table of Contents

***Abstract*** ..... ***2***

***Declaration of Originality*** ..... ***3***

***Copyright Declaration*** ..... ***4***

***Acknowledgement of Collaborations*** ..... ***5***

***Acknowledgements*** ..... ***6***

***Table of Contents*** ..... ***7***

***List of Figures*** ..... ***15***

***List of Tables*** ..... ***19***

***List of Equations*** ..... ***20***

***Abbreviations*** ..... ***21***

***Amino Acids*** ..... ***24***

***Chapter 1: Introduction to Lipid Membranes, Membrane Remodelling Proteins, and the Dynamin Superfamily*** ..... ***25***

**1.1 Biological Lipids Arrange into both Lamellar Bilayers and Non-bilayer Phases** ..... **25**

1.1.1 Lamellar Bilayers are a Thermodynamically Favoured Lipid Configuration that Act as Selectively Permeable Barriers ..... 26

1.1.2 Bilayer Properties are Modulated by their Lipid Composition and Specialised Lipids have Roles in Various Biological Processes ..... 27

1.1.3 Lipid Bilayers Provide Cells with Barriers to their External Environment ..... 29

1.1.3.1 Gram-negative (Diderm) Cell Envelopes Comprise Two Lipid Bilayers ..... 30

1.1.3.2 Gram-Positive Cell Envelopes Comprise a Single Lipid Bilayer and Larger Peptidoglycan Sacculus ..... 32

1.1.3.3 Archaea Exhibit Diverse Cell Envelope Structures ..... 32

1.1.4 Bilayers are also used for Intracellular Compartmentalisation ..... 33

1.1.4.1 Intracellular Compartmentalisation can also be Achieved by Liquid-liquid Phase Separation (LLPS) ..... 34

1.1.5 Lipids can Arrange into Non-bilayer Phases and the Phase Lipids Spontaneously Adopts is Determined by their Shapes ..... 35

1.1.6 Lipids can form Highly Curved Bilayer Arrangements in a Regular Cubic Lattice known as the Cubic Phase ..... 37

1.1.6.1 The Cubic Phase has Important Biological Functions..... 38
1.1.7 Non-bilayer Lipids Modulate the Material Properties of Lamellar Bilayers..... 39
1.1.8 Non-bilayer Lipids and Phases have Important Biological Functions ..... 41
1.1.8.1 Non-bilayer Lipids Promote Membrane Fission and Fusion via the Hemi-fission or Hemi-fusion Membrane Stalk..... 42
1.1.9 Energy-transducing Membranes Comprise ~50 % Non-bilayer Lipids..... 44
1.1.10 Mitochondria are Dynamic Double-membrane Organelles that House the Machinery Required for Oxidative Phosphorylation ..... 46
1.1.10.1 Non-bilayer Lipids and Phases have Important Functions in Mitochondria ..... 49
1.1.11 Thylakoid Membranes House the Photosynthetic Electron Transport Chain Machinery, which is Highly Regulated in Response to Changing Light Conditions ..... 50
1.1.11.1 Non-bilayer Thylakoid Lipids and Phases have Important Roles in Response to Changing Light Conditions..... 52
1.1.11.2 Non-bilayer Lipids may have Played an Important Role in the Evolution of Thylakoid Membranes..... 54
1.1.12 Summary of Lipid Membranes ..... 55
**1.2 Membrane Remodelling is Essential to Life and Mediated by Various Protein Families..... 56**
1.2.1 Membrane Remodelling Proteins Induce Membrane Curvature ..... 56
1.2.1.1 Actin and Tubulin Remodel Membranes During Cell Division and are Involved in Cell Shaping and Motility ..... 57
1.2.1.2 Clathrin and the SNAREs are Involved in Vesicle Shaping and Fusion ..... 58
1.2.1.3 Bar-Domain Proteins Induce Curvature During Vesiculation..... 58
1.2.1.4 ESCRT-III Proteins Induce Extreme Curvature to Achieve Membrane Fission and Repair..... 58
1.2.2 Membrane Remodelling Summary..... 59
**1.3 The Dynamin Superfamily is an Ancient Family of Membrane Remodelling Proteins..... 59**
1.3.1 Eukaryotic Dynamins have Various Functions often Including Membrane Fission or Fusion ..... 61
1.3.2 Many Bacterial Dynamins have not been Classified as Fission or Fusion Dynamins ..... 63
1.3.3 Dynamins Self-assemble onto Membrane to Constrict and Remodel the Underlying Bilayer ..... 65
1.3.4 The Dynamin Superfamily Shares a Conserved Domain Architecture with Variable Membrane-Interacting and Additional N- and C-terminal Domains ..... 65
1.3.4.1 The Dynamin Superfamily Membrane-interacting Domains are Diverse ..... 66
1.3.4.2 The Classical Dynamin Proline-rich Domain is involved in Signalling and Regulation..... 67
1.3.5 Dynamins Self-assemble into Rings and Helical Filaments ..... 67
1.3.6 Dynamins have both Highly-conserved and Specialised Oligomerisation Interfaces ..... 68
1.3.6.1 Dynamins Dimerise across a Conserved GTPase Domain Interface to Catalyse GTP hydrolysis 70
1.3.7 The role of Nucleotide Binding and Hydrolysis during Membrane Remodelling is Inconsistent across the Dynamin Superfamily ..... 73

1.3.8 Conformational Flexibility of Two Conserved Hinges is Essential to Dynamin Function ..... 74
1.3.9 GTP Hydrolysis Drives Power-strokes and Rung Sliding in Fission Dynamin Filaments to Constrict the Underlying Membrane ..... 76
1.3.10 The Mechanisms of Dynamin-mediated Membrane Fusion are not well Characterised ..... 79
1.3.10.1 Mitofusin-like Dynamins Tether and Dock Membranes in Trans to Achieve Fusion ..... 79
1.3.10.2 Opa1-like Dynamins can form Helical Polymers on Membranes, and this may be Required to Achieve Membrane Fusion ..... 80
1.3.11 Several Dynamins Require Partner Dynamins to Remodel Membrane ..... 82
1.3.12 Several Dynamins are Regulated by Binding Partners ..... 82
1.3.13 Summary of the Conserved Principles of DSF-mediated Membrane Remodelling ..... 83

**1.4 Bacterial Dynamin-Like Protein (BDLP) is a Mitofusin Homologue with Unknown Function, Encoded by the Cyanobacterium *Nostoc punctiforme* ..... 83**

1.4.1 *Nostoc Punctiforme* is a Cyanobacterium with a Complex Life-cycle ..... 84
1.4.1.1 Hormogonia are short *N. punctiforme* Filaments Dedicated to Motility ..... 86
1.4.2 BDLP Undergoes Major Conformational Changes to Transition from a 'Closed' Off-Membrane State to a Membrane-bound Helical Polymer ..... 87
1.4.2.1 BDLP Dimerises across the Conserved G-dimer Interface and Coordinates Nucleotide via Conserved Motifs ..... 87
1.4.2.2 BDLP Forms Polymers with a Unique Helical Architecture ..... 89

**1.5 Study Overview ..... 90**

1.5.1 Motivations ..... 90
1.5.2 Study Summary ..... 91

***Chapter 2: The Theory of Cryogenic-Electron Microscopy and its Application to Biological Polymers ..... 92***

**2.1 Introduction to Cryo-EM ..... 92**

2.1.1 A Brief History of Electron Microscopy and the Development of Cryo-EM ..... 92
2.1.2 Advantages of Cryo-EM over other Structural Biology Techniques ..... 94

**2.2 Sample Preparation ..... 95**

2.2.1 Overview of Cryo-EM Sample Preparation ..... 95
2.2.2 Specimen Grids and Supports ..... 95
2.2.3 Vitrification ..... 96
2.2.4 Overcoming the Air-Water Interface (AWI) ..... 96
2.2.5 Cryo-FIB Milling of Cellular Samples ..... 97

**2.3 Anatomy of an Electron Microscope ..... 97**

2.3.1 Electron Sources ..... 98

2.3.1.1 Beam Coherence in Electron Microscopy ..... 98
2.3.1.2 Thermionic Electron Sources ..... 99
2.3.1.3 Field Emission Electron Sources ..... 99
2.3.1.4 Accelerator Stacks ..... 99
2.3.2 Lenses and Magnification in an Electron Microscope ..... 100
2.3.2.1 Electromagnetic Lenses ..... 100
2.3.2.2 Electron Microscope Lens Systems ..... 100
2.3.2.3 Lens System Arrangement with the Column ..... 101
2.3.2.4 Electromagnetic Lens Hysteresis ..... 101
2.3.3 Specimen Holders and the Cryogenic Stage ..... 101
2.3.4 Energy Filters ..... 102
2.3.5 Detectors ..... 102
2.3.5.1 Nyquist Frequency ..... 102
2.3.5.2 Detective Quantum Efficiency (DQE) ..... 102
2.3.5.3 Charge Coupled Detectors (CCDs) and Direct Electron Detectors (DEDs) ..... 103
2.3.6 Vacuum Systems ..... 103
**2.4 Theory of Image Formation in Cryo-EM ..... 104**
2.4.1 Electron-Specimen Interactions ..... 104
2.4.1.1 Elastic Scattering ..... 104
2.4.1.2 Inelastic Scattering ..... 104
2.4.2 Contrast Mechanisms ..... 104
2.4.2.1 Amplitude Contrast ..... 105
2.4.2.2 Phase Contrast ..... 105
2.4.3 Factors Affecting Image Formation ..... 105
2.4.3.1 Spherical Aberration ..... 105
2.4.3.2 Chromatic Aberration ..... 106
2.4.3.3 Astigmatism ..... 106
2.4.4 Contrast Transfer Function (CTF) ..... 106
2.4.4.1 Bragg's Law in Electron Microscopy ..... 106
2.4.4.2 CTF Definition ..... 107
2.4.4.3 Imaging Setup Factors that Affect Terms of the CTF ..... 109
2.4.4.3.1 CTF Curve Envelopes ..... 110
**2.5 Cryo-EM Data Processing ..... 111**
2.5.1 Overview of the Cryo-EM Data Processing Pipeline ..... 111
2.5.2 Beam-induced Motion Correction ..... 112
2.5.3 CTF Estimation and Correction ..... 112
2.5.4 Particle Picking ..... 113

2.5.5 Particle Alignment and Classification ..... 113
2.5.5.1 2D Classification ..... 113
2.5.5.1.1 Multivariate Statistics ..... 114
2.5.5.2 Overarching principles of 3D reconstruction ..... 114
2.5.5.3 Initial Model Generation ..... 115
2.5.5.4 Model Refinement ..... 115
2.5.5.4.1 Maximum Likelihood and Bayesian Approaches ..... 116
2.5.5.4.2 Avoiding Overfitting ..... 117
2.5.5.4.2.1 Fourier Shell Correlation (FSC) ..... 117
2.5.5.4.2.2 Regularisation ..... 117
2.5.5.4.2.2.1 Non-uniform Refinement (CryoSPARC) ..... 117
2.5.5.4.2.2.2 BLUSH (RELION) ..... 118
2.5.5.5 3D Classification ..... 118
2.5.5.6 Assessing Resolution ..... 119
2.5.6 Improving Resolution and Map Interpretability Further ..... 119
2.5.6.1 Sharpening ..... 119
2.5.6.2 Per-Particle CTF Refinement ..... 120
2.5.6.3 Per-Particle Motion Correction ..... 121
2.5.6.4 Handling Heterogeneity ..... 121
2.5.6.4.1 Discrete Heterogeneity ..... 121
2.5.6.4.2 Continuous Heterogeneity ..... 121

**2.6 Helical Reconstruction in Cryo-EM ..... 122**
2.6.1 Helices in Biology ..... 122
2.6.2 Helical Lattices and their Layer Lines ..... 123
2.6.2.1 Indexing Layer Lines ..... 123
2.6.2.1.1 Real Space Indexing ..... 124
2.6.3 Fourier-Bessel Reconstruction ..... 125
2.6.4 Iterative Helical Real-space Reconstruction ..... 125

**2.7 Conclusion ..... 127**
2.7.1 Outlook and Future Directions ..... 127

***Chapter 3: Materials and Methods ..... 129***

**3.1 Materials ..... 129**
3.1.1 Media ..... 129
3.1.2 Antibiotics ..... 129
3.1.3 Buffers ..... 129
3.1.4 Kits ..... 131

3.1.5 Lipids ..... 131
3.1.6 Bacterial Strains and Plasmids ..... 131
3.1.7 Commercial Columns ..... 133
3.1.8 Commercial Chemicals ..... 133
**3.2 Methods ..... 134**
3.2.1 Competent Cells ..... 134
3.2.1.1 Bacterial Transformation ..... 135
3.2.2 Tobacco-Etch Virus Protease Purification ..... 135
3.2.3 SDS-PAGE ..... 136
3.2.4 DNA Manipulation ..... 137
3.2.4.1 Primer Design ..... 138
3.2.4.2 Polymerase Chain Reaction ..... 138
3.2.4.3 Agarose Gel Electrophoresis ..... 139
3.2.4.3.1 DNA Gel-based Purification ..... 140
3.2.4.4 Isothermal DNA Assembly ..... 140
3.2.4.5 Plasmid Purification ..... 141
3.2.4.6 Restriction Digestion ..... 141
3.2.4.7 DNA Sequencing ..... 141
3.2.5 Protein Expression ..... 141
3.2.5.1 Protein Expression Tests ..... 142
3.2.6 BDLP Purification ..... 142
3.2.6.1 Cell Lysis ..... 142
3.2.6.2 Affinity Chromatography ..... 143
3.2.6.3 TEV Cleavage ..... 143
3.2.6.4 Size Exclusion Chromatography ..... 143
3.2.6.5 Buffer Exchange ..... 144
3.2.6.6 Protein Concentration ..... 144
3.2.6.7 Concentration Determination ..... 144
3.2.7 Liposome Preparation ..... 144
3.2.8 Tubulation Reactions ..... 144
3.2.9 Co-Sedimentation Assays ..... 145
3.2.10 Electron Microscopy ..... 145
3.2.10.1 Negative-stain Electron Microscopy ..... 145
3.2.10.2 Cryo-Electron Microscopy ..... 146
3.2.10.3 Data Processing ..... 146
3.2.10.3.1 Model Building ..... 148
3.2.10.4 Cryo-Electron Tomography ..... 150

*Chapter 4: GMPPNP-Bound BDLP Filament Structure ..... 152*

**4.1 Introduction ..... 152**

**4.2 Results and Analysis ..... 153**

*4.2.1* BDLP Expression is Upregulated During Development of *N. Punctiforme* Motile Hormogonia ..... 153

4.2.2 HexII Phase Lipids were observed in Hormogonia Over-expressing BDLP-GFP ..... 156

4.2.3 Cryo-EM Structure of GMPPNP-bound BDLP Reveals a Novel Membrane Binding Domain ..... 161

4.2.3.1 BDLP Purification and Filament Optimisation ..... 161

4.2.3.2 Helical Parameter Identification of the GMPPNP-bound BDLP Protein-lipid FIlament ..... 164

4.2.3.3 Overall $BDLP_{GMPPNP}$ Architecture ..... 166

4.2.3.4 GTPase Domain Dimerisation and Nucleotide Coordination ..... 167

4.2.3.5 Hinges 1 and 2 Conformational Changes ..... 170

4.2.3.6 The Trunk Domain Rearranges to Form a Novel Membrane Binding Domain (MBD). ..... 171

4.2.4 The BDLP MBD has a Higher Affinity for High PG-Content Membranes ..... 172

4.2.4.1 Cryo-EM Structure of GMPPNP-bound BDLP Filaments on PG Liposome Templates ..... 174

4.2.5 A MBD Mutant can Tubulate PG Liposomes but cannot Achieve Tight Constriction ..... 177

**4.3 Discussion ..... 179**

4.3.1 A Putative Novel Bacterial DRP Function ..... 179

4.3.2 BDLP Filament Ultrastructure Insights ..... 183

4.3.3 The Novel BDLP Membrane Binding Domain might help Identify Membrane Binding Domains of other DRPs. ..... 186

4.3.4 Conclusions and Outstanding Questions ..... 189

*Chapter 5: GDP-Bound BDLP Filament Structure ..... 191*

**5.1 Introduction and Aims ..... 191**

**5.2 Results and Analysis ..... 192**

5.2.1 A GDP-Bound BDLP Filament Reveals Additional Residues that Displace Lipids from the Bilayer ..... 192

5.2.1.1 BDLP can tubulate PG liposomes when GDP-bound ..... 192

5.2.1.2 Helical Reconstruction of a Super-constricted GDP-bound BDLP Filament ..... 193

5.2.1.3 $BDLP_{GDP}$ Model Building and G-dimer Interface ..... 195

5.2.1.4 Overall $BDLP_{GDP}$ Architecture ..... 197

5.2.1.5 Nucleotide Hydrolysis Induces Trunk and MBD Conformational Changes ..... 197

5.2.2 Comparison of $BDLP_{GDP}$ and $BDLP_{GMPPNP}$ Filament Architectures Reveals that GTP Hydrolysis Breaks Lateral GTPase Domain Contacts ..... 199

5.2.3 Nucleotide Hydrolysis Drives Membrane Displacement by Increasing Inter-rung MBD Contacts ..... 202

5.2.3.1 Lateral Contacts in $BDLP_{GMPPNP}$ are Consistent with those of $BDLP_{GMPPNP(PG)}$ ..... 207

5.2.4 Thick GDP-bound BDLP Filaments Represent Intermediate States ..... 208

5.2.4.1 Cryo-EM Reconstruction of Thick GDP-bound BDLP Filaments ..... 208
5.2.4.2 $BDLP_{GDP(L2)}$ Reconstruction ..... 208
5.2.4.3 $BDLP_{GDP(L3)}$ Reconstruction ..... 211
5.2.5 Comparison of $BDLP_{GDP(L2)}$ and $BDLP_{GDP(L3)}$ with $BDLP_{GMPPNP}$ and $BDLP_{GDP}$ ..... 213
5.2.5.1 Rigid-body Fitting to Generate $BDLP_{GDP(L2)}$ and $BDLP_{GDP(L3)}$ Models ..... 213
5.2.5.2 G-Dimer Interface ..... 213
5.2.5.3 Hinge 2 ..... 214
5.2.5.4 Trunk and MBDs ..... 216
5.2.5.5 Lipid Channel Geometry ..... 217
5.2.6 BDLP Filaments Induce a Lamellar to HexII Lipid Phase Transition *in vitro*. ..... 220

**5.3 Discussion ..... 228**

5.3.1 The Role of Nucleotide in BDLP-mediated Membrane Remodelling ..... 229
5.3.1.1 From Membrane-binding to Super-constriction ..... 229
5.3.1.2 Intermediate States ..... 232
5.3.2 A Conserved Membrane Displacement Mechanism? ..... 234
5.3.3 Structural Comparisons Reveal MBD Conservation Across the Mitofusin-like Dynamin Clade ..... 235
5.3.4 BDLP-mediated Lipid Phase Changes ..... 240
5.3.5 Conclusions ..... 241

***Chapter 6: Discussion ..... 243***

**6.1 The Inverse-hexagonal Phase in *N. punctiforme* hormogonia ..... 243**

**6.2 Potential Applications for BDLP-mediated Phase Changes in Drug Delivery ..... 245**

**6.3 A model for BDLP-mediated Lipid Phase Changes ..... 246**

**6.4 Conserved Principles of DSF-mediated Membrane Remodelling ..... 249**

**6.5 Final Remarks ..... 250**

***References ..... 252***

***Appendices ..... 292***

**Collaborator Methods ..... 292**

**PLiMAP and GTPase Activity Assay Methods ..... 292**

***N. punctiforme* Strain Construction and Analysis ..... 293**

# List of Figures

Figure 1. Lipid Bilayer Arrangement and Glycerophospholipid Chemical Structure.....26

Figure 2. Bacterial Cell Envelopes. .....31

Figure 3. Lipid Shape and Phase Relationships. .....36

Figure 4. Non-bilayer Lipid-induced Lateral Pressure and Frustration. .....41

Figure 5. The Hemifusion stalk.....43

Figure 6. Lipid Polymorphism of Thylakoid Membranes. .....45

Figure 7. Overview of Mitochondrial Membrane and Respiratory Electron Transport Chain Arrangements. .....48

Figure 8. The Photosynthetic Electron Transport Chain. .....51

Figure 9. Dynamin Phylogenetic Tree. .....60

Figure 10. DSF Roles in Eukaryotes in Bacteria. .....63

Figure 11. DSF Conserved Domain Architecture. .....65

Figure 12. DSF Oligomerisation Interfaces. .....69

Figure 13. GTPase Domain Dimerisation in Filaments or Solution. .....71

Figure 14. Conserved GTPase Domain Catalytic Motifs and Nucleotide Coordination. .....72

Figure 15. Hinge 1 and Hinge 2 Conformational Flexibility. .....74

Figure 16. Mechanisms of DSF-mediated Membrane Fission. .....77

Figure 17. Mechanisms of Mitochondrial Membrane Fusion. .....81

Figure 18. *Nostoc punctiforme* Life Cycle. .....85

Figure 19. BDLP Conformational Flexibility. .....88

Figure 20. Arrangement of Components within an Electron Microscope. .....98

Figure 21. Relationship Between Spatial Frequency and Phase Shift. .....108

Figure 22. Effect of Defocus on CTF Curves. .....109

Figure 23. The Effect of Envelope Functions on CTF Curves. .....110

Figure 24. TEV protease purification. .....136

Figure 25. Primer Design and Gibson Assembly. .....138

Figure 26. BDLP Expression and Localisation in *N. punctiforme*. .....154

Figure 27. Cryo-FIB-CLEM of hexII Nanoparticles in Hormogonia of a *N. punctiforme* BDLP-GFP Overexpression Strain. .....156

Figure 28. BDLP Association with hexII Nanoparticles. .....159

Figure 29. Size Exclusion Chromatography of BDLP. .....162

Figure 30. Optimisation of GMPPNP-bound BDLP Protein-Lipid Filaments for Cryo-EM. ....163

Figure 31. GMPPNP-bound BDLP Filament Bessel Order Assignment. .....165

Figure 32. GMPPNP-bound BDLP Helical and Local Refinements, Map Resolutions and Model Building. .....167

Figure 33. Nucleotide Coordination by GMPPNP-bound BDLP G-dimers. .....169

Figure 34. Hinge, Trunk, and Membrane Binding domain Conformations in $BDLP_{GMPPNP}$. ...171

Figure 35. BDLP PG Liposome Affinity. .....172

Figure 36. GMPPNP-bound BDLP-PG Liposome Filament Lattice Indexing and FSC Curve...175

Figure 37. $BDLP_{GMPPNP(PG)}$ Map and Model. .....176

Figure 38. $BDLP_{F583E}$ Membrane Binding and Constriction. .....178

Figure 39. Structural Predictions of Proteins in the BDLP Operon. .....182

Figure 40. Proposed Mitofusin Topologies. .....187

Figure 41. DSF Conserved Membrane Interface Features. .....188

Figure 42. NS-EM Analysis of PG Liposome-bound BDLP.....193

Figure 43. $BDLP_{GDP}$ Filament Indexing and Reconstruction. .....194

Figure 44. $BDLP_{GDP}$ Model Building and Tetramer Focussed Refinement.....196

Figure 45. GTP Hydrolysis-driven Trunk and MBD Conformational Changes. .....198

Figure 46. Architecture of the $BDLP_{GMPPNP}$ and $BDLP_{GDP}$ Filaments. .....200

Figure 47. Positioning of Conserved Catalytic Motifs in the $BDLP_{GMPPNP}$ G-dimer Relative to Tyrosine-137. .....202

Figure 48. MBD Helical Architecture and Lipid Channel Formation. .....203

Figure 49. Lipid Channel Surface Potential and Geometry. .....206

Figure 50. $BDLP_{GMPPNP(PG)}$ Filament Architecture. .....208

Figure 51. $BDLP_{GDP(L2)}$ Indexing and Filament Map. .....210

Figure 52. $BDLP_{GDP(L3)}$ Indexing and Filament Map. .....212

Figure 53. Thick GDP-bound BDLP Filament G-Dimer Interface Analysis. .....214

Figure 54. $BDLP_{GDP(L2)}$ and $BDLP_{GDP(L3)}$ Neck, Trunk and MBD Conformations. .....216

Figure 55. $BDLP_{GDP(L2)}$ and $BDLP_{GDP(L3)}$ Helical Models and Lipid Channels. .....220

Figure 56. NS-EM Analysis of BDLP Interactions with MGDG-containing Liposomes. .....221

Figure 57. Cryo-ET Analysis of BDLP-mediated Remodelling of MGDG Liposomes. .....221

Figure 58. Analysis of BDLP-generated Ordered Lipid Arrays. .....223

Figure 59. Multiple Super-Constricted BDLP Filaments Contributing to Ordered Lipid Arrays. .....226

Figure 60. BDLP-mediated Remodelling of Liposomes Lacking MGDG.....228

Figure 61. Model for Mitofusin-mediated Membrane Fusion. .....235

Figure 62. BDLP Homologues Identified by Structural Homology. .....237

Figure 63. Conservation of the BDLP MDD. .....239

Figure 64. Model of BDLP-Mediated Lipid Phase Changes. .....246

# List of Tables

Table 1. Amino Acid Abbreviations and Properties. 24

Table 2. Lipid Compositions of Red Blood Cell, *E. coli* and Thylakoid Membranes. 28

Table 3. Bacterial Growth Media Compositions. 129

Table 4. Antibiotic Stock Solution Concentrations. 129

Table 5. Buffer Compositions. 130

Table 6. Commercial Kits 131

Table 7. Commercial Lipids 131

Table 8. Bacterial Strains 131

Table 9. Plasmids 132

Table 10. Oligonucleotides 132

Table 11. Commercial Columns 133

Table 12. Commercial Chemicals 133

Table 13. SDS-PA Gel Recipe. 137

Table 14. PCR Reaction Components. 139

Table 15. Touchdown and Gradient PCR Protocols. 139

Table 16. Gibson Assembly Master Mix. 140

Table 17. Data Collection and Model Refinement Statistics. 149

Table 18. Strains, Plasmids and Primers used for *N. punctiforme* Strain Construction. 295

# List of Equations

Equation 1. Critical Packing Parameter. ..... 35

Equation 2. de Broglie Wave Equation. ..... 93

Equation 3. Relationship Between an Electron's Phase and Energy. ..... 99

Equation 4. Magnification in a microscope. ..... 100

Equation 5. Lorentz Force Law. ..... 100

Equation 6. Nyquist Frequency. ..... 102

Equation 7. Detector Quantum Efficiency (DQE). ..... 103

Equation 8. Spatial Frequency. ..... 106

Equation 9. Bragg's Law. ..... 107

Equation 10. The Wave Function. ..... 107

Equation 11. Contrast Transfer Function (CTF) ..... 108

# Abbreviations

| Abbreviation | Full Term |
|---|---|
| AMPPNP | Adenylyl Imidodiphosphate |
| APS | Ammonium Persulfate |
| ATP | Adenosine Triphosphate |
| AWI | Air-water Interface |
| BDLP | Bacterial Dynamin-like Protein |
| BDLP-GFP | BDLP tagged with a C-terminal Green Fluorescent Protein |
| $BDLP_{GDP}$ | Super-constricted GDP-bound BDLP Filament Structure, formed on PG Liposome Templates |
| $BDLP_{GDP(L2)}$ | Alternate GDP-bound BDLP Filament Structure, with wider diameter |
| $BDLP_{GDP(L3)}$ | Alternate GDP-bound BDLP Filament Structure, with widest diameter |
| $BDLP_{GMPPNP}$ | GMPPNP-bound BDLP Filament Structure, formed on ETE Liposome Templates |
| $BDLP_{GMPPNP(PG)}$ | GMPPNP-bound BDLP Filament Structure, formed on PG Liposome Templates |
| BSA | Bovine Serum Albumin |
| CA | Correspondence Analysis |
| CCD | Charge-coupled Detector |
| CFEG | Cold Field Emission Gun |
| CLEM | Correlative Light-electron Microscopy |
| Cryo-CLEM | Cryogenic-Corelative Light-Electron Microscopy |
| Cryo-EM | Cryogenic-Electron Microscopy |
| Cryo-ET | Cryogenic-Electron Tomography |
| Cryo-FIB | Cryogenic-Focussed Ion Beam |
| CTF | Contrast Transfer Function |
| CV | Cross Validation |
| DED | Direct Electron Detector |
| DGDG | Digalactosyldiacylglycerol |
| DNA | Deoxyribonucleic acid |
| DOPC | 1,2-dioleoyl-sn-glycero-3-phosphocholine |
| DOPG | 1,2-dioleoyl-sn-glycero-3-phospho-(1'-rac-glycerol) |
| DQE | Detector Quantum Efficiency |
| DRP | Dynamin-related Protein |
| DSF | Dynamin Super-family |
| DTT | Dithiothreitol |
| EDTA | Ethylenediaminetetraacetic acid |
| EM | Electron Microscopy |
| EMDB | Electron Microscopy Data Bank |
| ETE | *E. coli* Total Extract |
| FEG | Field Emission Gun |
| FIB | Focussed Ion Beam |
| FSC | Fourier Shell Correlation |
| Fzo | Fuzzy Onion Protein |
| G-dimer | GTPase domain Dimer |
| GBP | Guanylate Binding Protein |

| | |
|---|---|
| GDP | Guanosine Diphosphate |
| GFP | Green Fluorescent Protein |
| GMPPNP | Guanosine 5'-(β,γ-imido)triphosphate |
| GTP | Guanosine Triphosphate |
| HexII | Inverted Hexagonal (phase) |
| IHRSR | Iterative Helical Real Space Reconstruction |
| IMM | Inner Mitochondrial Membrane |
| IPTG | Isopropyl β-D-1-thiogalactopyranoside |
| IRB | Isothermal Reaction Buffer |
| LaB6 | Lanthanum Hexaboride |
| LB | Luria-Bertani |
| LC | Lipid Channel |
| LLPS | Liquid-Liquid Phase Separation |
| Lm | Lamellar (phase) |
| LoG | Laplacian of Gaussian |
| LUV | Large Unilamellar Vesicle |
| MBD | Membrane Binding Domain |
| MBP | Maltose Binding Protein |
| MDD | Membrane Displacement Domain |
| MES | 2-(N-morpholino)ethanesulfonic acid |
| Mfn1 | Mitofusin 1 |
| Mfn2 | Mitofusin 2 |
| MGDG | Monogalactosyldiacylglycerol |
| MGDG Liposomes | Liposomes comprising 20 % MGDG, 60 % PG and 20 % PC. |
| Milli-Q | Ultrapure Water |
| MLV | Multi Lamellar Vesicle |
| MSA | Multivariate Statistical Analysis |
| MTF | Modulation Transfer Function |
| NAD | Nicotinamide Adenine Dinucleotide |
| NMR | Nuclear Magnetic Resonance |
| NS-EM | Negative Stain-Electron Microscopy |
| OMM | Outer Mitochondrial Membrane |
| PA | Phosphatidic Acid |
| PC | Phosphatidylcholine |
| PCA | Principle Component Analysis |
| PCR | Polymerase Chain Reaction |
| PE | Phosphatidylethanolamine |
| PG | Phosphatidylglycerol |
| PG Liposomes | Liposomes comprising 80 molar % PG, and 20% PC |
| PLiMAP | Proximity-base Labelling of Membrane Associated Proteins |
| ROI | Region of Interest |
| SDS | Sodium Dodecyl Sulphate |
| SDS-PA | Sodium Dodecyl Sulphate Polyacrylamide |
| SDS-PAGE | Sodium Dodecyl Sulphate Polyacrylamide Gel Electrophoresis |
| SEC | Size Exclusion Chromatography |
| SGD | Stochastic Gradient Descent |

| | |
|---|---|
| SNR | Signal-to-noise Ratio |
| TBE | Tris-Borate-EDTA |
| TEM | Transmission Electron Microscope |
| TEMED | N,N,N',N'-Tetramethylethylenediamine |
| TEV | Tobacco Etch Virus |
| TM | Thylakoid Membrane |
| Tr-Cryo-EM | Time-resolved Cryogenic-Electron Microscopy |
| Tris | Tris(hydroxymethyl)aminomethane |
| TSS | Transcription Start Site |
| UA | Uranyl Acetate |

# Amino Acids

**Table 1. Amino Acid Abbreviations and Properties.**

| Amino Acid | Three-Letter Code | Single-Letter Code | Side Chain Properties |
|---|---|---|---|
| Alanine | Ala | A | Nonpolar, aliphatic |
| Arginine | Arg | R | Positively charged, basic |
| Asparagine | Asn | N | Polar, uncharged |
| Aspartic Acid | Asp | D | Negatively charged, acidic |
| Cysteine | Cys | C | Polar, uncharged, can form disulphide bonds |
| Glutamic Acid | Glu | E | Negatively charged, acidic |
| Glutamine | Gln | Q | Polar, uncharged |
| Glycine | Gly | G | Nonpolar, smallest side chain |
| Histidine | His | H | Positively charged, basic, can act as a proton donor or acceptor |
| Isoleucine | Ile | I | Nonpolar, aliphatic |
| Leucine | Leu | L | Nonpolar, aliphatic |
| Lysine | Lys | K | Positively charged, basic |
| Methionine | Met | M | Nonpolar, contains sulphur |
| Phenylalanine | Phe | F | Nonpolar, aromatic |
| Proline | Pro | P | Nonpolar, aliphatic, cyclic structure |
| Serine | Ser | S | Polar, uncharged |
| Threonine | Thr | T | Polar, uncharged |
| Tryptophan | Trp | W | Nonpolar, aromatic |
| Tyrosine | Tyr | Y | Polar, aromatic |
| Valine | Val | V | Nonpolar, aliphatic |

# Chapter 1: Introduction to Lipid Membranes, Membrane Remodelling Proteins, and the Dynamin Superfamily

Membrane remodelling is essential for life. It is central to a multitude of cellular processes including cell division, endocytosis, and membrane maintenance. This process is typically mediated by specialised proteins. Although extensively studied, the mechanisms of membrane remodelling, and the function of many known membrane remodelling machines, are not fully elucidated. Furthermore, non-bilayer lipid phases are emerging as significant alternate lipid arrangements for biological processes; however, the precise manner in which bilayers are remodelled into non-bilayer phases and the role of membrane remodelling proteins in this process remain unresolved. This chapter reviews the properties of lipids, including non-bilayer arrangements and their biological significance, as well as the principles of membrane remodelling. It also highlights important and widely conserved membrane-remodelling protein families, with a focus on the dynamin superfamily (DSF) and Bacterial Dynamin-Like Protein (BDLP) - a mitofusin homologue with unknown function. Finally, this chapter provides an overview of this study.

## 1.1 Biological Lipids Arrange into both Lamellar Bilayers and Non-bilayer Phases

Lipid membranes serve as fundamental structures in biology, not only separating the complex cellular milieu from the external environment but also providing a means for intracellular compartmentalisation. Membranes are selectively permeable and play crucial roles in maintaining chemical gradients (Altamura *et al.*, 2017), facilitating selective molecular transport (Shi *et al.*, 2019), and serving as platforms for various cellular processes (Boye *et al.*, 2017; Sasaki, Kubota & Minami, 2021; Cheng & Smith, 2019).

### 1.1.1 Lamellar Bilayers are a Thermodynamically Favoured Lipid Configuration that Act as Selectively Permeable Barriers

Biological membranes are comprised of lipids in a bilayer arrangement. Bilayers are a thermodynamically stable configuration that spontaneously forms from amphipathic lipid molecules in solution (caveats to this are described in Section 1.1.5). This arrangement is favoured due to the hydrophilic lipid headgroups facing the aqueous environments on both sides of the membrane, while the hydrophobic tails interact with each other within the bilayer's core (Figure 1A) (Harayama & Riezman, 2018; Sezgin *et al.*, 2017). Within the bilayer, lipids are able to freely diffuse, making bilayers a fluid environment (Singer & Nicolson, 1972).

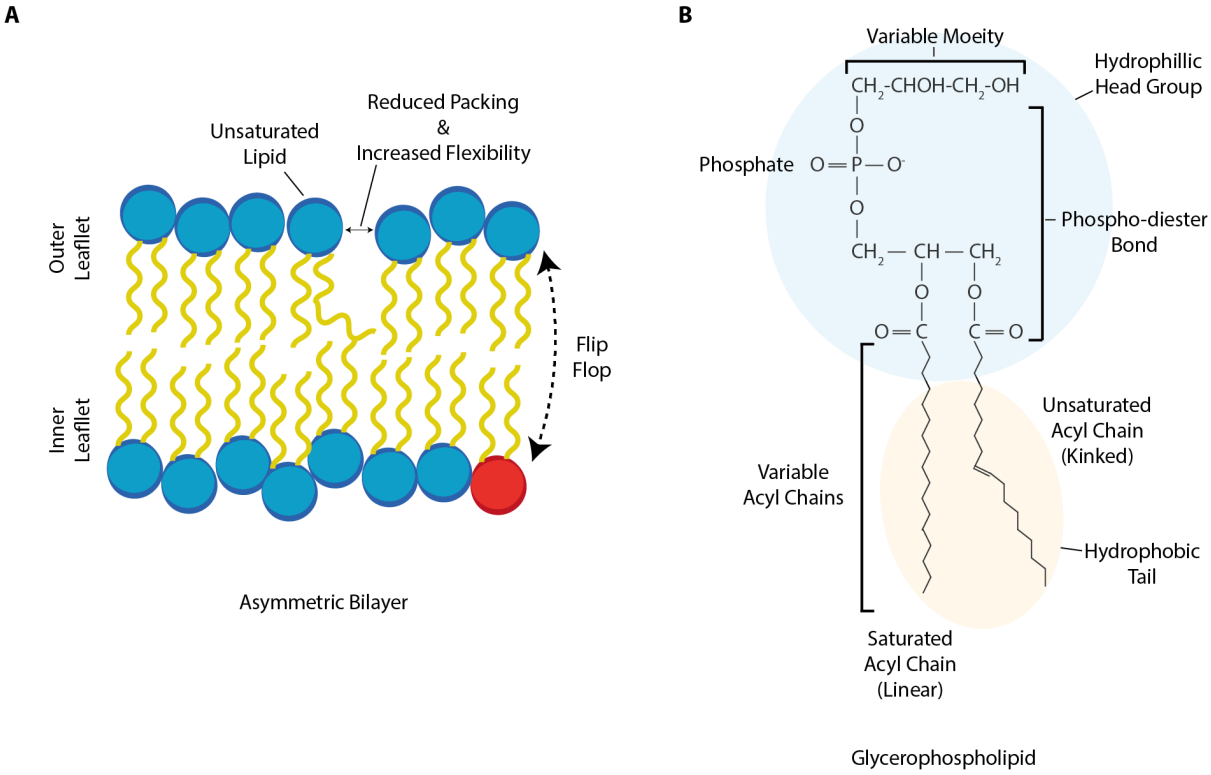


**Figure 1. Lipid Bilayer Arrangement and Glycerophospholipid Chemical Structure**
Lipids form bilayers via thermodynamically favourable packing of their hydrophobic tail groups. **A,** Schematic of an asymmetric lipid bilayer, highlighting the effect of unsaturated acyl chains on packing and flexibility. **B,** Chemical structure of phosphatidylglycerol as an example of glycerophospholipid structure.

The hydrophobic interior of the lipid bilayer renders it impermeable to polar molecules and ions, allowing cells and intracellular compartments to regulate their internal composition

independently of the external environment. However, biological membranes are not absolute barriers. Certain crucial small molecules, such as oxygen, can passively diffuse through the bilayer and such permeability can be influenced by lipid composition (Dotson *et al.*, 2017). Selective permeability to larger molecules is achieved via integral membrane proteins that facilitate the controlled translocation of specific molecules. For instance, aquaporins form water-selective channels that enable rapid water movement across membranes while retaining impermeability to other small molecules and ions (Kreida & Törnroth-Horsefield, 2015).

There is a high energetic penalty for lipids to switch leaflet within the bilayer (a process known as flip-flop - Figure 1A) (Williamson & Olmsted, 2018). As a result, the bilayer arrangement allows lipid composition asymmetry between the inner and outer leaflets. Asymmetry serves important functional roles, such as providing leaflets with different biophysical properties (Lorent *et al.*, 2020), modulating membrane protein structure (Matsuki, Iwamoto & Oiki, 2024; Lorent *et al.*, 2020), and involvement in signalling processes (Bevers & Williamson, 2016). The maintenance of this asymmetry is crucial for cellular homeostasis and is actively regulated by various membrane proteins, such as flippases and scramblases (Bai *et al.*, 2020; Bevers & Williamson, 2016). These integral membrane proteins facilitate the translocation of specific lipids between leaflets to achieve asymmetry.

### 1.1.2 Bilayer Properties are Modulated by their Lipid Composition and Specialised Lipids have Roles in Various Biological Processes

In biology, glycerophospholipids constitute a significant portion of the lipid diversity and are the basis of numerous lipid bilayers, as highlighted by the lipid compositions of fundamental bilayers in Table 2. Glycerophospholipids are composed of glycerol, two fatty acid hydrophobic chains, a phosphate group, and a variable head group attached to the phosphate (Figure 1B). The fatty acids are esterified to the first and second carbons of glycerol, while the phosphate group is esterified to the third carbon (van Meer, Voelker & Feigenson, 2008). Whilst glycerophospholipids are described here, the basic structure of a hydrophilic group that interacts with the aqueous environment covalently linked to a hydrophobic group that packs into the bilayer core applies to all lipids.

**Table 2. Lipid Compositions of Red Blood Cell, *E. coli* and Thylakoid Membranes.**
Data derived from Kobayashi, Yoshihara & Kubota-Kawai, 2023; Melzak *et al.*, 2020; Dodge & Phillips, 1967; Sohlenkamp & Geiger, 2016; and Raetz & Dowhan, 1990.

| Lipid | | Head Group Net Charge | Composition (%) | | |
|---|---|---|---|---|---|
| | | | Red Blood Cell | *E. coli* | Thylakoid |
| Glycerophospholipid | Phosphatidylethanolamine (PE) | 0 | 15 | 75 | - |
| | Phosphatidylglycerol (PG) | -1 | 1 | 20 | 11 |
| | Phosphatidylserine (PS) | -1 | 8 | trace | - |
| | Phosphatidylcholine (PC) | 0 | 16 | - | - |
| Other | Sphingomyelin | 0 | 14 | - | - |
| | Monogalactosyldiacylglycerol (MGDG) | 0 | - | - | 43 |
| | Digalactosyldiacylglycerol (DGDG) | 0 | - | - | 26 |
| | Sulfoquinovosyldiacylglycerol (SQDG) | -1 | - | - | 20 |
| | Cholesterol | 0 | 45 | - | - |
| | Cardiolipin | -2 | - | 5 | - |
| | Other | - | trace | trace | trace |

Biological membranes comprise a diverse range of lipids in addition to glycerophospholipids, each playing essential roles in membrane structure and function. In higher eukaryotes, cholesterol, a sterol with a planar rigid structure, orders the surrounding acyl chains of neighbouring lipids to decrease membrane fluidity and expand bilayer width (Czub & Baginski, 2006). Cardiolipin, found in bacterial and mitochondrial membranes, possesses four acyl chains, which aids in decreasing membrane fluidity (Paradies *et al.*, 2014), and its conical shape also contributes to negative curvature (Section 1.1.5).

Specialised lipids are crucial for protein function. In mitochondria, cardiolipin alters the helical architecture of dynamin-related protein 1 (Drp1) polymers to activate their membrane fission activity (Francy *et al.*, 2017) and stabilises the respiratory supercomplex (Hryc *et al.*, 2023). The galactolipids monogalactosyldiacylglycerol (MGDG) and digalactosyldiacylglycerol

(DGDG) are necessary for efficient photosynthesis in thylakoid membranes (Kobayashi, 2016). Low abundance lipids also play important roles. For example, the voltage-dependent calcium ion import channel TRPV5 is activated by phosphatidylinositol 4,5-bisphosphate (PIP2) (Ebner *et al.*, 2023). Switches between phosphatidylinositol 4-phosphate (PI(4)P) and phosphatidylinositol 3-phosphate (PI(3)P) presence in lysosomal membranes are also part of signalling networks that dictate lysosome function (Ebner *et al.*, 2023).

Despite lipids being able to freely diffuse, certain lipids can co-localise into lipid rafts that create membrane patches with distinct biophysical and chemical properties, based on their lipid composition (Cheng & Smith, 2019). This enhances various lipid-mediated processes and can organise and cluster proteins with affinity for specific lipid rafts (Ouweneel, Thomas & Sorci-Thomas, 2020; Lorent *et al.*, 2017). For instance, glycosphingolipid rafts in outer mitochondrial membranes are crucial for the recruitment of the fission machine Dynamin-like Protein 1 (DLP1) and subsequent mitochondrial fission (Ciarlo *et al.*, 2010). Cholesterol lipid rafts are well-known for their roles in signalling and disease (Isik & Cizmecioglu, 2023; Murai, 2012) and are implicated in SARS-CoV-2 entry into cells due to their ability to recruit and cluster receptors (Palacios-Rápalo *et al.*, 2021). The organisation of lipids into protein-associated membrane domains is not limited to eukaryotic membranes (Dupuy, Gutierrez & Neyrolles, 2023; Bramkamp & Lopez, 2015), and contributes to the β-lactam antibiotic resistance of methicillin-resistant *S. aureus* (García-Fernández *et al.*, 2017) and the assembly of its type-7 secretion system – a key pathogenicity factor (Mielich-Süss *et al.*, 2017).

The fluidity and rigidity of bilayers are primarily determined by the length and degree of saturation of acyl chains and the overall lipid shape. Lipids with saturated, and therefore more linear acyl chains pack more tightly, increasing membrane rigidity, while those with unsaturated, and therefore more kinked chains, promote fluidity (Figure 1A). Lipid rafts of loosely packing lipids with high flexibility can assist membrane remodelling events such as vesiculation (Manni *et al.*, 2018).

### 1.1.3 Lipid Bilayers Provide Cells with Barriers to their External Environment

The lipid world hypothesis posits that the spontaneous arrangement of amphipathic lipid molecules into spherical bilayers (liposomes) acted as the catalyst for development of cellular life (Subbotin & Fiksel, 2023). Consequently, a primary function of lipid bilayers is the

formation of a continuous barrier between the external environment and the organised cellular milieu – the cytoplasmic membrane. Eukaryotic cells exclusively rely on the cytoplasmic membrane as their primary barrier, as they often lack the additional extra-cytoplasmic membrane protective layers found in bacterial and archaeal cell envelopes. It is noted that additional eukaryotic external protective barriers do exist, and include the polysaccharide-based cell walls of plants and fungi (Colosimo *et al.*, 2021) and proteinaceous extracellular matrices secreted by eukaryotes (Naba, 2024). Yet overall, the cytoplasmic membrane of eukaryotes is responsible for several critical functions.

Given the cytoplasmic membrane is essential for cellular integrity, it is also utilised for immunogenic and programmable cell death. For instance, disruption of the cytoplasmic membrane by peptides is crucial for cancer cell removal through a form of immunogenic cell death known as poroptosis (Li *et al.*, 2022). The cytoplasmic membrane also functions as a foundation for external signal transduction and cell-cell communication (Tetsch & Jung, 2009) and provides a substrate for the cytoskeleton, with actin remodelling of the membrane playing a pivotal role in maintaining cell shape and cellular motility (Svitkina, 2018). The cytoplasmic membrane's impermeability to polar ions allows cells to establish ion gradients across the bilayer, particularly for calcium, sodium, and potassium ions. These gradients generate a membrane potential that is required for nutrient uptake (Lu *et al.*, 2023) and the propagation of action potentials in neurons (Bean, 2007).

Bacterial and archaeal cell envelopes typically have more 'complex' arrangements. This complexity and the role of lipid bilayers are briefly reviewed in the following sections.

#### 1.1.3.1 Gram-negative (Diderm) Cell Envelopes Comprise Two Lipid Bilayers

Bacterial Gram-negative cell envelopes comprise two distinct lipid bilayers separated by a periplasm containing a continuous peptidoglycan sacculus (Figure 2A) that essential for maintaining cell shape (Silhavy, Kahne & Walker, 2010). The inner bilayer is predominantly composed of phospholipids (Raetz & Dowhan, 1990) and serves as a platform for various cellular processes, analogous to eukaryotic cytoplasmic membranes. The inner membrane is also the site of respiration. Bilayer impermeability to protons allows a high proton concentration to be maintained in the periplasm and the consequent proton gradient

established across the inner membrane stores energy that is harnessed by ATPsynthases (Kaila & Wikström, 2021).

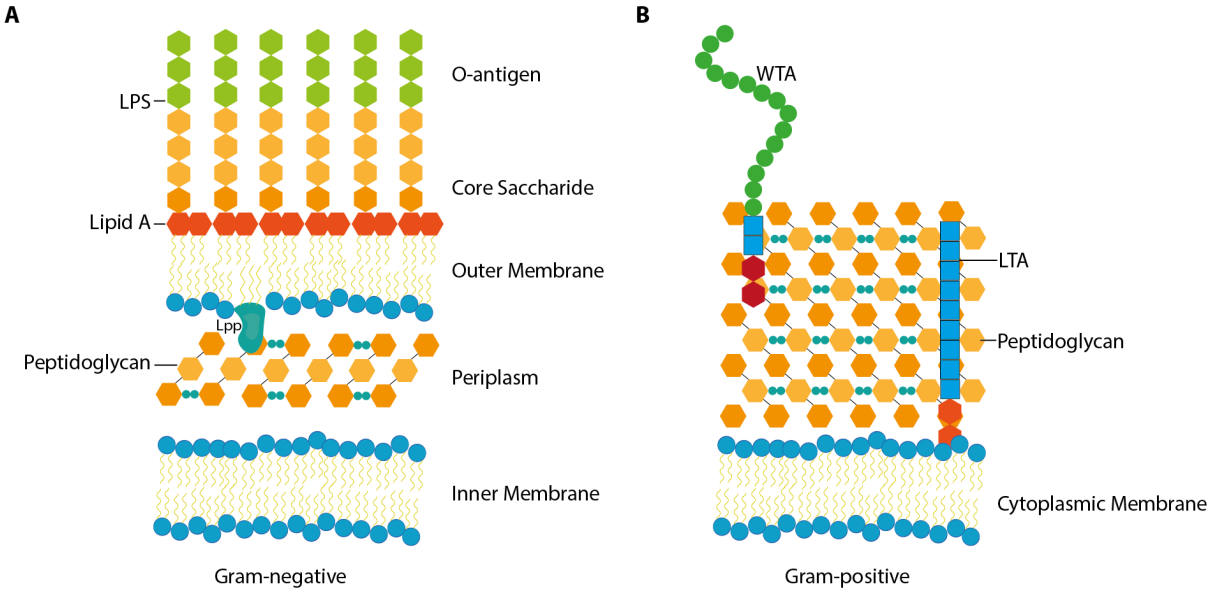


**Figure 2. Bacterial Cell Envelopes.**
**A,** Gram-negative cell envelope. Lpp is the inner-leaflet embedded lipoprotein that covalently cross-links the outer membrane to the peptidoglycan sacculus. LPS = lipopolysaccharide. **B,** Gram-positive cell envelope. LTA = lipoteichoic acid, WTA = wall teichoic acid. Figure adapted from (Silhavy, Kahne & Walker, 2010).

The peptidoglycan layer is a mesh-like structure composed of repeating units of N-acetyl glucosamine-N-acetyl muramic acid disaccharides cross-linked by pentapeptide side chains (Vollmer, Blanot & De Pedro, 2008). The elongasome guides peptidoglycan synthesis during cell elongation (Shambhavi, Kumar & Manjula, 2021) and the divisome guides peptidoglycan synthesis to form the septum during cell division (Scheffers & Pinho, 2005). The peptidoglycan sacculus is a single large polymer that determines cell shape and prevents lysis due to turgor pressure (Vollmer, Blanot & De Pedro, 2008).

The outer membrane is an asymmetric bilayer with distinct composition and functions. Its inner leaflet comprises phospholipids, whilst the outer leaflet consists of lipopolysaccharides (LPS) anchored by their Lipid A moiety, which possesses six or seven acyl chains (Silhavy, Kahne & Walker, 2010). LPS is a glucosamine disaccharide with a polysaccharide core and an

O-antigen and contributes to the barrier function of the outer membrane (Raetz & Whitfield, 2002). This structure renders the outer membrane relatively impermeable to hydrophobic molecules and large hydrophilic compounds. The outer membrane is covalently cross-linked to peptidoglycan by the inner-leaflet embedded lipoprotein Lpp (Mathelié-Guinlet *et al.*, 2020). The outer membrane can form extracellular outer-membrane vesicles with functions pertaining to virulence, antibiotic degradation and stress response (Schwechheimer & Kuehn, 2015).

#### 1.1.3.2 Gram-Positive Cell Envelopes Comprise a Single Lipid Bilayer and Larger Peptidoglycan Sacculus

In contrast to Gram-negative bacteria (diderms), Gram-positive bacteria (monoderms) possess a cell envelope with only one inner membrane (Figure 2B) (Silhavy, Kahne & Walker, 2010). Monoderms likely evolved from diderms via the loss of outer membrane tethering proteins (Witwinowski *et al.*, 2022). The peptidoglycan layer is significantly thicker in monoderms, measuring up to 100 nm (Pasquina-Lemonche *et al.*, 2020; Silhavy, Kahne & Walker, 2010). Surface proteins covalently linked to the peptidoglycan frequently function as key pathogenicity factors (Fischetti, 2019).

Teichoic acids are essential components of the Gram-positive cell wall. Wall teichoic acids (WTAs) are covalently attached to the peptidoglycan layer via a phosphodiester linkage to the C6 hydroxyl of N-acetylmuramic acid residues. They comprise a disaccharide linkage unit with an appended polyglycerolphosphate chain, containing up to 60 repeats (Brown, Santa Maria & Walker, 2013). Lipoteichoic acids (LTAs) are anchored to the cytoplasmic membrane via glycolipids and consist of polyglycerolphosphate polymers that extend from the cell surface into the peptidoglycan layer (Silhavy, Kahne & Walker, 2010). Both WTAs and LTAs provide negative charge, which facilitates cation capture (Hughes, Hancock & Baddiley, 1973), biofilm formation, and adherence (Gross *et al.*, 2001).

#### 1.1.3.3 Archaea Exhibit Diverse Cell Envelope Structures

Archaeal cells exhibit diverse morphologies and cell envelope arrangements, and their genomes encode homologues of bacterial and eukaryotic membrane remodelling proteins (van Wolferen *et al.*, 2022; Albers & Meyer, 2011; Liu *et al.*, 2021b). Due to a paucity of genetically tractable systems, archaea remain poorly understood and under-researched as

the third domain of life. Therefore many consider archaea to be the final frontier of cell biology (Laursen, Bowerman & Luger, 2021; van Wolferen *et al.*, 2022).

Archaeal lipids possess ether linkages between hydrophilic and hydrophobic groups, in contrast to the di-ester linkages of most bacterial and eukaryotic lipids. Archaeal membranes also contain tetraether lipids that span both leaflets of the bilayer (Caforio & Driessen, 2017). This lipid-divide between archaea and eukaryotes and bacteria raises questions regarding the origin of life and the last universal common ancestor. Archaea possess only a single cytoplasmic membrane, but exhibit diverse surrounding structures, including proteins that forms a regular lattice known as the S-layer (Gambelli *et al.*, 2024) and layers of pseudopeptidoglycan (Albers & Meyer, 2011; van Wolferen *et al.*, 2022).

### 1.1.4 Bilayers are also used for Intracellular Compartmentalisation

Lipid bilayers also play a crucial role in intracellular compartmentalisation, enabling cells to organise and segregate biochemical processes. Such compartmentalisation is extensive in eukaryotes. Examples include the double-membraned nucleus, endoplasmic reticulum (ER), Golgi body, mitochondria, peroxisomes, the endosome, and lysosome. The nucleus houses genetic material. The endoplasmic reticulum (ER), a single-membraned organelle continuous with the perinuclear space, is involved in membrane protein synthesis and folding (Gemmer *et al.*, 2023; Deolal *et al.*, 2024). In conjunction with the Golgi body, the ER is required for lipid synthesis and lipid and secretory protein transport to the cytoplasmic membrane (Schwarz & Blower, 2016). Furthermore, the ER coordinates both mitochondrial fission and fusion events (Gatti *et al.*, 2024). Mitochondria (Section 1.1.10) and chloroplasts (Section 1.1.11) are essential for bioenergetics, housing oxidative phosphorylation and oxygenic photosynthesis machinery, respectively. Peroxisomes, formed from the ER or existing peroxisomes, contribute to lipid metabolism, redox balance, and immune defence through synthesis of molecules that activate inflammatory responses (Kumar *et al.*, 2024). Endosomes, derived from the cytoplasmic membrane by endocytic vesiculation or phagocytosis, play a vital role in sorting and directing internalised material. Early endosomes serve as sorting hubs, where endosome cargo can be targeted for recycling back to the plasma membrane or degradation via lysosomes (O'Sullivan & Lindsay, 2020).

While bacteria generally have fewer intracellular compartments, some species have evolved specialised membrane-bound structures. Many cyanobacteria have intracellular thylakoid membranes to increase the area available for photon energy harvest (Section 1.1.11). Additionally, intracellular bilayers generated from the cytoplasmic membrane have been observed in *Gloeobacter sulfurreducens.* These bilayers house respiratory complexes to increase the efficiency of respiration, reminiscent of mitochondria used to compartmentalise oxidative phosphorylation in eukaryotes (Howley *et al.*, 2023). Anaerobic ammonium oxidising bacteria that convert ammonium and nitrate ions into nitrogen, utilise the electrons from this oxidation to generate proton motive force for ATP synthesis. These processes are confined to large internal membrane organelles known as anammoxosomes (Claret Fernández, Mesman & van Niftrik, 2020). Magnetotactic bacteria produce magnetosomes - membrane-bound crystals of magnetic iron minerals that align the cell with the Earth's magnetic field to facilitate navigation (Uebe & Schüler, 2016).

These diverse examples highlight the versatility and importance of lipid bilayers in cellular organisation and necessitate sophisticated and coordinated membrane remodelling proteins.

#### 1.1.4.1 Intracellular Compartmentalisation can also be Achieved by Liquid-liquid Phase Separation (LLPS)

While lipid bilayers constitute the foundation for numerous cellular compartments, liquid-liquid phase separation (LLPS) represents an alternative mechanism for intracellular compartmentalisation without lipid bilayers. LLPS is a process whereby specific molecules concentrate into a gel-like compartment that coexists with the surrounding liquid environment, forming membraneless organelles or condensates (Banani *et al.*, 2017). Phase separation is driven by multivalent interactions between proteins, frequently mediated by intrinsically disordered regions or low-complexity domains (Boeynaems *et al.*, 2018).

The significance of LLPS in biology is exemplified by its role in various cellular processes and pathologies (Wang *et al.*, 2021). For instance, LLPS of the bacterial transcription termination factor Rho is essential for adaptation of *B. thetaiotaomicron* gene expression to changes in its host mammalian gut environment (Krypotou *et al.*, 2023). Notably, biomolecular condensates can interact with lipid bilayers, leading to membrane deformations and remodelling (Yuan *et al.*, 2021). Membrane composition can also influence the behaviour of condensates (Babl *et*

*al.*, 2022). Therefore, LLPS of membrane-binding proteins represents an emerging mechanism of membrane remodelling beyond many of the structural scaffolds discussed in Section 1.2.1.

### 1.1.5 Lipids can Arrange into Non-bilayer Phases and the Phase Lipids Spontaneously Adopts is Determined by their Shapes

Despite lipid bilayers being fundamental to cellular life, not all lipids spontaneously form bilayers. Lipid shape determines how a homogenous sample of the lipid spontaneously arranges in three-dimensional space (Figure 3) (Cullis & De Kruijff, 1979). The planar bilayer arrangement of lipids discussed thus far is referred to as the lamellar (Lm) phase, and cylindrical-shaped lipids such as phosphatidylglycerol (PG) spontaneously assemble into Lm phase bilayers under physiological conditions (Figure 3A). Under the same conditions, conical-shaped lipids spontaneously adopt non-Lm phases (Huang & Gui, 2018). However, a lipid's shape does not restrict the lipid to a specific phase, as the phase lipids adopt is influenced by temperature and the hydration of their polar head groups (Fong, Hanley & Boyd, 2009; Wadsten-Hindrichsen *et al.*, 2007; Huang & Gui, 2018). Conical lipids incorporated into a Lm phase-favouring biologically relevant lipid mixture also adopt the lipid ensemble's bilayer configuration. The shape of a lipid can be described by its critical packing parameter (CPP) (Equation 1).

**Equation 1. Critical Packing Parameter.**
Where CPP is the critical packing parameter, V is the hydrophobic chain volume, a is the cross-sectional area of the hydrophilic head group, and l is the hydrophobic chain length (Huang & Gui, 2018).

$$CPP = \frac{V}{a \times l}$$

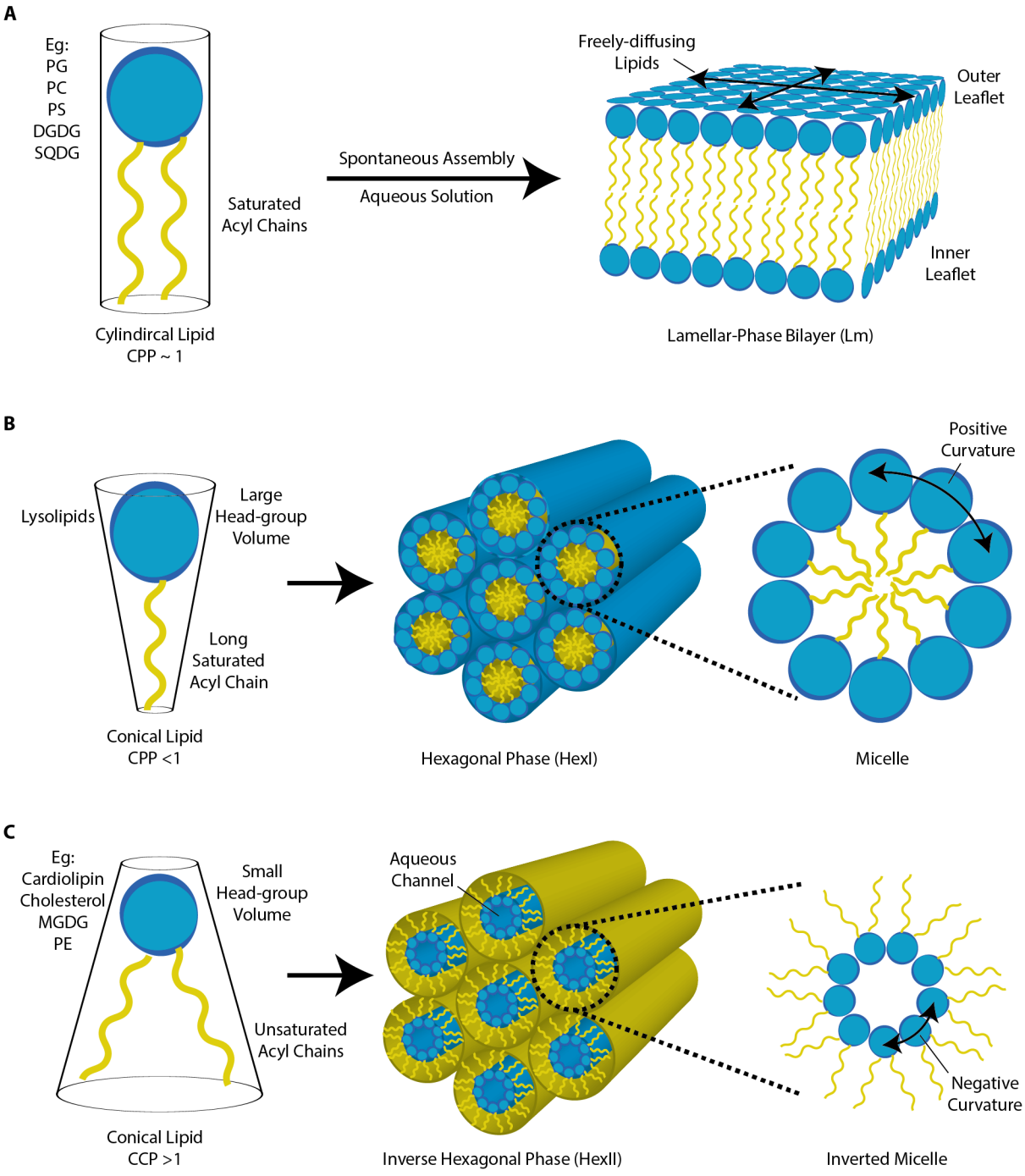


**Figure 3. Lipid Shape and Phase Relationships.**
The shape or Critical Packing Parameter (CPP) of a lipid determines the phase that a homogenous sample of the lipid spontaneously adopts. **A,** Cylindrical lipids (CPP = 1) spontaneously form lamellar phase bilayers under physiological conditions. Lipids can freely diffuse within leaflets of the bilayer. **B,** Conical lipids with CPP <1 spontaneously form micelles and the hexagonal phase under physiological conditions, owing to their preference for positive curvature. **C,** Conical lipids with CPP >1 spontaneously form inverted micelles in the inverse hexagonal phase, owing to their preference for negative curvature.

The conical shape of non-bilayer lipids induces curvature, resulting non-bilayer phases. Lipids with a CPP <1 exhibit a positive mean curvature, attributable to their relatively larger hydrophilic head groups. Lysolipids are common positive-curvature inducing lipids, as they comprise only a single acyl chain, in contrast to the two acyl chains of canonical glycerophospholipids (Fuller & Rand, 2001). The degree of acyl chain saturation also influences the overall shape of a lipid, with more linear saturated chains contributing to cylindrical or positive curvature-inducing conical shapes (Szule, Fuller & Rand, 2002). Under physiological conditions, positive mean curvature lipids spontaneously form micelles, coated with hydrophilic head groups (Figure 3B). Cylindrical micelles can arrange into a hexagonal lattice with long range 2D order (HexI phase). Furthermore, positive curvature lipids lend themselves to formation of the discontinuous and bicontinuous cubic phases (Section 1.1.6).

Lipids with a CCP >1, exhibit a negative mean curvature. Lipids such as MGDG and PE induce negative curvature due to their relatively smaller head groups (van Meer, Voelker & Feigenson, 2008). Under physiological conditions, such lipids form inverted water-filled cylindrical micelles that arrange in an inverted hexagonal lattice of tubular structures (HexII phase) (Figure 3C). Mean negative-curvature lipids also favour the reverse discontinuous and reverse bicontinuous cubic phases (Huang & Gui, 2018; Rajput *et al.*, 2022).

The biophysical properties of lipids are increasingly recognised as equally significant to their function as their chemical properties, as demonstrated by the observation that viable *E. coli* can be derived from mutants where PE is replaced by MGDG (Wikström *et al.*, 2004). MGDG is exogenous to *E. coli* and chemically distinct (PE is zwitterionic and negatively charged, whereas MGDG possesses a neutral galactose sugar moiety); however, they share the same conical shape and similar CPPs, which facilitates their interchangeability. The biological relevance of non-bilayer lipids and phases is examined in the following sections.

### 1.1.6 Lipids can form Highly Curved Bilayer Arrangements in a Regular Cubic Lattice known as the Cubic Phase

Lipids in the cubic phase are arranged into highly curved and interwoven bilayers adopting a regular cubic lattice (Rajput *et al.*, 2022). Experimentally, the cubic phase is useful for crystallisation of membrane proteins, owing to its regular lattice structure (Caffrey, 2015). Bicontinuous cubic phases contain continuous water channels separated by curved bilayers,

whereas discontinuous cubic phases can be conceptualised as micelles arranged in a cubic lattice such that they also form highly curved bilayers (Huang & Gui, 2018). Non-bilayer lipid content plays a significant role in promoting the cubic phase as they facilitate highly curved bilayers. The cubic phase is formed by fusion of stacked bilayers (Demurtas *et al.*, 2015). This process also requires high bilayer curvature and is promoted by high local conical lipid concentration (Section 1.1.8.1) (Fan *et al.*, 2016). In addition to conical lipids, plasmogens can promote the formation of cubic phases. Plasmogens are characterised by the substitution of canonical phospholipid di-ester phosphate bonds with vinyl ether bonds, and long polyunsaturated chains (Deng *et al.*, 2009; Braverman & Moser, 2012). Protein-lipid interactions also play a crucial role in the formation of the cubic phase (Almsherqi, Margadant & Deng, 2010).

#### 1.1.6.1 The Cubic Phase has Important Biological Functions

The cubic phase has been observed in association with bilayers at the plasma, mitochondrial, chloroplast and endoplasmic reticulum membranes (Deng & Almsherqi, 2015). The close relationship of cubic and Lm phases is highlighted in chloroplasts, where Lm-to-cubic (Kowalewska *et al.*, 2016) and cubic-to-Lm (Zhan, Lv & Deng, 2017) phase transitions have been observed. Furthermore, mitochondria are known to promote the cubic phase via upregulation of long-chain fatty acids (Deng *et al.*, 2009), suggesting significant functional implications of the cubic phase.

In mitochondria, the inherent ordered lattice of cubic phases may provide an alternative means of organisation to the cristae structure adopted by inner-mitochondrial membranes (Section 1.1.10) (Zhan, Lv & Deng, 2017). Additionally, the cubic phase is involved in mitochondrial stress responses (Deng & Almsherqi, 2015). Mitochondrial oxidative stress causes production of reactive oxygen species (damaging free-radicals). Oxidative stress is also associated with a Lm-to-cubic phase transitions (Deng, Kohlwein & Mannella, 2002). Moreover, the cubic phase is promoted in the G2 phase of cell proliferation, a period characterised by high mitochondrial activity in preparation for cytokinesis and consequently elevated levels of reactive oxygen species (Kong *et al.*, 2020). The cubic phase offers protection against reactive oxygen species, as the bilayers that separate the internal water channels are relatively impermeable to reactive oxygen species. This can provide protection

to mitochondrial RNAs that are easily damaged by reactive oxygen species (Deng & Almsherqi, 2015). The plasmogens that promote and are enriched in mitochondrial cubic phases also act as sacrificial oxidants to remove reactive oxygen species, owing to their ether bonds (Braverman & Moser, 2012; Brites, Waterham & Wanders, 2004). The mitochondrial membrane architecture and roles of other non-bilayer phases are elaborated upon in Section 1.1.10.

Viruses also utilise the cubic lipid phase. During viral replication cubic phase structures may protect nascent pre-assembly viral components from host immune responses (Deng *et al.*, 2010) – analogous to mitochondrial cubic membranes protecting mitochondrial RNA. Evidence also suggests that the regular lattice of the cubic phase functions as a secure viral assembly platform (Almsherqi *et al.*, 2005). Numerous viruses manipulate host cholesterol metabolism (Mackenzie, Khromykh & Parton, 2007), suggesting cholesterol's conical shape may be instrumental in viruses promoting cubic phase formation (Deng *et al.*, 2010).

### 1.1.7 Non-bilayer Lipids Modulate the Material Properties of Lamellar Bilayers

Whilst non-bilayer phases have important biological roles (Section 1.1.8), non-bilayer lipids also have significant biophysical properties when incorporated into Lm phase bilayers. The fluid-mosaic model of Lm phase bilayers conceptualised the bilayer as a freely diffusing but relatively inert assembly platform for membrane proteins (Singer & Nicolson, 1972; Nicolson, 2014). However, it did not account for the effect of lipid-protein interactions or the impact of non-bilayer lipids (Nicolson, 2014; Garab *et al.*, 2022). To acquire a more comprehensive understanding of the bilayer, it must be understood on the mesoscopic scale. This combines the atomistic chemical interactions, such as repulsive forces and lipid-protein interactions, with the wider-scale long-range forces of the lipid and protein ensemble (Brown, 2012).

Whereas non-bilayer lipids are well-documented for their direct interactions with membrane proteins, contributing to membrane protein function (Acehan *et al.*, 2011a; Brown, 2012; van den Brink-van der Laan, Antoinette Killian & de Kruijff, 2004), the long range interactions of the lipid ensemble are equally important for membrane protein function. This phenomenon is described by the lateral pressure (de Kruijff, 1997), flexible surface (Brown, 2012), and dynamic exchange (Garab *et al.*, 2000, 2022) models of bilayers. In these related models, non-bilayer curvature-inducing lipids contribute to the elastic stress of a bilayer, as they are

unfavourably maintained in the Lm phase. Repulsive interactions between acyl chains due to short-range steric forces within the bilayer are exacerbated by non-bilayer lipids help in the Lm phase. This introduces frustration energy into the bilayer's hydrophobic core (Figure 4) (Brown, 2012). Frustration exerts lateral pressure in the bilayer, which can directly modulate protein energetics and conformation or oligomerisation state (Botelho *et al.*, 2006; Kirchhoff *et al.*, 2007; Frewein *et al.*, 2016).

In addition to non-bilayer lipids modulating the frustration and lateral pressure of a bilayers, proteins can also modulate this phenomenon by inducing bilayer curvature (Brown, 2012). For instance, photon absorption by rhodopsin induces a conformational change that imparts curvature stress on the bilayer, which stores free energy as frustration. This frustration exerts lateral pressure that drives the packing of rhodopsin into an active oligomeric conformation (Botelho *et al.*, 2006).

The frustration of a bilayer system is higher when a greater proportion of non-bilayer lipids are present. As frustration and lateral pressure can modulate protein function and oligomerisation state, the proportion of non-bilayer lipids in a membrane can be used to modulate protein function and is considered a mechanism of homeostasis (Garab *et al.*, 2000, 2022; Frewein *et al.*, 2016). Such homeostasis is dependent on lipid polymorphism - the capacity of bilayer lipids to exit the bilayer and adopt alternate phases (van Eerden *et al.*, 2015), while also being able to reincorporate into bilayers (Simidjiev *et al.*, 2000). The mechanisms of such homeostasis are further elaborated in Section 1.1.9.

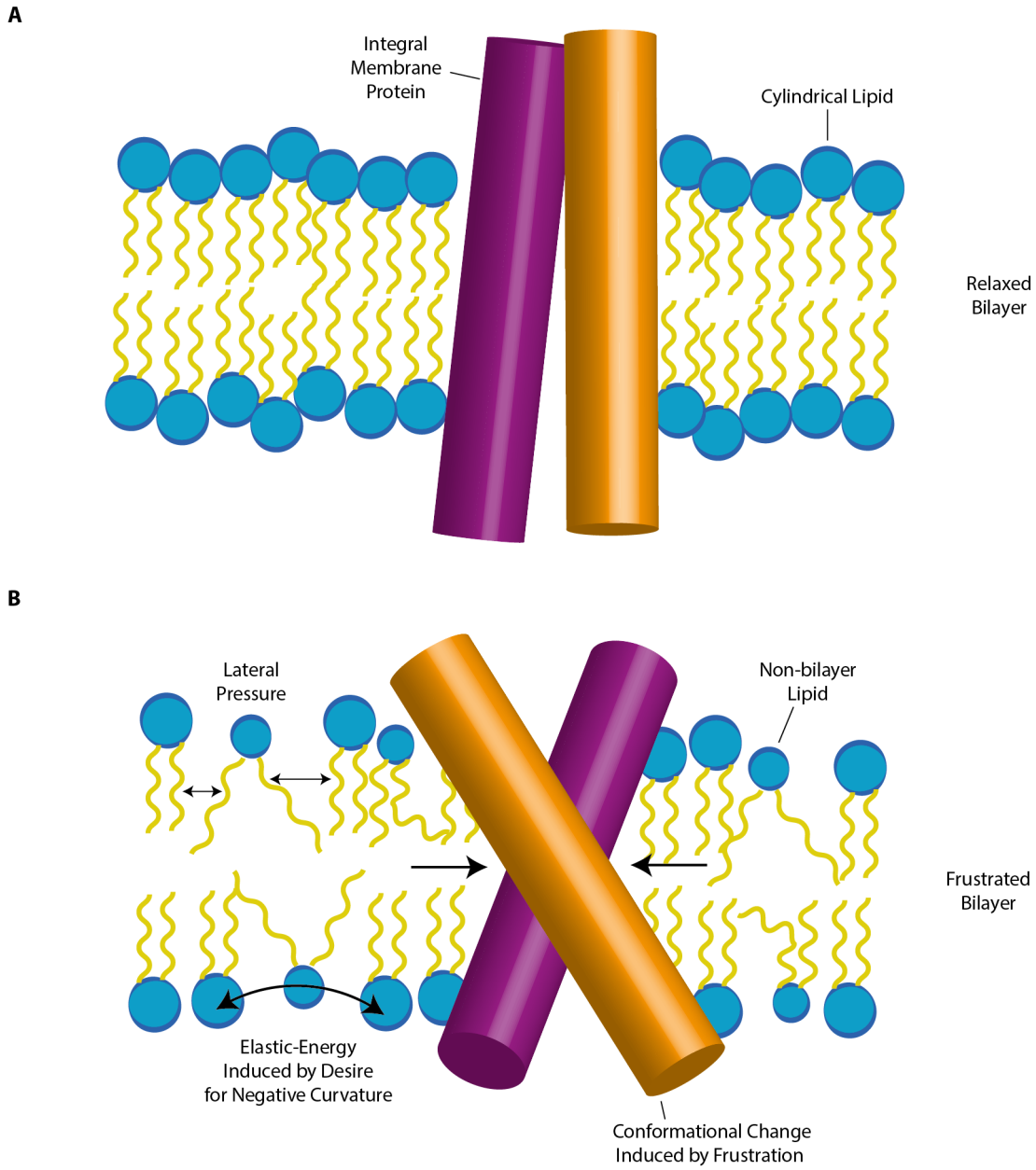


**Figure 4. Non-bilayer Lipid-induced Lateral Pressure and Frustration.**
**A,** A relaxed lamellar bilayer comprised of only cylindrical lipids. **B,** Non-bilayer lipids within the bilayer generate lateral pressure via their hydrophobic chain interactions. The ensemble long-range interactions can induce conformational changes in integral membrane proteins.

### 1.1.8 Non-bilayer Lipids and Phases have Important Biological Functions

Non-bilayer lipids and phases have critical roles in energy transducing membranes (Section 1.1.9) and during the fission and fusion of bilayers (Section 1.1.8.1). Their curvature-inducing properties also have significance for a variety of other cellular processes.

The planar structure of cholesterol is known to reduce the flexibility of bilayers by ordering the surrounding acyl chains (Czub & Baginski, 2006), yet cholesterol also induces negative curvature as it is a conical non-bilayer lipid (Chen & Rand, 1997). Combined cholesterol and PC (a cylindrical lipid) lipid rafts function as fusogenic membrane domains – a property exclusively attributed to membrane curvature induced by cholesterol (Tenchov, MacDonald & Siegel, 2006). Furthermore, asymmetry of cholesterol across leaflets alleviates membrane bending stress to promote membrane fusion (Pöhnl, Trollmann & Böckmann, 2023).

In general, the curvature-inducing properties of non-bilayer lipids are crucial for stabilising curved membranes. The negative-curvature of lipids such as PA stabilises the curvature induced by membrane-disrupting cyclic antimicrobial peptides and the curvature required for membrane repair (Bishop, 2014). Cells precisely regulate their lipid compositions and localisations during cell division (Atilla-Gokcumen *et al.*, 2014) and high local PE concentration stabilises membrane curvature during late-stage cytokinesis (Emoto *et al.*, 2005). High acyl chain unsaturation (which generates negative curvature-favouring non-bilayer lipids) in the cytoplasmic leaflet facilitates efficient vesiculation at the synapse (Manni *et al.*, 2018). Regulation of positive-curvature and negative-curvature non-bilayer lipid composition can function as a molecular switch, such as determining whether lipid droplets remain embedded in or emerge from the endoplasmic reticulum (Choudhary *et al.*, 2018).

Given the temperature dependence of lipid phases, non-bilayer phases may offer a means of thermosensing (Hayes *et al.*, 2021). In addition, while mechanisms exist to stabilise the Lm phase during thermal fluctuations (Tsvetkova *et al.*, 2002), the hexII phase remains essential for the functioning of chloroplasts under stress conditions (Dlouhý *et al.*, 2020; Garab *et al.*, 2022; Latowski, Akerlund & Strzałka, 2004). This topic is elaborated upon in Section 1.1.11.1.

#### 1.1.8.1 Non-bilayer Lipids Promote Membrane Fission and Fusion via the Hemi-fission or Hemi-fusion Membrane Stalk

Membrane fission and fusion events are fundamental to numerous essential cellular processes, including cell division, endocytosis, exocytosis, and mitochondrial dynamics, with dysfunction having implications in health and disease (Chen, Zhao & Li, 2023). Membrane fission and fusion progress via a membrane stalk intermediate (Figure 5), known as a hemi-fission or hemi-fusion state (Chernomordik & Kozlov, 2008; Bashkirov *et al.*, 2008). For clarity,

the stalk is discussed herein in the context of membrane fusion, although the general principles and involvement of non-bilayer lipids remain applicable to both.

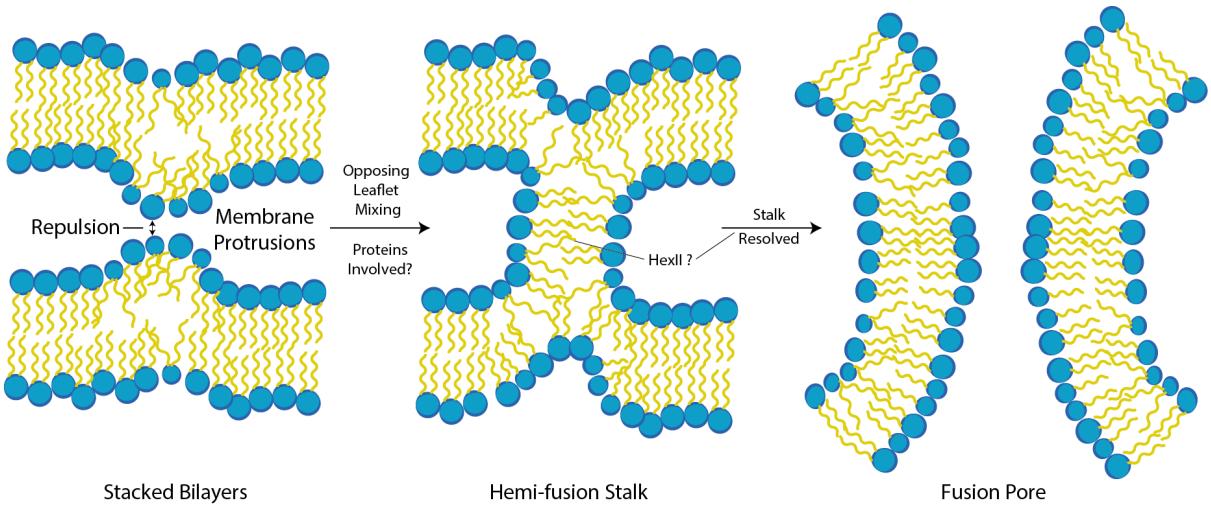


**Figure 5. The Hemifusion stalk.**
Fusion of opposing bilayers is facilitated by mixing of adjacent leaflets to form the fusion stalk. Fusion is completed once the fusion pore is formed. Non-bilayer lipids help form the required highly-curved lipid arrangements. Additionally, the hexII phase may transiently occur in fusion stalk and as the fusion stalk is resolved into a fusion pore. Figure adapted from (Chernomordik & Kozlov, 2008).

The fusion stalk is preceded by protrusions of adjacent bilayers, which facilitate the mixing of outer leaflet lipids to form the stalk (Chernomordik & Kozlov, 2008). The stalk topology is approximately analogous to the Holliday junction formed in homologous recombination (Song *et al.*, 2022). Stalk formation incurs a high energy cost as it necessitates overcoming repulsion of polar lipid head groups and inducing high curvature of a Lm phase bilayer; consequently, non-bilayer lipids play a crucial role. In addition to the negative curvature of hexII phase-favouring lipids within the bilayer being complementary to the stalk curvature, stalk formation is helped by the increase in elastic energy and frustration that non-bilayer lipids provide to the membrane, as discussed in Section 1.1.7 (Fan *et al.*, 2016). The role of non-bilayer lipids in promoting the fusion stalk is exemplified by the inner leaflets of typical plasma membranes, which are relatively enriched with hexII phase-favouring lipids, being more fusogenic than outer leaflets (Poojari, Scherer & Hub, 2021; Tenchov, MacDonald & Siegel, 2006). The fusion stalk may involve or resolve via a transient hexII phase intermediate

(Wolf *et al.*, 2019). Frequently, in addition to favourable lipid composition, formation of the fusion stalk is driven by membrane remodelling machines such as dynamins, ESCRT-III and SNAREs (Section 1.2.1) (Ozeir & Cohen, 2022; Warecki *et al.*, 2020; Hennig *et al.*, 2015; Han, Pluhackova & Böckmann, 2017). The precise mechanisms underpinning how membrane remodelling proteins induce extreme curvature that with the assistance of non-bilayer lipids that leads to fission or fusion remain unknown.

The fusion stalk and mixing of opposing membranes can resolve to create a fusion pore to complete fusion – a process also relevant for formation of the cubic phase (Demurtas *et al.*, 2015). Alternatively, if the stalk is extended, hexII phase tubular structures are generated (Marrink & Mark, 2004). How stalks resolve or extend is not fully understood.

### 1.1.9 Energy-transducing Membranes Comprise ~50 % Non-bilayer Lipids

Bilayers are impermeable to protons and therefore fundamental to the bioenergetics of life. Proton impermeability enables cells to capture and store energy in proton gradients across membranes, facilitating the synthesis of ATP through oxidative phosphorylation and photosynthesis. Lower-order organisms establish these gradients across their cytoplasmic membranes, whereas specialised, internalised and highly-organised membranes have evolved to enhance the efficiency of this process in higher order organisms – namely the inner mitochondrial membrane (IMM) and thylakoid membranes (TMs) (Section 1.1.10 and Section 1.1.11 respectively).

It is well established that IMMs and TMs are bilayers (Vereb *et al.*, 2003), which is unsurprising given the bilayer structure is requisite for proton impermeability and energy transduction. However, IMMs and TMs contain remarkably high proportions of hexII phase-favouring lipids. IMMs comprise approximately 34% PE and 18% cardiolipin, equating to a 52% hexII phase-favouring lipid content (Horvath & Daum, 2013). The remaining lipids are cylindrical and Lm phase favouring: PS, PC, and phosphatidylinositol. Despite their different lipid composition, TMs also contain approximately 50% hexII favouring lipid, namely MGDG (Kobayashi, Yoshihara & Kubota-Kawai, 2023). Similarly, the remaining 50% comprises Lm phase lipids (DGDG, SQDG and PG).

Therefore, the question arises regarding how IMMs and TMs adopt extensive bilayer arrangements. Both IMMs and TMs are saturated with protein, exhibiting protein-lipid ratios of approximately 0.3 (Schlame, 2021; Meredith *et al.*, 2021). The high protein content alone is sufficient to induce the high hexII phase-favouring lipid mixture into a bilayer configuration (Simidjiev *et al.*, 2000), resulting in highly frustrated bilayers with strong lateral pressure. It is noteworthy that IMMs and TMs demonstrate lipid polymorphism, as the hexII phase can spontaneously form from protein-free patches (van Eerden *et al.*, 2015; Dlouhý *et al.*, 2021b). This polymorphism is not limited to hexII lipids; cylindrical lipids such as PG, influenced by the ensemble of long-range interactions, uniformly exhibit the same phase behaviour (van Eerden *et al.*, 2015). The hexII phase remains in close proximity to the lamellar bilayer from which it originated, allowing spontaneous transitions back into the lamellar phase of its parent bilayer (Figure 6) (Garab *et al.*, 2022).

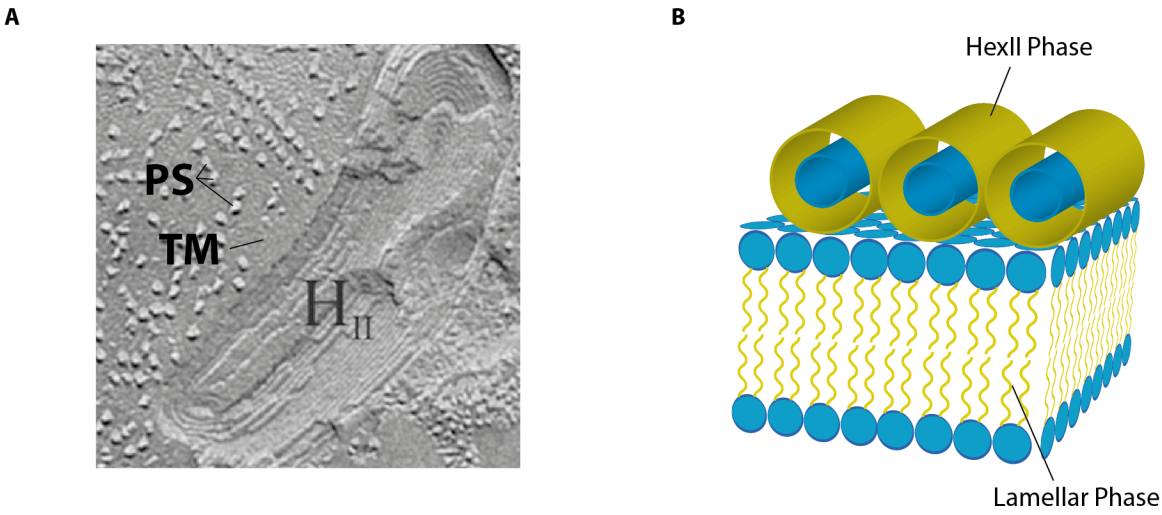


**Figure 6. Lipid Polymorphism of Thylakoid Membranes.**
Lipids that undergo spontaneous phase changes remain in association from their parent lamellar bilayer. **A,** Electron micrograph of hexII phase tubular structures ($H_{II}$) in association thylakoid membranes (TM). PS = ordered photosystem II arrays. Micrograph taken from (Kirchhoff *et al.*, 2007). **B,** Schematic demonstrating hexII phase tubular arrays spontaneously formed via lipid polymorphism from and in association with a Lm phase bilayer.

The principles of highly frustrated bilayers, maintained by high protein content, that can exhibit polymorphism under the dynamic exchange model (Garab *et al.*, 2000, 2022), allow hexII phase-favouring lipids to mediate homeostasis in IMMs and TMs. The electron transport

chain components of oxidative phosphorylation and oxygenic photosynthesis depend on conformational and oligomerisation state changes to regulate their activity in response to stress (Kirchhoff *et al.*, 2007; Liko *et al.*, 2016; Minagawa, 2011). Lipid polymorphism enables energy-transducing bilayers to self-regulate their bioenergetic activity, with the removal of lipids from the bilayer by Lm-hexII phase transition decreasing the lateral pressure on proteins embedded in the membrane, and hexII-Lm phase transitions increasing the lateral pressure. As established in Section 1.1.7, lateral pressure changes influence the energetics, packing and conformation of membrane-embedded components of electron transport chains (Garab *et al.*, 2022), thereby regulating their bioenergetic activity.

Bioenergetics are also regulated by bilayer fluidity (Garab *et al.*, 2022). Electron transport chains depend on membrane-embedded quinolones to transfer electrons along the chain, necessitating sufficient lipid volume and fluidity for quinolones to freely diffuse (Kirchhoff, Mukherjee & Galla, 2002). The high protein density of IMMs and TMs indicates that they operate in conditions approaching the limit for quinolone diffusion and protein semi-crystallisation (Tietz *et al.*, 2015). Consequently, lipid polymorphism can alter this balance by removing lipids from the bilayer via a Lm-hexII phase transition, thereby inhibiting electron transport by quinolone diffusion. In a self-regulatory manner, as more lipids are sequestered in hexII phase outside the bilayer, the increasing protein content in the bilayer would induce more lipids to return to the Lm bilayer, facilitating quinolone diffusion (Simidjiev *et al.*, 2000; Garab *et al.*, 2022).

Overall, the regulation of bioenergetic activity by lipid polymorphism and lateral force within the bilayer explains why IMMs and TMs evolved a high hexII phase-favouring lipid content. The more detailed mechanisms of this phenomenon and additional roles of non-bilayer lipids and phases in energy transducing membranes are expanded upon in the following sections.

### 1.1.10 Mitochondria are Dynamic Double-membrane Organelles that House the Machinery Required for Oxidative Phosphorylation

Mitochondria are dynamic membrane-bound organelles primarily known for their role in eukaryotic oxidative phosphorylation and ATP generation (Giacomello *et al.*, 2020). However, they also play crucial roles in various cellular processes, including signalling and apoptosis

(Frank *et al.*, 2001). The organisation and roles of their membranes are briefly reviewed herein to provide context for the roles of non-bilayer lipids discussed in Section 1.1.10.1.

Mitochondrial morphology and localisation are highly dynamic, with these organelles forming protein-mediated contacts with various cellular structures such as the endoplasmic reticulum, cytoplasmic membrane, lipid droplets, and endosomes (Korobova, Ramabhadran & Higgs, 2013; Singaravelu *et al.*, 2011; Benador *et al.*, 2018; Hsu *et al.*, 2018). These interactions significantly influence mitochondrial dynamics and function. Mitochondrial morphology is tightly regulated, and mitochondrial fission and fusion processes are mediated by dynamins, including Opa1, Mfn1, Mfn2, and Drp1 (Giacomello *et al.*, 2020). Fusion promotes elongated mitochondria and increased ATP production (Gomes, Di Benedetto & Scorrano, 2011), while fission results in fragmented mitochondria. Mitochondrial fission is essential for various cellular processes, including apoptosis signalling through cytochrome c release (Frank *et al.*, 2001), efficient mitochondrial partitioning during cell division (Taguchi *et al.*, 2007), and targeting damaged mitochondria for mitophagy (Ziviani, Tao & Whitworth, 2010).

The outer mitochondrial membrane (OMM) compartmentalises the organelle, while a second internalised bilayer, the inner mitochondrial membrane (IMM), is intricately folded into cristae (Figure 7A) which house the respiratory electron chain components. Cristae membranes are connected by inner boundary membranes and are linked at their base by cristae junctions - short tubular structures that connect the inner boundary membranes on either side of the cristae membranes (Frey, Renken & Perkins, 2002). This arrangement enhances ATP production efficiency by minimising ADP and proton diffusion away from the cristae-embedded ATPsynthase (Wolf *et al.*, 2019). Proper cristae formation is crucial for mitochondrial function (Acehan *et al.*, 2011b), with tighter cristae associated with respiratory chain supercomplex formation and increased respiration efficiency (Cogliati *et al.*, 2013).

Cristae dynamics are regulated by proteins and non-bilayer lipids. The multi-protein MICOS complex plays a key role in maintaining the folding of IMMs into cristae (Friedman *et al.*, 2015). IMM fusion dynamins, such as Opa1/Mgm1, also modulate cristae width (Faelber *et al.*, 2019). Additionally, ATP synthase dimers induce positive curvature and are predominantly localised to regions of highest curvature (Davies *et al.*, 2012).

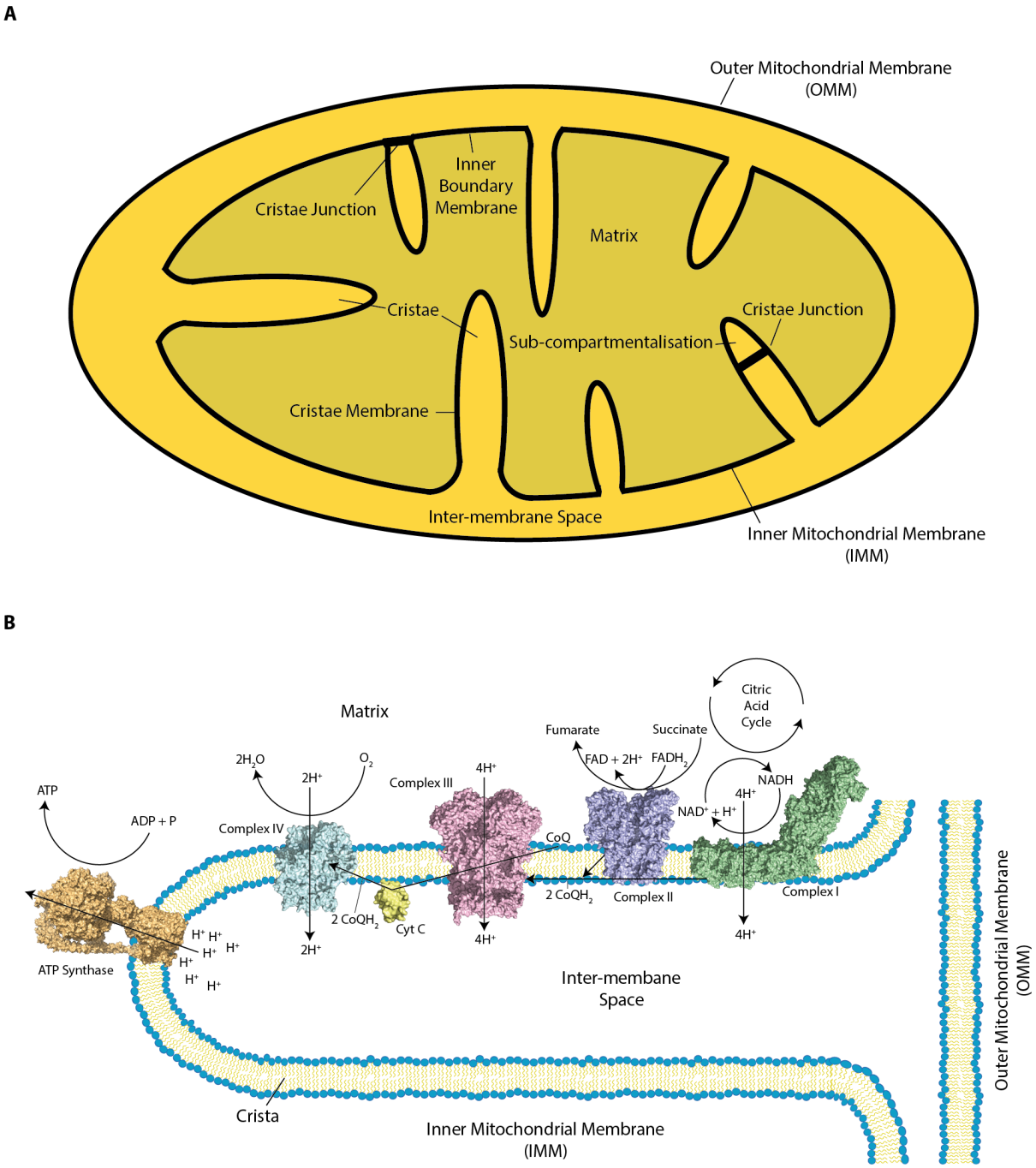


**Figure 7. Overview of Mitochondrial Membrane and Respiratory Electron Transport Chain Arrangements.**
**A,** Schematic of mitochondrial membrane organisation. The inner mitochondrial membrane is folded into cristae supported by cristae junctions **B,** ATP synthesis by the cristae membrane-embedded respiratory electron transport chain. Adapted from (Garab *et al.*, 2022). Free energy from the citric acid cycle is harnessed to transport protons from the matrix to the intermembrane space via complex I (PDB: 7NYR), complex III (PDB: 5XTE) and complex IV (PDB: 7JRO). Free energy stored as reducing power is transported along the chain by membrane embedded coenzyme-Q (CoQ), and the intermembrane space leaflet-associated cytochrome C (CytC, PDB: 6C4W). Additional reducing power comes from Complex II (PDB: 6WU6), which oxidises $FADH_2$. The terminal electron acceptor is oxygen, which is reduced to form water. The proton motive force generated by this system drives ATP synthase (PDB: 6VMB).

The electron transport chain is embedded in cristae membranes and comprises complexes I, II, III, IV, cytochrome c oxidase, and ATP synthase. This is summarised in Figure 7B. Briefly, the electron transport chain captures and transfers free energy from reducing agents produced by the citric acid cycle along the chain using high-energy electrons. This process results in the accumulation of protons in the intermembrane space, creating a proton gradient across the IMM that ATP synthase harnesses to generate ATP. Coenzyme Q (CoQ) freely diffuses within the bilayer and transports electrons between complexes (Garab *et al.*, 2022). Notably, the respiratory electron transport chain complexes can form supercomplexes, which enhance electron transfer efficiency and reduce reactive oxygen species production (Guan, Zhao & Peng, 2022).

#### 1.1.10.1 Non-bilayer Lipids and Phases have Important Functions in Mitochondria

HexII phase tubular structures have been observed within mitochondria (Murugova *et al.*, 2007). Indeed, the non-bilayer lipid content of mitochondrial membranes is highly regulated and non-bilayer lipids and phases play crucial roles in mitochondrial function and structure (Basu Ball, Neff & Gohil, 2018). Cardiolipin (CL) and phosphatidylethanolamine (PE), both hexII phase-favouring lipids, are particularly significant in mitochondrial membranes. Cardiolipin, owing to its charge and conical shape, stabilises respiratory chain super complexes and ATP synthase dimers that induce positive curvature (Dudek *et al.*, 2013; Lobo-Jarne & Ugalde, 2018). Furthermore, CL is involved in mitochondrial dynamics, recruiting membrane remodelling dynamins such as Drp1, Opa1 and Mgm1 for fission and fusion events (Fenton, Jongens & Holzbaur, 2021; von der Malsburg *et al.*, 2023; Yan *et al.*, 2020). While PE has a lesser role in direct interactions with respiratory chain proteins and dynamins, it is crucial for stabilising the negative curvature of cristae (Böttinger *et al.*, 2012). The conical shape of CL also drives membrane curvature and is essential for cristae formation (Khalifat *et al.*, 2011).

CL levels significantly influence cristae architecture (Anand *et al.*, 2020) and regulate cristae dynamics and consequently ATP synthesis efficiency (Joubert & Puff, 2021; Garab *et al.*, 2022). Cristae are capable of rapid remodelling through fission and fusion processes and therefore are highly dynamic (Kondadi *et al.*, 2020). Lipid polymorphism and the hexII phase are crucial for such rapid remodelling (Joubert & Puff, 2021; Garab *et al.*, 2022). The dynamic cristae junctions are also formed by hexII phases (Garab *et al.*, 2022). These junctions not only exist

at the base of cristae but also along their length, creating sub-compartments within the cristae (Wolf *et al.*, 2019). Junctions ensure that cristae are not excessively compressed, thereby allowing efficient ADP diffusion to transporters that translocate ADP from the inter-cristae space to the matrix, where ADP is required for ATP synthesis (Afzal *et al.*, 2021). Overall, the involvement of hexII phase in cristae remodelling is crucial for efficient ATP synthesis (Garab *et al.*, 2022).

Non-bilayer lipids also play a role in the recruitment of protons to ATPsynthase. Recent evidence suggests that rather than freely diffusing in the intermembrane space, protons are transported along the membrane surface from one respiratory complex to another (Nesterov *et al.*, 2021). Cardiolipin helps to facilitate this process, as its phosphate groups can be protonated. Protonation also enhances the negative curvature of cardiolipin. This increased negative curvature likely directs protons to regions of maximum curvature where ATPsynthase is located, due to the altered charge distribution. This effectively increases the proton-retaining interface for ATP synthesis (Garab *et al.*, 2022).

In conclusion, non-bilayer lipids, particularly CL and PE, are integral to mitochondrial function. They influence membrane curvature, cristae architecture, respiratory chain and ATP synthesis efficiency, and recruit membrane remodelling machinery.

### 1.1.11 Thylakoid Membranes House the Photosynthetic Electron Transport Chain Machinery, which is Highly Regulated in Response to Changing Light Conditions

Thylakoid membranes are internalised and organised stacked lamellar bilayers that house the photosynthetic machinery of plants and most cyanobacteria. In cyanobacteria, the complexity of thylakoids can vary (Mareš *et al.*, 2019). In plants, thylakoids are housed in chloroplasts, which are double membrane-bound organelles. Chloroplast thylakoids exhibit higher levels of organisation into stacked grana and interconnecting lamellae, and the dynamic structure of these can regulate photosynthesis (Johnson & Wientjes, 2020). As with the mitochondrial IMMs, TMs provide compartmentalisation and proton-impermeable barriers to facilitate proton gradients. Non-bilayer lipids have critical functions in thylakoid membranes and the regulation of photosynthesis (Section 1.1.11.1). The photosynthetic electron transport chain is briefly reviewed here as context for the non-bilayer lipid functions in TMs.

The thylakoid-embedded photosynthetic electron transport chain is summarised in Figure 8. In brief, photons harvested by the antennae of the photosystem II complex provide energy for the oxidation of water. The high-energy electrons generated by this process are transported along the chain to the photosystem I complex, which also utilises photon energy to elevate the energy state of these electrons to ultimately reduce NADP+ to NADPH, which is utilised in the Calvin cycle for carbon fixation. Photosystems I and II comprise relatively conserved core reaction centres and surrounding antennae formed of arrays of light harvesting complexes one and two (LHCI & LHCII), respectively (Garab *et al.*, 2022). The light harvesting complexes efficiently capture and transfer photon energy towards the core complex (Huang *et al.*, 2021). Along the electron transport chain, photon energy is additionally utilised to generate a proton gradient across the thylakoid membrane, which is harnessed by an ATP synthase to synthesise ATP for the Calvin cycle.

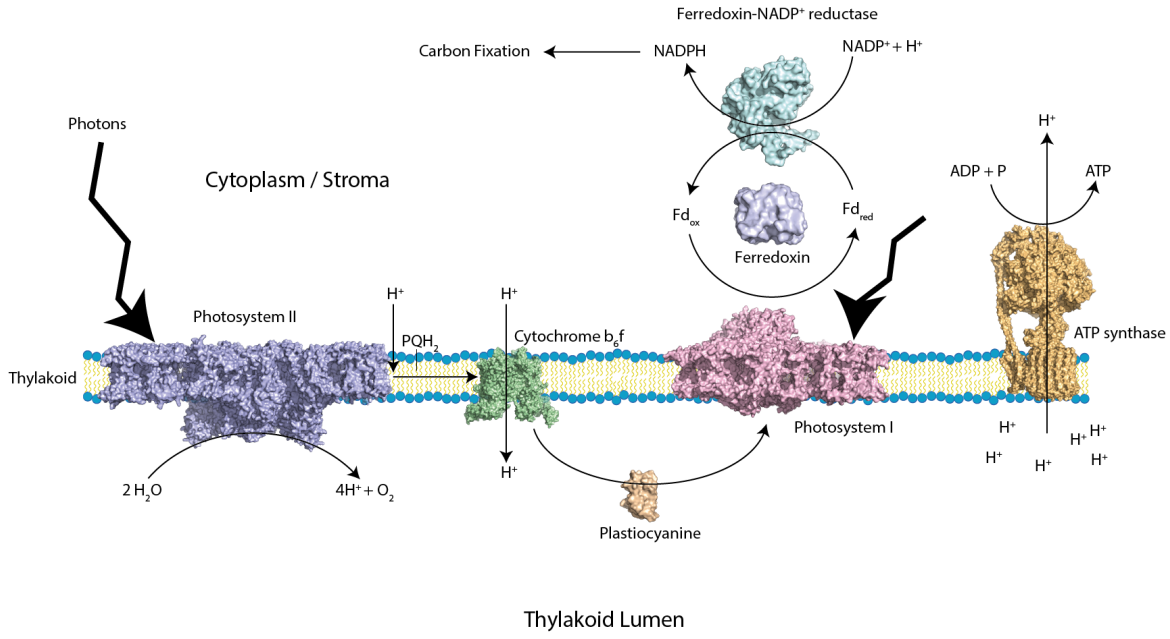


**Figure 8. The Photosynthetic Electron Transport Chain.**
Photons absorbed by photosystem II (PDB: 5MDX) excite coordinated chlorophyll molecules to provide energy to liberate electrons and reduce the membrane embedded plastoquinone. Such electrons are replaced by water oxidation by the oxygen evolving complex of photosystem II. Reduced plastoquinone ($PQH_2$) diffuses through the membrane to cytochrome b6f (PDB: 6RQF), which reduces plastocyanin (a soluble protein within the thylakoid lumen, PDB: 1AG6), which in turn provides electrons to photosystem I (PDB: 6IGZ). Photosystem I, akin to photosystem II, harvests photon energy to reduce ferredoxin (PDB: 5AUI), replacing the lost electrons with those provided by plastocyanin. Ferredoxin-NAP+ reductase (PDB: 5H59) simultaneously oxidises ferredoxin and reduces $NADP^+$ to generate NADPH, which is used in the Calvin cycle for carbon fixation. Both ferredoxin and ferredoxin-NADP+ reductase are soluble and found in the cytoplasm (or stroma of chloroplasts). This process generates

a proton gradient across the thylakoid membrane with a relatively low pH in the thylakoid lumen as (1) protons are removed from the cytoplasmic/stromal side in the reduction of PQ and $NADP^+$ and (2) protons are deposited in the thylakoid lumen by the splitting of water and active transport of protons by cytochrome b6f. The energy stored in the proton gradient is harvested by ATP synthase to synthesise ATP at the cytoplasmic/stromal side of the membrane, which is also used by the Calvin cycle for carbon fixation. *Figure adapted from (Garab et al., 2022).*

Photosynthesis is regulated in response to various stresses such as heat, drought and high and low light conditions (Muhammad *et al.*, 2021). Under intense light conditions, xanthophyll pigments (embedded in the bilayer) contribute to the protection of the photosynthetic machinery against photodamage and reactive oxygen species (Ruban, 2016). De-epoxidation (chemical modification) of xanthophylls enhances their non-photosynthetic quenching properties, whereby they dissipate excess energy as heat to mitigate photodamage (Goss & Latowski, 2020; Welc *et al.*, 2021). De-epoxidation is mediated by enzymes such as violaxanthin de-epoxidase (VDE), which is localised to the thylakoid lumen (Ruban, 2016). Xanthophylls are also known to stabilise the bilayer (Gruszecki & Strzałka, 2005; Szilágyi, Selstam & Åkerlund, 2008).

To ensure photosystem II is providing sufficient energy to photosystem I in low light conditions, the abundance of photosystem II is reduced, some LCHII complexes dissociate from the photosystem, and LCHII is also upregulated. Consequently, an increased number of free LHCII are found in the membrane to capture and deliver sufficient photon energy to the lower abundance photosystem II core reaction centres (Kirchhoff *et al.*, 2007; Bailey *et al.*, 2001). Furthermore, dissociation of LCHII complexes from photosystem II leads to formation of semi-crystalline photosystem II arrays. Such arrays facilitate more efficient diffusion-dependent electron transfer by plastoquinone in a bilayer saturated with LHCII complexes (Tietz *et al.*, 2015).

#### 1.1.11.1 Non-bilayer Thylakoid Lipids and Phases have Important Roles in Response to Changing Light Conditions

Non-bilayer lipids are essential for the complex arrangement of thylakoids in plants (Mazur *et al.*, 2019). HexII ordered tubular arrays have been observed in association with thylakoids (Figure 6A) in response to low light (Kirchhoff *et al.*, 2007), sugars (Williams, Brain & Dominy, 1992) and low temperature (Semenova, 1999) and may represent a stress response

mechanism. Furthermore, non-bilayer lipids and phases play crucial roles in both the intense- and low-light adaptations of photosynthesis.

Recent measurements indicate that only 40 % of lipids in thylakoids are found in the Lm phase, highlighting the significance of lipid polymorphism (Dlouhý *et al.*, 2021a). The remaining 60 % are attributed to various non-bilayer phases, including the hexII phase and isotropic phases. The isotropic phases encompass membrane fusion intermediates (van Eerden *et al.*, 2015; Dlouhý *et al.*, 2021b) and the association of lipids with protein such as VDE (Dlouhý *et al.*, 2020). Notably, the hexII phase itself, beyond the interaction of conical lipids with VDE, has been demonstrated as crucial for VDE activity (Latowski, Akerlund & Strzałka, 2004; Dlouhý *et al.*, 2020; Goss *et al.*, 2005), suggesting a significant role of non-bilayer phases in the response of thylakoids to intense light to enhance xanthophyll-mediated non-photosynthetic quenching (Garab *et al.*, 2022; Welc *et al.*, 2021).

Lipid polymorphism and the hexII phase also play critical roles in the response to low-light conditions. As xanthophylls are known to stabilise the bilayer (Szilágyi, Selstam & Åkerlund, 2008), lipid polymorphism may be promoted by the reduced xanthophyll content in the bilayer observed in low-light conditions (Thayer & Björkman, 1990). Removal of MGDG from the bilayer by lipid polymorphism decreases the lateral pressure in the bilayer (Section 1.1.7), which has a two-fold effect on LHCII. Firstly, the reduced lateral pressure may facilitate LHCII dissociation from photosystem II and the consequent rearrangement of photosystem II into ordered arrays, with implications for more efficient photon capture and plastoquinone diffusion (Kirchhoff *et al.*, 2007; Tietz *et al.*, 2015). Secondly, the reduced lateral pressure helps maintain LHCII in a light harvesting state, as lateral pressure exerted by MGDG is known to convert LHCII into an energy quenching and heat-dissipation state (Tietz *et al.*, 2020).

Overall, this suggests a homeostatic role of non-bilayer lipids and phases in TMs. Lipid polymorphism allows increased Lm-hexII phase transition sequestration of MGDG and reduced lateral pressure and to promote energy harvest. Whilst in reverse it allows increased MGDG content in the bilayer and increased lateral pressure to promote photo quenching and heat dissipation (Tietz *et al.*, 2020). However, it should be noted that the hexII phase increases VDE activity and subsequent photo quenching and heat dissipation of xanthophylls. Therefore, reducing hexII phase in that sense would not be beneficial for quenching per se.

Overall, non-bilayer lipids and phases and lipid polymorphism are involved in TM stress responses (Garab *et al.*, 2022).

#### 1.1.11.2 Non-bilayer Lipids may have Played an Important Role in the Evolution of Thylakoid Membranes

The evolution of oxidative phosphorylation and the subsequent development of complex life on Earth was facilitated by the Great Oxygenation Event (GOE) approximately 2.3 billion years ago, which significantly increased atmospheric oxygen. This event was contingent upon the evolution of oxygenic photosynthesis, whereby protocyanobacteria acquired genes to express both photosystem I and photosystem II (Guéguen & Maréchal, 2022). However, evidence suggests this acquisition event may have preceded the GOE by 1 billion years (Cardona, 2018; Cardona *et al.*, 2019). Consequently, the GOE can also be attributed to the evolution of more efficient oxygenic photosynthesis mediated by the organisation of photosynthetic membranes into thylakoids (Guéguen & Maréchal, 2022). The evolution of thylakoids increased the photosynthetic surface area and efficiency of photon harvest by protocyanobacteria (Mareš *et al.*, 2019).

Initial hypotheses for the early biogenesis of thylakoids in cyanobacteria were predicated on the budding of vesicles (mediated by membrane remodelling proteins) from the cytoplasmic membrane. However, there is limited experimental evidence to support this proposition (Guéguen & Maréchal, 2022) given the paucity of cytoplasmic membrane invaginations and contacts between thylakoid and cytoplasmic membranes in cyanobacteria (Gupta *et al.*, 2021), particularly when considering species with more primitive thylakoid arrangements (Mareš *et al.*, 2019). The prevalence of hexII phase-favouring lipids in protocyanobacteria and lipid polymorphism evidence a potential mechanism for the spontaneous and rapid formation of primitive thylakoid membranes.

The *Gloeobacter* genus of cyanobacteria organises its photosynthetic machinery into bioenergetic domains within its cytoplasmic membrane and lacks thylakoids, analogous to early cyanobacteria that would have also lacked thylakoid membranes prior to the GOE, rendering it a suitable model organism for understanding protocyanobacteria. Comparable to TMs, the *Gloeobacter* cytoplasmic membrane comprises approximately 50% hexII phase-favouring MGDG, and in regions of cytoplasmic membrane outside of the bioenergetic

domains, this proportion can reach up to 70% (Rexroth *et al.*, 2011). Such regions with lower protein density are predisposed to undergo spontaneous Lm-hexII phase transitions (Garab *et al.*, 2022). Despite the markedly different lipid synthesis and localisation pathways for chloroplasts and cyanobacteria, they share a conserved feature of topological separation of hexII and Lm phase-favouring lipid synthesis. The transient local accumulation of hexII phase-favouring lipids could, in part, be facilitated by the topological separation of their synthesis machinery (Guéguen & Maréchal, 2022), allowing spontaneous Lm-hexII phase transitions.

A reverse phase transition (hexII-Lm) would have facilitated the spontaneous formation of thylakoids on a rapid timescale without complex coordination of membrane remodelling proteins (Guéguen & Maréchal, 2022). The introduction of more Lm phase-favouring lipids into hexII phase arrangements would have contributed to triggering hexII-Lm phase transitions (Demé *et al.*, 2014). Membrane remodelling proteins such as Vipp1, which are known to transport lipids between thylakoids (Junglas & Schneider, 2018; Gupta *et al.*, 2021), are conserved in *Gloeobacter*. They may have had primitive roles in initiating the hexII-Lm phase transition and thylakoid formation by transporting Lm phase-favouring lipids to hexII phase structures (Guéguen & Maréchal, 2022). Furthermore, the absence of the cylindrical lipid sulfoquinovosyldiacylglycerol (SQDG) in *Gloeobacter* (Sato, Kamimura & Tsuzuki, 2016) may elucidate its lack of thylakoid membranes and the absence of thylakoids in cyanobacteria before the GOE. Without the Lm phase-favouring SQDG lipids they may have been unable to mediate a hexII-Lm phase transition to form thylakoids (Guéguen & Maréchal, 2022).

### 1.1.12 Summary of Lipid Membranes

Based on their biochemical and biophysical properties, lipid membranes are essential to life, functioning as barriers and platforms for various cellular processes. While Lm phase bilayers predominate in biology, non-lamellar lipid phases are emerging as significant lipid polymorphisms for diverse biological processes. The capacity of conical non-bilayer lipids to introduce frustration into bilayers is critical for membrane protein functions. Notably, non-bilayer phases and lipids have evolved as mechanisms of stress response and homeostasis. The high conical lipid content of energy transducing membranes indicates that non-bilayer lipids have particular importance in inner-mitochondrial and thylakoid membranes, and may have even contributed to the evolution of thylakoids themselves. How proteins remodel

bilayers in various cellular contexts is extensively studied and reviewed in the following sections. Conversely, there is limited evidence for membrane remodelling proteins inducing lipid phase transitions, despite the emerging importance of lipid polymorphism. The extent to which lipid polymorphisms are utilised by cells and the potential roles of membrane remodelling proteins in lipid polymorphism remain open questions.

## 1.2 Membrane Remodelling is Essential to Life and Mediated by Various Protein Families

Membrane remodelling events are ubiquitous throughout life, encompassing processes from cytokinesis, membrane repair, and morphological shaping to the complex dynamics of intracellular compartments and vesicle release. Membrane remodelling underpins all the diverse functions of lipid bilayers discussed in Section 1.1. Despite the reduced intracellular compartmentalisation of bacteria, membrane remodelling is equally crucial to bacterial persistence and can include events such as sporulation and responses to antibiotics (Bohuszewicz, Liu & Low, 2016). Underpinning all membrane remodelling events is the deformation of planar bilayers to induce curvature, whether mediated by lipid composition or asymmetry, or facilitated by curvature-inducing proteins. This section examines the diverse methods yet conserved principles developed by cellular life to remodel membranes using curvature-inducing proteins.

### 1.2.1 Membrane Remodelling Proteins Induce Membrane Curvature

Membrane remodelling proteins induce curvature and reshape lipid bilayers using various mechanisms. These mechanisms can be broadly categorised into scaffolding and non-scaffolding approaches.

Non-scaffolding mechanisms of membrane remodelling primarily rely on localised protein-lipid interactions to induce curvature. Two key mechanisms in this category are protein crowding and hydrophobic motif insertion. Protein crowding occurs when there is a local concentration of proteins on one side of a membrane, not necessarily requiring membrane insertion. Curvature is induced through steric effects of crowded proteins exerting pressure on the membrane surface and inducing lateral pressure within the proximal leaflet that leads to curvature (Stachowiak *et al.*, 2012). Hydrophobic motif insertion involves amphipathic

helices or hydrophobic loops that insert into one leaflet of the bilayer, causing local expansion and inducing curvature, particularly when multiple insertions occur in a confined region (McMahon & Boucrot, 2015). The curvature-inducing mechanisms of non-scaffolding proteins are also utilised by scaffold-forming proteins such as Vipp1 and dynamin 1 (Naskar *et al.*, 2023; Mehrotra, Nichols & Ramachandran, 2014).

Scaffolding membrane remodelling proteins rely on self-assembly and oligomerisation, often forming rings or helices, to induce extreme membrane curvature. These proteins play crucial roles in various cellular processes, from cell division to vesicle formation and intracellular trafficking.

#### 1.2.1.1 Actin and Tubulin Remodel Membranes During Cell Division and are Involved in Cell Shaping and Motility

One of the most conserved scaffolding proteins is the ancestral tubulin FtsZ, a bacterial homologue of tubulin. In eukaryotes, rapid polymerisation and depolymerisation of tubulin to assemble and disassemble microtubules can exert pushing and pulling forces to deform bilayers (Rodríguez-García *et al.*, 2020). Conversely, in bacteria, FtsZ forms multiple filaments in a ring-like structure at the site of cell division, known as the Z-ring. The Z-ring is part of a larger protein assembly called the divisome, which coordinates cell wall synthesis with membrane invagination during bacterial cell division (den Blaauwen, Hamoen & Levin, 2017; Du & Lutkenhaus, 2019). The Z-ring not only serves as a scaffold but also generates constrictive forces through GTP hydrolysis-driven filament sliding. This is reminiscent of the filament sliding mechanism employed by ESCRT-III polymerised on negatively curved membranes (Section 1.2.1.4) and dynamin (Section 1.3) (Osawa, Anderson & Erickson, 2008; Pfitzner *et al.*, 2020; Pannuzzo, McDargh & Deserno, 2018).

Whereas tubulin homologues drive bacterial cell division, in eukaryotes actin polymerises to form the actomyosin contractile ring to drive cell division. The actomyosin ring uses myosin motor-generated force to constrict rings of actin filaments, which induces membrane curvature from within the cell (Miller, 2011). Furthermore, the ability of actin to rapidly polymerise and depolymerise enables the actin cytoskeleton to be deform membranes. The force generated by actin polymerisation is involved in the final scission of dynamin- and

clathrin-mediated endocytosis (Serwas *et al.*, 2022). Similar pushing forces allow actin to induce membrane curvature to shape the cell surface and drive motility (Svitkina, 2018).

#### 1.2.1.2 Clathrin and the SNAREs are Involved in Vesicle Shaping and Fusion

A multitude of membrane remodelling proteins are involved in vesicle shaping, fission and fusion, as well as actin and dynamin. Clathrin and the SNARE (Soluble N-ethylmaleimide-sensitive factor Attachment protein Receptor) proteins also play critical roles. Clathrin is involved in curvature induction to shape endocytic vesicles emerging from the cytoplasmic membrane. It has a primary role in increasing curvature already established by other proteins by forming a cage-like structural scaffold (Cail, Shirazinejad & Drubin, 2022). Conversely, SNARE proteins form tight complexes that facilitate vesicle fusion with the cytoplasmic membrane. SNAREs cooperate to tether membranes in trans and self-assemble into a tight complex that brings membranes into close proximity, such that the membrane is destabilised and a hemifusion state is achieved (Jahn, Cafiso & Tamm, 2024).

#### 1.2.1.3 Bar-Domain Proteins Induce Curvature During Vesiculation

Bin/Amphiphysin/Rvs (BAR) domain containing proteins possess the capability to both detect and generate membrane curvature in their oligomeric forms. BAR domain proteins collaborate with dynamin to facilitate clathrin-coated vesicle scission (Daumke, Roux & Haucke, 2014), contribute to the induction of membrane curvature for organelle shaping (Simunovic *et al.*, 2019), and are also conserved in bacteria where they participate in outer membrane vesiculation (Phillips *et al.*, 2021). BAR domains induce local membrane curvature through crowding and hydrophobic motif insertion (Section 1.2.1), and their oligomerisation into scaffolds enables collective induction of extreme curvature to generate membrane tubules (Simunovic *et al.*, 2019).

#### 1.2.1.4 ESCRT-III Proteins Induce Extreme Curvature to Achieve Membrane Fission and Repair

ESCRT-III (Endosomal Sorting Complex Required for Transport-III) proteins polymerise into rings or filaments to induce extreme positive or negative curvature and are conserved across all three domains of life (Liu *et al.*, 2021b). ESCRT-III proteins are involved in cell division in eukaryotes and archaea (Carlton & Baum, 2023), and are also involved in viral budding, multivesicular body formation and membrane repair (Wang *et al.*, 2023; Alonso Y Adell,

Migliano & Teis, 2016; Olmos, 2022). Bacterial ESCRT-III homologues such as LiaH, PspA and Vipp1 have roles in both cytoplasmic and thylakoid membrane maintenance (Gupta *et al.*, 2021; Junglas *et al.*, 2021), which also contributes to antibiotic resistance (Yingxing *et al.*, 2024; Domínguez-Escobar *et al.*, 2014). In its polymeric, curvature-inducing forms, ESCRT-III interfaces exhibit flexibility that allows varying degrees of membrane curvature. This phenomenon is exemplified by recent cryo-EM and atomic force microscopy insights into Vipp1 and its capacity to transition between membrane-bound 2D lattices, filaments and rings to increase membrane curvature and facilitate membrane repair (Naskar *et al.*, 2023).

### 1.2.2 Membrane Remodelling Summary

In conclusion, cells have evolved a diverse array of protein machineries to facilitate membrane remodelling. Membrane remodelling protein families are frequently conserved across archaea, bacteria, and eukaryotes, underscoring their fundamental importance to life. These proteins employ various mechanisms to induce and stabilise membrane curvature, often functioning synergistically to achieve complex membrane reshaping events. A widely conserved principle of membrane remodelling proteins is their capacity to oligomerise to induce membrane curvature. The dynamin superfamily, discussed in the subsequent section, represents another major class of ancient membrane remodelling proteins with unique mechanisms of action, but conserved principles of self-assembly to remodel membranes.

## 1.3 The Dynamin Superfamily is an Ancient Family of Membrane Remodelling Proteins

The dynamin superfamily (DSF) is a large family of membrane remodelling GTPases found across all three domains of life (Figure 9) (Jimah & Hinshaw, 2019). Broadly categorised into classical dynamins most closely related to dynamin 1 and dynamin-related proteins (DRPs), the DSF members often exhibit relatively low sequence homology yet conserved domain architectures (Section 1.3.4). They share principles of self-assembly into helical polymers to induce curvature and remodel membranes via fission or fusion, leveraging their GTPase activity to drive conformational changes and membrane remodelling, although exceptions to this paradigm exist. Their presence across all domains of life and conserved membrane remodelling capabilities implicate DSF members as ancient machinery essential to life. Furthermore, the dysfunction of DSF-mediated membrane remodelling and DSF mutations

are associated with impaired vision (dominant optic atrophy), Alzheimer's disease, cancer, and diabetes (Alexander *et al.*, 2000; Bhatti *et al.*, 2023; Meng, 2017; Trochet & Bitoun, 2021; Fan *et al.*, 2021a).

The following sections review the conserved and diverse roles of the DSF, as well as the insights into the molecular mechanisms of dynamin-mediated membrane remodelling provided by recent structural biology advancements.

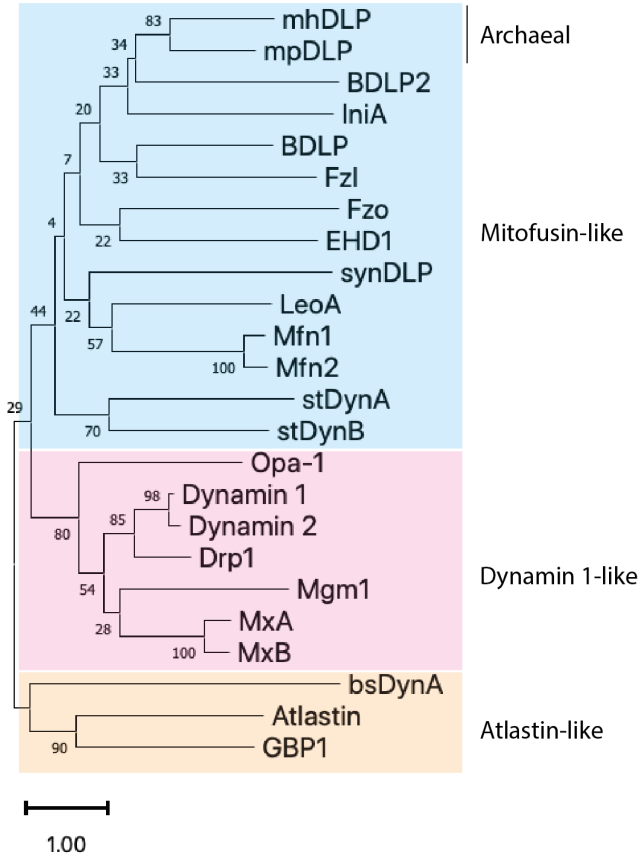


**Figure 9. Dynamin Phylogenetic Tree.**
The DSF can be broadly categorised into dynamin 1- and mitofusin-like clades. Phylogeny computed based on multiple sequence alignment of eukaryotic, bacterial, and archaeal dynamin amino acid sequences. Numbers indicate bootstrap values across 500 repetitions. Scale bar indicates evolutionary distance scale in substitutions per site. **Classical Dynamins:** Dynamin 1, Dynamin 2 (Human). **Mitochondrial Fission Dynamin:** Drp1 (human). **Outer mitochondrial membrane fusion dynamins:** Mfn1/Mfn2 (human), Fzo (*S. cerevisiae*). **Inner mitochondrial membrane fusion dynamins:** Opa-1 (human), Mgm1 (*S. cerevisiae*). **Antimicrobial dynamins**: MxA/MxB, GBP1 (human). **Other eukaryotic dynamins**: Fzl (*Arabidopsis thaliana*), EHD1 (human), Atlastin (human). **Bacterial dynamins:** BDLP/BDLP2 (*Nostoc punctiforme*), IniA (*M. tuberculosis*), stDynA/stDynB (*Streptomyces venezuelae*), LeoA (*E. coli*), synDLP (*Synechocystis sp.* PCC 6803), bsDynA (*B. subtillis*). **Archaeal**

**dynamins:** mhDLP (*Methanospirillum hungatei* JF-1, UniProt accession: Q2FQ75), mpDLP (*Methanocella paludicola*, UniProt accession: D1Z1G9). Sequences were aligned using MUSCLE (Edgar, 2004) and the maximum-likelihood evolutionary tree was computed and produced using MEGA11 (Tamura, Stecher & Kumar, 2021).

### 1.3.1 Eukaryotic Dynamins have Various Functions often Including Membrane Fission or Fusion

In eukaryotes, DSF members are localised to both cytoplasmic and organelle membranes, where specific members are known to mediate membrane fission or fusion (Figure 10A). The most extensively characterised members of the DSF are the classical dynamins. Humans possess three classical dynamins which have multiple splicing-derived isoforms (Meng, 2017). The most well-documented role of dynamins is the dynamin 1 mediated final scission of endocytic clathrin-coated vesicles (Antonny *et al.*, 2016), providing dynamins with critical functions at neurological synapses (Prichard *et al.*, 2022).

Mitochondrial fission and fusion dynamics play critical roles in health and disease (Chen, Zhao & Li, 2023). DRPs have well-established functions in such processes. Mitochondrial fission is mediated by dynamin-related protein 1 (Drp1), known as Dmn1 in yeast. Drp1 is a cytoplasmic dynamin recruited to OMMs where it polymerises to facilitate fission (Rochon *et al.*, 2024; Francy *et al.*, 2017). Drp1 also localises to and mediates fission of peroxisomes (Kamerkar *et al.*, 2018) and chloroplasts (Zhang & Hu, 2010). Mitochondrial fusion is mediated by other DRPs, namely mitofusins 1 and 2 (Mfn1/Mfn2) and optic atrophy 1 (Opa1). The mitofusins (Fzo in yeast) are responsible for OMM fusion (Zacharioudakis *et al.*, 2022), whereas Opa1 (Mgm1 in yeast) is responsible for IMM fusion (Ge *et al.*, 2020). Additionally, Opa1 is involved in cristae dynamics (Hu *et al.*, 2020; Fry *et al.*, 2024). Opa1 exists in two isoforms; long-form Opa1 (L-Opa1) is anchored to the IMM by an N-terminal transmembrane helix, which is proteolytically cleaved to form short-form Opa1 (s-Opa1). The capacity of s-Opa1 to polymerise on both negative and positive curvature membranes enables it to regulate cristae morphology (Faelber *et al.*, 2019). In summary, mitochondrial fission and fusion are mediated by distinct DRPs. However, evidence suggests that s-Opa1 is also associated with IMM fission as well as its established roles in fusion (Anand *et al.*, 2014).

Elsewhere in the cell, DRPs are involved in remodelling of thylakoid membranes (TMs) within chloroplasts (Jilly *et al.*, 2018). Fuzzy onion-like protein (Fzl) knockouts exhibit both chloroplast and TM morphology defects (Gao, Sage & Osteryoung, 2006). Fzl is known to mediate thylakoid fusion in intense light conditions (Findinier, Delevoye & Cohen, 2019), and is consequently required for efficient photosynthesis under variable light conditions (Ogawa *et al.*, 2023). A further DRP, atlastin, mediates endoplasmic reticulum fusion (Bryce *et al.*, 2023; Hu & Rapoport, 2016).

Certain DRPs have evolved immunity-related functions. Guanylate-binding proteins (GBPs) constitute a class of DRPs involved in the innate immune response to intracellular bacteria, whereby they function as sensors and binders of LPS (Weismehl *et al.*, 2024; Kutsch & Coers, 2021). GBP1 can also polymerise to form an immunogenic coatomer on the surface of bacteria (Zhu *et al.*, 2024; Weismehl *et al.*, 2024). Additionally, GBPs have functions pertaining to cell adhesion and migration (Vestal & Jeyaratnam, 2011; Bai, Chen & Deng, 2018). The DSF also encompasses some anti-viral proteins. Myxovirus resistance proteins (MxA & MxB) are DRPs that act as antiviral factors. Given that they can form helical polymers (Alvarez *et al.*, 2017) and also tubulate liposomes *in vitro* (von der Malsburg *et al.*, 2011), they likely achieve their antiviral activity by polymerising onto viral lipid envelopes (Chen *et al.*, 2017). MxB also affects mitochondrial dynamics and membrane morphology and localises to the IMM (Cao *et al.*, 2020). In contrast, in plants, DRPs involved in endocytic vesiculation have been utilised by potyviruses to enhance viral replication and cell-to-cell transfer (Wu *et al.*, 2018). Similarly, Drp2 interacts with Plantago asiatica mosaic virus to promote viral replication (Shinji *et al.*, 2023).

In addition to their membrane binding and remodelling activities, some dynamins interact with the cytoskeleton. Dynamin 1 bundles microtubules in its helical polymeric form (La *et al.*, 2020). Moreover, the polymerisation of dynamin 1 onto F-actin and its subsequent depolymerisation upon GTP hydrolysis facilitate the bundling of branched actin networks. This provides mechanical strength to actin networks that generate force protrusions responsible for inter-cell fusion synapses (Zhang *et al.*, 2020b).

In conclusion, notwithstanding the aforementioned diverse functions of eukaryotic DSF members, eukaryotic dynamins and DRPs generally possess well-defined roles in the fission or fusion of cytoplasmic and organelle membranes.

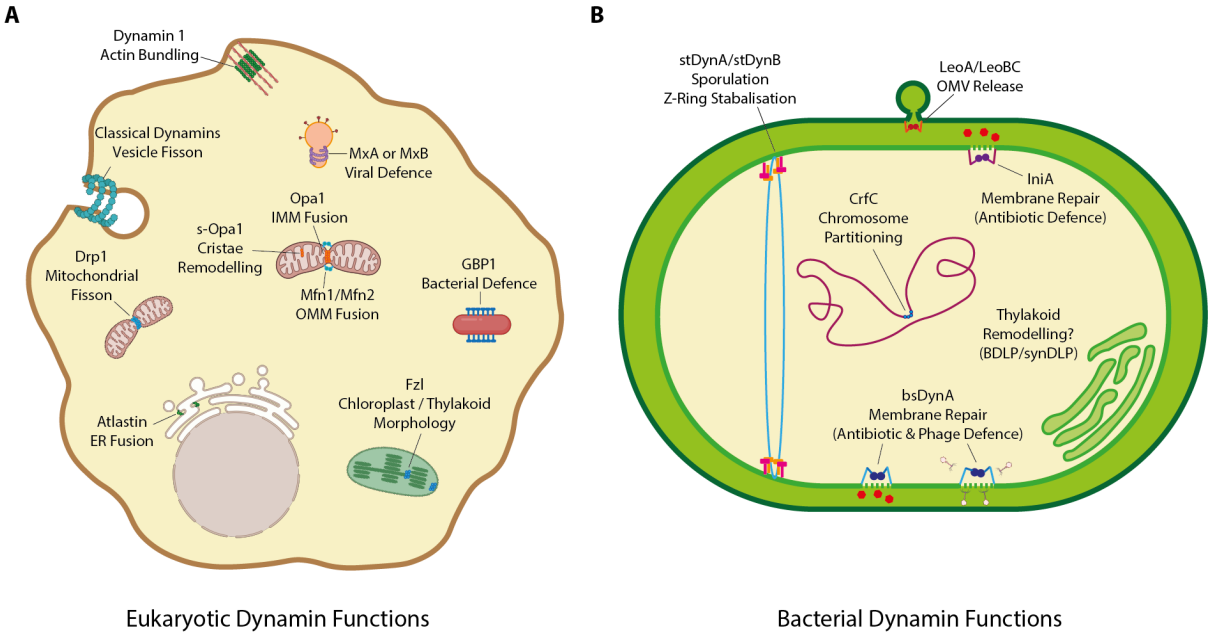


**Figure 10. DSF Roles in Eukaryotes in Bacteria.**
**A,** Known functions of eukaryotic dynamins and DRPs, with defined roles in fission and fusion. *Some icons created with BioRender.com.* **B,** The diverse functions of bacterial DRPs and speculative role of cyanobacterial DRPs at the thylakoid membrane.

### 1.3.2 Many Bacterial Dynamins have not been Classified as Fission or Fusion Dynamins

Despite sharing the canonical DSF domain architecture (Section 1.3.4) and membrane-binding and remodelling abilities of eukaryotic dynamins, the functions of bacterial DRPs are less well characterised and are likely more diverse. For instance, the first DRP characterised in bacteria was bacterial dynamin-like protein (BDLP) from *Nostoc punctiforme*. BDLP is structurally related to the mitofusins and shares approximately 30% sequence identity; however, no BDLP membrane fusogenic activity has been demonstrated thus far and its *in vivo* function remains elusive (Low & Löwe, 2006; Low *et al.*, 2009).

Notwithstanding the lack of evidence for BDLP-mediated fusion, some subsequently characterised bacterial DRPs can mediate fission and fusion *in vitro*. Despite its homology to

BDLP and the mitofusins, isoniazid-induced protein (IniA) of *Mycobacteria* is capable of mediating liposome fission (Wang *et al.*, 2019). Similarly, despite its structural resemblance to dynamin 3, synDLP from the cyanobacterium *Synechocystis sp. PCC 6803* has tentatively been demonstrated to mediate liposome fusion (Gewehr *et al.*, 2023). DynA of *Bacillus subtillis* (herein termed bsDynA), is a chimeric fusion of two DRPs and is capable of mediating liposome fusion (Bürmann *et al.*, 2011). Numerous other bacterial DRPs are yet to be conclusively characterised as fission or fusion DRPs (Low & Löwe, 2006; Schlimpert *et al.*, 2017; Michie *et al.*, 2014; Taniguchi *et al.*, 2019).

Like BDLP, an *in vivo* function of synDLP has not yet been established. However, experimental evidence suggests bacterial dynamins possess diverse cellular functions responsible for bacterial persistence and virulence (Figure 10B). IniA is proposed to mediate antibiotic resistance via its membrane fission activity at the cytoplasmic membrane (Wang *et al.*, 2019). Similarly, bsDynA mediates resistance to antibiotic- and phage-induced membrane stress, whereby it localises to membrane deformations and presumably repairs membranes via its fusogenic activity (Sawant *et al.*, 2016). When associated with unperturbed membranes, bsDynA modulates lipid diffusion rates. LeoA, LeoB and LeoC found in enterotoxigenic *E. coli* and are localised to the periplasm where they are involved in the release of toxins within outer membrane vesicles (Michie *et al.*, 2014). In *Streptomyces*, DynA (herein termed stDynA) and stDynB are BDLP homologues that are expressed under the control of the sporulation transcription regulator WhiH. Both stDynA and stDynB are required to stabilise the z-ring of the sporulation divisome (Schlimpert *et al.*, 2017). In contrast to membrane-associated functions of bacterial DRPs, the DRP CrfC (colocalisation of replication fork DNA by the clamp) is involved in equipartitioning of the *E. coli* chromosome (Taniguchi *et al.*, 2019).

In comparison to eukaryotic DRPs, the membrane remodelling activities of bacterial DRPs are less well defined. Bacterial DRPs also exhibit more diverse functions. Hence, whether bacterial DRPs follow conserved mechanisms of fission and fusion remains an open question. Consequently, the study of bacterial DRPs presents an opportunity to elucidate the most fundamental principles of DSF-mediated membrane remodelling.

### 1.3.3 Dynamins Self-assemble onto Membrane to Constrict and Remodel the Underlying Bilayer

The mechanisms by which the DSF mediates membrane remodelling, specifically fission and fusion, remain an active area of investigation. The processes of membrane fission by classical dynamins are the most well-established, while fusion mechanisms are less comprehensively understood. Both phenomena appear to necessitate the constriction of membranes into a hemi-fission or hemifusion state (Section 1.1.8.1). Dynamins accomplish this through self-assembly into helical polymers on membrane surfaces that constrict the underlying bilayers at the filament lumen. This ability has been demonstrated in both eukaryotes and bacteria (Low *et al.*, 2009; Zhang *et al.*, 2020a). The subsequent sections explore the domain architecture and diversity of the DSF, how they self-assemble, the role of nucleotide in membrane remodelling, and the mechanisms of DSF-mediated fission and fusion, in the context of recent structural insights.

### 1.3.4 The Dynamin Superfamily Shares a Conserved Domain Architecture with Variable Membrane-Interacting and Additional N- and C-terminal Domains

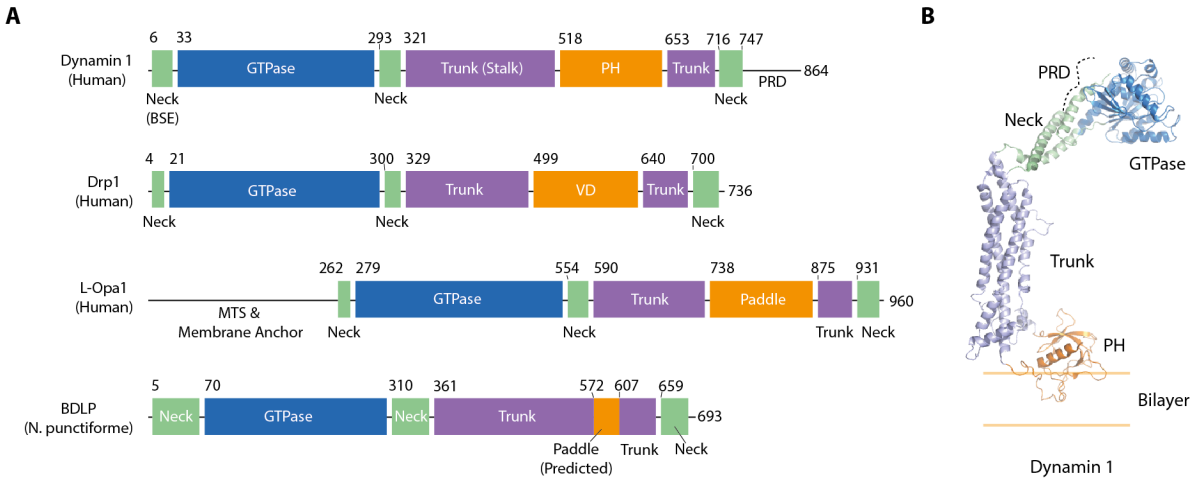


**Figure 11. DSF Conserved Domain Architecture.**
The DSF shares a conserved domain arrangement. **A,** Sequence diagrams of four dynamins labelled with BDLP domain nomenclature (Low & Löwe, 2006). Coloured boxes indicate the four conserved domains. Green = neck, blue = GTPase, purple = trunk, orange = membrane interacting domain. **This domain colour scheme is used throughout this thesis.** BSE = bundle signalling element, PH = pleckstrin homology domain, PRD = proline rich domain, VD = variable domain, MTS = mitochondrial targeting sequence. **B,** The discontinuous neck and trunk domains of the DSF fold into conserved helical bundles. Cartoon of a GMPPCP-bound dynamin 1 monomer from a membrane-constricting filament, PDB: 6DLU. Domains are coloured according to the boxes in panel A. Orange lines indicate a rough positioning of the bilayer.

Dynamins comprise four domains (Figure 11A). The most conserved domain is a large (~300 amino acids) GTPase domain. The remaining residues of dynamins have traditionally been categorised as the middle domain and the GTPase effector domain (GED), as well as some form of membrane-interacting domain separating the two (Ford & Chappie, 2019). However, full-length dynamin structures have revealed that the middle domain and GED do not form distinct domains, but rather combine to form two helical bundles (Figure 11B)(Low *et al.*, 2009; Zhang *et al.*, 2020a). These helical bundles have varying nomenclatures depending on the dynamin to which they belong. For simplicity, the nomenclature used for BDLP (Low & Löwe, 2006) is applied to all dynamins herein. The helical bundle proximal to the GTPase domain is termed the neck - the bundle signalling element (BSE) in dynamin 1 nomenclature. The helical bundle distal to the GTPase domain is termed the trunk - the stalk in dynamin 1 nomenclature. At the tip of the trunk is the membrane-interacting domain. The membrane-interacting domains are the least well conserved amongst dynamins, and their diversity and nomenclature are described in the following section.

#### 1.3.4.1 The Dynamin Superfamily Membrane-interacting Domains are Diverse

The membrane-interacting domains of dynamins are diverse and can confer lipid-specificity (Figure 11A). Classical dynamins, such as dynamin 1, interact with the membrane via a pleckstrin homology (PH) domain, which functions as both a negative charge sensor and membrane anchor (Mehrotra, Nichols & Ramachandran, 2014). DRPs lack a PH domain and have evolved alternative mechanisms of membrane binding. For instance, Drp1 possesses a disordered variable domain (VD) that binds cardiolipin (Mahajan *et al.*, 2021). BDLP is hypothesised to bind the membrane via a short helix-loop-helix paddle domain at the trunk tip, which is predicted to insert into the outer leaflet of lipid bilayers (Low *et al.*, 2009; Low & Löwe, 2006). Opa1 also possesses a paddle, which forms a distinct four-helix bundle and can similarly embed into the outer leaflet (von der Malsburg *et al.*, 2023). In addition to the paddle, L-Opa1 has an N-terminal membrane binding domain adjacent to the neck and GTPase domains (Del Dotto *et al.*, 2018). s-Mgm1 is also capable of interacting with membrane via its GTPase domain (Yan *et al.*, 2020). Concurrently, LeoB and LeoC have a membrane anchor within their shared GTPase domain (Michie *et al.*, 2014). Instead of a paddle, the mitofusins have two predicted transmembrane helices. Computational predictions of the full-length Fzo structure have indicated that these transmembrane helices

penetrate both leaflets of the bilayer in a two-helix X-shaped bundle (De Vecchis *et al.*, 2017). Perhaps the most divergent membrane binding domain exists in GBP1, which undergoes post-translational farnesylation at the trunk tip to facilitate LPS binding (Ji *et al.*, 2019).

#### 1.3.4.2 The Classical Dynamin Proline-rich Domain is involved in Signalling and Regulation

Some dynamins possess additional domains, including N-terminal peptides for targeting to specific organelles or for additional membrane anchoring (Ramachandran & Schmid, 2018). Classical dynamins also possess a C-terminal proline-rich domain (PRD), which is involved in signalling and regulation. The PRD interacts with the SH3 domains of BAR domain-containing proteins found at the pits of nascent clathrin-coated vesicles (Daumke, Roux & Haucke, 2014). Moreover, the PRD mediates interactions with other regulators such as syndapin 1, which anchors dynamin 1 to the membrane to facilitate ultrafast endocytosis (Imoto *et al.*, 2022). The PRD is also requisite for the dynamin 1-mediated actin bundling (Zhang *et al.*, 2020b).

### 1.3.5 Dynamins Self-assemble into Rings and Helical Filaments

Dynamins exhibit a remarkable and conserved ability to self-assemble into oligomers, filaments, and rings, which is requisite for membrane remodelling. All determined cryo-EM structures of DSF filaments possess a membrane-distal lattice of GTPase domains, connected by the neck and trunk to a lattice of membrane-interacting domains, which are proximal to the membrane (Figure 12A) (Faelber *et al.*, 2019).

In addition to helical filaments, large oligomeric ring assemblies of DSF members have been observed, mainly in low-salt conditions. While Drp1 rings have been observed, filaments have also been identified in the same studies (Kalia *et al.*, 2018; Basu *et al.*, 2017). It has been proposed that such rings might provide the additional constriction required for the final stages of mitochondrial scission (Basu *et al.*, 2017). Furthermore, both rings and filaments of Vps1 (yeast dynamin 1) have been observed and nucleotide state determines whether rings or filaments are formed (Varlakhanova *et al.*, 2018). The physiological relevance of DSF rings remains uncertain, although tomograms of mitofusins forming rings when establishing docking complexes of mitochondria suggest functional significance (Brandt *et al.*, 2016).

The principles of dynamin self-assembly are examined in the following sections, with particular emphasis on helical assemblies given their established physiological relevance (Cheng *et al.*, 2021).

### 1.3.6 Dynamins have both Highly-conserved and Specialised Oligomerisation Interfaces

Extensive crystallography studies of dynamins have demonstrated that the minimal assembly unit of the DSF is a dimer (Ford & Chappie, 2019; Gao *et al.*, 2010; Faelber *et al.*, 2011; Frohlich *et al.*, 2013; Fribourgh *et al.*, 2014; Low & Löwe, 2006). Furthermore, dynamins and DRPs can exist as tetramers in solution (Reubold *et al.*, 2015) and dimers and tetramers constitute the building blocks of numerous DSF helical assemblies (Figure 12A) (Ford & Chappie, 2019; Liu *et al.*, 2021a; Nyenhuis *et al.*, 2023). The existence of monomers, dimers, or tetramers in solution varies among DSF members and is likely attuned to their function and regulation. Oligomeric state is often dependent on nucleotide state, the presence of membrane, or the presence of heterodimerisation partners (Low & Löwe, 2006; Liu, Noel & Low, 2018). Indeed, synDLP can self-assemble in solution into large oligomers without nucleotide or membranes (Gewehr *et al.*, 2023; Junglas *et al.*, 2024) and bsDynA can mediate fusion independent of nucleotide, suggesting substantial spontaneous self-assembly (Bürmann *et al.*, 2011).

Interfaces between trunk domains, within both crystallographic (solution-like) and filament structures, are fundamental to oligomerisation (Frohlich *et al.*, 2013; Fribourgh *et al.*, 2014; Faelber *et al.*, 2019; Liu *et al.*, 2021a; Nyenhuis *et al.*, 2023; Gao *et al.*, 2011; Reubold *et al.*, 2015; Rochon *et al.*, 2024). Indeed, trunk-trunk interactions are fundamental to all elucidated structures of DSF filaments (Figure 12A). Trunk interfaces between mitofusins tethered in trans across opposing membrane surfaces may also be significant for fusion mechanisms (Koshiba *et al.*, 2004). In addition to trunk interfaces, cryo-EM reconstructions have revealed membrane-interacting domain interfaces within filaments (Figure 12B) (Nyenhuis *et al.*, 2023; Faelber *et al.*, 2019) and interfaces between neck domains have also been observed (Low *et al.*, 2009; Liu, Noel & Low, 2018; Bohuszewicz & Low, 2018). Beyond the critical trunk-trunk interfaces of dimers, tetramers and filaments, other more specialised interfaces exist. For example, GTPase-trunk domain and back-to-back neck-trunk interfaces enable Mgm1 to form unique head-to-tail trimers and hexamers that potentially induce membrane curvature (Figure 12C) (Yan *et al.*, 2020). Intra-molecular GTPase-trunk domain interactions also

stabilise certain DRPs such as BDLP, IniA (Figure 12D) and *Cyanidioschyzon merolae* Dmn1 (cmDmn1) in a tightly-packed closed conformation (Low & Löwe, 2006; Bohuszewicz & Low, 2018; Wang *et al.*, 2019).

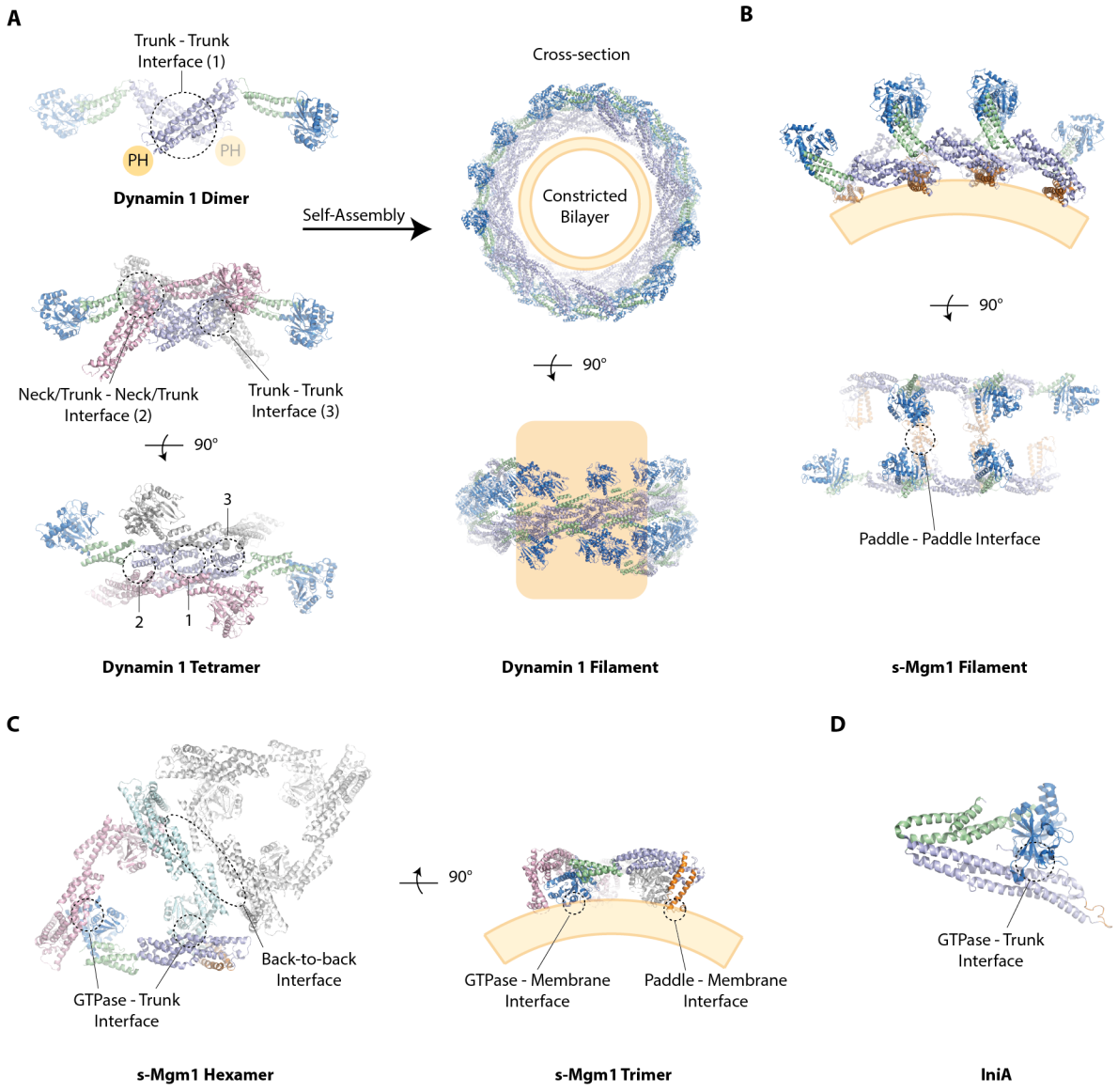


**Figure 12. DSF Oligomerisation Interfaces.**
Models are coloured by domain. GTPase domain = blue, neck = green, trunk = purple and membrane-interacting domain = orange. **A,** Trunk-trunk interactions are fundamental interactions for dimerisation and polymerisation of the DSF. Cartoon representations of dynamin 1 (PDB: 7AX3). Dynamin 1 dimers form the fundamental unit of dynamin 1 tetramers which have three trunk-mediated interfaces. Tetramers polymerise into helical filaments that constrict membrane. Such principles are broadly applicable to members of the DSF that form helical filaments. **B,** Helical filaments also mediate polymerisation interfaces between membrane-interacting domains. Cartoon representation of an s-Mgm1 helical filament (PDB: 6RZT), highlighting inter-rung paddle-paddle interfaces. **C-D,** Some DRPs exhibit other interaction interfaces. **C,** s-Mgm1 (PDB: 6JSJ) can form trimers and hexamers via novel GTPase-trunk and back-to-back neck-trunk domain interfaces. Such trimers can interact with

membrane via their GTPase domain to induce membrane curvature. **D,** IniA (PDB: 6J72) and BDLP form GTPase domain-trunk interfaces in a compact conformation.

Overall, trunk-trunk interfaces are crucial for dimerisation and polymerisation. However, a major conserved feature of dynamins is their ability to dimerise across their G-domains in a nucleotide-dependent manner. This can occur in solution (Low & Löwe, 2006; Qi *et al.*, 2016), or can require self-assembly into a helical polymer via the trunk-trunk interfaces first (Francy *et al.*, 2017).

#### 1.3.6.1 Dynamins Dimerise across a Conserved GTPase Domain Interface to Catalyse GTP hydrolysis

The DSF shares large (~300 amino acid) conserved GTPase domains, with the exception of distantly related Eps15 homology domain containing proteins (EHDs) that hydrolyse ATP (Daumke *et al.*, 2007; Melo *et al.*, 2017).

Dynamin GTPases are distinct from smaller canonical GTPases as they do not require guanine exchange factors due to their low affinity for nucleotide, and do not require GTPase activating proteins as dynamins exhibit assembly stimulated turnover (Daumke & Praefcke, 2016; Chappie *et al.*, 2010; Cao *et al.*, 2017). Indeed, self-assembly of dynamin 1 increases its nucleotide turnover 1000-fold (Stowell *et al.*, 1999). The basal hydrolysis rates and nucleotide affinities of dynamins can vary, presumably in relation to their function. For instance, Mfn1 exhibits a nine-fold lower nucleotide affinity relative to dynamin 1 (Qi *et al.*, 2016). Furthermore, whilst dynamin 1 exhibits GTP hydrolysis basal rate of ~1 $min^{-1}$, synDLP demonstrates a high basal rate of ~45 $min^{-1}$ due to its capacity to self-assemble in solution without nucleotide or lipid cofactors (Gewehr *et al.*, 2023).

The assembly-stimulated turnover of dynamins is attributed to dimerisation of their GTPase domains upon nucleotide binding (Figure 13), which stabilises and positions key catalytic residues and nucleotide in trans (Daumke & Praefcke, 2016). Herein, dimerised GTPase domains are referred to as G-dimers. Dynamin 1 polymerises into helical filaments that enable G-dimers to form between helical rungs (Figure 13A) (Liu *et al.*, 2021a). Similarly, Opa-1 and Mgm1 either form filaments with stable inter-rung G-dimers (Figure 12B), or filaments that position GTPase domains in optimal orientations to form inter-rung G-dimers (Faelber *et al.*,

2019; von der Malsburg *et al.*, 2023; Nyenhuis *et al.*, 2023). While Drp1 can form filaments on both PS- and cardiolipin-based membrane templates, only cardiolipin stimulates GTP turnover. This phenomenon is attributed to cardiolipin-binding induced changes in the filament architecture that facilitate G-dimer formation (Francy *et al.*, 2017). Conversely, mitofusins and related DRPs such as BDLP form G-dimers in solution (Figure 13B) (Qi *et al.*, 2016; Low & Löwe, 2006). In summary, nucleotide binding induces DSF GTPase domain dimerisation in solution or in self-assembled filaments, which stimulates GTPase activity.

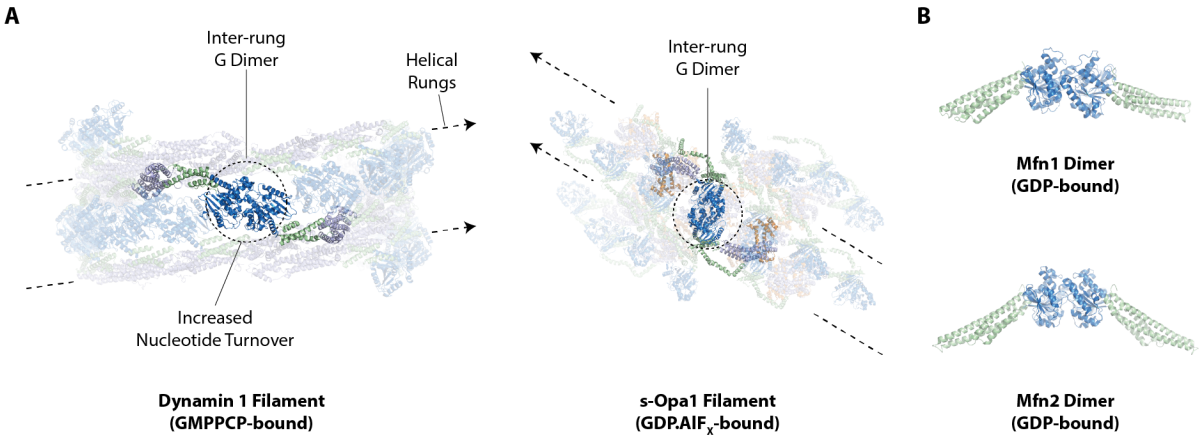


**Figure 13. GTPase Domain Dimerisation in Filaments or Solution.**
**A,** Self-assembly of dynamin 1 (PDB: 7AX3), s-Opa1 (PDB: 8EFR) and related DSF members into helical filaments aligns GTPase domains between rungs to allow dimerisation across a conserved interface, leading to assembly-stimulated nucleotide turnover. **B,** Mfn1 (PDB: 5GOM), Mfn2 (PDB: 6JKF) and related DRPs such as BDLP form G-dimers in the presence of nucleotide in solution. This is the major oligomerisation interface of mitofusin-like DRPs.

While the DSF GTPase domains and G-dimer interfaces are highly conserved, variations exist. For instance, synDLP exhibits an extended G-dimerisation interface (Junglas *et al.*, 2024) and, whereas classical dynamins utilise a catalytic cation for GTP hydrolysis, GBP1 employs an arginine finger (Daumke & Praefcke, 2016). Nevertheless, four key catalytic motifs are conserved amongst dynamin GTPase domains – G1-G4 (Figure 14A). The G1 motif (P-loop) is responsible for β-phosphate coordination and coordination of a cation to neutralise the negative charge developed in the transition state (Figure 14B) (Chappie *et al.*, 2010). The terminal serine or threonine residues of the G1 motifs are responsible for cation coordination. G2 and G3, known as switch 1 and switch 2 respectively, are stabilised and oriented by

G-dimerisation for catalysis (Chappie *et al.*, 2010; Praefcke & McMahon, 2004; Ford & Chappie, 2019). G2 is also responsible for cation coordination, and both G2 and G3 motifs coordinate the γ-phosphate, thus undergoing nucleotide state-determined conformational changes (Daumke & Praefcke, 2016). G4 stabilises the guanine base.

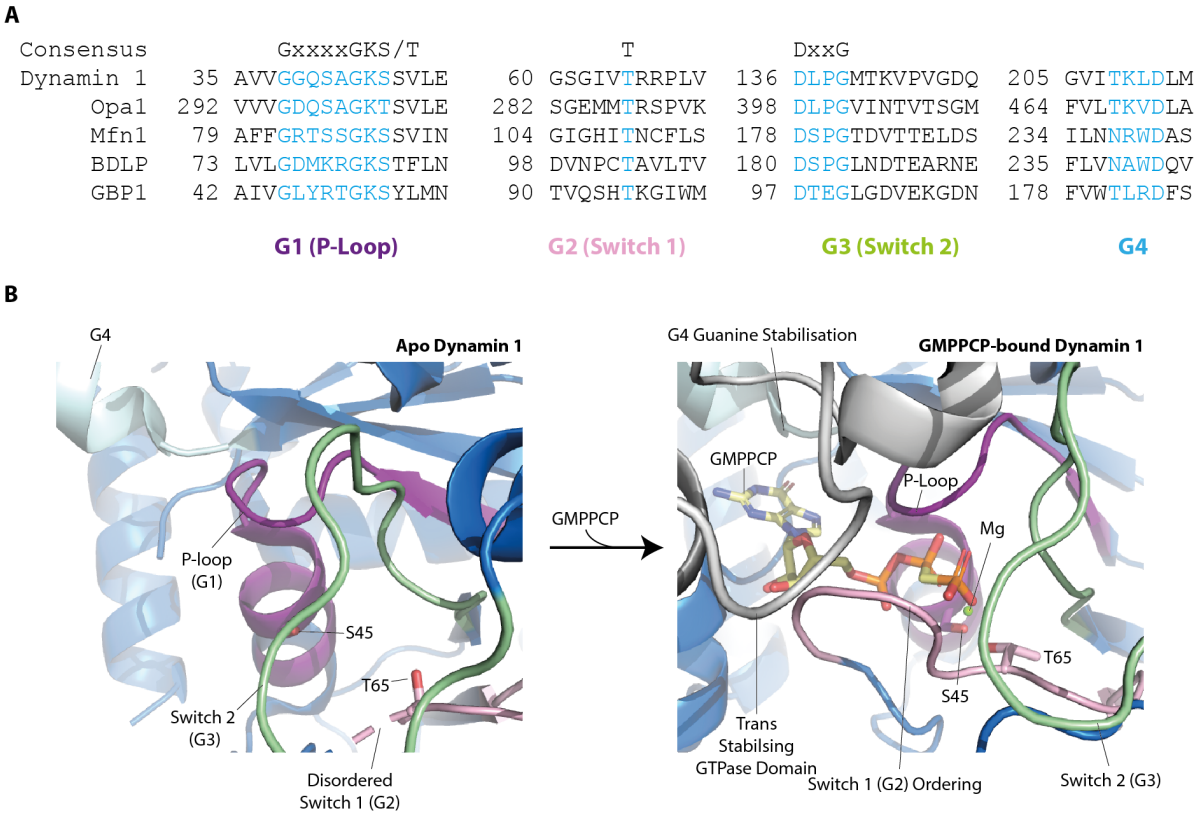


**Figure 14. Conserved GTPase Domain Catalytic Motifs and Nucleotide Coordination.**
The active site of DSF GTPases is characterised by four conserved motifs. **A,** Multiple sequence alignment of human dynamin 1 and DRPs, and BDLP from *N. punctiforme*. Four conserved motifs are responsible for nucleotide coordination and hydrolysis. **B,** Rearrangements within the nucleotide pocket of dynamin 1 upon transition from the apo (PDB: 6S9A) to GMPPCP-bound (PDB: 3ZYC) state. The P-loop (purple) coordinates the β-phosphate, and a magnesium ion via serine-45. Switch 1 (pink), which is largely disordered in the absence of nucleotide, also coordinates the magnesium ion via threonine-65. The P-loop, switch 1 and switch 2 (green) are stabilised in trans by a G-dimerisation partner (grey).

Changes in nucleotide state influence GTPase domain interactions with the neck domain and can result in significant conformational changes in the neck and trunk domains (Chappie *et al.*, 2011). How nucleotide state modulates such global conformational changes is not consistent among DSF members. Furthermore, although all dynamins hydrolyse GTP, the mechanism by which the energy harnessed from GTP hydrolysis is utilised to mediate

membrane fission and fusion remains a subject of debate, with contrasting models proposed. Conserved large conformational changes and the role of nucleotide are examined in the following sections.

### 1.3.7 The role of Nucleotide Binding and Hydrolysis during Membrane Remodelling is Inconsistent across the Dynamin Superfamily

The role of nucleotide and nucleotide hydrolysis in membrane remodelling is inconsistent across the dynamin superfamily (DSF). GTP hydrolysis is essential for vesicle scission by dynamin 1 (Antonny *et al.*, 2016), and mutations in nucleotide binding residues of mitofusins are associated with Charcot Marie Tooth syndrome (Qi *et al.*, 2016). However, bsDynA can facilitate nucleotide-independent liposome fusion (Sawant *et al.*, 2016). GTP hydrolysis induces constriction of dynamin 1 filament and the underlying bilayer (Jimah & Hinshaw, 2019), but also results in filament disassembly (Morlot *et al.*, 2012). Nucleotide binding and subsequent G-dimerisation are crucial for oligomerisation of Mfn1, BDLP and dynamin 1 (Cao *et al.*, 2017; Low *et al.*, 2009; Liu *et al.*, 2021a), whereas MxB can form filaments in the absence of nucleotide, and GTP binding promotes MxB filament disassembly (Alvarez *et al.*, 2017). In some Mgm1 and Opa1 filament structures G-dimerisation does not occur, yet both require nucleotide to polymerise (Zhang *et al.*, 2020a; Faelber *et al.*, 2019), and truncated constructs or other filament forms are able to form G-dimers (Yu *et al.*, 2020; Nyenhuis *et al.*, 2023).

Notwithstanding the inconsistent role of nucleotide, it is clear that nucleotide-induced conformational changes and their effect on domain arrangement and the helical filament architecture are critical for dynamin function. The varying responses of DSF members to nucleotide binding and state are likely adapted to their respective functions. For instance, Mfn1 and Mfn2 are simultaneously necessary for mitochondrial fusion and share high sequence identity, yet Mfn2 can form significantly tighter G-dimers that remain stable following nucleotide hydrolysis and exhibit higher hydrolysis rates (Li *et al.*, 2019; Ozeir & Cohen, 2022). This observation suggests that both proteins have distinct roles during membrane fusion, modulated by their response to nucleotide.

### 1.3.8 Conformational Flexibility of Two Conserved Hinges is Essential to Dynamin Function

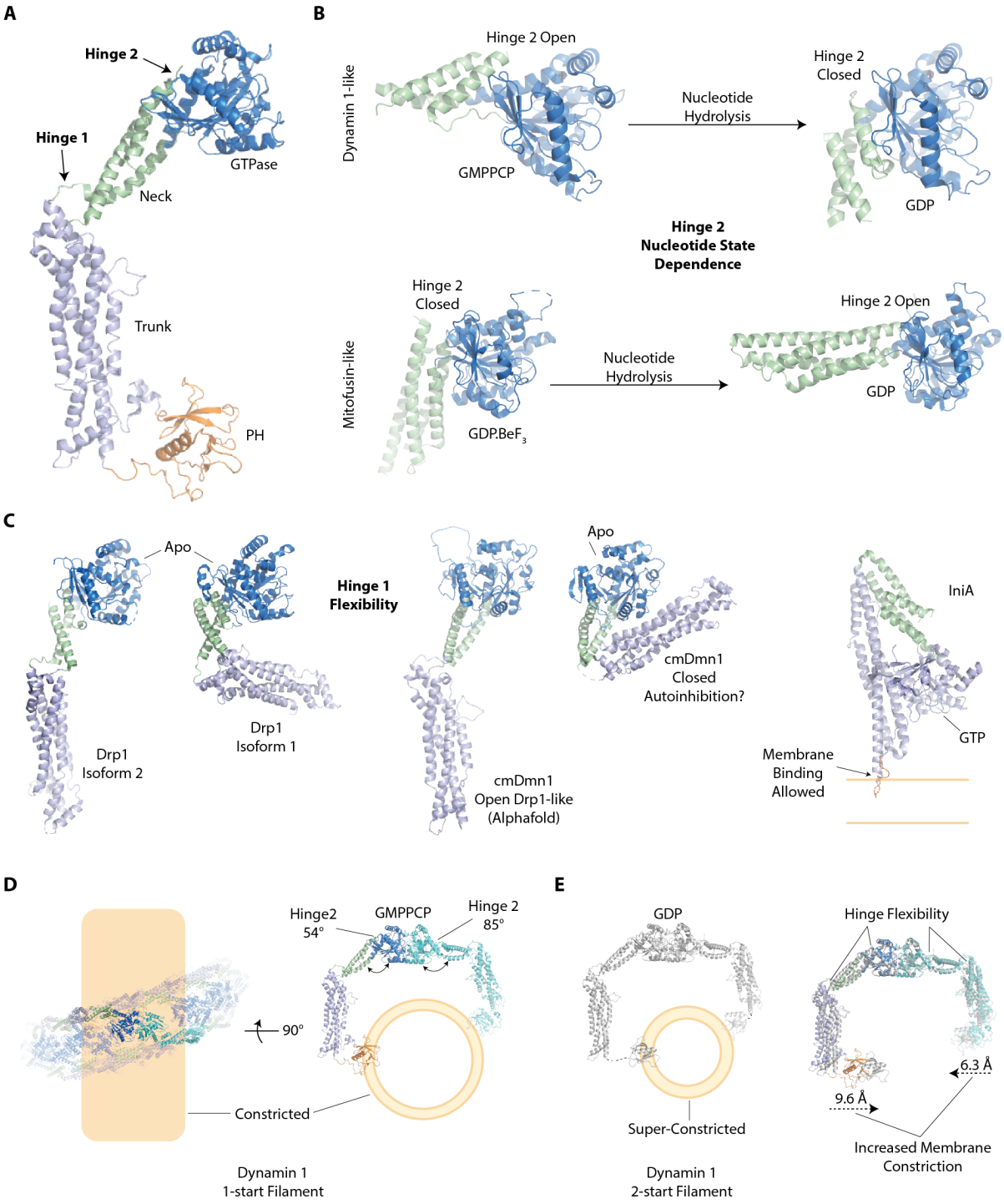


**Figure 15. Hinge 1 and Hinge 2 Conformational Flexibility.**
**A,** Hinge 1 and hinge 2 locations between domains, using dynamin 1 (PDB: 6DLU) as an illustration. **B,** Opening and closing of hinge 2 during nucleotide hydrolysis varies between DSF members. Dynamin 1-like response to nucleotide hydrolysis (top), where hydrolysis leads to hinge 2 closing, is observed in Drp1, Opa-1 and related homologues. Dynamin 1 is used as an example here, PDB: 37YC

(open), 5D3Q (closed). Mitofusin-like response to nucleotide hydrolysis (bottom), where hydrolysis leads to hinge 2 opening, is observed in BDLP, Fzo and related homologues. Mfn1 is used as an example here, PDB: 5YEW (closed), 5GOM (open). **C,** Demonstrations of hinge 1 flexibility. Left: crystal structures of Drp1 Isoform 1 (PDB: 8T1H) and Isoform 2 (PDB: 4BEJ) exhibit drastically different hinge 1 conformations as dimers in solution. Middle: the cmDmn1 crystal structure (PDB: 6FGZ) was observed in a compact hinge 1 and hinge 2 closed conformation in solution. Comparison with related dynamins suggests significant opening about hinge 1 occurs to enable polymerisation into a helical filament, as illustrated by the Alphafold predicted cmDmn1 structure (Varadi *et al.*, 2024). Right: Apo or GTP-bound IniA (PDB: 6J72) exhibits a closed hinge 1 conformation analogous to GDP-bound or Apo BDLP. An exposed paddle loop enables IniA to bind membrane despite the compact conformation. **D/E,** Hinge 1 and hinge 2 conformational flexibility is key to polymerisation and membrane constriction. **D,** 1-start helical filament of dynamin 1 (PDB: 6DLU) forms different hinge conformations between protomers of the same G-dimer to constrict the underlying membrane. **E,** Hinge flexibility allows dynamin 1 to super constrict underlying membrane to the point of hemifission in a 2-start filament (grey, PDB: 8SZU). Alignment of G-dimers from the 1- and 2-start helical filaments (right) illustrates how hinge conformational changes lead to repositioning of PH domains to constrict the membrane tube further.

Dynamins and DRPs exhibit significant conformational changes in response to nucleotide state, lipids, and polymerisation interactions about two hinges: Hinge 1 joins the neck and trunk domains, and hinge 2 joins the neck and GTPase domains (Figure 15A).

The proximity and contact of the neck and GTPase domains enable nucleotide-induced conformational changes in the GTPase domain to significantly influence the hinge 2 conformation. This is evidenced by multiple crystal structures of minimal dynamin or DRP constructs comprising solely the neck and GTPase domains (Li *et al.*, 2019; Wenger *et al.*, 2013; Varlakhanova *et al.*, 2018; Rennie *et al.*, 2014; Ford & Chappie, 2019). Generally, hinge 2 can be characterised in an open or closed conformation, whereby rotations about hinge 2 position the GTPase domain against the neck in a tight closed conformation, or displace the GTPase domain away from the neck in an open conformation (Rennie *et al.*, 2014). For classical dynamins and related DRPs in the apo and GDP-bound states, closed hinge 2 conformations are adopted (Figure 15B) (Anand, Eschenburg & Reubold, 2016; Rennie *et al.*, 2014). In the presence of non-hydrolysable GTP analogues, open hinge 2 conformations have been observed (Chappie *et al.*, 2010). The opposite is true for BDLP and the mitofusins – a hinge 2 closed conformation in the presence of GTP analogues, and hinge 2 open conformation in the presence of GDP (Low *et al.*, 2009; Low & Löwe, 2006; Li *et al.*, 2019; Yan *et al.*, 2018). Transition state analogues have yielded both open and closed conformations for different DSF members, further highlighting the function-dependent tuning of hinge 2 conformation in response to nucleotide state (Ford & Chappie, 2019).

Crystallography and cryo-EM structures of full-length dynamins and DRPs have also revealed conformational flexibility about hinge 1 (Figure 15C) (Low *et al.*, 2009; Liu, Noel & Low, 2018; Kalia *et al.*, 2018; Bohuszewicz & Low, 2018; Liu *et al.*, 2021a). Evidence for extreme hinge 1 flexibility initially emerged from BDLP, which exhibits a hinge 1 closed conformation when GDP-bound or nucleotide free, whereby the trunk packs against the GTPase domain (Low & Löwe, 2006). In such hinge 1 closed conformation, the predicted membrane-binding paddle is packed within the molecule; consequently, it was postulated that hinge 1 fully closed conformation represents a regulatory mechanism that maintains BDLP off the membrane in a nucleotide dependent manner. A compact hinge 1 closed conformation has also been observed for GBP1, IniA, and cmDmn1 and is proposed to exist in the mitofusins (Prakash *et al.*, 2000; Wang *et al.*, 2019; Bohuszewicz & Low, 2018; Cao *et al.*, 2017; Li *et al.*, 2019). The hinge 1 closed conformation of cmDmn1 regulates its activity by maintaining it in a soluble tetramer off the membrane and was the first demonstration of a eukaryotic DRP hinge 1 closed conformation (Bohuszewicz & Low, 2018). However, the extent to which the hinge 1 closed confirmation is conserved across the DSF remains an open question. Additionally, uncertainty persists regarding whether the hinge 1 closed confirmation universally maintains dynamins in an off-membrane state, as a hinge 1 closed conformation has been observed in MxB helical filaments (Alvarez *et al.*, 2017) and IniA can bind membrane in a nucleotide-independent manner (Wang *et al.*, 2019). Simulations indicates that Fzo, modelled on the BDLP hinge 1 closed conformation, can still bind membrane with its transmembrane helices in a closed conformation (De Vecchis *et al.*, 2017).

Flexibility of both hinges has been observed in dynamin filaments (Figure 15D and Figure 15E). Dynamin 1 filaments exhibit different hinge conformations between protomers of the same G-dimer (Figure 15D) (Kong *et al.*, 2018; Liu *et al.*, 2021a). Hinge flexibility is also crucial for increasing constriction of the underlying membrane (Figure 15E). Overall, the flexibility of hinges 1 and 2 and the nucleotide-dependence of their conformational state are crucial to the fission and fusion mechanisms discussed in the subsequent sections.

### 1.3.9 GTP Hydrolysis Drives Power-strokes and Rung Sliding in Fission Dynamin Filaments to Constrict the Underlying Membrane

The fundamental principle of DSF-mediated fission is polymer-driven constriction of the membrane to achieve a hemi-fission state. It is established that while self-assembled DSF

filaments can accomplish this constriction, membrane tension contributing to the elastic stress of the membrane is also necessary for fission (Morlot *et al.*, 2012). Two competing models have emerged to explain how nucleotide hydrolysis-mediated hinge 2 closing leads to membrane fission (Antonny *et al.*, 2016). The disassembly model proposes that self-assembly of the filament is sufficient to constrict the underlying membrane to a diameter (3-4 nm) required for hemifission. Concerted GTP hydrolysis within the filament would subsequently lead to rapid hinge 2 closing-induced. This would disrupt G-dimers and subsequently cause depolymerisation and spontaneous fission of the underlying hemi-fission state (Antonny *et al.*, 2016; Low *et al.*, 2009). An alternative 'power-stroke' model suggests that cycles of GTP hydrolysis cause rungs of the filament to slide past one another to increase constriction to the point of fission, driven by progressive cycles of hinge 2 closing and opening to break and reform G-dimers, analogous to the actin-myosin power stroke that drives contraction of skeletal muscle (Figure 16A) (Tyska & Warshaw, 2002; Antonny *et al.*, 2016).

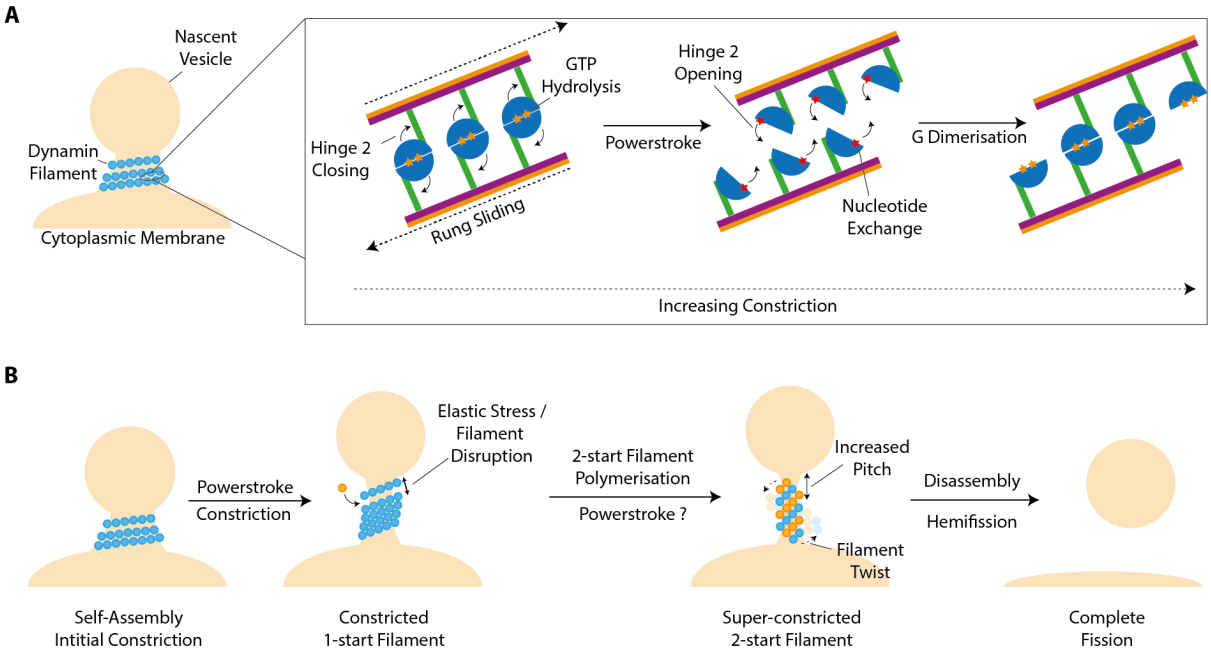


**Figure 16. Mechanisms of DSF-mediated Membrane Fission.**
**A,** Power-stroke model of filament constriction. Self-assembly of a helical dynamin filament induces membrane curvature. Increased constriction is achieved by GTP hydrolysis-driven power strokes, where rungs that interact via G-dimers slide past one another due to hinge 2 closing (and flexibility of hinge 1). Such rung sliding increases constriction of the underlying membrane. Following hydrolysis, nucleotide exchange and GTP binding allows new G-dimers to form and restart the cycle. **B,** Model of dynamin-mediated fission. Initial self-assembly of the dynamin helical filament induces membrane curvature, which is increased by power-stroke driven constriction. Elastic stress and breaking of G-dimers cause partial depolymerisation to allow formation of a super-constricted 2-start filament.

Within the super-constricted filament, the underlying membrane has reached a near-hemifission state. A twist and disassembly of the filament is required to complete fission via a hemifission stalk.

Recent evidence supports the power-stroke model. The depolymerisation model necessitates concerted GTP hydrolysis throughout the filament. However, high resolution fluorescence microscopy has demonstrated that GTP hydrolysis occurs in stochastic bursts at randomised locations within the filament (Galli *et al.*, 2017). Furthermore, simulations have indicated that the GTPase power-stroke is capable of performing the work required to constrict the membrane to a hemifission state (Ganichkin *et al.*, 2021). The disassembly model remains partially relevant, as simulations suggest that following filament sliding-driven constriction, disassembly is necessary to promote fission via a hemifission intermediate at the final stages of scission (Pannuzzo, McDargh & Deserno, 2018).

Cryo-EM structural analysis has provided mechanistic detail of the dynamin fission mechanism. In a super-constricted state, the PH domains of dynamin 1 filaments are tilted, which is proposed to facilitate super constriction of the bilayer by disrupting the outer leaflet (Sundborger *et al.*, 2014). This is consistent with simulations that demonstrate tilting of the filament along its longitudinal axis is required for fission. This tilting likely enhances the capacity of PH domains to disrupt the bilayer and facilitate super-constriction (Pannuzzo, McDargh & Deserno, 2018). Structures of both one-start and two-start dynamin filaments have been identified, and in all known cases, super-constriction necessitates a two-start filament (Kong *et al.*, 2018; Liu *et al.*, 2021a; Jimah *et al.*, 2024). The hinge flexibility discussed above in Section 1.3.8 is requisite for dynamins being able to adopt both one- and two-start helices (Figure 15E) (Liu *et al.*, 2021a). The two-start dynamin filament is energetically favourable as it experiences less elastic stress. If power-stroke-derived constriction of a one-start filament causes sufficient elastic stress to disrupt G-dimers and partially disassemble the filament before fission is achieved, it is hypothesised that partial disassembly allows a two-start filament to nucleate and stabilise the super-constriction required for hemifission (Figure 16B) (Liu *et al.*, 2021a). Indeed, post-GTP hydrolysis dynamin adopts a two-start helical conformation and can adopt multiple helical conformations *in* vivo, supporting this hypothesis (Jimah *et al.*, 2024). In summary, fission is achieved by GTP hydrolysis within self-

assembled filaments which drives sliding of filament rungs past one another to increase constriction of the underlying membranes to the point of hemi-fission.

### 1.3.10 The Mechanisms of Dynamin-mediated Membrane Fusion are not well Characterised

In comparison to fission, the mechanisms of DSF-mediated membrane fusion are less well characterised. For the mitofusins in particular, full length structures remain elusive and structural information is limited to truncated constructs or *in silico* simulations (Li *et al.*, 2019; Qi *et al.*, 2016; De Vecchis *et al.*, 2017). Fusion of membranes proceeds via a hemifusion intermediate. Given the capacity of Opa-1 and Mgm1 to polymerise onto membrane templates as helical filaments, it is plausible that IMM hemifusion stalks are achieved by constriction of opposing bilayers (Faelber *et al.*, 2019; von der Malsburg *et al.*, 2023). Beyond facilitating hemifusion intermediates, dynamins must also tether membranes in trans to facilitate fusion, drawing opposing membranes together (Shi *et al.*, 2024). Models of atlastin and mitofusin-mediated fusion suggest that the tight tethering of opposing bilayers, without filament-mediated constriction, may be sufficient to mediate lipid mixing and fusion (Shi *et al.*, 2024; Brandt *et al.*, 2016).

#### 1.3.10.1 Mitofusin-like Dynamins Tether and Dock Membranes in Trans to Achieve Fusion

For mitofusins to tether membranes in trans, they must be able to dimerise in trans while anchored to opposing membranes (Figure 17A). Although it has been suggested that dimerisation can occur in an anti-parallel topology between neck domains (Koshiba *et al.*, 2004), the ability of mitofusins to G-dimerise in a nucleotide-dependent manner (Yan *et al.*, 2018), and the requirement of GTP hydrolysis to achieve fusion (Brandt *et al.*, 2016) strongly suggest that mitofusins mediate trans tethering via G-dimerisation. Mitofusins and BDLP exhibit relatively slow hydrolysis rates (Cao *et al.*, 2017; Low & Löwe, 2006). As mitofusin G-dimerisation necessitates GTP binding (Yan *et al.*, 2018), their slow hydrolysis rates relative to fission dynamins could be attributed to their trans-tethering requirements, favouring prolonged G-dimerisation to maintain trans tethering of membranes (Hoppins & Nunnari, 2009).

Upon GTP hydrolysis, mitofusins exhibit BDLP-like hinge 2 conformational changes, whereby they transition from a hinge 2 closed to a hinge 2 open conformation (Yan *et al.*, 2018). Given

that mutations of mitofusin hinge 1 impede fusion and the mitofusins share homology with BDLP, it is hypothesised that the mitofusin hinge 1 can also undergo BDLP-like hinge 1 closing upon GTP hydrolysis (Cao *et al.*, 2017). Consequently, BDLP-like conformational closing of trans-tethered mitofusins upon GTP hydrolysis would draw opposing membranes into closer proximity. Eventual dissociation of the G-dimer following GTP hydrolysis would facilitate further G-dimerisation and membrane docking (Gao & Hu, 2021). Cryo-ET of mitofusin-docked OMMs indicates that tight docking is sufficient to form a fusion pore (Brandt *et al.*, 2016), consistent with models of atlastin docking membranes to induce fusion via G-dimerisation (Shi *et al.*, 2024). However, mitofusin filament-driven constriction of membranes to force a hemifusion stalk cannot be excluded given the capacity of BDLP to tubulate membranes (Low *et al.*, 2009). Furthermore, atlastin forms G-dimers in a criss-cross fashion, analogous to GBP1 (Shi *et al.*, 2024; Weismehl *et al.*, 2024), whereas mitofusins form BDLP-like G-dimers (Low & Löwe, 2006; Li *et al.*, 2019; Cao *et al.*, 2017). Unlike mitofusin-mediated fusion, atlastin-mediated fusion is achieved independent of GTP hydrolysis, as hydrolysis is only required for disassembly of atlastin dimers (Crosby & Lee, 2022). Therefore, it is not known whether mitofusins mediate fusion via tight docking of membranes, an unknown mechanism, or in an Opa1-like manner.

#### 1.3.10.2 Opa1-like Dynamins can form Helical Polymers on Membranes, and this may be Required to Achieve Membrane Fusion

The ability of Opa1 and Mgm1 to polymerise onto membranes in a dynamin-like manner suggests that Opa1-mediated IMM fusion is achieved via membrane constriction to form a hemifusion stalk (Figure 17) (Zhang *et al.*, 2020a; Faelber *et al.*, 2019; von der Malsburg *et al.*, 2023). This observation also indicates a potential role for GTP hydrolysis mediating a dynamin 1-like power-stroke to increase constriction. Trans tethering may be accomplished not through G-dimerisation but via other interfaces; crystallography and biochemical analysis of Mgm1 have demonstrated unique interfaces that facilitate back-to-back and head-to-tail association of Mgm1 protomers (Yan *et al.*, 2020). These unique interfaces also enable Mgm1 to form hexamers and tetramers that may induce initial membrane curvature in a BAR-domain-like manner prior to helical filament formation. As L-Opa1 is anchored to the membrane by an N-terminal domain (distinct and distal to its membrane-interacting paddle) and both L-Opa1 and s-Opa1 are required for fusion (Del Dotto *et al.*, 2018). Such novel

interfaces may enable L-Opa1 to recruit s-Opa1 to sites of membrane fusion to form curvature-inducing helical polymers (Yan *et al.*, 2020).

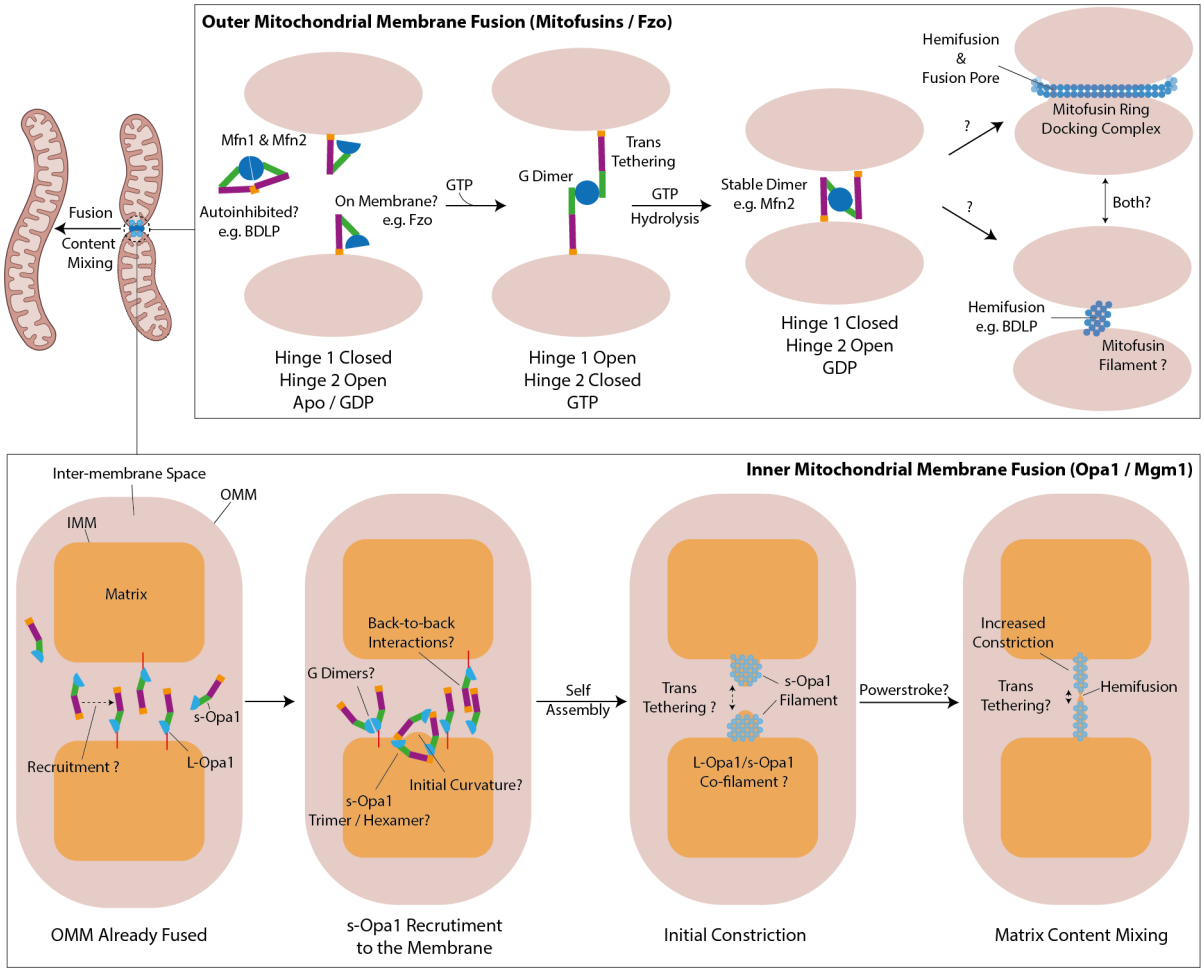


**Figure 17. Mechanisms of Mitochondrial Membrane Fusion.**
Mitochondrial fusion, leading to content mixing of both the inter-membrane space and matrix requires fusion of the inner and outer mitochondrial membranes. *Mitochondria icons made using BioRender.com* **Outer mitochondrial membrane fusion (OMM - top):** Mitofusins exhibit an overall compact and closed conformation in the apo or GDP-bound state, with hinge 1 closed and hinge 2 open. When GTP bound and tethered to the membrane via their transmembrane helices, they exhibit an overall open conformation, with hinge 1 open and hinge 2 closed. Such a conformation may allow G-dimers to form between mitofusins tethered to opposing OMMs. The slow hydrolysis rates of mitofusins may allow multiple trans-tethered G-dimers to form at once. Upon the eventual GTP hydrolysis, mitofusins will adopt a closed conformation again, bringing the opposing OMMs into close proximity. Mitofusins can maintain a G-dimer following nucleotide hydrolysis, which would keep opposing OMMs in proximity. Or release of the dimer would allow subsequent re-tethering and tighter docking of OMMs. Fusion of docked OMMs, leading to inter-membrane space content mixing, may occur spontaneously at regions of high curvature within a mitofusin docking ring complex, or via helical polymerisation of mitofusins to constrict the opposing membranes into a hemifusion state. **Inner mitochondrial membrane fusion (IMM – bottom):** L-Opa1, tethered to the IMM via an N-terminal domain, likely recruits s-Opa1 to the IMM via G-dimerisation or back-to-back interfaces. Furthermore, s-Opa1 may induce initial IMM curvature via trimerisation. s-Opa1 filaments or potentially L-Opa1/s-Opa1 co-filaments self-assemble to tubulate the IMM, with potential GTP power strokes allowing Opa1 to achieve tighter constriction.

Trans-tethering by Opa1 may be required to bring constricted IMMs into proximity. Such filaments leave the constricted IMMs in a hemifusion state, leading to fusion and matrix content mixing.

### 1.3.11 Several Dynamins Require Partner Dynamins to Remodel Membrane

In addition to both L-Opa1 and s-Opa1 being required for IMM fusion (Del Dotto *et al.*, 2018), Mfn1 and Mfn2 are required to act in tandem for OMM fusion and can form hetero G-dimers (Ozeir & Cohen, 2022; Li *et al.*, 2019). Such heterotypic interactions may be necessary for trans tethering. Further evidence for this comes from cjDLP1 and cjDLP2, which alone are both monomeric, but form a heterotetramer when combined that can tether membranes in trans (Liu, Noel & Low, 2018). Furthermore, bsDynA, which has known fusogenic activity, is a fusion of two DRP genes, and therefore another example of trans tethering by a dynamin pair (Bürmann *et al.*, 2011; Sawant *et al.*, 2016). Although not identified as a fusion dynamin, BDLP exists in a two-dynamin operon with BDLP2. Therefore BDLP may require its partner DRP to mediate membrane fusion (Low & Löwe, 2006; Bohuszewicz, Liu & Low, 2016). Many bacterial DRPs exist in multi-dynamin operons and therefore may require heterodimerisation to achieve their functions (Bohuszewicz, Liu & Low, 2016). Consistent with bacterial DRPs working in heterooligomeric partnerships to achieve fusion, LeoA works in tandem with LeoBC to achieve OMV release (Michie *et al.*, 2014).

### 1.3.12 Several Dynamins are Regulated by Binding Partners

Beyond heterooligomerisation in fusion processes, numerous other dynamins are regulated or function in conjunction with binding partners. The PRD of classical dynamins serves as a crucial site for recruitment by SH3 domain-containing proteins and facilitates regulation by kinases (Armbruster *et al.*, 2013). Drp1 also contains multiple phosphorylation and SUMOylation sites that regulate its activity and mitochondrial dynamics (Zerihun, Sukumaran & Qvit, 2023).

As Drp1 regulation and mitochondrial scission (involving fission of two membranes) is complex, multiple Drp1 binding partners have been identified. Cryo-EM reconstructions have demonstrated that Drp1 forms co-polymers with the mitochondrial receptor MID49, suggesting a potential mechanism for Drp1 targeting to specific sites to mediate mitochondrial fission (Kalia *et al.*, 2018). Although Drp1 alone is sufficient for constriction of

unilamellar membrane tubes *in vitro* (Kamerkar *et al.*, 2018), evidence indicates that colocalisation of GBP1 and Drp1 is necessary for the coordinated mediation of mitochondrial fission (Kalb *et al.*, 2024). Classical dynamins have also been observed at mitochondrial fission sites colocalised with Drp1 (Lee *et al.*, 2016), yet their necessity is disputed as mitochondrial fission is achieved in their absence (Fonseca *et al.*, 2019). Additionally, membrane destabilising proteins not related to dynamins, recently termed mitofissins, mediate membrane fission *in vitro* and are necessary for mitochondrial fission. Mitofissins may act in concert with Drp1 by destabilising the IMM and priming it for Drp1-mediated fission (Connor, Matta & Friedman, 2023; Fukuda *et al.*, 2023).

In conclusion, whilst dynamins and DRPs alone can mediate fission and fusion *in vitro*, a complete understanding of their regulation and complex functions *in vivo* remains elusive.

### 1.3.13 Summary of the Conserved Principles of DSF-mediated Membrane Remodelling

While DSF-mediated membrane remodelling mechanisms are diverse and not fully elucidated, the structural and biochemical insights reviewed here highlight fundamental conserved principles of the DSF. Specifically, dynamins and DRPs possess the ability to bind and hydrolyse GTP and dimerise via their GTPase domains. They exhibit considerable flexibility about two hinges. Nucleotide state influences the conformation of switches 1 and 2 within the GTPase domain, and on a consequent more global scale, the conformation of hinges 1 and 2. The impact of nucleotide state on G-dimers and the hinges is variable and adapted to dynamin function. Moreover, all DSF members self-assemble and can interact with membranes. These abilities often result in dynamin polymerisation into helical filaments on membrane templates that constrict the underlying bilayer.

## 1.4 Bacterial Dynamin-Like Protein (BDLP) is a Mitofusin Homologue with Unknown Function, Encoded by the Cyanobacterium *Nostoc punctiforme*

This study focuses on bacterial dynamin-like protein (BDLP), a DRP encoded by the genome of the cyanobacteria *Nostoc punctiforme*. Bacterial DRPs generally exhibit diverse functions (Section 1.3.2). 121 cyanobacterial DRPs have been identified in 56 different species (Jilly *et al.*, 2018), suggesting cyanobacterial DRPs are widely conserved and significant, yet

inadequately understood. BDLP-GFP forms punctate foci in *N. punctiforme* cells distributed across the cell periphery, with some evidence for localisation to the cell septum and rings that circumvent the cell body – suggesting potential roles in cell division (Low & Löwe, 2006). However, BDLP's *in vivo* function remains to be elucidated. BDLP thus serves as a valuable model DRP for investigating cyanobacterial dynamin function and, more broadly, bacterial DRP functions.

BDLP is found in the same clade of DRPs containing the mitofusins, Fzo, and Fzl, suggesting an ancient evolutionary origin of this class of DRP, potentially predating the endosymbiotic events that gave rise to eukaryotes or indicating a horizontal gene transfer. Nevertheless, BDLP has not been demonstrated to mediate membrane fusion like its eukaryotic homologues (Low & Löwe, 2006; Low *et al.*, 2009). Given the diverse functions of bacterial DRPs, BDLP may possess a hitherto unresolved unique function within *N. punctiforme*. Furthermore, mechanistic insights into mitofusin-mediated membrane remodelling have been limited, due to the poor stability of full-length constructs impeding crystallography and cryo-EM studies. Current structural information is derived from truncated mitofusin constructs and computational simulations of Fzo (Qi *et al.*, 2016; Cao *et al.*, 2017; Brandner *et al.*, 2019; De Vecchis *et al.*, 2017). Conversely, BDLP is readily expressed in *E. coli* and therefore constitutes a useful tool for understanding the mitofusin class of DRPs (Low & Löwe, 2006).

BDLP exhibits the conserved DSF characteristics G-dimerisation and a capacity to polymerise into filaments that constrict liposomes in the presence of the non-hydrolysable GTP analogue GMPPNP (Low & Löwe, 2006; Low *et al.*, 2009). Consequently, BDLP presents an opportunity to elucidate the most conserved principles of DSF-mediated membrane remodelling.

### 1.4.1 *Nostoc Punctiforme* is a Cyanobacterium with a Complex Life-cycle

As a cyanobacterium, *N. punctiforme* facilitates oxygenic photosynthesis localised to internalised TMs (Cardona *et al.*, 2007). *N. punctiforme* encodes four DRPs, and whether any of these are involved in TM biogenesis or remodelling remains to be elucidated (Bohuszewicz, Liu & Low, 2016). *N. punctiforme* is also a nitrogen fixing species that exists in symbioses with plant roots (Lindberg, Lindblad & Cournac, 2004).

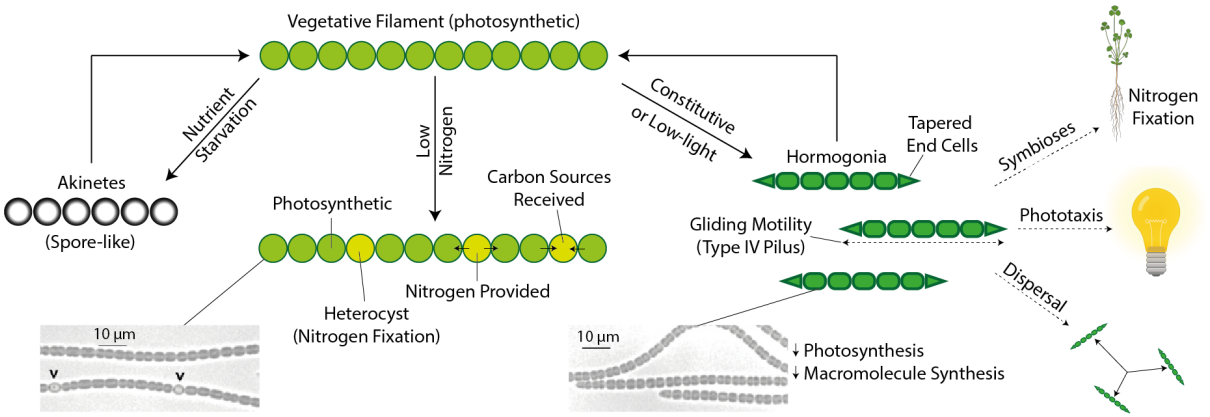


**Figure 18. *Nostoc punctiforme* Life Cycle.**
*N. punctiforme* differentiates into various cell types in response to different conditions. Vegetative cells form linear photosynthetic filaments whereas heterocysts and hormogonia cease photosynthesis and are dedicated to nitrogen fixation and motility, respectively. Akinetes are spore-like cells. *N. punctiforme* differentiates into hormogonia constitutively or in response to low-light conditions. Hormogonia motility facilitates phototaxis, dispersal and establishment of new nitrogen-fixing symbioses with plant roots (e.g., *Anthoceros punctatus*). *Brightfield microscopy images acquired by Douglas Risser (v indicates heterocysts). Figure adapted from (Risser, 2023). Some icons made using BioRender.com.*

Cyanobacterial membranes contain high amounts of hexII phase favouring lipids. Under standard growth conditions, the lipid content of *N. punctiforme* is similar to that of other cyanobacteria (van Eerden *et al.*, 2015), comprising roughly 44% MGDG, 20 % DGDG, 24% SQDG and 12% PG (Mikhaylenko, Skorokhod & Kholodny, 1998). Changes to growth conditions can alter this balance. For example, the addition of glucose to the growth medium causes the disappearance of SQDG. If a photosystem-II inhibitor is added to the growth medium, DGDG is lost and PG is reduced, changing the lipid composition to roughly 72% MGDG, 23% SQDG and 5% PG – a remarkably high hexII phase-favouring lipid content (Mikhaylenko, Skorokhod & Kholodny, 1998).

*N. punctiforme* is classified into the taxonomic subgroup IV of cyanobacteria as it exhibits a complex lifecycle characterised by multiple developmental stages (Figure 18) (Risser, 2023). Under normal growth conditions, *N. punctiforme* exists as filaments composed of photosynthetic vegetative cells. In response to nitrogen depletion, some cells within these filaments undergo terminal differentiation into heterocysts. These specialised cells cease photosynthetic activity and instead focus on nitrogen fixation, providing fixed nitrogen to surrounding vegetative cells in exchange for carbon sources. This arrangement establishes a symbiotic relationship between heterocysts and vegetative cells within the filament.

Additionally, *N. punctiforme* can form akinetes, which are spore-like cells, in response to nutrient (such as phosphate) depletion or unfavourable light and temperature conditions. Furthermore, *N. punctiforme* undergoes constitutive development into motile hormogonia that possess gliding motility ability (Risser, 2023).

#### 1.4.1.1 Hormogonia are short *N. punctiforme* Filaments Dedicated to Motility

Hormogonia are characterised by shorter filaments composed of smaller rod-shaped cells, resulting from reductive cell division. This represents a significant alteration in morphology, and the end cells of the filaments exhibit tapered ends. Hormogonia also produce gas vesicles for buoyancy (Armstrong, Hayes & Walsby, 1983; Risser, 2023). Hormogonia are specialised for gliding motility, with extremely reduced photosynthetic activity, reduced synthesis of most major macromolecules and a notable absence of nitrogen-fixing heterocysts (Campbell & Meeks, 1989; Risser, 2023). Hormogonia differentiate via rapid genetic and morphological changes within a 12-hour period (Campbell & Meeks, 1989). Motility is achieved through type IV pili and is crucial for dispersal, establishing nitrogen-fixing symbioses, and phototaxis (Risser, 2023).

While hormogonium development is constitutive (Risser, 2023), certain factors can promote differentiation into hormogonia. Sucrose represses hormogonium development, thereby maintaining beneficial symbiotic relationships with plant roots (Khamar *et al.*, 2010). Conversely, poor light conditions can promote hormogonia differentiation by affecting gene regulatory networks (Risser, 2023). The hormogonium gene regulatory network involves key transcription sigma factors: SigC, SigJ, and SigF (Risser, 2023). SigJ is promoted by hormogonium differentiation signals and, in turn, promotes SigC and SigF expression (Risser, 2023). Amongst other regulatory roles, SigC promotes reductive cell division and SigF promotes type IV pilus transcription (Gonzalez *et al.*, 2019).

In summary, the morphological changes in hormogonia are substantial and play a crucial role in establishing symbiotic relationships and locating favourable conditions. Such significant changes likely require the coordination of complex membrane remodelling events.

### 1.4.2 BDLP Undergoes Major Conformational Changes to Transition from a 'Closed' Off-Membrane State to a Membrane-bound Helical Polymer

BDLP is one of four dynamins encoded by the *N. punctiforme* genome (Figure 19A) and exhibits a canonical DSF domain architecture, comprising a large GTPase domain connected by hinge 2 to a four-helix neck bundle, and a four-helix trunk bundle distal to the GTPase domain joined to the neck domain by hinge 1 (Figure 19B). At the tip of the trunk is a small hydrophobic paddle hypothesised to insert into the outer leaflet of lipid bilayers.

Crystallographic analysis revealed that in the apo or GDP-bound states, BDLP adopts a tightly packed hinge 1 closed and hinge 2 open conformation (Figure 19B). The hinge 2 open conformation facilitates G-dimerisation of GDP-bound BDLP in solution, wherein the membrane-binding paddle is buried within the core of the dimer (Low & Löwe, 2006). Subsequent cryo-EM analysis of BDLP filaments constricting an underlying template of *E. coli* total extract (ETE) liposomes demonstrated that BDLP undergoes substantial conformational changes in the presence of GMPPNP and lipids (Figure 19C) (Low *et al.*, 2009). Although the reconstruction achieved a medium resolution of 11 Å, rigid body fitting of the crystal structure-derived domains facilitated the construction of a pseudo-atomic model, which demonstrated that the G-dimer is maintained within the filament and forms a more compact interface. Additionally, hinges 1 and 2 undergo rearrangements that allow BDLP to polymerise onto and constrict membranes.

#### 1.4.2.1 BDLP Dimerises across the Conserved G-dimer Interface and Coordinates Nucleotide via Conserved Motifs

BDLP exhibits a low nucleotide affinity of 69 μM, which is characteristic of dynamins, and a low basal hydrolysis rate of 0.53 $min^{-1}$ (Low & Löwe, 2006). Analogous to Mfn1, the weak affinity and low basal hydrolysis are attributed to the absence of a guanine cap (Qi *et al.*, 2016; Low & Löwe, 2006). BDLP possesses the typical G1-G4 motifs for nucleotide coordination and hydrolysis. In the apo state, aspartate-98 obstructs the P-loop (G1) and switch 1 (G2) is displaced. Conversely, GDP binding positions switch 1 and the P-loop for coordination. Furthermore, as GDP binding establishes a G-dimer, the nucleotide and GTPase domains are stabilised in trans (Low & Löwe, 2006). When G-dimerised, the nucleotide pocket is occluded – allowing BDLP to remain G-dimerised when GDP-bound, similar to Mfn2 which also remains G-dimerised after nucleotide hydrolysis (Li *et al.*, 2019; Low & Löwe, 2006). No lipid- and

therefore polymerisation-stimulated GTP turnover has been detected in the presence of *E. coli* or *N. punctiforme* lipids (Low & Löwe, 2006).

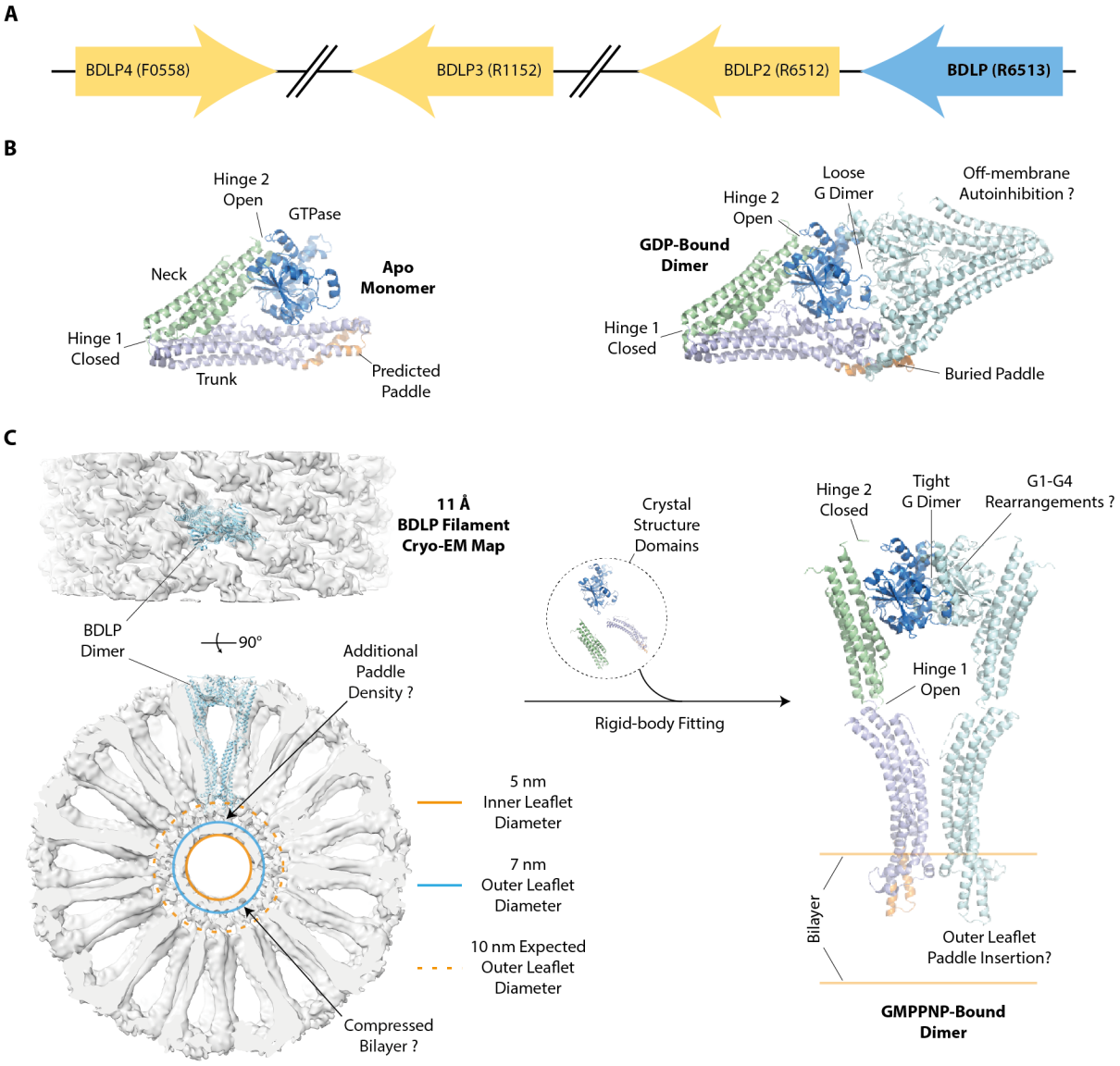


**Figure 19. BDLP Conformational Flexibility.**
**A,** Four DRP encoding genes of the *N. punctiforme* genome. The BDLP gene (blue) is located proximal and upstream of BDLP2. Gene name provided in brackets. **B,** Crystal structures show BDLP forms a compact closed structure in the apo (PDB: 2J69) and GDP-bound (PDB: 2J68) states. In both, hinge 2 is open and hinge 1 is closed. GDP-bound BDLP forms a loose G-dimer, and the predicted membrane-binding paddle is buried within the dimer. **C,** Rigid-body fitting of the crystal structure-derived domains indicates a drastic opening of the BDLP dimer when GDP is exchanged for GMPPNP. Left: 11 Å cryo-EM reconstruction of a BDLP filament formed on a constricted ETE liposome template in the presence of GMPPNP (Low *et al.*, 2009). Fit of a BDLP dimer (cyan) is shown. The bilayer is constricted to a 5 nm diameter. Circles indicate the suggested positioning of inner and outer leaflet phospholipid head groups, and the expected positioning (dotted line) of outer leaflet head groups if the bilayer was uncompressed. Right: Pseudo-atomic model of a GMPPNP-bound BDLP dimer in the helical filament

(PDB: 2W6D). Orange lines indicate predicted positioning of the bilayer given the predicted hydropathy of the paddle.

#### 1.4.2.2 BDLP Forms Polymers with a Unique Helical Architecture

Compared to helical filaments of classical dynamins and Opa-1, BDLP forms a novel helical lattice. Polymerisation is predominantly mediated by G-dimers, and left-handed helical rungs are formed by back-to-back association of dimers via neck-neck and trunk-trunk parallel interactions (Low *et al.*, 2009). Conversely, classical dynamins form polymers predominantly mediated by trunk-trunk interactions which facilitate G-dimerisation between rungs (von der Malsburg *et al.*, 2023; Liu *et al.*, 2021a). In this regard, the BDLP arrangement exhibits similarity to the GBP1 coatomer, except GBP1 G-dimers form in a criss-cross arrangement, whereas BDLP G-dimers are face-to-face (Weismehl *et al.*, 2024; Low *et al.*, 2009).

Although the cryo-EM reconstruction of the BDLP filament only permitted the placement of rigid bodies (Figure 19C), it demonstrated key hinge 1 and 2 conformational changes induced by lipid and GMPPNP binding; Hinge 2 closes when GDP is exchanged for GMPPNP, and hinge 1 opens (Low *et al.*, 2009). This architecture is accompanied by a tighter G-dimer interface, presumably positioning catalytic residues for hydrolysis, and aligns the neck and trunk such that they are oriented orthogonally to the helical axis.

The membrane-interface was predicted by hydropathy plots that indicated a short paddle at the tip of the trunk that interfaces with membrane. This was validated by an F583E paddle mutation which prevented lipid binding (Low *et al.*, 2009). Density for the outer leaflet phosphate groups of the constricted bilayer tube within BDLP helical filaments suggested the bilayer diameter is compressed from 10 to 7 nm. However, due to the low resolution of the filament reconstruction in this region, the membrane interface remains to be elucidated. Additionally, the cryo-EM map suggested the paddle does not fit well in this region and may adopt a more extended conformation than that of the GDP-bound or apo crystal structures (Low *et al.*, 2009).

In conclusion, BDLP forms a compact soluble arrangement in the apo and GDP-bound states, facilitated by a hinge 1 closed and hinge 2 open conformation. Upon GTP binding, BDLP dimerises across a G-dimer interface and polymerises into a helical filament that constricts

and tubulates membrane. This is facilitated by the opening of hinge 1 to expose the paddle and closing of hinge 2 to maintain the G-dimer interfaces in a helical arrangement. Due to limited resolution, numerous questions remain unresolved. How does BDLP interface with membrane? How does nucleotide state mediate conformational changes and tighter G-dimerisation? What is the role of GTP hydrolysis?

## 1.5 Study Overview

### 1.5.1 Motivations

The overarching aim of this study is to elucidate the fundamental principles of DSF-mediated membrane remodelling. To achieve this objective, I have selected BDLP as a model system given its novel helical architecture and evolutionary separation from the better characterised classical dynamins and Drp1. This approach provides unique opportunities to enhance our understanding of the diverse roles of bacterial DRPs and to investigate the function of cyanobacterial dynamins – an aspect that has not been elucidated thus far. *N. punctiforme* has a high MGDG content and thylakoid membranes – for which alternate lipid phases have been identified as crucial for the regulation of photosynthesis and as a stress response mechanism (Section 1.1.11.1). To date, there is limited evidence for protein machinery actively remodelling bilayers into alternate lipid phases. Within the DSF thus far, only Drp1 has been shown to mediate Lm-hexII phase transitions of high cardiolipin-content bilayers (Stepanyants *et al.*, 2015). Given the documented diversity of bacterial DRP functions and high cyanobacterial MGDG content in cyanobacteria, it is plausible that BDLP and cyanobacterial dynamins have roles, not in fission or fusion, but in mediating lipid phase changes.

Moreover, by identifying the mechanisms of BDLP-mediated membrane remodelling and comparing them to the diverse DSF, the most ancient and conserved characteristics of the DSF can be elucidated. Although some bacterial DRPs have been assigned functions or explicit fission or fusion activities, the precise mechanisms by which they achieve this have not been fully described. Furthermore, the process by which mitofusins mediate mitochondrial fusion is not well understood. Given the shared homology of BDLP and the mitofusins, and the shared characteristics of hinge 2 conformation changes upon nucleotide hydrolysis, BDLP

provides a valuable tool for understanding the mechanisms of mitofusin-mediated OMM fusion.

### 1.5.2 Study Summary

Cryo-EM has become indispensable for elucidating the mechanisms of DSF-mediated membrane remodelling by dynamins and DRPs that form large polymers and oligomers. Therefore cryo-EM is a fundamental technique presented in this study. Consequently, Chapter 2 reviews the theory of cryo-EM, its modern developments, and their application to helical filaments. Chapter 3 employs a combination of transcriptomic analysis, *in situ* cryo-electron tomography and *in vitro* cryo-EM to elucidate the function of BDLP within *N. punctiforme* and its mechanism of membrane constriction and binding. Chapter 4 extends this work to investigate the role of nucleotide hydrolysis in BDLP-mediated membrane remodelling. These findings are discussed in the context of the DSF and their potential implications for our understanding of conserved DSF features and the mechanistic action of the mitofusins.

# Chapter 2: The Theory of Cryogenic-Electron Microscopy and its Application to Biological Polymers

Cryogenic-electron microscopy (cryo-EM) is an ideal tool for studying proteins that form extensive multimeric structures, such as rings or helical polymers, including those involved in membrane remodelling. Furthermore, cryo-EM has dramatically expanded our understanding of DSF-mediated membrane remodelling, providing insights into the polymeric arrangements that constrict lipid bilayers. This chapter explores the theoretical foundations of cryo-EM. It reviews the development of electron microscopy, underscoring the advancements enabling near-native visualisation of these proteins. Topics include the fundamental principles of electron microscopy, sample preparation, and the theory of image formation and data processing. Special emphasis is placed on helical reconstruction techniques, which are vital for examining filamentous BDLP and DSF assemblies. This chapter aims to establish a theoretical basis for the cryo-EM structural studies presented in subsequent chapters.[1]

## 2.1 Introduction to Cryo-EM

Cryo-EM merges high-resolution electron microscopy with preservation techniques that maintain biological specimens in near-native states. Section 2.1 offers an overview of the historical development of these techniques and a comparison with other structural biology methods.

### 2.1.1 A Brief History of Electron Microscopy and the Development of Cryo-EM

Louis de Broglie's theory on the wave-particle duality of electrons underpins electron microscopy (Orlova & Saibil, 2011). This theory asserts that electrons, like light, have both particle and wave properties. The wavelength of electrons is inversely proportional to their momentum, as per the de Broglie equation (Equation 2). By accelerating electrons to high

[1] Much of the understanding for this chapter was helped by the Grant Jensen lecture series on Cryo-EM (Jensen, 2021).

velocities, electron microscopes achieve wavelengths of 1-10 pm, much shorter atomic structural features, allowing for the resolution of much finer details than light microscopy (Cheng, 2018).

**Equation 2. de Broglie Wave Equation.**
Where λ is the wavelength, h is Planck's constant, m is the electron mass, and v is its velocity.

$$\lambda = \frac{h}{m \times v}$$

Ruska and Knoll built the first electron microscope in 1931 (Freundlich, 1963). However, using electron microscopy to visualise biological samples poses challenges, mainly due to specimen radiation damage and dehydration and collapse under the high-vacuum environment (Kourkoutis, Plitzko & Baumeister, 2012). Early sample preparation methods involved positive or negative staining, or plastic embedding. In negative stain-electron microscopy (NS-EM), sample is adsorbed onto a carbon coated grid alongside a heavy metal salt solution, such as uranyl acetate. This highlights the shape and surface features of biological molecules by forming a dense coat around the specimen while keeping the background electron-transparent. NS-EM was used to determine structures for various biological systems, with negative stain structures being published until relatively recently (Low *et al.*, 2014).

The advent of cryo-EM in the 1980s marked a significant breakthrough for imaging of biological specimens, whereby biological samples were frozen in a thin layer of vitreous ice, preserving high-resolution features and their native structure in a near-physiological state. The vitrification process, achieved by plunge-freezing the sample in liquid ethane cooled by liquid nitrogen, results in cooling rates of $10^5$–$10^6$ $K.s^{-1}$ (Dubochet *et al.*, 1982, 1988). Imaging samples under cryogenic conditions also reduces radiation damage from the electron beam, as the low temperatures limit the diffusion of free radicals formed by electron-sample interactions. This reduced radiation damage permits higher electron doses, enhancing signal-to-noise ratios and allowing finer structural details to be resolved (Henderson, 2015; Glaeser, 2016; Cheng, 2018).

Improvements in cryo-EM hardware, along with progress in image processing algorithms, have driven the "resolution revolution" in cryo-EM (Kühlbrandt, 2014). Crucially, advancements in detector technology, notably the development of direct electron detectors

(DEDs), have pushed the limits of achievable resolution of biological specimens to sub-angstrom resolution (Gallagher-Jones *et al.*, 2018). The ongoing "resolution revolution" in cryo-EM is evidenced by the growing number of high-resolution structures that significantly enhance our understanding of biological systems.

### 2.1.2 Advantages of Cryo-EM over other Structural Biology Techniques

Cryo-EM complements traditional methods like X-ray crystallography and nuclear magnetic resonance (NMR) spectroscopy, offering unique benefits for studying complex biological systems, including large macromolecular assemblies and membrane-associated proteins like DRPs.

Unlike X-ray crystallography, which requires well-ordered crystals, cryo-EM images macromolecules in 'solution', which negates crystal packing artefacts and the challenges of producing protein crystals that diffract to high resolution (Timofeev & Samygina, 2023). This also means cryo-EM demands less protein sample, which is particularly beneficial for often poorly-expressing membrane proteins, which can be visualised in near-native environments such as nanodiscs (Denisov & Sligar, 2016; Wang & Wang, 2017). Unlike crystallography, phase information is retained in cryo-EM data (Section 2.4), which negates the need for heavy-atom derivatives or homology models for reconstructing density maps (Wang & Wang, 2017).

Cryo-EM excels in visualising large assemblies, which provide better image contrast and are more easily aligned during image processing (Section 2.5.5). Such assemblies may not crystallise in biologically relevant arrangements, and therefore cryo-EM offers a unique opportunity to elucidate structural details of interfaces that were previously inaccessible to structural biology, as evidenced by the insights provided into DSF filamentous assemblies (Ford & Chappie, 2019). Cryo-EM also addresses structural heterogeneity, that was previously only accessible to complex NMR experiments and *in silico* simulation studies (Hu *et al.*, 2021). Vitrification captures the conformational ensemble of biological specimens and advanced image classification algorithms allow heterogeneous particles to be sorted into homogeneous subsets, allowing reconstruction of multiple structural states from a single sample (Scheres, 2016; Zhong *et al.*, 2021b; Punjani & Fleet, 2023; Amann *et al.*, 2023). This is vital for understanding the dynamic reality of biological processes. For example, time-resolved cryo-

EM (Tr-cryo-EM) sample preparation techniques have recently been used to determine the structures of several intermediates in the formation of a G-protein-coupled receptor (GPCR) and a G-protein complex (Papasergi-Scott *et al.*, 2024), showcasing cryo-EM's capability to elucidate biologically relevant dynamic molecular mechanisms.

Cryo-electron tomography (cryo-ET) involves collecting a series of images as the sample is tilted through increasing angles, which are then computationally combined into a 3D tomogram. This allows visualisation of macromolecular complexes within their cellular context, linking cellular and molecular structural biology and establishing cryo-EM as a multi-scale imaging technique (Berger *et al.*, 2023). This multi-scale imaging approach has provided insights into the structural detail and broader cellular context of the bacterial membrane-remodelling protein Vipp1 (Gupta *et al.*, 2021).

In summary, the development of cryo-EM has provided advantageous capabilities, particularly relevant to the study of large macromolecular complexes in dynamic contexts on multiple imaging scales.

## 2.2 Sample Preparation

### 2.2.1 Overview of Cryo-EM Sample Preparation

Sample preparation often determines the success of cryo-EM structural studies. The typical workflow for preparation of biological samples in a thin layer of vitreous ice involves grid selection and preparation, sample application, blotting to create a thin film, and rapid vitrification (Grassucci, Taylor & Frank, 2007; Thompson *et al.*, 2016). Each step can affect factors like ice thickness and particle distribution, which are crucial for high-resolution reconstructions (Drulyte *et al.*, 2018; Noble *et al.*, 2018).

### 2.2.2 Specimen Grids and Supports

Specimen grids consist of metal grid of square openings. They come in various materials, typically copper or gold. Copper grids are cost-effective, while gold grids provide better thermal conductivity and mechanical stability, reducing beam-induced motion during imaging (Russo & Passmore, 2014). A support film, usually amorphous carbon, is applied to the grid squares. Perforated holey carbon films are commonly used to suspend the sample in ice,

thereby reducing background signal (Passmore & Russo, 2016; Russo & Passmore, 2016). Alternatively, gold support films, such as those used in commercially available UltraAuFoil grids, also reduce the effects of beam-induced motion (Russo & Passmore, 2014). Occasionally, graphene or ultrathin carbon supports are layered over holes to provide an atomically thin substrate with low background signal, offering a defined surface for protein adsorption, which is useful for low concentration samples (Naydenova, Peet & Russo, 2019). Before sample is applied to grids, they are typically pre-treated to improve hydrophilicity and sample distribution. Glow discharge and plasma cleaning expose grids to a low-pressure plasma of air or gas mixtures, creating a negatively charged surface that aids in spreading aqueous samples across the grid (Aebi & Pollard, 1987).

### 2.2.3 Vitrification

To prepare a grid and sample for vitrification, a small volume (~2-4 µL) of sample is applied to the grid surface, with continuous support films generally requiring lower protein concentrations (0.1-1 mg/mL) than grids with holey films without additional support (1-5 mg/mL) (Drulyte *et al.*, 2018; Thompson *et al.*, 2016). Excess sample is removed by blotting to create a thin film sample, which is vitrified by plunge-freezing into liquid cryogens such as liquid ethane or ethane-propane mixtures. These cryogens have a high specific heat capacity that facilitates rapid heat transfer and cooling rates over $10^6$ K/s that prevent formation of crystalline ice, which is detrimental to biological structures and high resolution imaging (Dubochet *et al.*, 1988; Tivol, Briegel & Jensen, 2008).

### 2.2.4 Overcoming the Air-Water Interface (AWI)

When using traditional blotting methods, macromolecules often adsorb to the AWI within milliseconds, leading to protein denaturation, complex dissociation, and orientation bias, which obscures high resolution details in electron density maps (Noble *et al.*, 2018; Liu & Wang, 2023; Glaeser, 2018). Additives can protect protein molecules from the AWI. Detergents such as CHAPSO, self-assembling monolayers of hydrophobins, and glycerol (despite its cryo-protective properties that can lead to crystalline ice formation) have all improved particle quality, orientation distribution, and final cryo-EM map reconstructions (Chen *et al.*, 2019; Basanta *et al.*, 2022; Fan *et al.*, 2021b). Chemical crosslinking methods like GraFix can prevent dissociation of protein complexes at the AWI (Kastner *et al.*, 2008). Grids

with functionalised support films with specific ligands to capture target proteins away from the AWI also offer a method of on-grid protein purification (Ramlaul *et al.*, 2023). Alternative blotting-free methods of sample application involve spraying small droplets onto the grid just before plunge-freezing to mitigate the AWI by minimising the time the sample has to interact with the AWI before it is vitrified (Feng *et al.*, 2017). This requires self-wicking grids with a specialised nanowire mesh to promote rapid sample spreading and thinning without blotting (Wei *et al.*, 2018).

### 2.2.5 Cryo-FIB Milling of Cellular Samples

Imaging proteins in their native state within cells using cryo-ET is impeded by the excessive thickness of bacterial and eukaryotic cell samples, which electrons cannot penetrate effectively (Villa *et al.*, 2013). Therefore cryo-focused ion beam (cryo-FIB) milling is used to prepare electron-transparent lamellae from vitrified cellular samples, whereby a focused ion beam ablates material from the vitrified sample (Zachs *et al.*, 2020; Sexton *et al.*, 2022; Wagner *et al.*, 2020). Correlative light and electron microscopy (CLEM) uses fluorescence microscopy to identify regions of interest (ROIs) in vitrified samples, which are then targeted for cryo-FIB milling and subsequent cryo-ET imaging (Sexton et al., 2022), allowing precise localisation of cellular features and protein complexes within the cell.

## 2.3 Anatomy of an Electron Microscope

An overview of key components of modern electron microscopes summarised in Figure 20 is provided in the following sections.

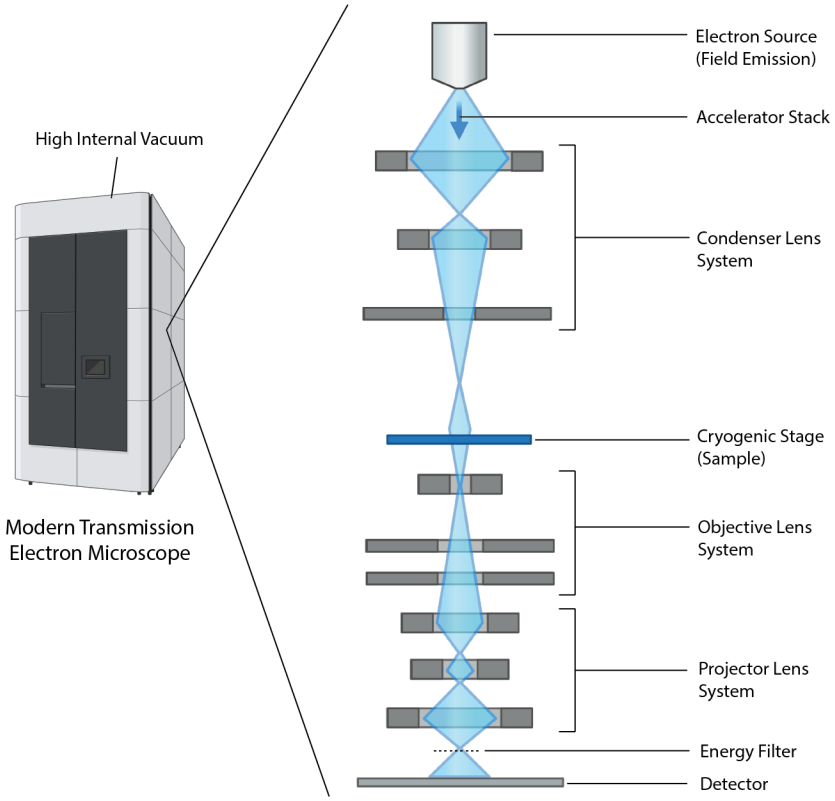


**Figure 20. Arrangement of Components within an Electron Microscope.**
*Figure icons created in Biorender.com*

## 2.3.1 Electron Sources

### 2.3.1.1 Beam Coherence in Electron Microscopy

Coherence in electron microscopy refers to the correlation between the phases of electron waves in the beam. The importance of this is highlighted by the image formation process (Section 2.4). A high-coherence beam is characterised by high spatial and temporal coherence. Spatial (lateral) coherence describes the phase correlation of electron waves across the beam's cross-section. In a spatially coherent beam, electrons from different parts of the source maintain a constant phase relationship, resulting in a more parallel beam with uniform wavefronts (Latychevskaia, 2017). Spatial coherence is determined by the size of the electron source. Temporal (longitudinal) coherence relates to the phase correlation of electrons along the beam's propagation direction and is linked to the energy spread of the electrons. As per

Equation 3, the phase of an electron wave is proportional to its energy and time. Therefore, electrons have high temporal coherence and maintain their phase relationship over longer distances when they have a narrow energy spread (Williams & Carter, 2009d).

**Equation 3. Relationship Between an Electron's Phase and Energy.**
Where φ is the phase of an electron wave, h is Plank's constant, E is the energy of an electron, and t is time.

$$\varphi = \frac{2\pi}{h} \times E \times t$$

#### 2.3.1.2 Thermionic Electron Sources

Thermionic sources emit electrons by heating a filament to high temperatures, giving electrons enough energy to overcome the material's work function—the minimum energy needed for an electron to escape a solid's surface into a vacuum (Thompson *et al.*, 2016). Tungsten filaments and lanthanum hexaboride ($LaB_6$) crystals are common thermionic sources (Chua *et al.*, 2022). $LaB_6$ sources produce a more spatially-coherent beam due to their smaller source size, and a more temporally-coherent beam due to their lower energy spread (Venugopal *et al.*, 2024).

#### 2.3.1.3 Field Emission Electron Sources

Unlike thermionic sources that use heat to overcome a material's work function, field emission guns (FEGs) use a strong electric field to extract electrons from an extremely fine metal tip, which creates a highly spatially coherent beam (Thompson *et al.*, 2016). Cold FEGs operate at lower temperatures and have extremely low energy spreads (~0.3 eV), providing high extremely high temporal coherence (Chua *et al.*, 2022). Given the superior coherence they provide, FEGs are favoured in modern electron microscopes.

#### 2.3.1.4 Accelerator Stacks

The accelerator accelerates emitted electrons towards the sample and consists of metal plates with progressively decreasing potentials, with the final plate grounded. This setup creates a strong electric field, which propels electrons from the source towards the specimen (Williams & Carter, 2009d). High end microscopes typically operate at 300 kV, which means electron travel at about 70% of the speed of light, resulting in a de Broglie wavelength of approximately 1.97 pm (Equation 2).

### 2.3.2 Lenses and Magnification in an Electron Microscope

Electron microscopes operate on principles similar to light microscopes. When electrons scatter upon interacting with the specimen, they do so at various angles. Lenses refocus these scattered electrons at the image plane. According to Equation 4, if the image plane is farther from the lens than the object plane (v > u), the magnification exceeds one, producing an enlarged specimen image (Williams & Carter, 2009k).

**Equation 4. Magnification in a microscope.**
Where M is magnification, v is the image distance from a lens, and u is the object distance from a lens.

$$M = \frac{v}{u}$$

#### 2.3.2.1 Electromagnetic Lenses

Electromagnetic lenses consist of a wire coil carrying an electric current, creating a magnetic field. This magnetic field acts similarly to a convex lens in optical physics to change the path of an electron. Electrons traversing the lens are subjected to a force perpendicular to both their velocity and the magnetic field, in accordance with the Lorentz force law, detailed in

Equation 5 (Williams & Carter, 2009f).

**Equation 5. Lorentz Force Law.**
F is the force felt by an electron, q is the electron charge, v is the electron velocity, and B is the magnetic field.

$$F = q(v \times B)$$

This force directs electrons in a spiral toward the lens's optical axis, with stronger force felt by electrons further from the axis, creating a focusing effect similar to a glass lens on light rays, where edge photons refract more strongly (Williams & Carter, 2009f). Adjusting the coil current modifies the magnetic field strength, allowing precise control over the lens's focal length and consequently magnification.

#### 2.3.2.2 Electron Microscope Lens Systems

An electron microscope lens system includes a deflector, a stigmator, and an aperture arranged around the lens coil (Williams & Carter, 2009f). Deflectors adjust the beam's trajectory into the lens using electromagnetic fields, compensating for the practical impossibility of perfectly aligning the electron beam with the lens's optical axis. Stigmators

apply additional magnetic fields to counteract beam asymmetry caused by lens imperfections such as wire thickness variations (Williams & Carter, 2009f). Apertures limit the angular range of electrons exiting the lens system, which can enhance image contrast and be used to manage the electron dose a sample receives (Williams & Carter, 2009i).

#### 2.3.2.3 Lens System Arrangement with the Column

Electron microscopes have several lens systems arranged sequentially to control the electron beam (Figure 20). From top to bottom following the electron gun, these are: the condenser lens system, objective lens system, and projector lens system. The condenser lens system directs and shapes the electron beam onto the sample. The objective lens creates the first magnified image of the sample focussed on the image plane, hence its strength determines the initial magnification, typically around 50-100 times (Williams & Carter, 2009f). The projector system, comprising multiple lenses, increases and controls magnification. Projector lenses are often pre-set to specific excitations to reduce hysteresis and manage image rotations (Williams & Carter, 2009j).

#### 2.3.2.4 Electromagnetic Lens Hysteresis

Electromagnetic lenses in electron microscopes suffer hysteresis, whereby the magnetic field depends on both the current applied and the lens's magnetic history. Lens normalisation cycles are used to mitigate the effects of hysteresis on achieving consistent magnifications and alignments (Williams & Carter, 2009j).

### 2.3.3 Specimen Holders and the Cryogenic Stage

Specimen holders and cryogenic stages maintain samples at liquid nitrogen temperatures while enabling precise positioning within the microscope (Dubochet *et al.*, 1988). Side-entry holders, used in older systems, insert a single grid through a port in the microscope column, whereas modern autoloaders handle multiple grids stored in a cassette, reducing the need for frequent holder exchanges and handling of delicate samples, and facilitating continuous data collection over extended periods (Thompson *et al.*, 2016).

### 2.3.4 Energy Filters

When electrons interact a specimen, some may lose energy due to unwanted inelastic scattering events (Section 2.4.1.2), which contributes to noise. Energy filters block inelastically scattered electrons, using a magnetic prism to disperse electrons by energy, followed by a slit or aperture that permits only electrons within a specific energy range (elastic electrons) to pass (Kourkoutis, Plitzko & Baumeister, 2012).

### 2.3.5 Detectors

Initially, photographic film was the primary medium for recording electron microscopy images, potentially achieving resolutions around 3-4 Å (Henderson, 1995). However, actual resolutions were often lower, with initial BDLP filament reconstructions reaching only 11 Å (Low *et al.*, 2009). The introduction of modern electron detectors (charge-coupled and direct electron detectors) has enhanced cryo-EM resolutions and throughput. Key terms used to describe detectors and their quality are discussed below.

#### 2.3.5.1 Nyquist Frequency

The Nyquist frequency indicates the maximum spatial frequency that a pixelated detector with a given pixel size can sample (Nyquist, 1928), as shown Equation 6.

**Equation 6. Nyquist Frequency.**
Where $f_N$ is Nyquist frequency and p is pixel size of the detector.

$$f_N = \frac{1}{2p}$$

Nyquist dictates that the pixel size must be at least half the size of the smallest feature to resolve it. For example, to resolve 3 Å features, the pixel size should be 1.5 Å or smaller.

#### 2.3.5.2 Detective Quantum Efficiency (DQE)

DQE describes a detector's ability to preserve the signal-to-noise ratio (SNR) of the microscope, indicating the quality of electron recording, as defined by Equation 7 (McMullan *et al.*, 2009). Ideally, DQE should be near 1 across all resolutions (spatial frequencies). In reality it typically decreases with increasing spatial frequency.

**Equation 7. Detector Quantum Efficiency (DQE).**

$$DQE = \frac{\left(\frac{Signal}{Noise}\right)^2_{out}}{\left(\frac{Signal}{Noise}\right)^2_{in}}$$

#### 2.3.5.3 Charge Coupled Detectors (CCDs) and Direct Electron Detectors (DEDs)

In CCDs, a scintillator converts electrons into photons, which are detected by a CCD sensor and transformed into an electrical signal. The scintillator is a source of noise and reduces the DQE (Faruqi & Henderson, 2007). DEDs have higher DQE across all spatial frequencies as they directly detect electrons without a scintillator (Ruskin, Yu & Grigorieff, 2013). Their high frame rate allows multi-frame movies to be captured in a single exposure, enabling correction of beam-induced motion (Section 2.5.2) (Zivanov, Nakane & Scheres, 2019; Li *et al.*, 2013). Additionally, their speed supports super-resolution imaging, locating electron events with sub-pixel accuracy and effectively doubling the Nyquist frequency (Li *et al.*, 2013). Leading DED cameras include the Gatan K3, (Sun *et al.*, 2021), and Thermo Fisher's Falcon 4 (Nakane *et al.*, 2020).

### 2.3.6 Vacuum Systems

In electron microscopes, a high-vacuum environment is crucial for minimising interactions between electrons and gas molecules, which scatter the electron beam, and for protecting the electron source, especially the filament, from oxidation and degradation (Williams & Carter, 2009h). To achieve this vacuum, a series of pumps are employed:

- Rotary Pumps: Mechanical pumps for initial evacuation, reducing the system from atmospheric pressure to rough vacuum, using a rotating valve to expel air (Williams & Carter, 2009h).
- Turbomolecular Pumps: High-speed rotating blades impart momentum to gas molecules out of the column (Williams & Carter, 2009h).
- Oil Diffusion Pumps (ODPs): Heated oil vapor traps and removes gas molecules, with condensed oil extracting trapped gas via a mechanical backup pump (Williams & Carter, 2009h).

- Ion Getter Pumps (IGPs): An electric field ionises residual gas molecules, embedding them into a titanium surface. IGPs are the final pump used to achieve the highest vacuums (Williams & Carter, 2009h).

## 2.4 Theory of Image Formation in Cryo-EM

### 2.4.1 Electron-Specimen Interactions

To image a sample with electrons, it must interact with and scatter the incident electron beam. These interactions can be categorised into useful elastic scattering and destructive inelastic scattering.

#### 2.4.1.1 Elastic Scattering

Elastic scattering occurs when incident electrons interact with the Coulomb field of atomic nuclei – the electrostatic potential of a nucleus and its surrounding electron cloud (Marques, Purdy & Yeager, 2019). Such scattering occurs without energy loss, alters the electron's trajectory and simultaneously induces a phase shift (Williams & Carter, 2009c). Heavier atoms scatter electrons more strongly due to the larger electron cloud and nuclei (Williams & Carter, 2009c). As sample thickness increases, the likelihood of multiple elastic scattering events rises, affecting the weak phase object approximation used in cryo-EM image analysis that assumes an electron only undergoes a single scattering event when traversing the specimen (Henderson, 1995).

#### 2.4.1.2 Inelastic Scattering

Inelastic scattering occurs when electrons interact with the sample and lose energy (Dickerson *et al.*, 2022). Energy is lost when inelastically scattered electrons transfer energy to valent electrons, causing them to jump to higher energy states. Valent electrons may gain sufficient energy to escape their corresponding nucleus as a secondary electron, adding to noise (Williams & Carter, 2009e; Dickerson *et al.*, 2022). Inelastic scattering contributes to radiation damage by breaking bonds and creating free radicals, which degrade sample integrity (Williams & Carter, 2009e).

### 2.4.2 Contrast Mechanisms

Both amplitude and phase contrast improve sample visibility.

#### 2.4.2.1 Amplitude Contrast

Amplitude contrast arises from the scattering or absorption of electrons by the specimen that removes electrons from the beam by the time it reaches the detector, generating contrast between electron-transparent and opaque regions. Amplitude contrast indicates thicker and thinner areas of sample (Williams & Carter, 2009a). In cryo-EM, amplitude contrast is minor compared to phase contrast, contributing about 7% of the total image contrast for biological specimens (Toyoshima & Unwin, 1988).

#### 2.4.2.2 Phase Contrast

Phase contrast arises from the interference patterns of elastically scattered electrons that experience phase shifts due to interactions with the specimen and unscattered electrons. Phase shift is directly proportional to the specimen's electrostatic potential, generating contrast for light atoms and intricate structural detail of biological specimens (Henderson, 1995; Toyoshima & Unwin, 1988). Phase contrast can be enhanced by intentionally increasing the phase shift between scattered and unscattered electrons, by defocusing the objective lens (Zhu *et al.*, 1997), or by using a phase plate to introduce an additional phase shift to unscattered electrons (Danev & Baumeister, 2016; Danev *et al.*, 2014). The role of phase shifts in contrast is discussed further in Section 2.4.4.

### 2.4.3 Factors Affecting Image Formation

Several factors of the imaging setup affect image formation as discussed in the following sections.

#### 2.4.3.1 Spherical Aberration

Spherical aberration occurs when electrons passing through the lens periphery focus differently than those passing through the centre, causing blurred or distorted images (Hetherington, 2004). Multipole correctors can counteract spherical aberration within the microscope (Hetherington, 2004) and spherical aberrations can be accounted for computationally (Zivanov, Nakane & Scheres, 2020). Spherical aberration is elaborated upon in Section 2.4.4.3).

#### 2.4.3.2 Chromatic Aberration

Chromatic aberration arises from the energy spread of the beam, causing electrons with different energies to focus at distinct points by electromagnetic lenses (Williams & Carter, 2009f). Hence a high temporal coherence beam (Section 2.3.1.1) is beneficial.

#### 2.4.3.3 Astigmatism

Astigmatism, as discussed in Section 2.3.2.2, occurs due to irregularities in electromagnetic lenses, causing a non-uniform field that focuses electrons differently depending on their lateral position within the lens (Williams & Carter, 2009f).

### 2.4.4 Contrast Transfer Function (CTF)

The Contrast Transfer Function (CTF) is a mathematical description of how an imaging system affects transfer of information from the specimen to the image. The CTF is explained here alongside factors that influence it.

#### 2.4.4.1 Bragg's Law in Electron Microscopy

Previously, elastic scattering was described in terms of incident electrons interacting with the electrostatic potential of atoms in the specimen (Section 2.4.1.1). However, when considering the collective arrangement of these atoms, scattering is caused by "scattering features" or "scattering planes." These features represent periodic arrangements of atoms or electron density within the specimen. In crystalline materials and x-ray crystallography, these are actual planes of atoms. In non-crystalline biological specimens in ice, these features correspond to recurring structural motifs at different length scales (Frank, 2006c, 2006a). The distance (d) between two points in a biological specimen, such as two carbon atoms, determines the spatial frequency (k) of a particular scattering feature (Equation 8).

**Equation 8. Spatial Frequency.**
The spatial frequency (k) is the inverse of the spacing (d).

$$k = \frac{1}{d}$$

At the back focal plane of the objective lens, a diffraction pattern emerges from the interference of scattered and unscattered electrons. Unscattered electrons form the centre of the image whilst scattered electrons are off-axis (Figure 21) (Williams & Carter, 2009b).

According to Bragg's Law (Equation 9), higher spatial frequencies (smaller d, larger k) produce larger scattering angles, whereas lower spatial frequencies (larger d, smaller k) yield smaller scattering angles.

**Equation 9. Bragg's Law.**
Where λ is wavelength, d is distance (and k is spatial frequency) and θ is angle of scattering.

$$\lambda = 2d \sin\theta$$

$$Therefore: \sin\theta = \frac{\lambda k}{2}$$

#### 2.4.4.2 CTF Definition

A wave function describes an electron wave in terms of its amplitude and phase (Equation 10). At the back focal plane of the objective lens, the electron's wave function is the pre-specimen electron wave function adjusted for phase shifts caused by scattering features in the biological sample (Frank, 2006a). The objective lens applies an inverse Fourier transform to this wave function, forming an image by focusing electrons at the image plane, thereby preserving the phase information of elastic scattering in the specimen within the wave function of the image (Frank, 2006a).

**Equation 10. The Wave Function.**
Where Ψ is the wave function, r is a given point in space, A is the Amplitude and Φ is the phase.

$$\psi(r) = A(r).e^{i\phi(r)}$$

A scattered electron's phase shifts by 90 degrees compared to an unscattered electron, plus an additional shift influenced by the scattering angle; electrons scattered at higher angles travel further when focused by the objective lens to the detector, resulting in the extra phase shift (Figure 21). Additionally, scattered electrons exhibit lower amplitudes than unscattered electrons (Williams & Carter, 2009c).

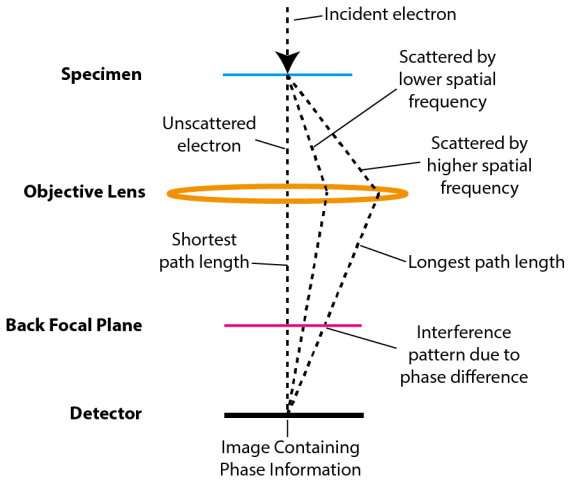


**Figure 21. Relationship Between Spatial Frequency and Phase Shift.**
An incident electron is scattered at higher angles by higher spatial frequencies, and lower angles by lower spatial frequencies. Elastic scattering introduces a 90° phase shift but does not change the energy and therefore wavelength of the electron. Higher-angle scattered electrons travel a longer path length to the back focal plane than lower-angle scattered or unscattered electrons, undergoing a different number of oscillations in this time. At the objective lens, an interference pattern occurs due to the spatial frequency-determined phase shifts of scattered electrons. At the detector (image plane) this spatial frequency-determined phase relationship is maintained.

The phase of a scattered electron determines whether it will interfere constructively or destructively with the unscattered electron at the image plane, determining the amplitude of the electron's wave function at the image plane. To form an image, the electron detector measures the amplitudes of incident electrons. Hence, the scattering angle (based on the spatial frequency of the scattering feature) significantly influences the detected amplitude. The impact of the scattering feature on the detected amplitude (contrast) varies with its spatial frequency, as described by the contrast transfer function (CTF) (Wade, 1992; Jensen, 2021).

**Equation 11. Contrast Transfer Function (CTF)**
Where CTF is the contrast of a given spatial frequency (k), Δz is defocus, λ is wavelength of the electron and $C_s$ is objective lens spherical aberration coefficient.

$$CTF(k) = \left[(-\pi.\Delta z.\lambda.k^2) + \frac{\pi.C_s.\lambda^3.k^4}{2}\right]$$

When CTF is plotted as a function of spatial frequency, it starts and 0 and oscillates between negative and positive contrast (Figure 22).

### 2.4.4.3 Imaging Setup Factors that Affect Terms of the CTF

The microscope's imaging system configuration affects the terms of the CTF in Equation 11.

**Spherical aberration ($C_s$)**: Spherical aberration affects how electrons are focussed depending on their position in the objective lens. This causes additional phase shifts leading to the oscillatory behaviour of the CTF. This is a known value that can be used in CTF estimation (Section 2.5.3).

**Electron Wavelength (λ)**: Inelastic scattering (which causes varying electron wavelengths) contributes to noise and therefore reduces contrast. As there is no energy loss in elastic scattering, elastically scattered electrons retain the same wavelength as unscattered electrons, meaning the accelerating voltage alone determines the electron wavelength.

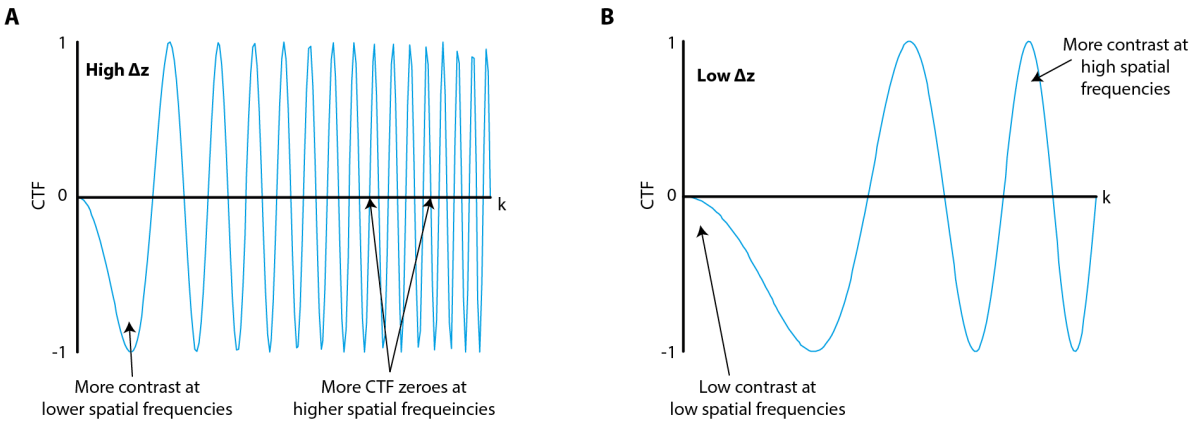


**Figure 22. Effect of Defocus on CTF Curves.**
Simulated CTF plotted as a function of spatial frequency (k). **A,** Contrast transfer in an image collected at high defocus. **B,** Contrast transfer in an image collected close to focus.

**Defocus (Δz):** Defocus modulates the oscillations of the CTF curve when plotted as a function of spatial frequency (Figure 22). Experimentally this means at high defocus, low spatial frequency information has good contrast in the image, as the CTF curve rapidly approaches strong negative contrast (Figure 22A). Conversely, more CTF zeroes are present for higher spatial frequencies. At low defocus, higher spatial frequencies have improved contrast, but lower spatial frequencies have reduced contrast (Figure 22B) (Wade, 1992; Williams & Carter, 2009g). Cryo-EM data is usually collected at varying defocus levels to retrieve high-contrast

information across a wide range of spatial frequencies, but also ensuring high enough low spatial frequency contrast for effective particle picking during data processing (Section 2.5.4) (Langlois *et al.*, 2014).

#### *2.4.4.3.1 CTF Curve Envelopes*

The CTF curve is dampened by an exponential envelope function that has an increasing effect at higher spatial frequencies (Figure 23) (Frank, 2006a).

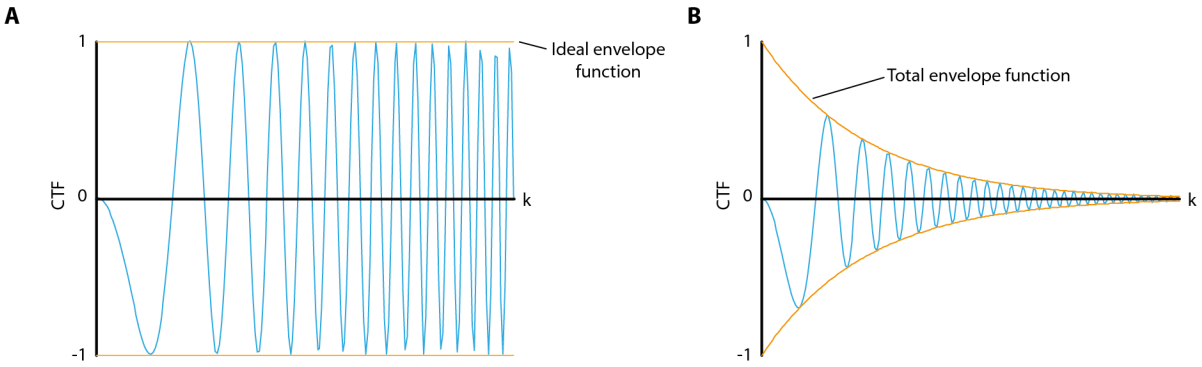


**Figure 23. The Effect of Envelope Functions on CTF Curves.**
Simulated CTF curves plotted as a function of spatial frequency. **A,** CTF curve with an ideal envelope function that does not affect contrast across all spatial frequencies. **B,** CTF curve affected by the total envelope function, which is formed of envelope function caused by envelope functions created by factors such as defocus and beam incoherence.

Several features of the imaging system generate envelope functions that modulate the CTF curve. As the electron beam does not have perfect spatial coherence, electrons enter the specimen at varying angles, leading to image blurring. This blurring is more significant at higher spatial frequencies, as offset electrons scattered by high spatial frequencies are more likely to destructively interfere than when they are scattered by low spatial frequencies, creating a spatial envelope that modulates the CTF (Wade, 1992; Frank, 2006a). Temporal incoherence means different energy electrons are focused on different planes, resulting in varying defocus values and CTFs. At higher spatial frequencies, the differences between CTFs for electrons of different energies become more pronounced, increasing CTF curve dampening and generating a temporal incoherence envelope (Wade, 1992; Frank, 2006a; Jensen, 2021). Defocus also generates an envelope. At larger defocus values, envelope

functions decay more rapidly with increasing spatial frequency due to more pronounced phase shifts that exacerbate beam incoherence effects. Conversely, lower defocus values allow envelopes to extend to higher spatial frequencies, transferring more high resolution information (Vulović *et al.*, 2013; Frank, 2006a). The total envelope function is a combination of all the envelope functions that cause CTF dampening (Figure 23B)

## 2.5 Cryo-EM Data Processing

### 2.5.1 Overview of the Cryo-EM Data Processing Pipeline

Single particle cryo-EM aims to reconstruct three-dimensional (3D) structures from two-dimensional (2D) projection images of randomly oriented particles. This process relies on the central section theorem, which states that the 2D Fourier transform of a projection image corresponds to a central slice through the 3D Fourier transform of the object (De Rosier & Klug, 1968). By combining information from many particles in different orientations, a 3D reconstruction can be obtained.

The data processing pipeline in cryo-EM typically involves the following steps:

1. Motion correction: Compensating for beam-induced motion between movie frames (Zheng *et al.*, 2017).
2. CTF estimation: Estimating the contrast transfer function parameters of each motion-corrected micrograph (Rohou & Grigorieff, 2015).
3. Particle picking: Identifying and extracting individual particle images from micrographs (Wagner *et al.*, 2019).
4. 2D classification: Grouping similar particle images to improve signal-to-noise ratio, improve homogeneity and assess data quality (Scheres, 2012).
5. Initial model generation: This can be generated *ab initio* from the data or from similar structures.
6. 3D classification: Sorting particles into different structural states or conformations (Scheres, 2016).
7. 3D refinement: Determining precise orientations of particles to generate a high-resolution 3D reconstruction (Scheres, 2012).

8. Post-processing: Applying additional corrections and validations to the final map (Ramírez-Aportela *et al.*, 2020).

### 2.5.2 Beam-induced Motion Correction

To address beam-induced sample motion, rapid cameras allow collection of dose-fractionated movies which allow motion correction algorithms to align and sum the movie frames to reduce image blurring. Early methods, such as MotionCorr, corrected whole-frame motion using least-squares estimates of relative image shifts between frames (Li *et al.*, 2013). Advanced methods like MotionCor2 address both whole-frame and local motions, by dividing each frame into patches and iteratively determining the anisotropic motion patterns of the micrograph (Zheng *et al.*, 2017). Most workflows apply motion correction early in processing. Later-stage per-particle and referenced-based motion correction algorithms are discussed in Section 2.5.6.3.

### 2.5.3 CTF Estimation and Correction

Estimating the CTF is essential for high-resolution cryo-EM to accurately correct image distortions introduced by the microscope's optical system. CTF maximums and zeroes are easily identified in Fourier transforms of cryo-EM micrographs, which reflect the interference pattern formed at the back focal plane. The primary objective of CTF estimation is fitting a theoretical model to the experimentally observed Fourier transform, to determine key parameters like defocus and astigmatism which shape the CTF. CTF correction is achieved in later data processing stages by dividing the experimental image by the CTF model in Fourier space (Frank, 2006a).

CTFFIND4, determines CTF parameters by calculating a micrograph's power spectrum (square of the Fourier transform) and subtracting the background to enhance the CTF-derived Thon rings. The algorithm then identifies the astigmatism angle and performs a 2D search for defocus values, followed by a 3D refinement of astigmatism and defocus parameters together (Rohou & Grigorieff, 2015). In alternative software, Gctf employs GPU acceleration for faster computation (Zhang, 2016) and WARP estimates global CTF and a localised CTF model, which is useful for tilt series datasets (Tegunov & Cramer, 2019). Similarly, CryoSPARC can perform local patch-based CTF estimation (Punjani *et al.*, 2017).

### 2.5.4 Particle Picking

Initially, particles coordinates were visually identified and selected from micrographs manually. Although precise, this was time-consuming and prone to user bias, making it impractical for large datasets (Zhu *et al.*, 2004). To address this, automated particle picking techniques have been developed.

Reference-free automated picking methods use a peak-detection algorithm that identifies particle coordinates based on the enhanced features (Scheres, 2015), often convoluting the image with a filter such as a Laplacian of Gaussian (LoG) filter, which enhances edges and blob-like features. Template-based methods use 2D projections of reference structures or 2D class averages (Section 2.5.5.1) as templates and compute the cross-correlation between the templates and the micrograph, identifying peaks in the correlation map as potential particle coordinates (Scheres, 2015).

Deep learning techniques can learn complex features of micrographs to achieve more accurate particle picking (Wagner *et al.*, 2019; Bepler *et al.*, 2019). Software such as Topaz and crYOLO provide pre-trained weights for their neural networks, facilitating rapid picking. Alternatively, the neural networks can be trained on a specific dataset by manually picking particles on a subset of micrographs. Neural networks can also be used to denoise micrographs, and in combination with neural-network based picking software, are useful tools for identifying particles in low-contrast micrographs (Bepler *et al.*, 2020).

### 2.5.5 Particle Alignment and Classification

#### 2.5.5.1 2D Classification

2D classification is the initial step in single-particle analysis post-particle picking and is used to remove low-quality particles and create templates for precise particle picking, by aligning, grouping, and averaging similar particles. Additionally, 2D classification reveals particle orientations, crucial for assessing completeness of Euler angles or potential anisotropy that would prevent isotropic 3D reconstructions. It also helps identify broad compositional and conformational sample heterogeneity.

To compare and classify particles, particles are aligned by computing their translations and in-plane rotations relative to a reference 2D image or average. Translational alignment

involves determining the x and y shifts to centre each particle image against references by cross-correlation (Sigworth, 2015; Frank, 2006d). Similarly, in-plane rotational alignment determines the best rotation angle by correlating the particle with a reference at various angles. Cross-correlation calculations are performed in Fourier space to allow CTF correction and for computational efficiency (Scheres, 2012).

Initial low-resolution 2D references are generated by averaging random particle subsets and are iteratively refined through alignments and classification (Sigworth, 2015; Frank, 2006d). Iterations alternate between classifying particles to reference images based on similarity and improving particles alignments to generate new references (Scheres, 2012). Multivariate statistical analysis (Section 2.5.5.1.1) and maximum likelihood (Section 2.5.5.4.1) principles are used in this process. Well-defined classes suggest high-quality data, while fuzzy or inconsistent features may indicate damaged particles, contaminants, or flexible regions (Sigworth, 2015).

#### *2.5.5.1.1 Multivariate Statistics*

Multivariate Statistical Analysis (MSA) simplifies high-dimensional image data (pixel intensities) into a lower-dimensional space for easier classification. Techniques like Correspondence Analysis (CA) and Principal Component Analysis (PCA) are applied to aligned particle images, which are treated as a point in higher dimensional space defined by their pixel intensities (van Heel & Frank, 1981). PCA is widely adopted over CA in modern cryoEM data processing for its suitability for continuous data (Scheres, 2012). In MSA, eigenvectors represent directions of greatest data variation. Projecting high-dimensional data onto significant eigenvector-defined space allows classification and clustering of images. This dimensionality reduction also mitigates noise, as less significant eigenvectors often correspond to random variations rather than meaningful structural differences (Frank, 2006d). MSA reveals the most significant dataset variations, such as different compositions and conformations by their shape and orientation variations, subunit arrangements, and staining patterns (in NS-EM) (van Heel & Frank, 1981).

### 2.5.5.2 Overarching principles of 3D reconstruction

Cryo-EM three-dimensional reconstruction aims to deduce the 3D structure of macromolecules from two-dimensional projections, based on the central section theorem.

This theorem states that the 2D Fourier transform of a projection corresponds to a central plane in the 3D Fourier transform of the object (De Rosier & Klug, 1968). The common lines method exploits the fact that any two 2D projections of a 3D object share a common line in Fourier space. By identifying these lines and matching their amplitudes and phases, the relative orientations of projections are established (Van Heel, 1987). This theorem was foundational for early angular assignment algorithms and initial model generation.

#### 2.5.5.3 Initial Model Generation

Although common lines methods provide a theoretical basis for 3D reconstruction, they often struggle with noisy experimental data, especially for smaller or asymmetric particles. An incorrect or biased initial model can lead to model bias in the final reconstruction (Henderson, 2013). Conversely, a high-quality initial model can accelerate convergence and improve the likelihood of achieving a high-resolution final structure.

One contemporary approach to initial model generation is the stochastic gradient descent (SGD) approach, first implemented in cryoSPARC (Punjani *et al.*, 2017). SGD iteratively updates a 3D model using small data subsets, efficiently exploring possible structures and being less susceptible to local optima. This method is particularly effective for challenging datasets with low signal-to-noise ratios or significant structural heterogeneity. DRGN-AI (Deep Reconstructing Generative Networks - Ab Initio) leverages a neural network to learn the conformational landscape of large noisy datasets (Levy *et al.*, 2024). DRGN-AI can reconstruct unbiased initial models of multiple heterogeneous states in one-shot, which has revealed previously missed conformational states in cryo-EM datasets and provides useful models for subsequent 3D classification (Section 2.5.5.5).

#### 2.5.5.4 Model Refinement

3D reconstruction is typically iterative, starting with low-resolution initial models that are refined with higher-resolution data. Each iteration involves projecting the current 3D model in various orientations, comparing experimental data with these projections, identifying the best-matching orientations for the particles images, and updating the reconstruction based on new angular assignments (Frank, 2006b). This cycle continues until convergence, indicated by no significant improvements in resolution or model quality. Modern algorithms for 3D reconstruction often integrate advanced statistical methods to handle noise and data

uncertainty, including MSA, maximum likelihood and Bayesian approaches. Additionally, strategies are employed to prevent overfitting (Section 2.5.5.4.2).

#### *2.5.5.4.1 Maximum Likelihood and Bayesian Approaches*

Sigworth (1998) proposed using the maximum likelihood approach to handle noisy data. When using a maximum likelihood approach, each image is compared to the model projections and a probability for each angular assignment is calculated, rather than assigning each image to a single projection. The likelihood function incorporates terms for experimental images, possible orientations, and model parameters, and is maximised to identify the most likely model (map) given the angular assignment probabilities (Sigworth, 1998). By considering multiple orientations for each particle, this approach retains information that conventional methods might discard or misalign, which is especially beneficial for datasets with low SNR where determining a single best orientation is challenging (Scheres *et al.*, 2005).

Scheres (2012) introduced a Bayesian method in the RELION software for maximum likelihood estimation. The Bayesian framework includes prior information about expected parameter distributions, enabling automatic adjustment of parameters that would otherwise require user intervention. This approach reduces the need for user expertise, enhancing objectivity and reproducibility. Additionally, priors help regularise the reconstruction (Section 2.5.5.4.2.2), preventing overfitting (Scheres, 2012).

RELION applies this method using an expectation-maximisation algorithm. During the expectation step, the software calculates the probabilities of each possible orientation for each particle based on the current model. In the maximisation step, it updates the model to maximise the model likelihood given these probabilities. This process repeats until convergence (Scheres, 2012).

The THUNDER algorithm (Hu *et al.*, 2018) builds upon this framework to effectively manage poor-quality particle images. THUNDER accounts for varying image quality by incorporating a novel likelihood function that efficiently minimises the impact of low-quality particles during model refinement. THUNDER sometimes achieves higher resolution reconstructions, especially for heterogeneous datasets. It also reduces the need for extensive particle sorting and classification before 3D reconstruction (Hu *et al.*, 2018).

#### *2.5.5.4.2 Avoiding Overfitting*

Overfitting data causes noise to be misinterpreted as structural features. Shatsky *et al.* (2009) illustrated this in their "Einstein from noise" experiment, where recognisable features of Einstein's face (the initial model) were reconstructed from pure noise due to insufficient constraints in the reconstruction process. This underscores the importance of rigorous validation and regularisation techniques in cryo-EM data processing.

##### 2.5.5.4.2.1 Fourier Shell Correlation (FSC)

Fourier Shell Correlation (FSC) is used to assess resolution and prevent overfitting. FSC calculation involves splitting the dataset into two halves, generating separate 3D reconstructions, and computing their 3D Fourier transforms (Grigorieff, 2000). The correlation between these transforms is then measured within concentric shells of increasing radius (spatial frequency). The resulting FSC curve plots this correlation against spatial frequency, with resolution reported at the spatial frequency where the FSC curve crosses a threshold, commonly 0.143 (Rosenthal & Henderson, 2003).

Gold-standard FSC reconstruction methods prevent overfitting by ensuring that two half-datasets are processed independently, so that reconstructed noise does not inform FSC estimated resolution (Grigorieff, 2000). Refinement algorithms use the FSC curve to apply resolution-dependent filters, only including high-frequency information in the model that is present in both half-maps (Scheres, 2012).

##### 2.5.5.4.2.2 Regularisation

Regularisation prevents overfitting by adding constraints to favour simpler, more plausible solutions. Priors encode expectations like model smoothness or bounded density values. This balance between fitting data and adhering to prior expectations helps to prevents fitting noise to the model (Scheres, 2012; Punjani, Zhang & Fleet, 2020).

###### 2.5.5.4.2.2.1 Non-uniform Refinement (CryoSPARC)

Non-uniform refinement in cryoSPARC addresses the limitations of uniformly applying regularisation across a 3D map. Conventional methods use Fourier Shell Correlation (FSC) between two half-maps to set regularisation parameters, leading to uniform smoothing across all structure regions (Punjani, Zhang & Fleet, 2020). Biological structures, however,

often have varying flexibility and order. For example, membrane proteins may feature well-ordered transmembrane domains alongside cytoplasmic flexible regions. Uniform regularisation can over-smooth well-ordered areas, obscuring high-resolution features, while under-smoothing flexible regions, retaining noise (Punjani, Zhang & Fleet, 2020).

Non-uniform refinement employs an adaptive regularisation scheme using cross-validation (CV) to optimise parameters for different map regions. CV divides data into subsets for training and validation, ensuring that regularisation parameters reflect local map characteristics while being correctly validated (Punjani, Zhang & Fleet, 2020). Separate regularisation parameters are determined for each half-map, adhering to the 'gold-standard' refinement principle (Scheres & Chen, 2012; Punjani, Zhang & Fleet, 2020). Non-uniform refinement preserves more high-resolution features in well-ordered regions and appropriately smooths noisier, flexible areas (Punjani, Zhang & Fleet, 2020).

#### 2.5.5.4.2.2.2 BLUSH (RELION)

BLUSH (Bayesian Local Uncertainty SHarpening) performs regularisation using neural networks that incorporate prior knowledge about biological macromolecular structures (Kimanius *et al.*, 2024). Similar to non-uniform refinement, BLUSH improves reconstructions with spatially varying regularisation but uses a pre-trained denoising network trained on noisy half-map pairs from high-resolution structures in the Electron Microscopy Data Bank (EMDB). In effect, the network has learnt to enhance common cryo-EM map features (Kimanius *et al.*, 2024). To avoid overfitting and resolution overestimation, BLUSH employs "spectral trailing," using the Fourier Shell Correlation (FSC) between independently refined half-maps to set a resolution cut-off. Beyond this cut-off, Fourier components of the denoised half-maps are zeroed out (Kimanius *et al.*, 2024). BLUSH is particularly effective for datasets with low SNR, small complexes, and maps with significant local resolution variations. It enabled the reconstruction of an amyloid with just 30 ordered residues in its core and a protein-RNA complex with a molecular weight of only 40 kDa, approaching the theoretical lower size limit for cryo-EM structure determination (Kimanius *et al.*, 2024).

### 2.5.5.5 3D Classification

3D classification excels at distinguishing particles based on subtle conformational differences not observable in 2D classifications, isolating homogeneous subsets and potentially revealing

different functional states of macromolecular complexes (Sigworth, 2015; Scheres, 2016). 3D classification compares experimental particle images with 2D projections of multiple 3D reference models simultaneously in an iterative process, refining and updating the models based on particle assignments. The maximum likelihood approach with Bayesian parameter optimisation and MSA, used in 2D classification and 3D refinement, is also applied here (Scheres *et al.*, 2007).

#### 2.5.5.6 Assessing Resolution

Evaluating the resolution of cryo-EM reconstructions is crucial for assessing their quality and interpretability. FSC (Section 2.5.5.4.2.1) provides a global resolution measure with a 0.143 threshold, correlating approximately to a map correlation coefficient of 0.5 between the EM map and the true structure, akin to the figure of merit measure used in X-ray crystallography (Rosenthal & Henderson, 2003).

However, global resolution measures overlook local variations in map quality caused by regions of differing flexibility. To address this, local resolution estimation methods such as ResMap and MonoRes (Kucukelbir, Sigworth & Tagare, 2014; Vilas *et al.*, 2018), assess local features against noise levels, determining the highest resolution where features can be distinguished from noise. This creates a spatially varying resolution map. Neural networks are also used for local resolution estimation. CryoRes, is trained with EMDB data and ResMap-derived local resolutions to estimate local resolution (Dai *et al.*, 2023) and DeepRes is trained on real and simulated maps derived from high-resolution models (Ramírez-Aportela *et al.*, 2019).

### 2.5.6 Improving Resolution and Map Interpretability Further

#### 2.5.6.1 Sharpening

The B-factor, or temperature factor, describes the attenuation of structure factors due to thermal motion and other blurring factors. In cryo-EM, the effective B-factor includes sources of high-resolution signal degradation like beam-induced motion, particle alignment inaccuracies, and structural heterogeneity. Map sharpening enhances high-resolution features and reveals finer structural detail in cryo-EM density maps by applying a negative B-factor in Fourier space, thereby boosting high-resolution Fourier components (Rosenthal & Henderson, 2003). A B-Factor estimate is determined by plotting the natural logarithm of

cryo-EM map amplitudes against the square of the resolution (a Guinier plot) (Rosenthal & Henderson, 2003). The plot's slope provides the B-factor for map sharpening. Using the 'gold-standard' FSC approach for resolution estimates mitigates overfitting contributing to B-factor estimation (Scheres & Chen, 2012).

Approaches like LocalDeblur account for local resolution variations by applying different B-factors to map regions based on their local resolution estimate (Ramírez-Aportela *et al.*, 2020). This helps to prevent over- and under-sharpening of low and high local resolution regions respectively. Additionally, neural network-based software such as DeepEMhancer use networks trained on cryo-EM maps and corresponding atomic models to enhance map features and interpretability (Sánchez-Garcia et al., 2021).

While DeepEMhancer aids model building and map interpretation, it is essential to validate these enhanced maps against the original reconstructions to prevent artefacts or over-interpretation. Refining atomic models using DeepEMhancer-generated maps is inappropriate, as these maps are artificial, and resulting statistics will not accurately reflect model quality in relation to the experimental data.

#### 2.5.6.2 Per-Particle CTF Refinement

Accurate CTF estimation is crucial for high-resolution cryo-EM reconstructions (Section 2.4.4.2). Per-particle CTF refinement is used to improve the accuracy of CTF estimations beyond the initial global estimates (Fernandez-Gimenez, Carazo & Sorzano, 2023). In RELION, CTF refinement assumes the Euler angles assigned to particles by 3D refinement is accurate and uses the reference structure to refine CTF parameters. It compares the 3D model's reference projection (unmodulated by the CTF) with the particle image (which is modulated by CTF) to improve CTF estimation (Zivanov *et al.*, 2018). Similar methods are applied in Xmipp (Strelak *et al.*, 2021) and CryoSPARC (Punjani *et al.*, 2017). Gctf performs global CTF estimation followed by local refinement that accounts for particle location in the context of neighbouring particles with a Gaussian weighting scheme (Zhang, 2016). Per-particle CTF refinement can sometimes decrease resolution and different algorithms can fail to converge on the same solution. This highlights the complexity and challenges of local CTF estimation (Fernandez-Gimenez, Carazo & Sorzano, 2023).

#### 2.5.6.3 Per-Particle Motion Correction

Reference-based per-particle beam-induced motion correction methods, such as those in FREALIGN (Brilot *et al.*, 2012; Campbell *et al.*, 2012) and RELION (Scheres, 2014), estimate particle positions and orientations for each movie frame using the reference structure and known alignments. To address radiation damage, which affects high spatial frequencies more rapidly (Hayward & Glaeser, 1979), dose-weighting schemes down weight the contribution of later frames to high-resolution information. Bayesian polishing in RELION incorporates prior knowledge about particle motions and leverages information from the entire particle ensemble to inform individual particle motion estimates, which is particularly beneficial for smaller particles or low SNR images (Zivanov, Nakane & Scheres, 2019).

#### 2.5.6.4 Handling Heterogeneity

High-resolution cryo-EM reconstructions necessitate a homogeneous particle stack, yet biological samples frequently display structural heterogeneity that impedes resolution.

##### *2.5.6.4.1 Discrete Heterogeneity*

3D classification (Section 2.5.5.5) addresses discrete heterogeneity by categorising particles into distinct classes representing different structural states or compositions (Scheres, 2016). Biochemical methods like cross-linking can stabilise inherently heterogeneous samples (Kastner *et al.*, 2008). Generally, particle alignment is guided by larger, more rigid regions. Partial signal subtraction and focused refinement can enhance resolution of less defined areas by forcing 3D refinements to align particles based on features of a user-defined region (Nakane *et al.*, 2018; Scheres, 2016). Multi-body refinement allows independent refinement of user-defined rigid bodies, assuming relative movements between them. It employs a maximum likelihood approach to determine the relative orientation of each region, to improve signal subtraction accuracy and focussed refinement of each rigid body iteratively (Nakane *et al.*, 2018).

##### *2.5.6.4.2 Continuous Heterogeneity*

Continuous heterogeneity, such as domain flexibility or large-scale conformational changes, often eludes traditional discrete classification methods, which fail to capture the full conformational ensemble that is present in rapidly vitrified samples (Toader, Sigworth &

Lederman, 2023). CryoDRGN (cryogenic electron microscopy Deep Reconstructing Generative Networks) uses neural networks to learn a continuous distribution of density maps from image data, mapping the specimen's conformational landscape in a low-dimensional latent space (Zhong *et al.*, 2021b). Building on these concepts, the DynaMight and 3DFlex algorithms apply learned deformations to individual particles to refine a single consensus structure from the conformational ensemble (Punjani & Fleet, 2023; Schwab *et al.*, 2024).

Modern methods to handle continuous heterogeneity enhance reconstruction resolution but also provide insights into the dynamic behaviour of macromolecular complexes. This bridges the gap between static structural models and the dynamic reality of biological systems, essential for understanding their function.

## 2.6 Helical Reconstruction in Cryo-EM

### 2.6.1 Helices in Biology

Helical structures like the T4 bacteriophage tail and tobacco mosaic virus were early focuses in electron microscopy and structural biology (De Rosier & Klug, 1968; Klug, 1999). Helices are prevalent in biology, spanning scales from the DNA double helix to large macromolecular assemblies like bacterial flagellum. This prevalence can be attributed to the energetic favourability, functional versatility, and unique mechanical properties of helices. At the molecular level, helices represent energetically favourable conformations. The α-helical conformation in proteins maximizes hydrogen bonding between backbone atoms (Pauling, Corey & Branson, 1951) and the DNA double helix allows base stacking and hydrogen bonding, creating a stable yet accessible structure for genetic information storage (Franklin & Gosling, 1953; Watson & Crick, 1953).

Helical architectures provide mechanical properties that are essential for many biological processes. For example, at a critical concentration, the thermodynamic properties of helical polymers enable actin monomers to rapidly polymerize into filaments, allowing quick cellular structure remodelling (Oosawa & Kasai, 1962; Fujiwara, Vavylonis & Pollard, 2007; Pollard & Borisy, 2003). Despite lacking sequence homology, both the archaeallum and bacterial flagellar filament have converged upon homologous coiled-coil helical filaments to achieve reversible motility, highlighting the importance of helical mechanical properties

(Kreutzberger *et al.*, 2022). In membrane remodelling, the helical structure of dynamin filaments allows a ratcheting mechanism for membrane constriction, with helical rungs sliding past one another (Ganichkin *et al.*, 2021). The helical arrangement of the membrane-tethering protein EEA1 enables it to form both rigid and flexible filaments, and enables EEA1 to bring intracellular vesicles and the endosome together upon collapse of the rigid filament (Murray *et al.*, 2016). The ability of the helical filament to alter its elastic properties also modulates membrane fluidity (Ghosh & Spakowitz, 2024).

The frequent occurrence and variety of helical structures in biology emphasise their significance in numerous cellular processes, necessitating effective methods to examine these assemblies at high resolution. Cryo-EM has become a potent tool for revealing the structures and functions of helical assemblies across various biological scales.

### 2.6.2 Helical Lattices and their Layer Lines

Helical structures can be envisioned as planar crystal lattices rolled into cylinders, creating a periodic subunit arrangement along the helical axis and producing characteristic layer line reflections in Fourier space (Glaeser *et al.*, 2007). These layer lines arise from principles of constructive and destructive interference, akin to those in electron microscopy image formation (Section 2.4). Electrons interacting with a helical structure cause scattered waves from the periodic subunits to interfere. Constructive interference, where waves are in phase, generates layer lines, while destructive interference, where waves are out of phase, results in signal absence between layer lines (Diaz, Rice & Stokes, 2010). Similar to diffraction spots representing vectors in a 2D crystal lattice, layer lines represent each helical repeat (family) of the helical lattice (Glaeser *et al.*, 2007; Diaz, Rice & Stokes, 2010).

Layer lines differ from crystal diffraction spots in their continuous nature along the radial direction due to the cylindrical symmetry of helices, where each subunit can occupy any azimuthal angle around the helical axis. In contrast, crystal lattices exhibit discrete periodicity in all three dimensions, resulting in distinct diffraction spots (Glaeser *et al.*, 2007).

#### 2.6.2.1 Indexing Layer Lines

Indexing layer lines involves interpreting the Fourier space lattice to deduce real-space helical parameters. The order of the helical repeat reflects the repetition frequency of a feature

along the helical axis in real space – its Bessel order (Glaeser *et al.*, 2007). In Fourier space the order of a layer line is inversely proportional its distance from the meridian. The layer line distance from the equator is inversely proportional to the helical pitch, the vertical distance for one complete helical turn in real space. Each layer line corresponds to a specific helical family, and their combination describes the complete helical lattice (Glaeser *et al.*, 2007; Diaz, Rice & Stokes, 2010).

Precise layer line measurement can be challenging due to small, hard-to-distinguish distances in Fourier space equating to large misidentification of real-space helical parameters, along with sample heterogeneity, helical disorder, and limited resolution. Tools like Helixplorer and PyHI (Zhang, 2022) assist in layer line analysis, but indexing ambiguity often necessitates testing multiple potential helical parameters. The advent of rapid computational algorithms has enabled a more empirical approach to helical reconstruction, whereby helical refinements are used to test different helical parameters derived from ambiguous Fourier space indexing. Refinements with detailed reconstructions likely represent the true helical parameters (He & Scheres, 2017).

#### *2.6.2.1.1 Real Space Indexing*

Given high-quality, homogenous data, reconstructing helical assemblies in C1 without symmetry can achieve sufficient resolution to directly derive helical parameters in real space, bypassing ambiguities of traditional Fourier space indexing (He & Scheres, 2017). Hi3D resamples helical maps into cylindrical coordinates and sums along the radial direction to transform reconstructions into a 2D lattice. This enables automated detection of helical parameters by identifying density maxima in a 2D lattice (Sun, Gonzalez & Jiang, 2022).

Incorrect indexing and consequent incorrect symmetry application can average out subtle heterogeneity in helical assemblies. Gambelli, Isupov & Daum (2022) showed that reconstructions might exhibit "hidden symmetry," where the apparent symmetry does not reflect the structure's true symmetry. Validation of helical parameters, via real-space examination of high-resolution non-symmetry imposed reconstructions, helps identify asymmetric features or heterogeneity that symmetry imposition might obscure and provides an indication of helical parameters that capture the map heterogeneity (Gambelli, Isupov & Daum, 2022). Overall, deriving helical parameters in real space complements traditional

Fourier space methods, potentially resolving ambiguities, and revealing overlooked structural details.

### 2.6.3 Fourier-Bessel Reconstruction

Fourier-Bessel reconstruction is a method for deriving the three-dimensional structures of helical assemblies from electron micrographs without particle alignment (De Rosier & Klug, 1968). The Fourier transform of a helical structure is the convolution of a delta function, analogous to diffraction spots in a 2D crystal, and a Bessel function describing the helix's cylindrical shape (Diaz, Rice & Stokes, 2010). Bessel functions oscillate in Fourier space with increasing radial distance, with all orders except n=0 being zero at the origin. The maximum amplitude of a Bessel function typically occurs at a radius approximately equal to its order plus two (Diaz, Rice & Stokes, 2010). A fundamental principle in Fourier-Bessel reconstruction is that a 2D Fourier transform rotated about the helical axis equates to a 3D Fourier transform of the helical structure. For any given layer line, the amplitude remains constant as it rotates around the meridian, but the phase varies with the azimuthal angle. As the phase oscillates, the number of periods completed by the Bessel function in one rotation around the meridian equals the Bessel order of that layer line (Diaz, Rice & Stokes, 2010).

Fourier-Bessel reconstruction starts with boxed segments of helical filaments from 2D micrographs, which are Fourier transformed to extract amplitudes and phases along each layer line. Correct indexing assigns Bessel function orders to each layer line accurately. A reverse Fourier-Bessel transform of each indexed layer line generates a 3D map of the helical family. Combining Fourier-Bessel transforms of each layer line yields a complete 3D map of the filament (Diaz, Rice & Stokes, 2010).

Fourier-Bessel reconstruction directly derives 3D structures from 2D projections of helical assemblies but assumes perfect helical symmetry, limiting its use for flexible helices. Despite these constraints, it remains a valuable tool for initial structure determination and validating other methods (Glaeser *et al.*, 2007; Diaz, Rice & Stokes, 2010).

### 2.6.4 Iterative Helical Real-space Reconstruction

Iterative Helical Real-space Reconstruction (IHRSR) integrates single-particle analysis with helical symmetry refinement to overcome the limitations of traditional Fourier-Bessel

reconstruction, particularly for flexible or imperfectly symmetric helical filaments (Egelman, 2000). IHRSR starts with an initial model, often a cylinder or simulated helix (He & Scheres, 2017), and refines it iteratively using single-particle reconstruction principles (Section 2.5.5.2). IHRSR includes additional steps to determine and apply helical symmetry during refinement. After each cycle of back-projection and model optimisation, new helical parameters are derived from the 'asymmetric' model using a least-squares fit. These refined parameters are applied in real space, providing an updated model for subsequent back-projections (Egelman, 2000). An accurate initial estimate of helical parameters is essential, thus not eliminating the need for layer line indexing.

In RELION, symmetry is applied in Fourier space before the maximisation step for accurate signal-to-noise ratio estimates and FSC calculation. Following maximisation, the helical parameters are refined in real space based on the unsymmetrised model, and then applied to the model before the next iteration. Helical parameters are estimated separately for each half map to maintain the gold-standard refinement principles (Section 2.5.5.4.2.1) and the helical parameters of each half map are averaged after each iteration (He & Scheres, 2017).

For IHRSR, filaments are segmented into overlapping boxes, with overlap extent determining the number of unique asymmetric units per box. This affects the number of times a ‘particle’ can have helical translations applied during the expectation step, where it is compared against back projections in Fourier space (He & Scheres, 2017). RELION's IHRSR algorithm uses tilt and psi priors to enhance the accuracy of angular assignments. The tilt prior confines the tilt angle of these segments to near 90°, as helical filaments generally lie flat on the grid. The psi prior aligns the helical axis of each segment (established during filament picking) with the y-axis of the micrograph. These priors are particularly beneficial in early refinement stages and for smaller helical segments (He & Scheres, 2017).

In IHRSR reconstruction, the lowest Bessel order, usually n=1, is used to determine helical parameters, as it passes through all lattice points and describes the full helical lattice. Higher-order Bessel functions may miss structural details. Using the lowest Bessel order ensures the fundamental helical symmetry is accurately represented (Diaz, Rice & Stokes, 2010; He & Scheres, 2017; Egelman, 2000).

## 2.7 Conclusion

This chapter has provided a foundation in cryo-EM theory, essential for the experimental work presented in Chapter 4 and Chapter 5. From its historical roots to the current "resolution revolution", the fundamental principles of electron-specimen interactions and image formation were described, as well as the critical importance of sample preparation techniques in preserving biological specimens, and a detailed examination of modern microscope components. Furthermore, data processing methods, including particle picking, alignment, classification, and statistical approaches like maximum likelihood estimation and Bayesian inference, have been explored. This theoretical groundwork, in particular IHRSR, is crucial for the high-resolution structural insights into BDLP-mediated membrane remodelling determined by cryo-EM in the following chapters.

### 2.7.1 Outlook and Future Directions

The field of cryo-EM is rapidly advancing, routinely reaching resolutions, and providing biological insights that were previously unattainable. One key trend is the creation of more accessible and cost-effective cryo-EM technologies. Russo and colleagues have shown that high-resolution structure determination is feasible using lower voltage (100 keV) microscopes (McMullan *et al.*, 2023). This could reduce the cost and complexity of cryo-EM, broadening its availability.

Artificial intelligence and machine learning are increasingly applied in cryo-EM data processing. Neural network-based programmes are being developed for various workflow stages, including particle picking, regularisation, flexibility analyses and map sharpening. These AI-driven methods are expected to become more integrated into standard workflows, automating data processing and improving structure determination speed and accuracy, especially for heterogeneous datasets (Levy *et al.*, 2024; Punjani & Fleet, 2023).

*In situ* structural biology allows the study of macromolecular complexes in cellular contexts. Advances in cryo-ET and sample preparation techniques like focused ion beam milling enable visualisation of molecular machines within their cellular context at unprecedented resolution (Berger *et al.*, 2023). These methods can bridge structural and cellular biology, offering a holistic understanding of biological processes.

The development of high-resolution cryo-EM methodologies means it is now being adopted by the drug discovery and the pharmaceutical industry for structure-based drug design and the rational development of therapeutics. Cryo-EM is especially useful for studying difficult drug targets, such as membrane proteins and large macromolecular complexes, which are challenging to crystallise for X-ray crystallography (Renaud *et al.*, 2018; Merk *et al.*, 2016). Cryo-EM has allowed observation of small molecule protein binding in near-native states, offering crucial insights into drug-target interactions (Zhang *et al.*, 2020c). Additionally, cryo-EM's ability to capture multiple protein conformations in one experiment is invaluable for understanding protein dynamics and identifying potential allosteric binding sites (Merk *et al.*, 2016). Cryo-EM was crucial in determining the SARS-CoV-2 spike protein structure, aiding the rapid development of COVID-19 vaccines and therapeutic antibodies (Wrapp *et al.*, 2020). As the technology advances with better throughput and automation, cryo-EM is set to play a central role in drug discovery, potentially reducing the time and cost of bringing new therapeutics to market.

With ongoing innovations, cryo-EM will increasingly contribute to structural biology, drug discovery, and understanding fundamental biological processes, unlocking new insights into molecular mechanisms, as is demonstrated in the following chapters.

# Chapter 3: Materials and Methods

## 3.1 Materials

### 3.1.1 Media

Bacterial growth media was prepared by dissolving pre-mixed powder from the manufacturer in de-ionised water to the listed concentrations (Table 3) before autoclaving.

**Table 3. Bacterial Growth Media Compositions.**

| Medium | Supplier | Composition |
|---|---|---|
| 2XYT | Melford | 16 g/L digest peptone, 10 g/L yeast extract, 5 g/L sodium chloride |
| LB Agar | Melford | 10 g/L casein digest peptone, 5 g/L yeast extract, 5 g/L sodium chloride, 15 g/L agar |
| Luria-Bertani Broth (LB Broth) | Melford | 10 g/L casein digest peptone, 5 g/L yeast extract, 5 g/L sodium chloride |

### 3.1.2 Antibiotics

Antibiotic stock solutions (Table 4) were prepared for addition to growth media by dissolving antibiotic salts in appropriate solvents to make a 1000X stock solutions, filter sterilised and stored at 4°C for no longer than 1 month.

**Table 4. Antibiotic Stock Solution Concentrations.**

| Antibiotic | Solvent | Stock Concentration | Working Concentration |
|---|---|---|---|
| Ampicillin | Milli-Q | 100 mg/mL | 100 μg/mL |
| Chloramphenicol | 70% Ethanol | 30 mg/mL | 30 μg/mL |
| Kanamycin | Milli-Q | 50 mg/mL | 50 μg/mL |

### 3.1.3 Buffers

Buffers components were dissolved in Milli-Q (ultrapure water), the pH was adjusted using hydrochloric acid or sodium hydroxide, and the final solution was filtered through a 0.2 μm

membrane. Stock solutions of common components (e.g Tris-HCl and sodium chloride) were prepared in the same manner. Buffer compositions are listed in Table 5.

**Table 5. Buffer Compositions.**

| Buffer | Composition | Use |
|---|---|---|
| 10x SDS-PAGE Running Buffer (1 L) | MES sodium salt 97.6 g, Trizma-base 60.6 g, SDS 10 g, EDTA 3 g | SDS-PAGE |
| 10x TBE (1 L) | Trizma-base 1 g, boric acid 55 g, EDTA 5 g, final pH ~8.0 | Agarose gel electrophoresis |
| 5x IRB (Isothermal Reaction Buffer) | 500 mM Tris-HCl pH 7.5, 50 mM $MgCl_2$, 1 mM dGTP/dATP/dCTP/dTTP, 50 mM DTT, 5 mM NAD, 25% PEG-8000 | Gibson reaction |
| BDLP Elution Buffer | 50 mM Tris-HCl pH 8.5, 1 M imidazole | BDLP purification |
| BDLP Lysis Buffer | 50 mM Tris-HCl pH 8.0, 1.25 M NaCl | BDLP purification |
| BDLP Wash Buffer | 50 mM Tris-HCl pH 8.5, 500 mM NaCl, 20% glycerol | BDLP purification |
| Reaction Buffer | 20 mM Tris-Cl pH 7.2, 130 mM NaCl, 5 mM KCl, 1 mM EGTA, 5 mM MgCl2 | Tubulation |
| SimplyBlue (1 L) | 1% Brilliant Blue G 10 mL, Ethanol 100 mL, 37% HCl 2.94 mL | SDS-PAGE |
| TEN Buffer | 20 mM Tris-HCl pH 7.5, 1 mM EDTA, 1mM sodium azide | BDLP purification, SEC column storage |
| TEV Elution Buffer | 50 mM Tris-Hcl pH 7.5, 500 mM NaCl, 25% glycerol, 1 M imidazole | TEV purification |
| TEV Lysis Buffer | 50 mM Tris-Hcl pH 7.5, 300 mM NaCl, 5 mM imidazole | TEV purification |
| TEV Storage Buffer | 25 mM Tris-Hcl pH 7.5, 150 mM NaCl, 50% glycerol, 2 mM EDTA | TEV purification |
| TEV Wash Buffer | 50 mM Tris-Hcl pH 7.5, 500 mM NaCl, 25% glycerol | TEV purification |

### 3.1.4 Kits

Commercially available kits used in DNA purification are listed in Table 6.

**Table 6. Commercial Kits**

| Kit | Company | Use |
|---|---|---|
| Monarch DNA Gel Extraction Kit | NEB | PCR product purification |
| Wizard Plus SV Miniprep DNA Purification System | Promega | Plasmid purification |

### 3.1.5 Lipids

Lipids used in this work (Table 7) were purchased in lyophilised powder form and stored at -20°C before use.

**Table 7. Commercial Lipids**

| Lipid | Company | Abbreviation |
|---|---|---|
| 1,2-dioleoyl-sn-glycero-3-phosphocholine | Avanti | DOPC |
| 1,2-dioleoyl-sn-glycero-3-phospho-(1'-rac-glycerol) (sodium salt) | Avanti | DOPG |
| *E. coli* Total Extract | Avanti | ETE |
| Monogalactosyldiacylglycerol (Plant) | Avanti | MGDG |

### 3.1.6 Bacterial Strains and Plasmids

Various bacterial strains (Table 8), plasmids (Table 9) and primers (Table 10) were used to generate constructs and in protein expression.

**Table 8. Bacterial Strains**

| Strain | Source | Use |
|---|---|---|
| *E. coli* BL21(DE3) | Dr Harry Low / This Work | Protein expression |
| *E. coli* BL21(Star) | Dr Harry Low / This Work | Protein expression |
| *E. coli* C41(DE3) | Dr Harry Low / This Work | Protein expression |

| | | |
|---|---|---|
| *E. coli* C43(DE3) | Dr Harry Low / This Work | Protein expression |
| *E. coli* Top 10 | Dr Harry Low / This Work | Plasmid amplification |
| *E. coli* Rosetta(DE3) (JS1524) | Dr Matteo Tassinari | TEV protease expression |

**Table 9. Plasmids**

| Plasmid | Source | Features | Source DNA and Primers Used to Generate |
|---|---|---|---|
| $pOPTM_{BDLP}$ | Dr Harry Low (Low *et al.*, 2009) | N-terminal MBP tag and TEV protease recognition sequence, C-terminal 6x histidine tag. Ampicillin resistance. IPTG inducible T7 promoter. | - |
| $pOPTM_{BDLP\text{-}10His}$ | - | N-terminal MBP tag and TEV protease recognition sequence, C-terminal 10x histidine tag. Ampicillin resistance. IPTG inducible T7 promoter. | 10xHis_insertF, 10xHis_insertR, $pOPTM_{BDLP}$ |
| $pOPTM_{BDLP_F583E}$ | Dr Harry Low (Low *et al.*, 2009) | N-terminal MBP tag and TEV protease recognition sequence, C-terminal 6x histidine tag. Ampicillin resistance. IPTG inducible T7 promoter. | |

**Table 10. Oligonucleotides**

| Primer | Sequence | Source |
|---|---|---|
| 10xHis_insertF | catcaccatcaccactaaaagcttggtaccacgc | IDT |
| 10xHis_insertR | gtggtgatggtgatgatgatgatgatggctatag | IDT |

### 3.1.7 Commercial Columns

Pre-packed commercial columns used in this work are listed in Table 11.

**Table 11. Commercial Columns**

| Column | Source |
|---|---|
| HiPrep 16/60 Sephacryl S-300 HR column | Cytvia |
| HiPrep 26/60 Sephacryl S-300 HR column | Cytvia |
| HiPrep 16/60 Sephacryl S-200 HR column | Cytvia |
| HiPrep 26/60 Sephacryl S-200 HR column | Cytvia |
| HisTrap HP 5 mL | Cytvia |
| PD-10 desalting columns packed with Sephadex G-25 resin | Cytvia |

### 3.1.8 Commercial Chemicals

Chemicals used in this work are listed in Table 12. All other standard buffer components such as sodium chloride were purchased from Melford.

**Table 12. Commercial Chemicals**

| Chemical | Company | Use |
|---|---|---|
| 1kb Plus Gene Ruler | Thermo Fisher | Agarose gel electrophoresis |
| 40% Acrylamide/Bis 37.5:1 | Biorad | SDS-PAGE |
| 4x Bolt LDS Sample Buffer | Thermo Fisher | SDS-PAGE |
| 6x Gene Ruler DNA Loading Dye | Thermo Fisher | Agarose gel electrophoresis |
| Acrylamide 4k (30%) 37.5:1 | AppliChem | SDS-PAGE |
| Ammonium Persulfate | Sigma-Aldrich | SDS-PAGE |
| Amylose Resin | NEB | Protein purification |
| Bradford Reagent | Biorad | Protein concentration determination |
| Brilliant Blue G | Sigma-Aldrich | SDS-PAGE |
| cOmplete™, Mini, EDTA-free Protease Inhibitor Cocktail Tablets | Merck | Protein purification |

| | | |
|---|---|---|
| DNase I from bovine pancreas | Merck | Protein purification |
| Guanosine 5′-[β,γ-imido]triphosphate trisodium salt hydrate (GMPPNP) | Sigma-Aldrich | Tubulation |
| Guanosine 5′-diphosphate sodium salt (GDP) | Sigma-Aldrich | Tubulation |
| Guanosine 5′-triphosphate sodium salt hydrate (GTP) | Sigma-Aldrich | Tubulation |
| Isopropyl-D-1-thiogalactopyranoside (IPTG) | Melford | T7 promoter induction |
| Lysozyme (from egg white) | Merck | Protein purification |
| Oligonucleotides | IDT | PCR |
| Phusion High-Fidelity DNA Polymerase | NEB | Gibson |
| Q5 High GC Enhancer | NEB | PCR |
| Q5 High-Fidelity DNA Polymerase | NEB | PCR |
| Q5 Reaction Buffer Pack | NEB | PCR |
| Quick Start Bovine Serum Albumin Standard | Biorad | Bradford Assay |
| SYBR Safe | Invitrogen | DNA Stain |
| T5 Exonuclease | NEB | Gibson |
| TEMED | Sigma-Aldrich | SDS-PAGE |
| Unstained Precision Plus Protein Standard | Biorad | SDS-PAGE |
| Uranyl Acetate | Polysciences | Negative stain EM |

## 3.2 Methods

### 3.2.1 Competent Cells

Competent cells are bacteria primed to efficiently uptake foreign DNA during transformation (Section 3.2.1.1). Chemical competence is typically induced by treating cells with divalent cations, usually calcium chloride, to aid DNA adhesion to the cell envelope followed by a heat shock to reduce membrane potential and fluidity, facilitating DNA uptake (Panja *et al.*, 2006, 2008). The precise mechanism of DNA uptake is still unknown.

To generate competent cells in this work, an overnight culture of cells (Table 8) grown in 2XYT broth was used to inoculate a 2 L culture in the same medium. When the optical density at

600 nm (OD600) reached 0.5, the cultures were cooled on ice for 1 h. The culture was transferred to cooled centrifuge buckets (pre-sterilised with sodium hypochlorite and washed with autoclaved Milli-Q) and pelleted by centrifugation at 3220 *xg* for 30 minutes. The pellet was resuspended in autoclaved 10 mM NaCl for washing, then re-pelleted at the same speed for 15 minutes. The cells were then resuspended in 20 mL of autoclaved 75 mM $CaCl_2$ and agitated by shaking at 240 rpm for 35 minutes. Following another 15-minute centrifugation, the pellet was resuspended in 15 mL of 75 mM $CaCl_2$ containing 15% glycerol in a pre-cooled flask on ice. After 1 hour of incubation, 100 µL aliquots were frozen in dry-ice cooled microcentrifuge tubes and stored at -80 C.

#### 3.2.1.1 Bacterial Transformation

Bacterial transformation was performed to internalise plasmid DNA. To transform chemically competent cells, cells were thawed on ice, and 1-5 µL of plasmid DNA was added to 50 µL of competent cells. This mixture was incubated on ice for at least 15 minutes. The cells were then heat-shocked at 42°C for 45 seconds, followed by immediate cooling on ice for 1 minute. Subsequently, 250 µL of LB broth was added, and the cells were allowed to recover by shaking at 37°C for 1 hour, during which time expression of the antibiotic resistance genes from the plasmid was induced. Finally, the transformed cells were plated on LB agar plates supplemented with the appropriate antibiotic.

### 3.2.2 Tobacco-Etch Virus Protease Purification

Tobacco-Etch Virus (TEV) protease was used in this work to remove tags from purified proteins. TEV protease recognises an amino acid sequence of ENLYFQG, cleaving the protein between glutamine and glycine (Kapust & Waugh, 2000).

TEV protease was expressed and purified as follows: *E. coli* Rosetta cells containing the JS1524 plasmid for "Super" TEV expression were streaked on LB agar plates supplemented with 75 µg/mL carbenicillin and 50 µg/mL kanamycin and incubated overnight at 37°C. A single colony was used to inoculate an overnight preculture in 2XYT medium with the same antibiotics. 120 mL of this preculture was used to seed 12 L of 2XYT medium. At OD600 = 0.6, expression was induced with 1 mM IPTG and continued overnight at 17.5°C.

Cells were harvested by centrifugation (3500 xg, 18 min, 4°C) and resuspended in 140 mL TEV lysis buffer (Table 5) supplemented with DNase, lysozyme and a protease inhibitor cocktail. Lysis was performed by sonication (10 min, 75% power) on ice with gentle stirring, followed by centrifugation (35,000 rpm, Ti45 rotor, 45 min). The supernatant was loaded onto a 10 mL HisTrap column equilibrated in TEV wash buffer. The column was washed with 20 column volumes (CV) of wash buffer, followed by 20 CV of wash buffer containing 2% elution buffer (20 mM imidazole). Protein was eluted using a stepwise gradient to 250 mM imidazole.

Fractions were analysed by SDS-PAGE (Figure 24) and pooled. Buffer exchange was performed by two rounds of dialysis into TEV storage buffer. Protein concentration was determined by Bradford assay (4 mg/mL) and diluted to 2.5 mg/mL. Aliquots (1 mL) were flash-frozen in liquid nitrogen and stored at -80°C.

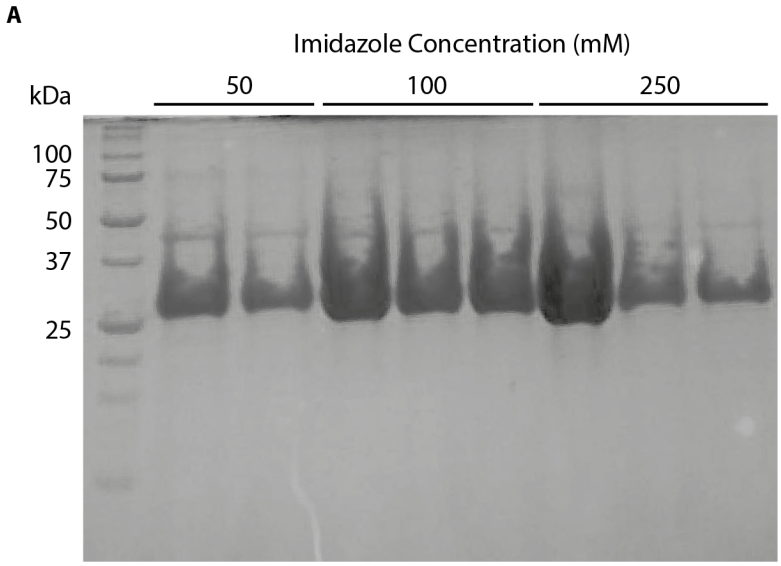


**Figure 24. TEV protease purification.**
A, Coomassie stained SDS-PA gel of fractions eluted from the nickel affinity column during TEV protease (27 kDa) purification.

### 3.2.3 SDS-PAGE

SDS polyacrylamide (SDS-PA) gels were prepared using chemicals specified in Table 13, with APS and TEMED added just before pouring. The resolving gel was set in 1 mm mini gel cassettes (ThermoFisher) under a layer of isopropanol to ensure a flat surface and prevent

drying. After removing the isopropanol, the stacking gel was poured and set around 10- or 12-well combs (ThermoFisher). Gels were stored in a humid environment at 4°C for up to two weeks.

**Table 13. SDS-PA Gel Recipe.**
Recipe is for 6 gels.

| Gel % | Mili-Q (mL) | 1.25 M Bis-Tris pH 6.8 (mL) | 30 % Acrylamide (mL) | 40 % Acrylamide (mL) | 10 % APS (µL) | TEMED (µL) |
|---|---|---|---|---|---|---|
| Resolving Gel | | | | | | |
| 10 | 14.5 | 10 | 10.5 | - | 175 | 37.5 |
| 12 | 11 | 10 | 14 | - | 175 | 37.5 |
| Stacking Gel | | | | | | |
| 4 | 9.25 | 4.3 | - | 1.5 | 150 | 52.5 |

For protein analysis, samples were mixed with 4x Bolt LDS Sample Buffer and loaded into wells, including at least one well with a molecular weight marker (Biorad Precision Plus Unstained Protein Standard). Electrophoresis was conducted at 200 V for 30 min in 1x SDS-PAGE running buffer (Table 5). Gels were Coomassie stained with SimplyBlue.

### 3.2.4 DNA Manipulation

To generate the desired constructs, primers to amplify a gene and linear vector (or a construct with a desired mutation) were designed (Section 3.2.4.1) and used to amplify the fragment by PCR (Section 3.2.4.2). Primers introduced the requisite overlaps to amplified fragments for the Gibson ligation procedure (Section 3.2.4.4). PCR fragments were validated and purified by agarose gel electrophoresis (Section 3.2.4.3), and circular plasmid DNA was generated by the Gibson procedure. Plasmids were transformed into TOP10 *E. coli* cells (Section 3.2.1.1). Individual colonies were used to seed overnight cultures (usually 4-6 colonies per cloning procedure), from which DNA was isolated, analysed by restriction digest (Section 3.2.4.6) and sequenced (Section 3.2.4.7).

### 3.2.4.1 Primer Design

Primers were designed using ApE (Davis & Jorgensen, 2022), with ≥18 bp overlap with the target fragment sequence and an additional ≥15 bp overhang complementary to the insertion point (Figure 25A). Similarly, mutation primers included a ≥15 bp overlap at the mutation site, which was also used to introduce the desired mutation (Figure 25B). Linear vectors were created using primers of ≥24 bp length, without overlaps. Forward and reverse primers for each PCR sample had melting temperatures within a 2°C range (calculated in ApE), considering both the full-length primer and the sequence excluding the additional overlap.

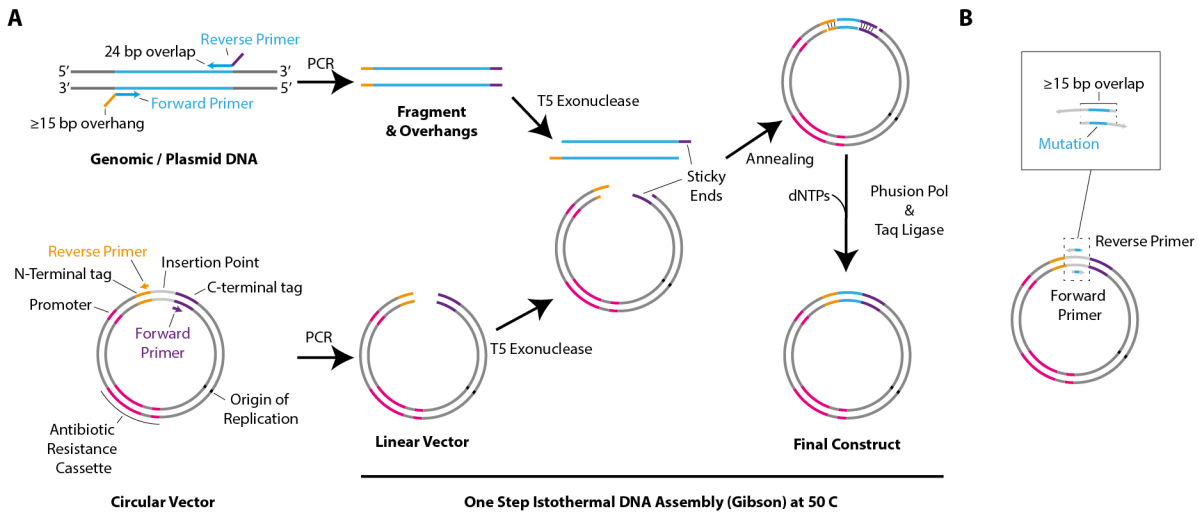


**Figure 25. Primer Design and Gibson Assembly.**
**A,** Primer design rationale for PCR fragment insertion (left) into a desired vector by Gibson assembly (right). **B,** Primer design rationale for mutagenesis. This step is followed by Gibson assembly to ligate the linear PCR product.

### 3.2.4.2 Polymerase Chain Reaction

PCR components were assembled in 50 µL reaction volumes as described in Table 14. Reactions were conducted in a SureCycler 8800 Thermal Cycler (Agilent) with protocols detailed in Table 15. Typically, the touchdown PCR protocol (Korbie & Mattick, 2008) succeeded on the first attempt. This protocol starts with annealing temperatures above the primer melting temperature, decreasing stepwise each cycle, often reducing the need for optimisation and yielding target PCR fragments without non-specific products (Korbie &

Mattick, 2008). If the touchdown PCR failed, optimisation included varying primer ratios and performing gradient PCR at various fixed temperatures.

**Table 14. PCR Reaction Components.**

| PCR Component | Volume / Mass |
|---|---|
| Primers | 130 ng for each primer (forward and reverse) |
| Template DNA | 50 ng (genomic), 7.5 ng (plasmid) |
| Q5 Reaction Buffer | 10 μL |
| Q5 High GC Enhancer | 10 μL |
| 10 mM dNTPs | 0.5 μL |
| Q5 Polymerase | 0.5 μL |
| Milli-Q | Make up to 50 μL |

**Table 15. Touchdown and Gradient PCR Protocols.**

| Step | Touchdown | | Gradient | |
|---|---|---|---|---|
| | Conditions | Cycles | Conditions | Cycles |
| Hot Start | 98 C, 2 min | 1 | 98 C, 2min | 1 |
| Denaturation | 98 C, 30 s | 45 | 98 C, 15 s | 45 |
| Annealing | 80 C to 50 C transition, with stepwise reduction in temperature each cycle, 30 s | | Single temperature 50-72 C | |
| Elongation | 72 C, 30 s/kb | | 72 C, 30 s/kb | |
| Final Elongation | 72 C, 20 min | 1 | 72 C, 5min | 1 |

### 3.2.4.3 Agarose Gel Electrophoresis

PCR products were validated, purified, and restriction digest results were analysed using agarose gel electrophoresis. A 1% agarose solution in 0.5x TBE (Table 5), supplemented with 1% SYBRsafe DNA stain, was prepared and solidified. DNA samples, mixed with 6x DNA loading buffer (5:1 ratio), were loaded into the gel alongside a 1 kb plus GeneRuler molecular

weight marker (Table 12). Gels were electrophoresed at 90 V for 30 min in 0.5x TBE buffer and DNA bands were visualised using a blue light trans-illuminator (Bio-helix).

#### *3.2.4.3.1 DNA Gel-based Purification*

PCR fragment bands were excised from agarose gels with a scalpel to ensure the correct fragment lengths for the Gibson procedure. DNA was extracted using the Monarch DNA Gel Extraction Kit (New England Biolabs). Following the manufacturer's protocol, solubilised gel bands were passed over the column twice, and DNA was eluted in 20 µL Milli-Q. If the product concentration was below 15 ng/µL, DNA was concentrated by vacuum evaporation (Eppendorf concentrator plus).

### 3.2.4.4 Isothermal DNA Assembly

PCR fragments were assembled using the Gibson method (Gibson *et al.*, 2009), which joins multiple DNA fragments in a single, isothermal reaction (Figure 25). This method utilises three enzymes: a 5' exonuclease, a DNA polymerase, and a DNA ligase. The 5' exonuclease generates single-stranded 3' overhangs by digesting the 5' ends of double-stranded DNA fragments. These overhangs, designed to be complementary between adjacent fragments, are introduced by PCR primers (Figure 25). The DNA polymerase fills in gaps created by annealed overhangs, and the DNA ligase seals the nicks in the assembled DNA. This allows for the joining of multiple DNA fragments with overlapping ends in a single-step, isothermal reaction.

**Table 16. Gibson Assembly Master Mix.**

| Gibson Component | Volume (for 120 µL total) |
|---|---|
| 5x IRB (**Table 5**) | 32 µL |
| 0.1x T5 Exonuclease | 0.64 µL |
| 2 U/µL Phusion DNA Polymerase | 2 µL |
| Milli-Q | 85.36 µL |

For Gibson assembly, a master mix was prepared as per Table 16 and stored at -20°C in 7.5 µL aliquots. Taq Ligase was omitted, relying on cellular machinery for final ligation and nick repair

(Fu *et al.*, 2014). Each aliquot was adjusted to 10 µL with 50 ng of linearized vector and >70 ng PCR fragment. The reaction was incubated for 1 hour at 37°C, followed by transforming 50 µL of chemically competent Top10 *E. coli* cells with 5 µL of Gibson mixture.

#### 3.2.4.5 Plasmid Purification

Plasmids were purified from Top10 *E. coli* cells by seeding 4 mL LB Broth cultures supplemented with relevant antibiotics with single colonies from transformation plates. After pelleting overnight cultures, plasmids were purified using a Wizard Plus SV Miniprep DNA Purification System kit (Promega), with modifications to the manufacturer's protocol including passing cleared cell lysate over the column twice and eluting DNA samples in 70 µL Milli-Q.

#### 3.2.4.6 Restriction Digestion

To validate the Gibson assembly products, 4 µL of purified plasmid was incubated with 0.5 µL restriction enzyme(s) and the appropriate reaction buffer (NEB) in 10 µL volumes at 37°C for 1 hour. Restriction enzymes were chosen (using ApE) to simultaneously cut the vector and insert, producing two distinct linear fragments. The sample was analysed via agarose gel electrophoresis (Section 3.2.4.3).

#### 3.2.4.7 DNA Sequencing

Plasmid DNA samples (15 µL containing up to 1.5 µg of DNA) were sequenced by Eurofins Genomics using their standard in-house primers. The sequencing data were analysed with ApE and Clustal Omega (Sievers *et al.*, 2011).

### 3.2.5 Protein Expression

*E. coli* strains used for protein expression (Table 8) contained a T7 RNA polymerase system controlled by a lac repressor (Studier & Moffatt, 1986; Becker *et al.*, 2013), with all plasmids (Table 9) using a T7 promoter for protein expression. The T7 system employs bacteriophage T7 RNA polymerase, known for its specificity and activity (Studier & Moffatt, 1986). The gene of interest is cloned downstream of a T7 promoter in an expression vector, while the host *E. coli* strain has the T7 RNA polymerase gene under lac promoter control. Expression is induced by adding isopropyl β-D-1-thiogalactopyranoside (IPTG), which binds to the lac

repressor, allowing transcription of the T7 RNA polymerase gene. The T7 RNA polymerase then transcribes the target gene, resulting in high-level protein production.

To express protein, single colonies of *E. coli* expression strains with the appropriate plasmids inoculated overnight cultures in 2XYT broth with appropriate antibiotics at 37°C. Each litre of 2XYT broth was seeded with 10 mL of overnight culture, totalling 12 L. At an OD600 of 0.4, protein expression was induced with 1 mM IPTG and continued overnight at 17.5°C. Cells were harvested by centrifugation at 3500 x g for 18 minutes at 4°C. The cell pellets were either stored at -80°C or used immediately for protein purification.

#### 3.2.5.1 Protein Expression Tests

Small-scale expression tests were conducted to determine the optimal expression strain for different constructs. Protein was expressed overnight in 15 mL cultures as described in Section 3.2.5. Cell pellets were resuspended in 1.5 mL lysis buffer (20 mM Tris-HCl pH 7.5, 25 or 200 mM NaCl, DNase, and lysozyme). Cells were lysed using a needle-tip sonicator (2 min, 40% power). Lysates were cleared by centrifugation at 15 000 rpm in a micro centrifuge (SciSpin) at 4°C. The supernatant was loaded onto a Ni-NTA Spin Column (Qiagen) pre-equilibrated with wash buffer (20 mM Tris-HCl pH 7.5, 25 or 200 mM NaCl, 15 mM imidazole). Lysates were passed through the column twice by centrifugation at 2,000 rpm, followed by three 700 µL wash buffer rinses. Proteins were eluted with 250 µL elution buffer (20 mM Tris-HCl pH 7.5, 25 or 200 mM NaCl, 300 mM imidazole). Samples were analysed by SDS-PAGE (3.2.3).

### 3.2.6 BDLP Purification

#### 3.2.6.1 Cell Lysis

Cell pellets were resuspended in lysis buffer (Table 5), supplemented with lysozyme, DNase, and a protease inhibitor cocktail (Table 12) in multiples of 70 mL, and gently stirred for 10 minutes. Cells were lysed by sonication (75% power, 2s on/off pulse, 10 minutes total) on ice with gentle stirring. Cell lysates were cleared at 35,000 rpm for 45 minutes at 4°C in a Ti45 rotor (Beckmann) to pellet cellular debris and membranes.

#### 3.2.6.2 Affinity Chromatography

Constructs in this study contained either maltose-binding protein (MBP) or polyhistidine (His) affinity tags, allowing purification by amylose or nickel affinity chromatography, respectively. MBP has a natural affinity for amylose and is eluted using maltose, which has a higher affinity for the binding site (Duong-Ly & Gabelli, 2015). The His-tag, comprising multiple histidine residues, binds to immobilised nickel ions and is eluted using imidazole, which competes for nickel binding (Petty, 1996).

Proteins in this study were purified by nickel affinity chromatography using ÄKTA pure systems. Cleared lysates were loaded onto pre-equilibrated 5 or 10 mL HisTrap columns at 3 mL/min. Columns were washed with 20 column volumes of wash buffer (Table 5) at 4.5 mL/min. Elution was performed using a stepwise imidazole gradient. Initially, 20 column volumes of wash buffer supplemented with elution buffer to a 20 mM imidazole concentration were applied, followed by stepwise increases to 5, 10, 250, 500, and 1000 mM imidazole. Fractions were analysed by SDS-PAGE.

#### 3.2.6.3 TEV Cleavage

TEV protease (Section 3.2.2) cleaved MBP after protein concentration (Section 3.2.6.6) and imidazole removal via buffer exchange into wash buffer (Section 3.2.6.5). Approximately 100 µL purified TEV protease per 1 mL sample was incubated overnight at room temperature with gentle agitation, and SDS-PAGE analysis verified tag removal.

#### 3.2.6.4 Size Exclusion Chromatography

Before column equilibration, buffer stability tests were performed by incubating 20 µL of concentrated protein with 500 µL of test buffer at 37°C for 20 minutes in a clean cuvette, followed by visual inspection for precipitation. Size-exclusion chromatography (SEC) was used to remove affinity tags and separate protein species. The ÄKTA pure system equilibrated and ran the SEC column, chosen based on protein molecular weight and expected oligomerisation state (Table 11), with the optimal SEC buffer for protein stability. Fractions were collected and analysed by SDS-PAGE.

#### 3.2.6.5 Buffer Exchange

In cases where buffer exchange by SEC was not appropriate, buffer was exchanged using a PD10 desalting column (Cytvia) following the manufacturer's protocol.

#### 3.2.6.6 Protein Concentration

Protein was concentrated following affinity chromatography (from ~40 mL to 2.5 mL) and SEC chromatography (to ~10 mg/mL) by filtration using Amicon Ultra 15 mL Centrifugal Filters (Merck) with molecular weight cut-offs at least half the molecular weight of the protein.

#### 3.2.6.7 Concentration Determination

Protein concentration was determined by Bradford assay, which relies on the colorimetric shift of Coomassie brilliant blue G-250 upon protein binding, altering its absorbance maximum from 465 to 595 nm (Bradford, 1976). A standard curve was generated using 2 mg/mL BSA standard dilutions (Biorad), and sample protein concentration was determined by measuring absorbance at 595 nm in triplicate.

### 3.2.7 Liposome Preparation

*E. coli* total extract (ETE), DOPG, DOPC and MGDG lipids (Avanti Polar Lipids) were dissolved in chloroform at 10 mg/ml, with DOPG and DOPC mixed in an 4:1 or 3:2 molar ratio or MGDG, DOPG and DOPC mixed in a 1:3:1 molar ratio. The mixtures were dried under a nitrogen gas stream, followed by >1 h vacuum desiccation at room temperature. The resulting thin lipid films were rehydrated in reaction buffer (Table 5) at 10 mg/ml, using gentle sonication for 10 min and 5 freeze-thaw cycles, and then stored at -80°C or used immediately. Liposomes were extruded through a polycarbonate membrane (1 µm pore size) using a mini-extruder (Avanti Polar Lipids) to form large unilamellar vesicles (LUVs) and stored at 4°C for no longer than 24 h.

### 3.2.8 Tubulation Reactions

For tubulation and membrane remodelling assays, BDLP (100 µM) was incubated with 0.75 mg/mL LUVs (ETE or DOPG-DOPC mixture) and 8 mM GMPPNP or GDP in reaction buffer at 37°C for 10 min. For membrane remodelling assays, BDLP (30 µM) was incubated with 1 mg/mL LUVs (MGDG-DOPG-DOPC or DOPG-DOPC mixtures) and 2 mM GTP in reaction buffer

for 2 h at 37°C. Between reactions, samples were stored at room temperature to prevent cold-shock breaking of filaments before application to EM grids (Electron Microscopy).

### 3.2.9 Co-Sedimentation Assays

To analyse protein-lipid binding, BDLP stock samples were centrifuged at 50 000 *xg* for 15 minutes at 25°C. The supernatant of this spin, with any aggregates removed, was used for the following assay. BDLP (30 µM) was incubated with and without LUVs (2.5 mg/mL) and with and without 8 mM nucleotide for 30 minutes at 37°C in a 30 µL reaction volume. Samples were centrifuged at 98 000 *xg* for 20 minutes at 25°C. Immediately after centrifugation, supernatants were removed and added to 30 µL 4X Bolt LDS Sample Buffer. 30 µL Bolt LDS sample buffer was also added to the pellet, and allowed to dissolve the pellet for 15 min. Subsequently gentle pipetting ensured the pellet was fully dissolved in the sample buffer, before 30 µL Milli-Q was also added to the pellet samples, ensuring each pellet and supernatant sample had a final volume of 60 µL. 10 µL of each sample was analysed by SDS-PAGE.

### 3.2.10 Electron Microscopy

#### 3.2.10.1 Negative-stain Electron Microscopy

Negative stain EM (NS-EM) was used check samples during protein purification, analyse mutants, and optimise tubulation and membrane remodelling reactions and buffer conditions for subsequent cryo-EM and cryo-ET studies.

300-mesh copper grids with a 28-30 nm thick carbon coating (Agar Scientific) were plasma cleaned for 50 s at 70 % power before applying 3.5 µL of sample to the carbon side for 1 min and blotting with filter paper. The grid was washed with two 10 µL Milli-Q droplets and one 2% uranyl acetate (UA) droplet (syringe-filtered), blotting after each droplet. The grid was stained for 45 s with another 10 µL UA droplet, blotted, and air-dried for ~1 min.

Negatively stained grids were visualised with either a FEI Tecnai G2 Spirit TWIN microscope equipped with a LaB6 filament and FEI 2k eagle camera, or a Tecnai T12 TWIN microscope equipped with a LaB6 filament and TVIPS fast frame 4k XF416 camera. Typical defocus ranged from -1.5 to -2.5 µm.

#### 3.2.10.2 Cryo-Electron Microscopy

Grids were prepared by applying 3.5 µL of the sample to the carbon side of a plasma-cleaned quantifoil R2/2 holey carbon grid (Electron Microscopy Sciences) for 1 min before plunge-freezing into liquid ethane using a Vitrobot Mark IV (FEI) at 25°C and 100% humidity. Blot time and force were optimised on a per-sample basis.

Grids were screened for optimal ice thickness and sample distribution using either a Glacios TEM system equipped with a FALCON 4 detector and Selectris X energy filter or a Tecnai T12 TWIN system equipped with a TVIPS fast frame 4K XF416 detector.

For the GMPPNP dataset with ETE liposome templates, cryo-EM data were collected at 300 kV on a Titan Krios with a Gatan K3 detector (LonCEM, The Francis Crick Institute) in super-resolution mode at a pixel size of 0.425 Å. A total of 21,191 movies were recorded with a defocus range of 0.7-1.7 µm, a total electron dose of 40 e-/Å² over 40 frames, and a 1.99 s exposure.

For the GDP dataset, cryo-EM data were collected at 300 kV on a Titan Krios with a Gatan Quantum K2 Summit detector (EBIC, Diamond Light Source), in super resolution mode at a pixel size of 0.415 Å, binned to 0.83 Å within EPU. A total of 23,881 movies were recorded with a defocus range of 0.5-1.5 µm, a total electron dose of 40 e-/Å² over 40 frames, and a 1.8 s exposure.

For the GMPPNP dataset with PG liposome templates, data were collected in-house at Imperial College on a 200 kV Glacios microscope with a FALCON 4 detector in super-resolution mode at a pixel size of 0.579 Å. A total of 2,517 movies were recorded with a defocus range of 0.5-1.5 µm, a total electron dose of 40 e-/Å² over 40 frames, and an exposure of 5.2 s.

#### 3.2.10.3 Data Processing

Movies were corrected for beam-induced motion using MotionCor2 ($BDLP_{GMPPNP}$ & GDP-bound datasets) (Zheng *et al.*, 2017) or CryoSPARC ($BDLP_{GMPPNP(PG)}$ dataset) (Punjani *et al.*, 2017). The $BDLP_{GMPPNP}$ and $BDLP_{GMPPNP(PG)}$ datasets were Fourier cropped to pixel sizes of 0.85 Å and 1.16 Å, respectively. CTF estimations were done using CTFFIND-4.1 (Rohou & Grigorieff, 2015). Filaments were picked with SPHIRE-crYOLO (Wagner *et al.*, 2019), and

coordinates were imported into RELION-5 (Kimanius *et al.*, 2021; Burt *et al.*, 2024). Filaments were boxed into overlapping particles with neighbouring boxes overlapping by 64 Å ($BDLP_{GMPPNP}$), 90 Å (GDP-bound dataset), and 70 Å ($BDLP_{GMPPNP(PG)}$), corresponding to left-handed 10, 7, and 12 start helical family pitches, respectively. The 7-start helix originated from the $BDLP_{GDP}$ filament. Using RELION-5, 291 969, 141 253, and 21 466 particles were extracted with 1180, 1160, and 898 pixel box sizes for the $BDLP_{GMPPNP}$, GDP-bound, and $BDLP_{GMPPNP(PG)}$ datasets, respectively. Particles were binned by a factor of 4 and sorted through iterative 2D classification in RELION-5, CryoSPARC, and THUNDER (Hu *et al.*, 2018). Low-quality particles were discarded, and for the GDP-bound dataset, the particles were sorted into symmetry bins based on the Fourier transform of their 2D class averages.

A C1 reconstruction of the $BDLP_{GMPPNP}$ filament was generated in cisTEM (Grant, Rohou & Grigorieff, 2018) using particles assigned to the highest resolution 2D class average. Helical parameters were deduced in real space using HI3D (Sun, Gonzalez & Jiang, 2022) and confirmed by indexing helical layer lines, aided by pyHI (Zhang, 2022). Layer line indexing provided several possible helical parameters for the $BDLP_{GDP}$, $BDLP_{GDP(L2),}$ $BDLP_{GDP(L3)}$ and $BDLP_{GMPPNP(PG)}$ filaments, which were tested in CryoSPARC using helical refinement of a cylindrical starting model. Symmetries yielding reconstructions with obvious secondary structure features and lacking incorrect symmetry-related artefacts were used for refinement of cylindrical starting models RELION-5, applying C2, C3 and C6 symmetries to the $BDLP_{GMPPNP}$, $BDLP_{GDP(L3)}$ and $BDLP_{GMPPNP(PG)}$ filaments, respectively. Iterative rounds of 3D classification using these reconstructions as initial models yielded final stacks of 118 531, 50 223, 15 948, 1440 and 4016 filament segments for the $BDLP_{GMPPNP}$, $BDLP_{GDP}$, $BDLP_{GDP(L2),}$ $BDLP_{GDP(L3)}$ and $BDLP_{GMPPNP(PG)}$ filaments respectively.

Particles were re-extracted without binning and underwent iterative rounds of gold standard-FSC 3D IHRSR auto refinement, with two rounds of CTF refinement (Zivanov, Nakane & Scheres, 2020) and one round of Bayesian polishing (Zivanov, Nakane & Scheres, 2019) for the $BDLP_{GMPPNP}$, $BDLP_{GDP}$ and $BDLP_{GMPPNP(PG)}$ particle stacks. A mask covering 30% of the filament centre was used, and BLUSH regularisation was applied during the final refinement (Kimanius *et al.*, 2024). Refinements for $BDLP_{GMPPNP}$, $BDLP_{GDP}$, $BDLP_{GDP(L2),}$ $BDLP_{GDP(L3)}$ and $GMPPNP_{DOPG\text{-}DOPC}$ filaments converged on rises of 6.84, 10.13, 3.47, 20.57 and 17.79 Å and twists of 68.1, 45.6, 94.9, -37.8 and 21.5°, respectively. Final resolutions of 4.2, 4.5, 9.0, 8.7

and 7.8 Å, respectively, were determined using gold-standard Fourier shell correlations (FSC=0.143). Maps were sharpened in RELION-5, applying B-factors of -160.872, -157.102, -398.547, -558.471 and -536.946 Å², respectively. Local resolution was estimated with ResMap (Kucukelbir, Sigworth & Tagare, 2014).

Models for the central asymmetric units of $BDLP_{GMPPNP}$ and $BDLP_{GDP}$ were docked into their filament maps, and artificial densities representing these coordinates were generated in Chimera using the molmap function (Pettersen *et al.*, 2004). These densities were used to create masks in RELION-5 for particle subtraction, with new particles centred on the mask density. Subtracted particles were back-projected to create an initial model, which was 3D auto-refined in RELION-5 with BLUSH regularisation and angular and translational searches were limited to 0.5 and 2 pixels, respectively. The subtracted particle box sizes were 530 and 650 for the asymmetric units of the $BDLP_{GMPPNP}$ and $BDLP_{GDP}$, respectively. Final resolutions based on gold standard FSC were 3.5 and 5.2 Å and maps were sharpened with RELION-5 post-processing using B-factors of -89.176 and -179.994 Å². Local resolutions were estimated using ResMap.

#### *3.2.10.3.1 Model Building*

The map quality varied for $BDLP_{GMPPNP}$ and $BDLP_{GDP}$ across different domains, necessitating an iterative model-building process. The GTPase and neck domains of the $BDLP_{GMPPNP}$ dimer, with excellent side chain details, were built *de novo* using Coot and ISOLDE (Emsley et al., 2010; Croll, 2018) into the focused refinement map. For the $BDLP_{GDP}$ tetramer, ModelAngelo (Jamali *et al.*, 2024) was used to build an initial model of the trunk and MBD domains into the filament map, which were then refined using Coot and ISOLDE. H18 from the GDP-bound BDLP crystal structure (Low & Löwe, 2006) served as a template to model the $H18_{\alpha}$ and $H18_{\beta}$ helices, with adjustments made in ISOLDE to ensure sensible chemistry.

An initial complete $BDLP_{GMPPNP}$ dimer model was assembled from GTPase and neck domains built into the $BDLP_{GMPPNP}$ dimer-focused map, and trunk and MBD domains of $BDLP_{GDP}$ Dimer A built into the $BDLP_{GDP}$ filament map. H18 was modelled as a rigid body from the GDP-bound BDLP crystal structure. An initial complete $BDLP_{GDP}$ tetramer model was constructed using the trunk and MBD domains built using the $BDLP_{GDP}$ filament map, and the $BDLP_{GMPPNP}$ G-dimers and neck domains built into the $BDLP_{GMPPNP}$ dimer-focused map. The

GTPase and neck domains were refined using the focused refinement map of the $BDLP_{GDP}$ tetramer in ISOLDE.

Subsequent model-building iterations used both filament and focused refinement maps to improve the $BDLP_{GMPPNP}$ dimer and $BDLP_{GDP}$ tetramer models in Coot and ISOLDE. Regions corresponding to poor resolution map features were treated as rigid bodies. The asymmetric units were fit into filament maps, and helical parameters were applied in Chimera to create a filament model, removing protomers not in contact with the central asymmetric unit. These models were used to refine the $BDLP_{GMPPNP}$ dimer and $BDLP_{GDP}$ tetramer in the context of their helical contacts in ISOLDE and using Phenix real-space refinement (Liebschner *et al.*, 2019). Model refinement in the context of helical contacts was iterated, with the central asymmetric unit used to generate a new helical model within each iteration to build a new model of the asymmetric unit in the context of its neighbouring subunits. Subsequently, full helical models were also iteratively refined by Phenix real space refinement, again generating a new helical model based on the central asymmetric unit after each iteration. Throughout, model regions correlating with low resolution regions of the maps were treated as rigid bodies.

The $BDLP_{GMPPNP}$ dimer model was fit into the $BDLP_{GMPPNP(PG)}$ filament map and helical parameters applied in Chimera for a complete filament model, and this model was iteratively refined by Phenix real space refinement with dimers treated as rigid bodies. Construction of $BDLP_{GDP(L2)}$ and $BDLP_{GDP(L3)}$ models was done using rigid bodies of $BDLP_{GMPPNP}$ and $BDLP_{GDP}$ models as described in Section 5.2.5.1.

Throughout, disordered residues lacking supporting map density were not modelled. The final data collection and model validation statistics are presented in Table 17.

**Table 17. Data Collection and Model Refinement Statistics.**
Model refinement statistics reported for the filament assembly, $BDLP_{GMPPNP}$ = 80mer, $BDLP_{GDP}$ = 68mer, and $BDLP_{GMPPNP(PG)}$ = 144mer. Model composition is for one asymmetric unit.

| **Data collection and processing** | **$BDLP_{GMPPNP}$** | **$BDLP_{GDP}$** | **$BDLP_{GDP(L2)}$** | **$BDLP_{GDP(L3)}$** | **$BDLP_{GMPPNP(PG)}$** |
|---|---|---|---|---|---|
| Voltage (kV) | 300 | 300 | 300 | 300 | 200 |
| Electron exposure (e-/ Å$^2$) | 40 | 40 | 40 | 40 | 40 |
| Defocus range (μm) | 0.7-1.7 | 0.5-1.5 | 0.5-1.5 | 0.5-1.5 | 0.5-1.5 |
| Pixel size (Å) | 0.85 | 0.83 | 0.83 | 0.83 | 1.16 |
| Symmetry imposed | C2 and helical | C1 and helical | C1 and helical | C1 and helical | C6 and helical |
| Final # of particle images | 118 531 | 50 223 | 15 948 | 1440 | 4547 |
| Helical rise (Å) | 6.84 | 10.13 | 3.47 | 20.57 | 17.7 |
| Helical twist (°) | 68.14 | 45.6 | 94.9 | -37.8 | 21.4 |
| Filament Map resolution (Å, FSC = 0.143) | 4.2 | 4.5 | 9.0 | 8.7 | 7.8 |

| | | | | | |
|---|---|---|---|---|---|
| *Asymmetric unit focussed refinement map resolution (Å, FSC = 0.143)* | 3.4 | 5.2 | - | - | - |
| **Model Refinement** | | | | | |
| CC mask | 0.81 | 0.52 | - | - | 0.74 |
| Map sharpening B-Factor ($Å^2$) | -160.872 | -157.102 | -398.547 | -558.471 | -536.946 |
| *Focussed map sharpening B-Factor ($Å^2$)* | -89.1762 | -179.994 | - | - | - |
| **Model composition** | | | | | |
| Nonhydrogen atoms | 10368 | 21362 | - | - | 10368 |
| Protein residues | 1284 | 2662 | - | - | 1284 |
| **RMSDs** | | | | | |
| Bond lengths (Å) | 0.003 | 0.004 | - | - | 0.003 |
| Bond angles (°) | 0.457 | 0.572 | - | - | 0.457 |
| **Validation** | | | | | |
| MolProbity score | 1.69 | 2.03 | | | 1.78 |
| Clashscore | 8.25 | 14.73 | - | - | 9.99 |
| Rotamer outliers (%) | 0.01 | 0.01 | - | - | 0.01 |
| Ramachandran plot | | | | | |
| Favoured (%) | 96.39 | 95.88 | - | - | 96.39 |
| Allowed (%) | 3.61 | 4.12 | - | - | 3.61 |
| Disallowed (%) | 0 | 0 | - | - | 0 |
| B-Factors/ADP | | | | | |
| Minimum | 20.13 | 16.34 | - | - | 47.08 |
| Maximum | 400.79 | 158.79 | - | - | 342.49 |
| Mean | 168.5 | 82.79 | - | - | 162 |

### 3.2.10.4 Cryo-Electron Tomography

Vitrified samples of membrane remodelling assay samples (Section 3.2.8) were prepared by mixing the sample with 10 nm bovine serum albumin-coated gold beads (ThermoScientific), applied to quantifoil R2/2 holey carbon grid (Electron Microscopy Sciences) for 1 min before plunge-freezing into liquid ethane using a Vitrobot Mark IV (FEI) at 25°C and 100% humidity.

The in-house (Imperial College) 200 kV Glacios microscope with a FALCON 4 detector and Selectris energy filter was used to collect tilt series. Tilt series movies were collected in super-resolution mode with a pixel size of 0.95 Å/pixel and defocus of -6 to -8 μm, using a dose-symmetric scheme with a cumulative dose of 80 $e^-/Å^2$. The grid was tilted to ± 64° in 4° increments. Additionally, the 80 $e^-/Å^2$ included a pre-exposure used to screen the tomogram location for potential ordered arrays, such that each movie within the tilt series received a total dose of 2.35 $e^-/Å^2$.

Movies frames were aligned and corrected for beam-induce motion in RELION-5, during which super-resolution movies were 2x binned to a final pixel size of 1.9 Å/pixel. Tilt series were aligned using the IMOD software package (Kremer, Mastronarde & McIntosh, 1996) and the

final aligned stack was 4x binned. Final tomograms were reconstructed with a SIRT filter using Tomo3D (Agulleiro & Fernandez, 2011). Additionally, to aid interpretation, tomograms were denoised using Topaz (Bepler *et al.*, 2020).

# Chapter 4: GMPPNP-Bound BDLP Filament Structure

## 4.1 Introduction

Membrane remodelling is a fundamental process in cellular life, essential for various functions including cell division, endocytosis, and organelle maintenance (Jimah *et al.*, 2024; Schlimpert *et al.*, 2017; Gao & Hu, 2021). These events involve the deformation of planar bilayers to induce curvature, which can be mediated by lipid composition and leaflet asymmetry or by curvature-inducing proteins (Harayama & Riezman, 2018; Sezgin *et al.*, 2017; Bohuszewicz, Liu & Low, 2016).

An understudied aspect of membrane dynamics is lipid polymorphism, where lipids can adopt non-bilayer phases under certain conditions. Non-bilayer phases such as the inverted hexagonal (HexII) phase, have been implicated in membrane fusion or fission intermediates and stress responses (Marrink & Mark, 2004; Fan *et al.*, 2016; Kirchhoff *et al.*, 2007; Garab *et al.*, 2022). In energy-transducing membranes such as thylakoids, the capacity for lipids to transition between lamellar (Lm) and HexII phases is thought to be involved in regulating photosynthetic activity and responding to environmental stresses (Garab *et al.*, 2022). However, whether membrane remodelling proteins are involved in inducing these phase changes remains largely unknown.

Among the protein machinery involved in membrane remodelling, the DSF stands out as a group of large GTPases found across all domains of life (Jimah & Hinshaw, 2019). Members of the DSF share several conserved characteristics, including the ability to bind and hydrolyse GTP, self-assemble into oligomers and filaments, and interact with membranes. They typically possess a large GTPase domain, a neck domain, and a trunk domain, with variable membrane-interacting motifs (Ford & Chappie, 2019). While eukaryotic dynamins and dynamin-related proteins (DRPs) often have well-defined roles in membrane fission or fusion, bacterial DRPs exhibit more diverse and less understood functions (Bohuszewicz, Liu & Low, 2016). The biological roles of any cyanobacterial DRPs have not been identified. This functional diversity coupled with the homology of bacterial and eukaryotic DRPs presents an

opportunity to elucidate the most fundamental principles of DSF-mediated membrane remodelling. Notably, the DSF member Drp1 that constricts membranes has been shown to induce transient lipid phase changes *in vitro* (Stepanyants *et al.*, 2015), but the involvement of DRPs in mediating stable lipid phase transitions as well as or instead of fission or fusion has not been identified.

Bacterial dynamin-like protein (BDLP) from the cyanobacterium *Nostoc punctiforme* serves as a valuable model for investigating cyanobacterial DRP function. *N. punctiforme* exhibits a complex life cycle with multiple developmental stages, including the formation of motile hormogonia, nitrogen-fixing heterocysts, and spore-like akinetes (Risser, 2023). These morphological changes necessitate significant membrane remodelling events, but the involvement of DRPs in these processes is not well understood. BDLP shares structural homology with mitofusins but has not been shown to mediate membrane fusion (Low & Löwe, 2006). Previous studies have demonstrated BDLP's ability to self-assemble into filaments and constrict liposomes in the presence of a non-hydrolysable GTP analogue (Low *et al.*, 2009). However, the high-resolution filament ultrastructure of the GMPPNP-bound BDLP filament and its membrane interface remains unresolved. Moreover, the *in vivo* function of BDLP in *N. punctiforme*, particularly during its various life cycle stages, is unknown.

This chapter investigates the expression and localisation of BDLP in *N. punctiforme*, with a focus on its role during hormogonium development. Additionally, it presents a high-resolution cryo-EM structure of the GMPPNP-bound BDLP filament, providing insights into its helical ultrastructure, nucleotide coordination and catalytic mechanism, and membrane binding mechanism. These findings aim to enhance understanding of cyanobacterial DRP function, the fundamental mechanisms of DSF-mediated membrane remodelling, and the potential roles of DRPs in cyanobacterial development and thylakoid membrane dynamics.

## 4.2 Results and Analysis

### *4.2.1* BDLP Expression is Upregulated During Development of *N. Punctiforme* Motile Hormogonia

To investigate the *in vivo* function of BDLP in *N. punctiforme*, Douglas Risser generated a strain lacking BDLP (gene name: Npun_R6513). Furthermore, as the BDLP gene is situated adjacent to the BDLP2 gene (Npun_R6512) in the *N. punctiforme* genome (Bohuszewicz, Liu & Low,

2016), a strain lacking BDLP2 was also generated. This demonstrated that both genes were non-essential, and their deletion did not result in any observable colony, motility, or cell morphological phenotypes.

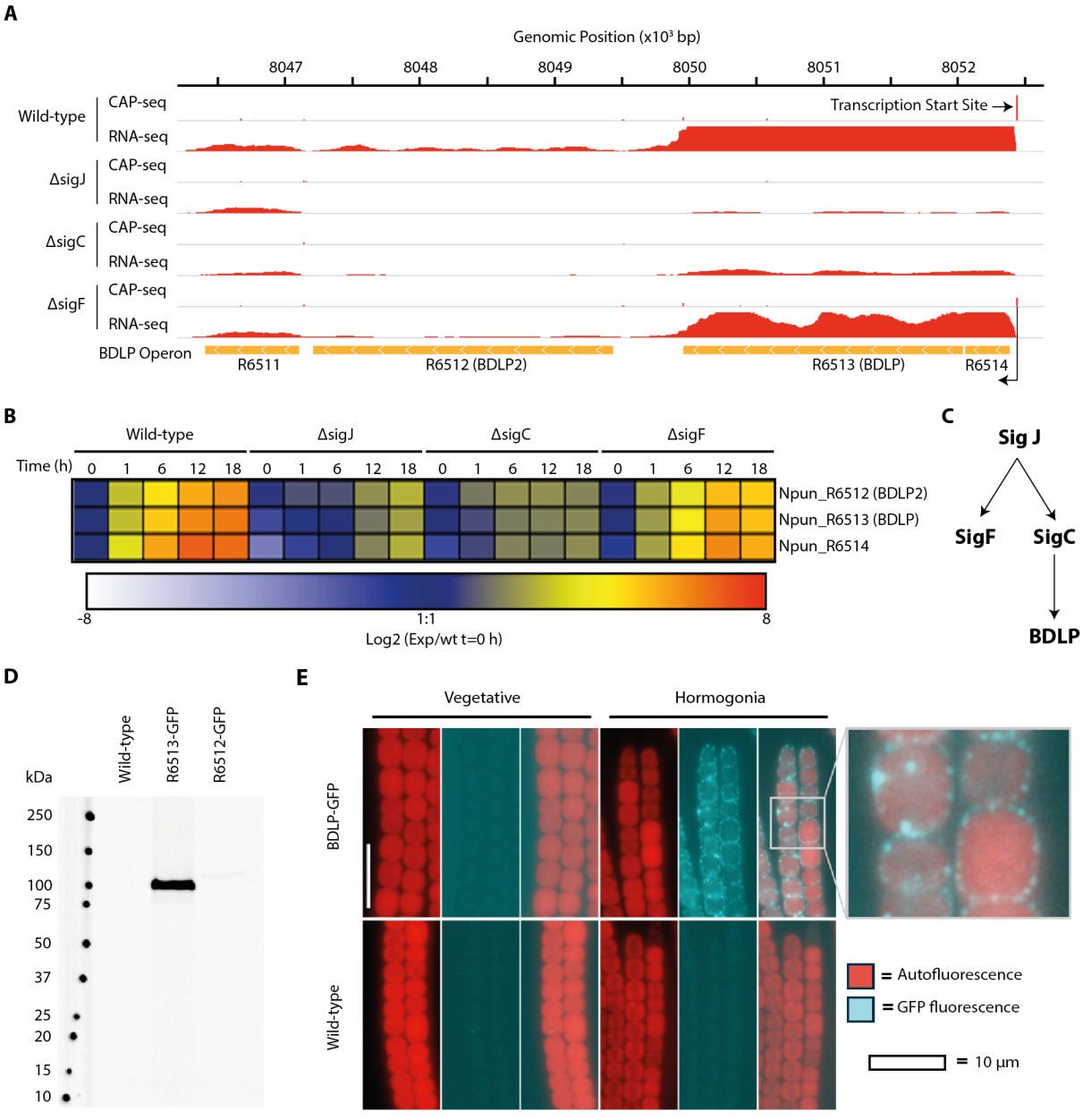


**Figure 26. BDLP Expression and Localisation in *N. punctiforme*.**
BDLP expression was specifically upregulated in hormogonia. **A,** RNA-seq based transcriptomic analysis of gene expression during hormogonium development in wild-type cells and strains carrying hormogonium-specific sigma factor deletions (ΔsigJ, ΔsigC, ΔsigF) indicated BDLP expression is under the control of hormogonium-specific sigma factors. Readmap coverage (red) indicates the relative transcription of each genomic position. Transcription start site (TSS) was derived from cappable-seq (CAP-seq) data. Orange bars show the genomic positions of genes within the BDLP operon. All data derived from (Gonzalez *et al.*, 2019). **B,** Heat map representation of RNA-seq transcriptomic data in

panel A, as a function of time following hormogonium induction. **C,** Schematic diagram depicting the regulatory cascade of hormogonium-specific sigma factors controlling the BDLP locus gene expression. **D,** Western blot analysis of wild-type hormogonia and hormogonia expressing GFP-tagged BDLP or BDLP2, using anti-GFP antibodies**.** Only BDLP-GFP was well-expressed. Expected molecular weights of BDLP-GFP and BDLP2-GFP are ~105 and 110 kDa, respectively. **E,** Fluorescence microscopy of vegetative and hormogonium filaments, showing channels of autofluorescence (red), GFP fluorescence (blue), and a merge. Zoom panel indicates the localisation of BDLP-GFP into punctate foci at the cytoplasmic or thylakoid membranes in hormogonia. *All novel data and analyses in this figure were collected and performed by Douglas Risser.*

To elucidate whether BDLP or BDLP2 instead possess roles in specific *N. punctiforme* life cycle stages, Douglas Risser analysed RNA-seq transcriptomic data recorded during hormogonium development (Gonzalez *et al.*, 2019) to determine the involvement of BDLP or BDLP2 in hormogonium development. The analysis revealed that BDLP expression increased over an 18 hour period during hormogonium development (Figure 26A & Figure 26B). Furthermore, BDLP expression was significantly higher than BDLP2 expression over the 18 hours. This observation suggested a hormogonium-specific function of BDLP. To elucidate the BDLP operon architecture and regulation, cappable-seq (CAP-seq) data (Gonzalez *et al.*, 2019) were analysed to identify transcription start sites (TSSs) that mediate expression of BDLP and BDLP2. This analysis revealed a single TSS upstream of BDLP, responsible for transcription initiation of a four-gene operon (Figure 26A). Within this operon, the BDLP gene was positioned downstream of a 108 amino acid protein encoding sequence (Npun_R6514), and upstream of BDLP2 and Npun_R6511. RNA-seq data from *N. punctiforme* strains carrying deletions of hormogonium-specific sigma factors (SigJ, SigC, and SigF) indicated that operon expression was regulated by SigJ and consequently SigC signalling (Figure 26A, Figure 26B & Figure 26C), further supporting the observation that BDLP expression was specifically upregulated during hormogonium development.

To further investigate the hormogonium-specific upregulation of BDLP, Douglas Risser generated strains expressing BDLP and BDLP2 tagged with GFP at their C-termini under native promoter control, and synchronised differentiation into hormogonia was induced by removal of sucrose from the growth medium (Khamar *et al.*, 2010). Western blot analysis of these strains demonstrated significant BDLP-GFP expression, yet low BDLP2-GFP expression (Figure 26D), consistent with the RNA-seq data. Fluorescence microscopy of vegetative and hormogonium cells revealed that BDLP-GFP formed punctate foci exclusively in hormogonia,

localised at the cell periphery (Figure 26E). Given the proximity of thylakoid and cytoplasmic membranes in cyanobacteria (Rast *et al.*, 2019), this observation suggested that BDLP-GFP was associated with either or both membranes in motile hormogonia. In summary, both transcriptomic and fluorescence microscopy data indicated that BDLP is specifically expressed in motile hormogonia of *N. punctiforme*.

### 4.2.2 HexII Phase Lipids were observed in Hormogonia Over-expressing BDLP-GFP

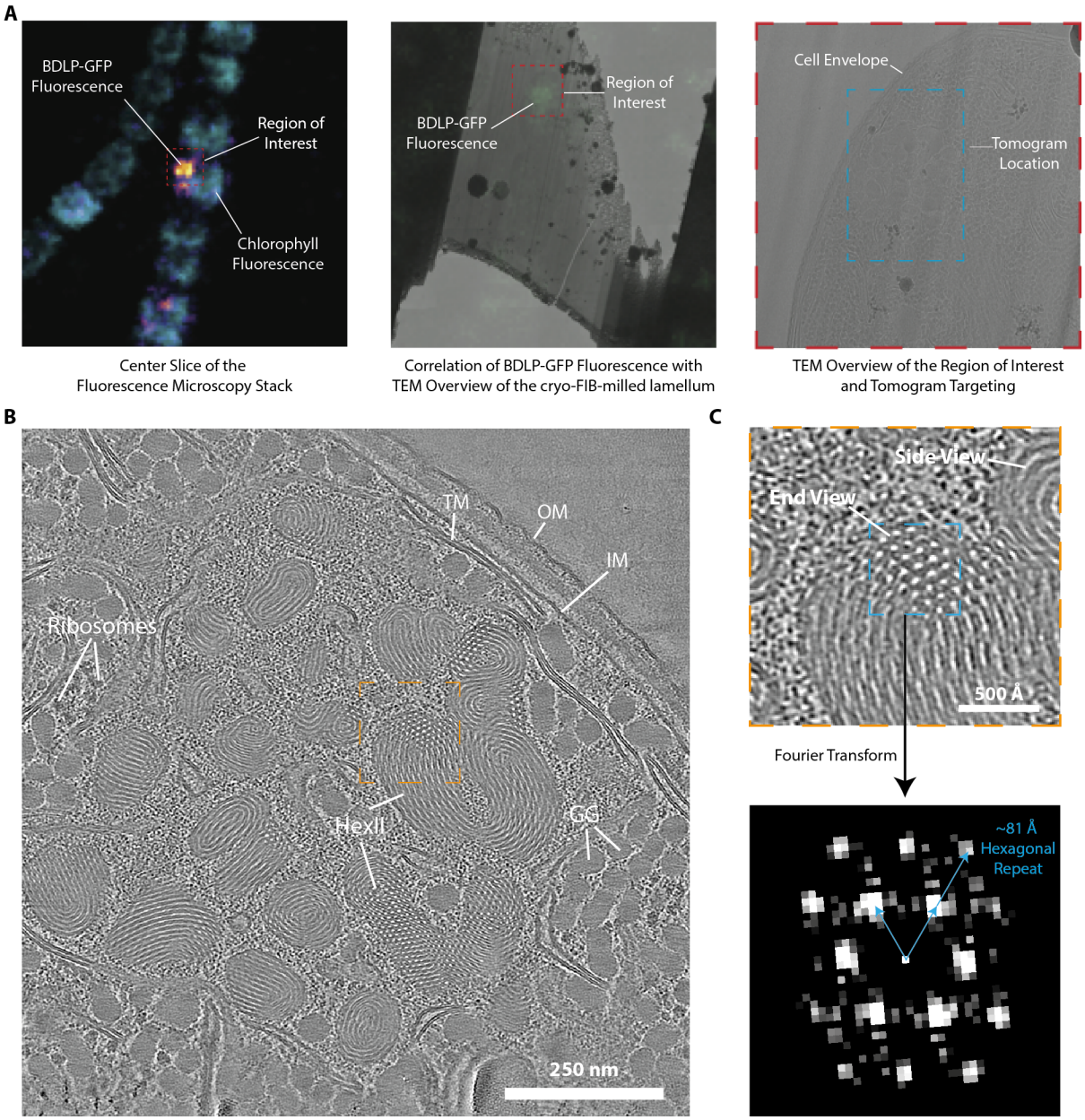


**Figure 27. Cryo-FIB-CLEM of hexII Nanoparticles in Hormogonia of a *N. punctiforme* BDLP-GFP Overexpression Strain.**
A cryo-CLEM pipeline targeting regions of bright BDLP-GFP fluorescence revealed large hexII phase lipid structures in hormogonia overexpressing BDLP-GFP. **A,** Representative example of the BDLP-GFP tomogram targeting procedure. Red box = the region of interest, blue box = tomogram location.

Left: fluorescence microscopy indicating anticorrelation of BDLP-GFP fluorescence and intrinsic chlorophyll fluorescence, used to target FIB-milling at the region of interest containing BDLP-GFP fluorescence. Middle: Low magnification cryo-EM micrograph of the FIB-milled lamella correlated with BDLP-GFP fluorescence which was bright and disperse across the region of interest. Right: Overview cryo-EM micrograph used to target the tomogram acquisition within the region of interest. Note that bright and disperse BDLP-GFP fluorescence is correlated with the tomogram location. **B,** Slice through a representative tomogram. OM = outer membrane, IM = inner / cytoplasmic membrane, TM = thylakoid membrane, HexII = hexII nanoparticle, GG = glycogen granule. **C,** Zoom image focussing on the region indicated by the orange box in panel B (top), indicating side and end-on views of the hexII nanoparticle. 2D Fourier transform (bottom) of the end-on view region highlighted by the blue box above. The Fourier space lattice is characteristic of a hexagonal lattice resulting from the hexII phase nanoparticles. *The BDLP GFP overexpression strain was generated by Douglas Risser and the samples were prepared and tomograms were acquired and reconstructed by Annemarie Perez Borema, Wojciech Wietrzynski, Ricardo Righetto and Ben Engel.*

To investigate whether BDLP-GFP puncta were associated with cytoplasmic or thylakoid membranes, a Douglas Risser generated a BDLP-GFP overexpression strain, and the strain was analysed by collaborators in the Engel group using cryogenic-focused ion beam milling and correlative light-electron microscopy (cryo-FIB-CLEM). Cells were induced to differentiate into motile hormogonia by removal of sucrose from the growth medium (Khamar *et al.*, 2010), and subsequently vitrified by plunge-freezing. The sample was thinned by cryo-FIB milling (Schaffer *et al.*, 2017), targeting regions of intense fluorescence using cryo-CLEM (Tuijtel *et al.*, 2019) to generate thin lamellae containing punctate-localisation of BDLP-GFP (Figure 27A). The thin lamellae were visualised by cryo-ET, and a total of five tomograms were collected and denoised using either cryo-CARE (Buchholz *et al.*, 2019) or DeepDeWedge (Wiedemann & Heckel, 2023) to enhance contrast and interpretability.

Within all the tomograms, the outer, cytoplasmic, and thylakoid membranes, as well as ribosomes and glycogen granules, were clearly resolved with high contrast (Figure 27B). Notably, several densely packed tubular lipid structures distributed within the cytoplasm were observed in each tomogram, reminiscent of hexII phase lipid tubes observed by cryo-EM of thylakoid membranes under low-light stress (Kirchhoff *et al.*, 2007) and hexII phase lipid nanoparticles observed by cryo-ET (Pattipeiluhu *et al.*, 2024). Moreover, no distortions of the cytoplasmic membranes were observed, and the densely packed lipid structures were frequently localised distal from the cytoplasmic membrane and associated with thylakoid membranes, indicating these structures were derived from the thylakoids. The fluorescence microscopy stacks also demonstrated that BDLP-GFP fluorescence and intrinsic chlorophyll fluorescence were anticorrelated; the BDLP-GFP fluorescence was intense and dispersed

across the entirety of the selected tomogram locations, without chlorophyll fluorescence (Figure 27A). Collectively, this suggested the thylakoids and thylakoid-derived densely packed tubular lipid structures did not contain photosynthetic machinery, consistent with the drastically reduced photosynthetic activity of hormogonia (Risser, 2023) and the densely packed arrangements of lipids that would be unable to accommodate large protein complexes due to steric hindrance. Furthermore, ribosomes and glycogen granules were excluded from the cytoplasmic regions containing the densely packed lipid structures. This, in conjunction with the dispersed and intense BDLP-GFP fluorescence, suggested BDLP-GFP and the tubular lipid structures were associated in distinct partitioned zones within the cytoplasm. This phenomenon could be attributed to liquid-liquid phase separation (LLPS) of BDLP-GFP in association with the tubular lipid structures, as LLPS of dynamin associated with membrane has previously been observed (Imoto *et al.*, 2022). In summary, cryo-FIB-CLEM revealed BDLP-GFP was associated with cytoplasmic densely packed tubular lipid structures derived from the thylakoids in hormogonia. To our knowledge, such extensive tubular lipid structures and drastic remodelling of thylakoids have not been observed thus far, suggesting BDLP-GFP overexpression may have played a significant role.

The elongated and spiral structures in the side views of the tubular lipid structures exhibited a remarkable visual similarity to the side views of hexII phase lipids previously observed by cryo-ET (Pattipeiluhu *et al.*, 2024). Due to the random orientations of the tubular lipid structures within the tomograms, end-on views were also observed (Figure 27B & Figure 27C). These views revealed bright white puncta in a hexagonal arrangement, which are attributed to the water channels found within the hexII phase lipid arrangement (Pattipeiluhu *et al.*, 2024). To confirm the hexII phase arrangement of the tubular lipid structures, I computed 2D Fourier transforms of 15 end-on views (Figure 27C). The Fourier transforms displayed a patterning characteristic of a hexagonal lattice (Dal Negro & Boriskina, 2012). An average of 90 measurements of the hexagonal repeat in Fourier space indicated a hexagonal spacing of 81 ± 1.8 Å (standard deviation) for the tubular lipid structures. This is consistent with simulations of hexII phase lipids that describe a 45-72 Å hexagonal spacing of PE in solution, dependent on acyl-chain length and hydration (Marrink & Mark, 2004), and a 87-97 Å hexagonal spacing of MGDG (Bratek *et al.*, 2019). In conclusion, Fourier space analysis was

suggestive of the lipid tubular structures being hexII phase structures, which are henceforth referred to as hexII nanoparticles.

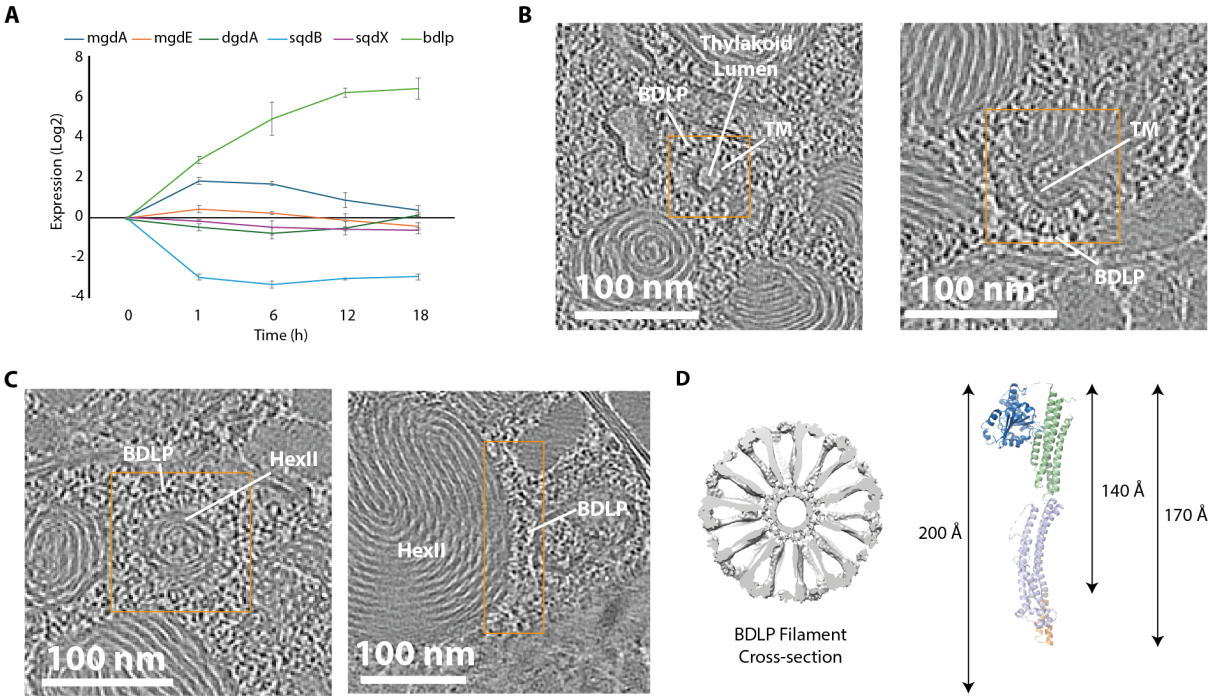


**Figure 28. BDLP Association with hexII Nanoparticles.**
BDLP-like structures were observed bound to hexII nanoparticles and thylakoid membranes. **A,** Transcription of genes encoding BDLP and lipid synthesis machinery as a function of time following induction of differentiation into hormogonia, indicating hexII phase-favouring lipid synthesis is increased in hormogonia, whilst Lm phase-favouring lipid synthesis is decreased. RNA-seq data derived from (Gonzalez et al., 2019). Error bars represent one standard deviation of data recorded in triplicate. *mgdA* and *mgdE* are genes required for the synthesis of MGDG, a hexII phase-favouring lipid. *dgdA* is a gene required for DGDG synthesis and *sqdB* / *sqdX* are genes required for SQDG synthesis, which are both Lm phase-favouring lipids. Following hormogonium induction, BDLP and hexII lipid synthesis genes have increased transcription, whereas Lm lipid synthesis genes have decreased transcription. **B**, Tomogram slices showing BDLP-like decorations thylakoid membranes, highlighted by orange boxes. TM = thylakoid membrane. **C**, Tomogram slices showing BDLP-like decorations on hexII nanoparticles, highlighted by orange boxes. **D**, Cross-section of the membrane constricting GMPPNP-bound BDLP filament map (Low *et al.*, 2009) and a BDLP monomer in an open conformation (PDB: 2W6D). The semi-ordered decoration of membranes in panels B and C is reminiscent of the BDLP filament cross-section, with BDLP in an open conformation. The BDLP monomer measures 170 Å in length, and the filament surface is 140 Å from the start of the predicted paddle. *RNA-seq data were analysed by Douglas Risser, Tomograms were collected, reconstructed and denoised by Annemarie Perez Borema, Wojciech Wietrzynski, Ricardo Righetto and Ben Engel.*

To ascertain whether the hexII nanoparticles are functionally relevant in hormogonia or were an artefact of BDLP-GFP overexpression, Douglas Risser analysed RNA-seq transcriptomic data (Gonzalez *et al.,* 2019) describing transcription of the BDLP gene and genes associated

with lipid synthesis. This analysis revealed that in the hours following hormogonium induction, genes required to synthesise monogalactosyldiacylglycerol (MGDG) were upregulated in motile hormogonia alongside the BDLP gene, while genes required to synthesise digalactosyldiacylglycerol (DGDG) and sulfoquinovosyldiacylglycerol (SQDG) were downregulated (Figure 28A). These findings suggest the existence of an unknown gene-regulatory mechanism in hormogonia that promotes the remodelling of thylakoids into hexII nanoparticles, as hexII-favouring lipid (MGDG) synthesis is upregulated, and Lm-favouring lipid (DGDG and SQDG) synthesis is downregulated. Increasing the already high MGDG content of the thylakoid membranes (Mikhaylenko, Skorokhod & Kholodny, 1998) would favour a Lm-hexII phase transition (Dlouhý *et al.*, 2021b). As BDLP-GFP fluorescence was correlated with the hexII nanoparticles and BDLP expression was also upregulated in hormogonia, these data further suggested that BDLP may play an active role in the remodelling of thylakoids alongside changes in lipid synthesis during hormogonium development.

To further investigate the role of BDLP in thylakoid remodelling into hexII nanoparticles, I examined the denoised tomograms for evidence of BDLP-GFP self-assembly. Strikingly, I observed BDLP decoration of apparently tubulated thylakoid membranes (Figure 28B) and hexII nanoparticles (Figure 28C). The putative BDLP decorations exhibited semi-ordered arrays reminiscent of the GBP1 coatomer (Weismehl *et al.*, 2024) and the helical arrangement of BDLP assembled on constricted membrane tubes (Figure 28D) (Low *et al.*, 2009); the decorations were suggestive of BDLP adopting an extended conformation on the TMs and hexII nanoparticle surfaces with a semi-ordered lattice of GTPase domains distal to, and connected by radial spokes to, the membrane. To confirm the extended conformation of BDLP, the putative BDLP assemblies within the tomograms were measured. Approximate measurements of the distance from the TM or hexII nanoparticle surfaces to the exterior of the putative BDLP decorations ranged from 165 to 220 Å. This was consistent with the dimensions of BDLP in an extended open conformation, with a paddle-tip to GTPase domain exterior distance of 170 Å (Figure 28D). However, the distance between the GTPase-proximal end of the predicted hydrophobic paddle to the GTPase domain exterior is only 140 Å. As the paddle is expected to be at least partially inserted into the bilayer, and measurements of the putative BDLP decorations reached up to 220 Å, this suggested BDLP may adopt an, as-yet

unknown, more extended conformation when polymerised on membranes. This observation is consistent with findings that the crystal structure of the BDLP paddle did not fit well into the medium-resolution cryo-EM map of the BDLP helical filament and additional density adjacent to the bilayer was unaccounted for (Low *et al.*, 2009). In summary, cryo-ET revealed hexII nanoparticles correlated with regions of hormogonia demonstrating strong BDLP-GFP fluorescence. In addition, thylakoids and hexII nanoparticles were decorated by open conformation BDLP-like structures. Whether BDLP is involved in active remodelling of the thylakoids into hexII nanoparticles was not demonstrated, and questions arose regarding the conformation BDLP adopts to interface with lipids.

### 4.2.3 Cryo-EM Structure of GMPPNP-bound BDLP Reveals a Novel Membrane Binding Domain

Previously, a cryo-EM map of BDLP protein-lipid tubes at 11 Å resolution enabled a molecular model of the filament to be generated by rigid body fitting of the GTPase, neck and trunk domains derived from the GDP-bound crystal structure (Low *et al.*, 2009). Whilst this showed the large-scale conformational changes BDLP undergoes, mediated by hinges 1 and 2, to transition from an off-membrane to membrane-bound assembly state, it did not support *de novo* model building of the GMPPNP-bound structure so that high-resolution filament ultrastructure and the critical mechanism of membrane binding remain unknown. To address this, BDLP was purified and the structure of the GMPPNP-bound helical filament was determined by cryo-EM, as detailed in the following sections.

#### 4.2.3.1 BDLP Purification and Filament Optimisation

In order to produce a sample of BDLP for reconstitution of BDLP helical filaments on liposome templates, a I expressed a BDLP construct, with an N-terminal MBP tag and C-terminal 6x-histidine tag, in *E. coli* and purified BDLP by nickel-affinity chromatography. This construct eluted from the nickel-affinity column at relatively low imidazole concentrations between 20 and 50 mM. To enhance sample homogeneity, a construct with an additional four histidine residues appended onto the histidine tag was cloned, to generate a construct with greater affinity for the nickel resin. The new construct eluted from the column in the presence of 250 mM imidazole, and consequently contaminants that non-specifically bound the nickel resin and eluted in the presence of 50 mM imidazole were no longer present in the BDLP sample,

which exhibited high purity. The MBP-tag was cleaved from BDLP by TEV protease digestion. To obtain a homogeneous BDLP sample and separate BDLP from MBP and the TEV proteases, BDLP was further purified by size-exclusion chromatography (SEC). Initially, an s200 Sephacryl column was utilised for SEC as it was able to optimally separate BDLP (~78 kDa) from MBP and TEV protease (~ 43 and 27 kDa, respectively) (Figure 29A). However, this also resulted in significant contamination of the BDLP elution with the void volume elution, which adversely affected the quality of the filaments produced downstream. Therefore, an s300 Sephacryl column was employed based on its capacity to separate higher molecular weight proteins and complexes. SEC using this column improved the separation between the void volume and BDLP and maintained separation between BDLP and MBP elution. Overall, the expression and purification of this construct yielded a high-purity and high-concentration (10 mg/mL) sample of BDLP which gel-filtrated as a single species (Figure 29B).

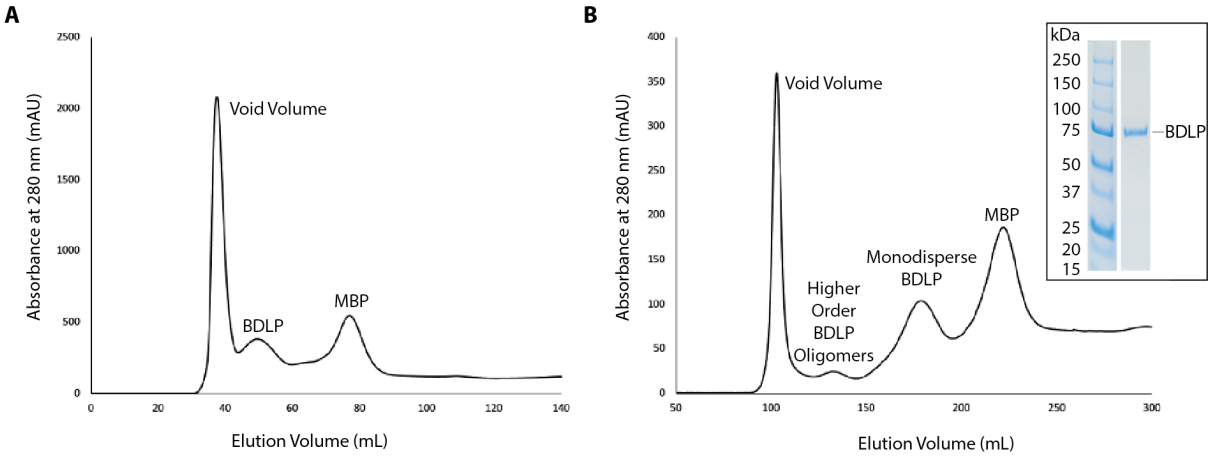


**Figure 29. Size Exclusion Chromatography of BDLP.**
Chromatograms of the BDLP, MBP and TEV sample separated over a s200 16/60 Sephacryl column (**A)** or s300 26/60 Sephacryl column (**B**). **B,** Inset is an SDS-PA gel of a 1 μL concentrated sample of BDLP obtained from the indicated monodisperse BDLP peak, stained with Coomassie.

To generate a sample of BDLP helical filaments for analysis by cryo-EM, the BDLP sample was incubated with the non-hydrolysable GTP analogue GMPPNP and *E. coli* total extract (ETE) liposomes at 37 °C. NS-EM analysis of this sample revealed that BDLP self-assembled into helical filaments of ~500 Å diameter that constricted the underlying liposomes (Figure 30), consistent with previous *in vitro* reconstitutions of the BDLP filament (Low *et al.*, 2009).

However, numerous large aggregations of filaments and liposomes, untubulated liposomes and short or highly curved filaments were observed. Successful and efficient high-resolution cryo-EM reconstructions necessitate linear and dispersed filaments with good long-range order. To enhance the sample quality for subsequent cryo-EM imaging, the conditions of filament self-assembly were optimised (Figure 30). Filaments were obtained using varying ratios of liposome and BDLP, as well as varying GMPPNP concentrations, liposome size, temperatures, and incubation times to identify conditions that produced an optimal sample of BDLP filaments. Generally, an excess of BDLP and nucleotide yielded the most favourable results. The final sample of filaments was self-assembled on 0.75 mg/mL 1 μm ETE liposomes, utilising 100 μM BDLP in the presence of 8 mM GMPPNP at 37 °C for 15 minutes.

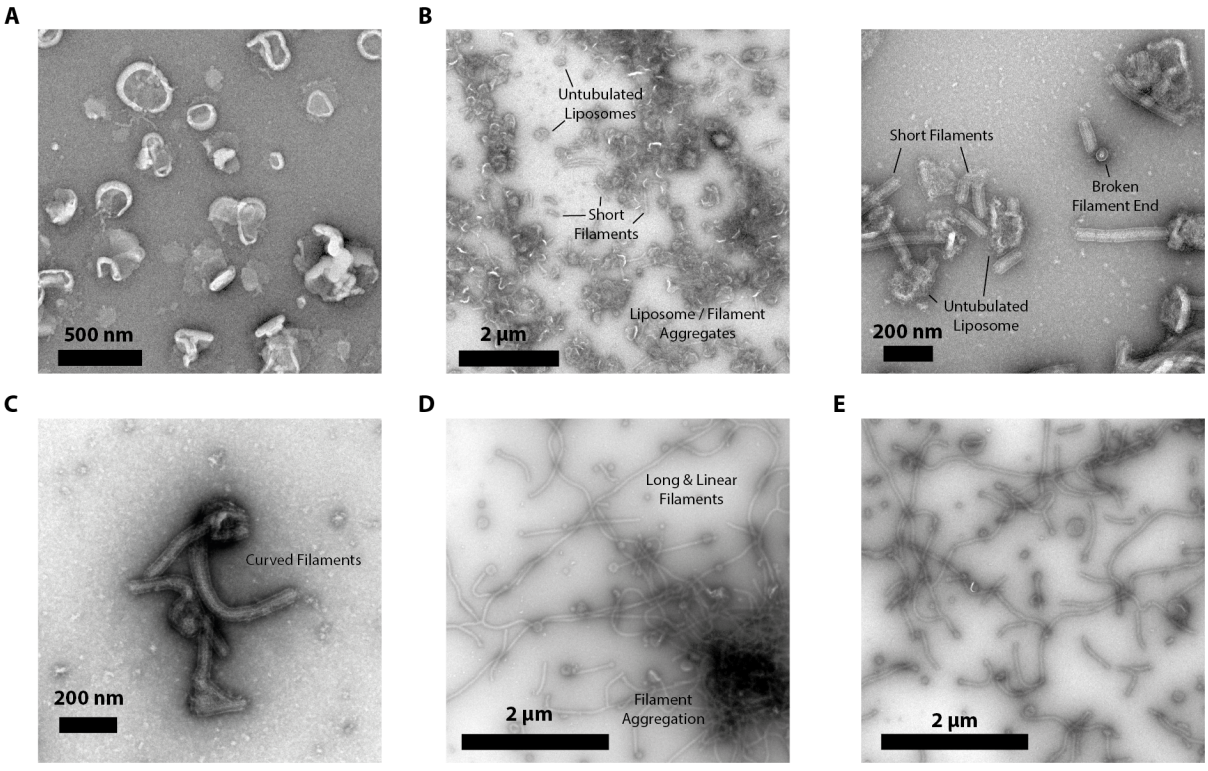


**Figure 30. Optimisation of GMPPNP-bound BDLP Protein-Lipid Filaments for Cryo-EM.**
NS-EM micrographs of self-assembly of BDLP filaments formed under different conditions **A,** ETE liposomes in the absence of BDLP. **B,** Low BDLP-lipid ratio (2 mg/mL liposome, 30 μM BDLP) with 2 mM GMPPNP **C,** Increased BDLP-lipid ratio (1 mg/mL liposome, 50 μM BDLP) with 2 mM GMPPNP. **D,** High BDLP-lipid ratio (1 mg/mL liposome, 75 μM BDLP) with 8 mM GMPPNP. **E,** High BDLP-lipid ratio (0.75 mg/mL liposome, 100 μM BDLP) with 8 mM GMPPNP. Note the linear, disperse filaments optimal for cryo-EM.

#### 4.2.3.2 Helical Parameter Identification of the GMPPNP-bound BDLP Protein-lipid FIlament

To elucidate the high-resolution ultrastructure of the GMPPNP-bound BDLP protein-lipid filament, the filament samples were vitrified by plunge freezing and visualised by cryo-EM (Figure 31A). Two-dimensional class averages and their Fourier transforms indicated the presence of a homogenous filament species in the sample, sharing a single helical lattice. Utilising the helical rise and twist previously reported (3.17 Å and 63.53°) (Low *et al.*, 2009) for iterative helical real space reconstruction (IHRSR), the cryo-EM map refined to an overall resolution of 7.2 Å (FSC=0.143). This resolution was insufficient for constructing an atomic model to elucidate the membrane interface and helical ultrastructure. Consequently, to ascertain whether incorrect helical parameters were limiting the achievable resolution (Gambelli, Isupov & Daum, 2022), the filament was indexed *de novo*. Initially, a cylindrical starting model was refined without symmetry imposition to produce a low-resolution map of the filament that remained true to the helical lattice present in the data. Although the model was anisotropic, as expected given that helical symmetry was not imposed, the lattice of GTPase domains was clearly resolved, enabling the determination of the helical rise and twist using HI3D (Figure 31B) (Sun, Gonzalez & Jiang, 2022). This analysis suggested that the map possessed C2 symmetry, and the helical family that contacted all lattice points, thus describing the complete helical symmetry of the filament, was a two-start helix with a rise and twist of 6.82 Å and 68.1°, respectively.

To corroborate this finding, the helical lattice was also indexed in Fourier space, utilising the summed Fourier transforms of helical segments aligned by 2D classification (Figure 31C). Given the ambiguity in assigning Bessel orders in Fourier space, multiple possible helical parameters were derived and used to refine a cylindrical starting model. The helical parameters that refined the cylinder to a reasonable map with clear secondary structural detail were in agreement with the two-start helical family identified by real-space indexing (Figure 31D).

Utilising the newly-assigned helical parameters, the BDLP filament was refined by the IHRSR gold-standard FSC approach (He & Scheres, 2017), with BLUSH regularisation (Kimanius *et al.*, 2024), to an overall resolution of 4.3 Å with a final rise and twist of 6.84 Å and 68.1°, respectively (Figure 32A). The outer diameter of the filament measured 488 Å, while the

lumen diameter was 60 Å. Local resolution estimates indicated high resolution and order in the outer regions of the map where the GTPase domains were situated, and lower resolution and flexibility towards the inner regions of the map where the membrane interface was located (Figure 32B). These findings suggested that BDLP formed filaments with strong lateral GTPase domain contacts and weaker lateral contacts at the membrane interface when GMPPNP-bound.

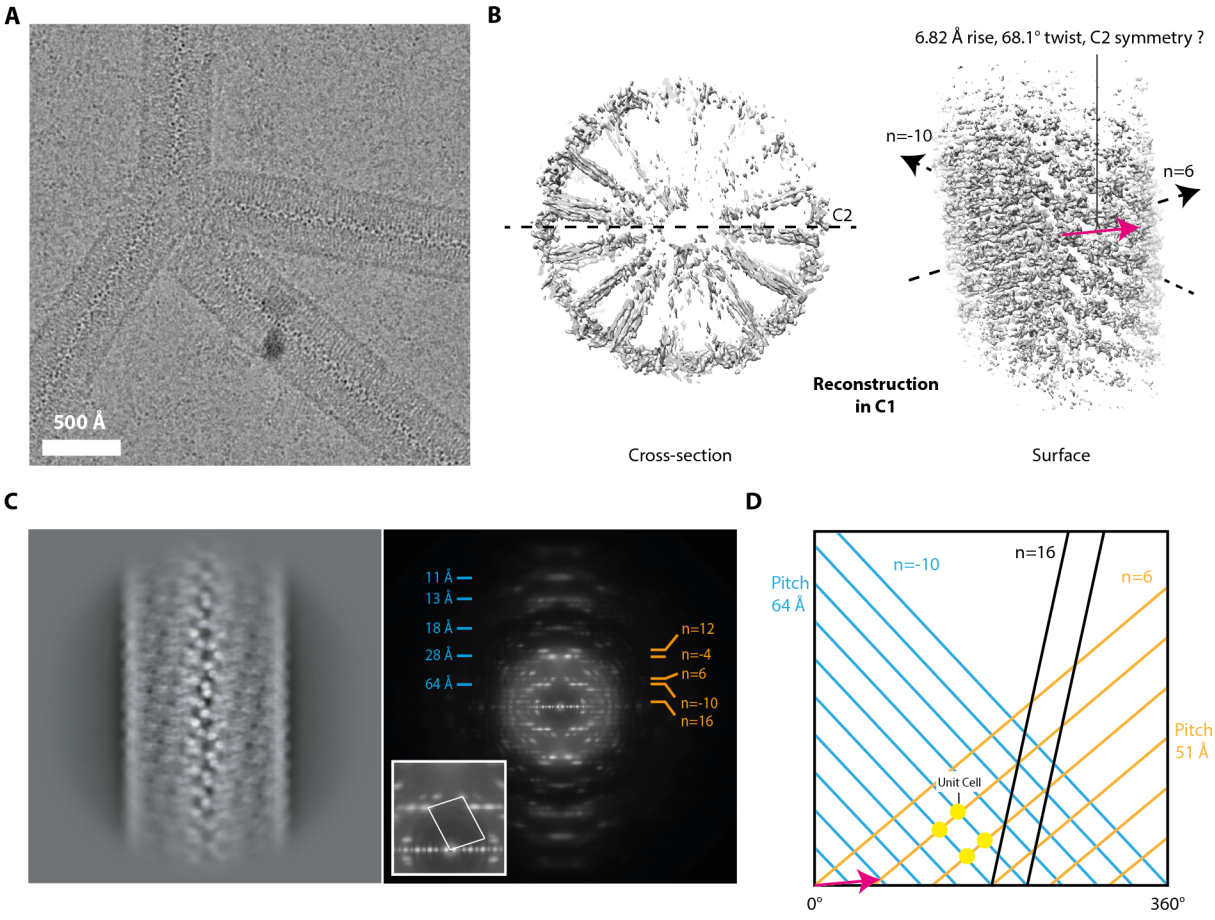


**Figure 31. GMPPNP-bound BDLP Filament Bessel Order Assignment.**
**A**, Representative cryo-EM micrograph of GMPPNP-bound BDLP protein-lipid filaments formed on ETE liposomes. **B,** Refinement of the filament without symmetry imposition. The map suggested C2 symmetry and a unit cell comprising helical families with Bessel orders of -10 and 6. Pink arrow indicates helical rise and twist suggested by HI3D (Sun, Gonzalez & Jiang, 2022), which represents the n=2 helical family. **C,** 2D filament class average (left) and averaged Fourier transform of helical segments assigned to that class (right). Bessel orders of key layer lines are shown. Inset shows drawing of a unit cell in Fourier space. **D,** Helical assembly drawn as 2D lattice with arrangement of key Bessel orders. Pink arrow represents one rise and twist of the n=2 helical family.

#### 4.2.3.3 Overall $BDLP_{GMPPNP}$ Architecture

The minimal assembly unit of the filament (asymmetric unit) comprised a dimer with each subunit related by C2 symmetry, and focused refinement of the asymmetric unit enhanced the map resolution to 3.5 Å (Figure 32C & Figure 32D). This facilitated the construction of a complete dimer model, with the exception of residues 1-5 and 498-543, which were disordered (Figure 32E, Figure 32F & Figure 32G). For comprehensive details on model construction, please refer to Section 3.2.10.3.1. The dimer was subsequently fitted into the helical filament map, and helical parameters were applied to generate a filament model, designated $BDLP_{GMPPNP}$ (Figure 32H).

Within each asymmetric unit of $BDLP_{GMPPNP}$, GTPase domains formed classical G-dimers with nucleotide sandwiched within the interface (Figure 33A), exhibiting structural similarity to the Mfn1 GTP-bound G-dimer (Yan *et al.*, 2018). Within each monomer, the GTPase domain was connected via hinge 2 to the four-helix bundle neck domain. The neck formed continuous helices with the trunk, and hinge 1 and the top of the trunk consisted of a two-helix bundle. The trunk was composed of a three-helix bundle, and BDLP interfaced with the membrane via a novel membrane binding domain (MBD) positioned below the trunk. In the GDP-bound BDLP crystal structure, the trunk was a four-helix bundle and the predicted membrane binding paddle was situated at the trunk tip (Low & Löwe, 2006).

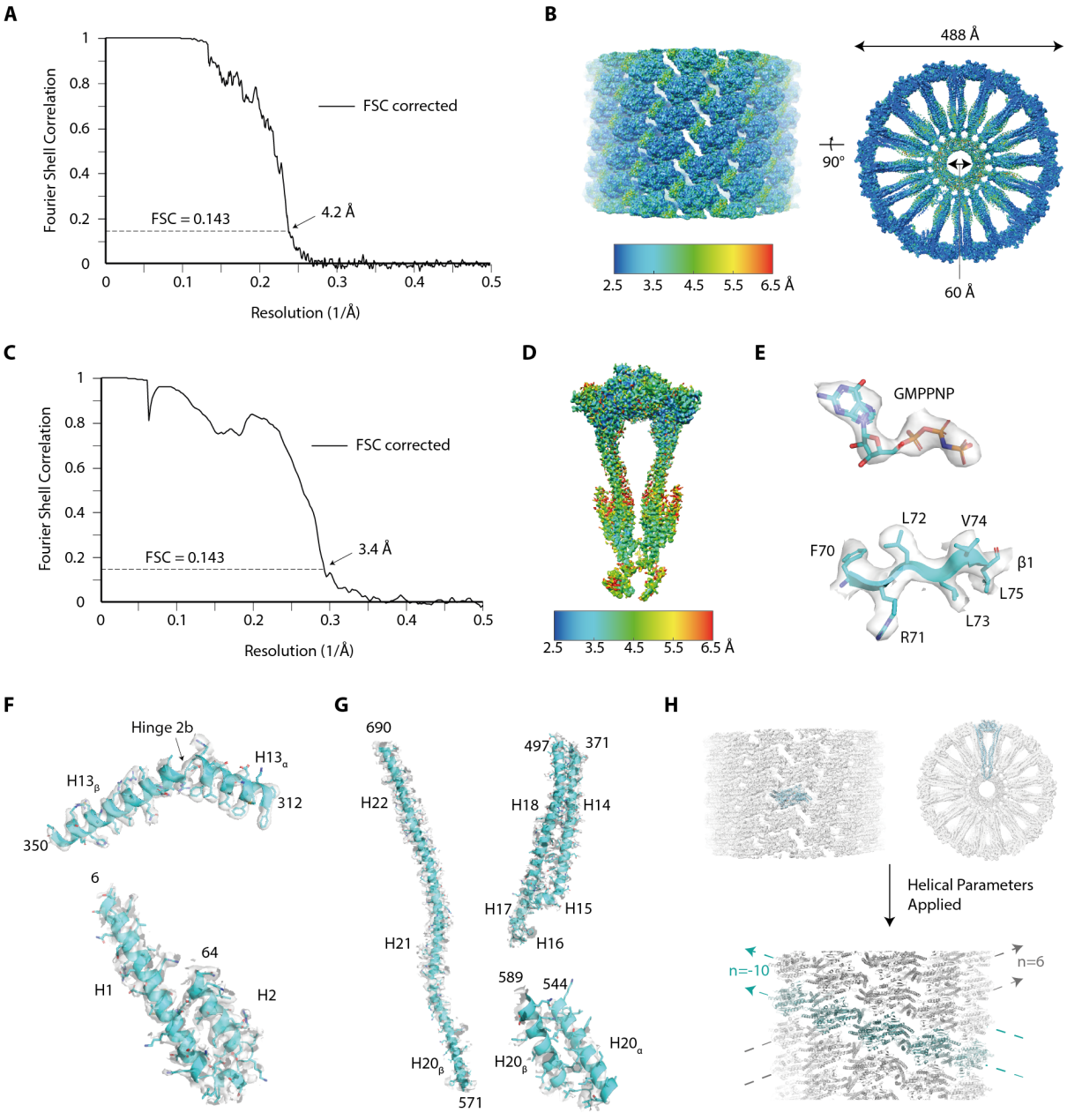


**Figure 32. GMPPNP-bound BDLP Helical and Local Refinements, Map Resolutions and Model Building.**
**A,** Helical refinement FSC curve. **B,** Cryo-EM map of the helical filament, coloured by local resolution estimation and contoured at 3σ. **C,** Asymmetric unit (dimer) focussed refinement FSC curve. **D,** Focussed refinement map, coloured by local resolution estimation, and contoured at 6σ. **E-G,** Representative examples of the dimer model built within the focussed refinement map. **E,** GTPase domain. **F,** Neck and hinge 2b. **G,** Lumen-to-surface continuous helix, trunk and membrane binding domains. **H,** Building of the helical filament model, termed $BDLP_{GMPPNP}$, into the filament map.

### 4.2.3.4 GTPase Domain Dimerisation and Nucleotide Coordination

The GTPase domain exhibited a comparable overall fold to the apo and GDP-bound BDLP crystal structures, with root mean squared deviations (RMSDs) of 2.0 Å and 1.9 Å between

the GMPPNP-bound GTPase domain and the apo and GDP-bound GTPase domains, respectively (Figure 33B). To elucidate the BDLP catalysis mechanism, the active site and G-dimer interface were analysed. Comparison with the GDP-bound BDLP G-dimer (Low & Löwe, 2006) revealed a more compact G-dimer interface in $BDLP_{GMPPNP}$ (Figure 33C), suggesting significant conformational changes induced by GMPPNP binding and self-assembly.

GMPPNP was coordinated by the conserved G1-G4 motifs, including the P-loop and switches 1 and 2, as is characteristic of dynamin GTPase domains (Figure 33D). Specifically, the GMPPNP ribose moiety was coordinated by asparagine-238, alanine-239 and aspartate-241 of the G4 motif and was trans-stabilised by the G-dimer. This included a trans interaction with the backbone amide nitrogen of serine-236. The same trans-ribose coordination occurs in the less compact GDP-bound G-dimer. The P-loop coordinated the α- and β-phosphates. Notably, lysine-82 was positioned to coordinate both phosphates but is not positioned to do so in the GDP-bound BDLP crystal structure. Switch 1, disordered in the GDP-bound G-dimer, was ordered, and was also involved in phosphate coordination. Additionally, the switch 1 ordering also positioned threonine-103 to coordinate a magnesium ion, alongside serine-83 of the P-loop. The magnesium ion was positioned to coordinate the γ-phosphate and stabilise the negative charge built up in the transition state during hydrolysis, rendering the positioning of threonine-103 and serine-83 critical to the catalytic mechanism. Switch 2 was positioned to stabilise both the P-loop and switch 1, and coordinate the γ-phosphate via an interaction with the backbone amide of glycine-183. In the GDP-bound G-dimer, switch 2 was not positioned to coordinate the γ-phosphate, suggesting an important role in the catalytic cycle for this interaction. In summary, the G4 and P-loop motifs were positioned for nucleotide coordination in the apo, GDP- and GMPPNP bound states, although the absence of a guanine cap in the apo state means that without G-dimerisation, the basal affinity for nucleotide is low (Low & Löwe, 2006). Upon G-dimerisation and GTP, or in this case GMPPNP, coordination, ordering of switch 1 and repositioning of switch 2 positions key catalytic residues for GTP hydrolysis and facilitates high-affinity coordination of the nucleotide.

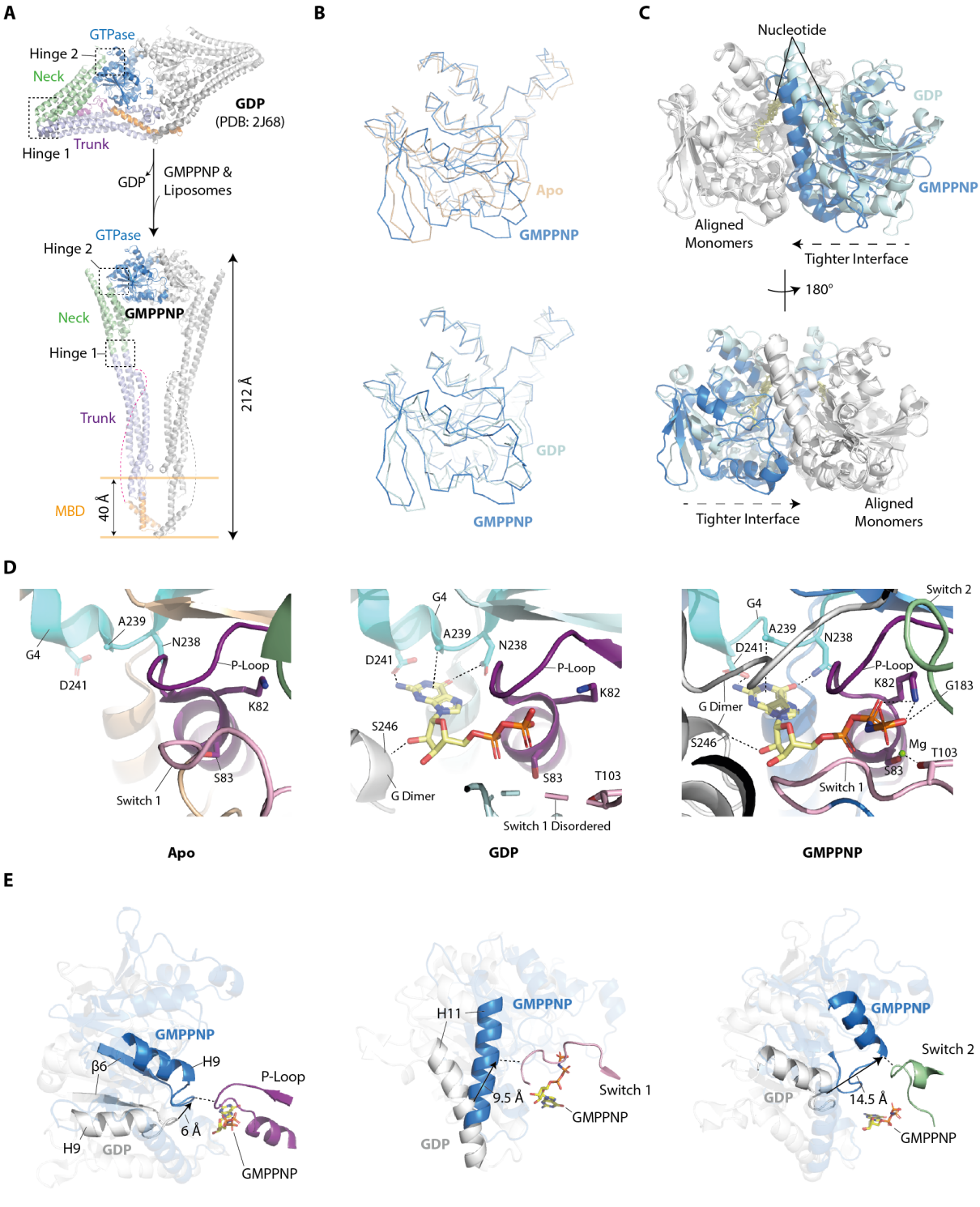


**Figure 33. Nucleotide Coordination by GMPPNP-bound BDLP G-dimers.**
BDLP forms a tight G-dimer interface when GMPPNP-bound, which primes conserved catalytic motifs to mediated nucleotide hydrolysis. **A,** BDLP-GDP dimer crystal structure (PDB: 2J68) and $BDLP_{GMPPNP}$ dimer coloured by domain, indicating the conformational changes occurring upon nucleotide exchange and lipid binding. Orange lines represent rough positioning of the bilayer **B,** Nucleotide state does not significantly impact the global GTPase domain fold. Alignment of the $BDLP_{GMPPNP}$ GTPase domain with the apo (PDB: 2J69) and GDP-bound GTPase domain crystal structures, with RMSD values of 2.0 and 1.9 Å, respectively. **C,** GMPPNP binding induces a tighter G-domain interface relative to GDP-bound BDLP dimers in solution. Alignment of the GDP- and GMPPNP-bound G-dimers anchored on just one monomer (grey), highlighting the tighter G-dimer interface in $BDLP_{GMPPNP}$. **D,** Comparison of the BDLP active site in the apo and GDP- or GMPPNP-bound states. Conserved catalytic motifs are positioned

to hydrolyse nucleotide when GMPPNP-bound only. **E,** Alignment of the GMPPNP- and GDP-bound G-dimers as in panel B. This time the monomer on which the alignment was anchored is not shown, except for the nucleotide and catalytic motifs of $BDLP_{GMPPNP}$. The key interactions of the tighter G-dimer interface with the conserved catalytic motifs are highlighted by dotted lines.

To elucidate the role of the tighter G-dimer interface in GTP coordination, or conversely how GTP coordination, relative to GDP coordination, induces a tighter G-dimer interface, trans interactions with the conserved catalytic motifs were analysed. Three key trans interfaces that stabilised the P-loop, switch 1 and switch 2 were facilitated by the tighter G-dimer interface (Figure 33E). The P-loop was stabilised by an interface with the β6-H9 connecting loop which was displaced 6 Å by the tighter G-dimerisation relative to the looser G-dimer interface of GDP-bound BDLP. Furthermore, the position of switch 2 was stabilised by the N-terminus of H9 which was displaced by 14.5 Å. Switch 1 was stabilised and presumably ordered by H11 which was displaced 9.5 Å in the tightened G-dimer interface. In summary, GMPPNP binding and a tight G-dimer interface facilitated the positioning of key catalytic residues primed to mediate hydrolysis.

#### 4.2.3.5 Hinges 1 and 2 Conformational Changes

The overall open membrane-binding BDLP conformation was facilitated by the closure of hinge 2 to maintain the G-dimer interface and the opening of hinge 1 (Figure 34A). At hinge 2, the neck domain rotated 75 degrees towards the GTPase domain, mediated by a break in the H13 helix to form $H13_{\alpha}$ and $H13_{\beta}$ (Figure 34B). Hinge 1 exhibited an open conformation, wherein $H13_{\beta}$ and H14 (hinge 1a) and H21 and H22 (hinge 1b) formed continuous helices between the neck and trunk domains (Figure 34C). In the trunk, residues 498-543 connecting H18 and H20 were disordered and consequently not modelled in $BDLP_{GMPPNP}$ (Figure 34D).

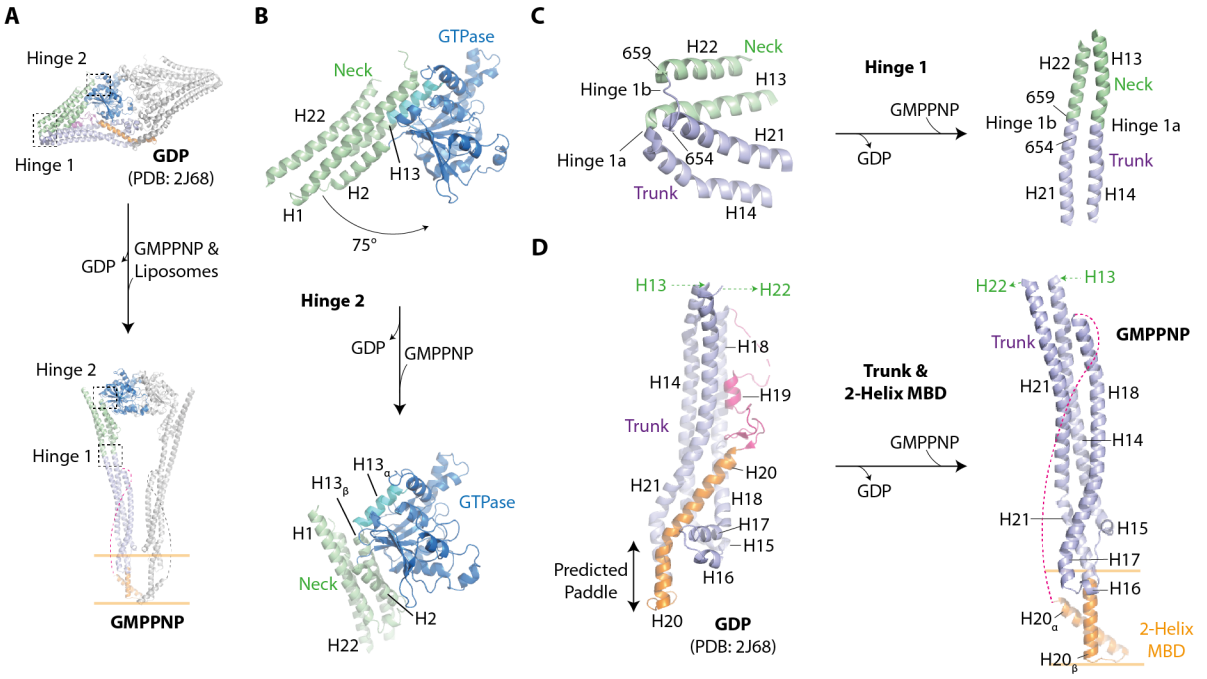


**Figure 34. Hinge, Trunk, and Membrane Binding domain Conformations in BDLP$_{GMPPNP}$.** BDLP undergoes major structural rearrangements to bind GMPPNP and constrict lipid templates. **A,** Overview of the GDP-bound BDLP closed conformation and BDLP$_{GMPPNP}$ open conformation. **B,** Hinge 2 conformational changes occurring upon nucleotide exchange and lipid binding. A H13 helix break is required for a 75 degree rotation of the neck domain relative to the GTPase domain. **C,** Hinge 1 conformational changes occurring upon nucleotide exchange and lipid binding. **D,** Trunk conformational changes occurring upon nucleotide exchange and lipid binding to form a 2-helix membrane binding domain (MBD). MBD is formed by a rearrangement of H20 into two helices below the trunk (H20α and H20β). The pink residues connecting H18 and H20, including H19, are disordered in BDLP$_{GMPPNP}$.

### 4.2.3.6 The Trunk Domain Rearranges to Form a Novel Membrane Binding Domain (MBD).

Previously, hydropathy plots predicted that membrane binding was mediated by a helical paddle domain located at the trunk tip (the C-terminus of H20 and N-terminus of H21) (Low & Löwe, 2006). The dimensions of the paddle suggested it would insert into the membrane, spanning only the outer leaflet of the bilayer. However, the BDLP$_{GMPPNP}$ structure revealed that large-scale rearrangements in the trunk and paddle formed a novel membrane binding domain (MBD) (Figure 34D). The MBD was formed by a significant rearrangement of H20 into a two-helix bundle (H20$_\alpha$ and H20$_\beta$) below the trunk, which, given its 31 Å length, inserted into the bilayer across both leaflets. Notably, this arrangement was identical to the simulated Fzo1 membrane binding domain (De Vecchis *et al.*, 2017). This resulted in a 180 Å continuous helix formed from H20$_\beta$ (MBD), H21 (trunk), and H22 (neck), connecting the filament lumen to the exterior.

### 4.2.4 The BDLP MBD has a Higher Affinity for High PG-Content Membranes

Given the striking similarity of the $BDLP_{GMPPNP}$ MBD and the Fzo transmembrane helices (De Vecchis *et al.*, 2017), and consequently the probable homology to the two mitofusin transmembrane helices (Cohen & Tareste, 2018), the two-helix MBD is likely a conserved feature of the mitofusin-like DRPs. Mitofusin-mediated mitochondrial fusion can be induced by phosphatidic acid (PA) (Kameoka *et al.*, 2018), and the BDLP and mitofusin homologue IniA exhibits a preference for negatively charged lipids (Wang *et al.*, 2019). The only phospholipid present in *N. punctiforme* membranes is the anionic phospholipid phosphatidylglycerol (PG) (Mikhaylenko, Skorokhod & Kholodny, 1998). Therefore, to investigate whether the $BDLP_{GMPPNP}$ MBD also conferred specificity for negatively charged lipids, Keerti Singh prepared liposomes with varying ratios of PG and PC (a neutral phospholipid), and tested the ability of BDLP to bind these liposomes using a proximity-based labelling of membrane-associated proteins (PLiMAP) assay. PLiMAP assays utilise liposomes supplemented with a fluorescent reporter lipid (BDPE) that crosslinks to membrane-bound proteins (Jose & Pucadyil, 2020). BDLP incubated with these liposomes was analysed by SDS-PAGE (Figure 35A). Quantification of the BDLP band fluorescence indicated an approximately 50% increase in BDLP binding to liposomes with a 0.8 PG:PC ratio (herein termed PG liposomes) or higher, suggesting a strong preference for negatively charged lipids.

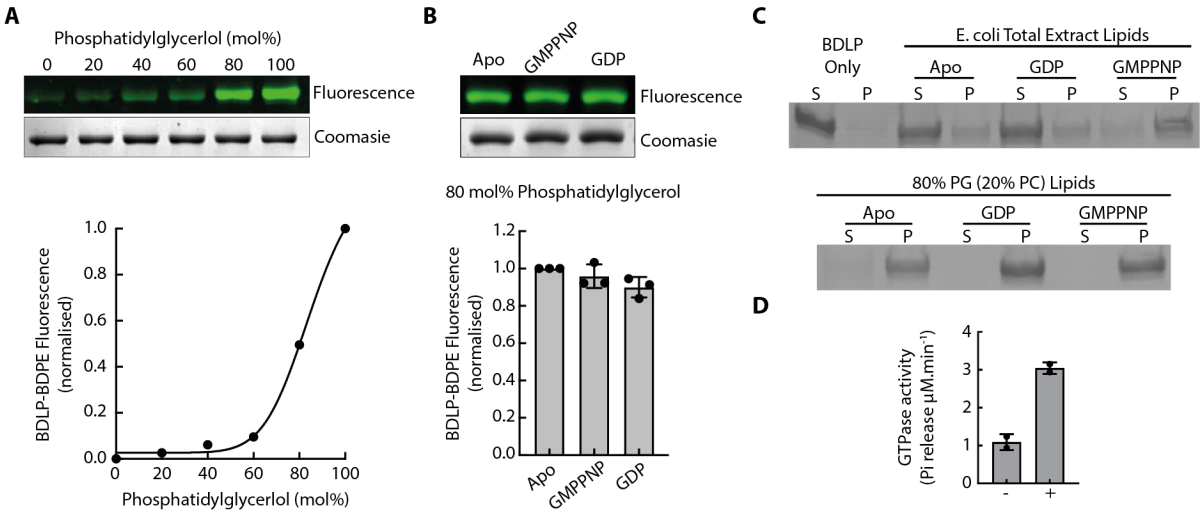


**Figure 35. BDLP PG Liposome Affinity.**
BDLP has a high affinity for membranes containing >80 % PG. **A,** PLiMAP assay (Jose & Pucadyil, 2020) testing BDLP binding affinity to liposomes with increasing PG composition (and decreasing PS

composition). Top: SDS-PAGE analysis of the PLiMAP assay showing Coomassie stained control alongside fluorescence of BODIPY-diazirine phosphatidylethanolamine (BDPE) covalently linked to BDLP that bound liposomes. Bottom: Quantification of the band fluorescence observed in the gel of two separate experiments, plotting BDLP-BDPE fluorescence normalised to fluorescence observed in the 100% PG sample as a function of PG ratio. **B,** PLiMAP assay using 80% PG (20% PC) liposomes and BDLP in the apo, GDP- or GMPPNP-bound states and quantification of fluorescence normalised to the fluorescence observed in the brightest apo sample. Error bars represent standard deviation of triplicate results. **C,** BDLP can efficiently bind PG liposomes in the apo and GDP-bound states, but not *E.* coli total extract liposomes. SDS-PAGE analysis of a co-sedimentation assay stained with Coomassie. BDLP that did not bind liposomes is found in the supernatant (S), whilst BDLP that bound liposomes was pelleted (P). **D,** PG liposomes stimulate nucleotide turnover. GTPase hydrolysis activity of 1 μM BDLP alone (-) or incubated with 100 μM of 80% PG-containing liposomes (+). Data recorded in duplicate. *PLiMAP and GTPase assays performed and analysed by Keerti Singh and Thomas Pucadyil.*

To ascertain whether nucleotide state and self-assembly influenced the capacity of BDLP to bind PG liposomes, Keerti repeated the assay in the presence of GMPPNP and GDP. Nucleotide state did not affect this phenomenon; apo and nucleotide-bound BDLP effectively bound PG liposomes (Figure 35B). To corroborate this finding, I examined BDLP binding to the same liposomes using a co-sedimentation assay, the results of which were consistent with the PLiMAP assay, whereby BDLP co-sedimented with PG liposomes independent of nucleotide state (Figure 35C). To compare these results with the ability of BDLP to bind the ETE liposomes utilised in this and previous studies (Low & Löwe, 2006; Low *et al.*, 2009), I repeated the co-sedimentation assay with ETE liposomes. In contrast to the nucleotide-independent PG liposome binding, BDLP effectively bound ETE liposomes when GMPPNP-bound only, although some minimal binding in the apo and GDP-bound states was observed. Given *E. coli* membranes contain approximately 25% anionic lipid (Sohlenkamp & Geiger, 2016), this suggested that in the absence of high anionic lipid content, BDLP self-assembly was necessary to facilitate lipid binding by the MBD.

Previously, no BDLP lipid-stimulated nucleotide turnover increase was detected in the presence of ETE or *N. punctiforme* total extract lipids (Low & Löwe, 2006). Therefore, Keerti examined the BDLP GTPase activity in the presence of PG liposomes, given the strong affinity of BDLP for PG. PG liposomes induced a three-fold increase in GTPase activity relative to BDLP in the absence of lipids (Figure 35D). Considering the observed tight G-dimers of $BDLP_{GMPPNP}$ on constricted ETE liposomes that primed the active site for catalysis (Figure 33), this raised significant questions regarding how the high PG content specifically stimulated lipid turnover. Such a phenomenon has been observed for Drp1, which can tubulate both PS- and cardiolipin-

based lipid templates, yet cardiolipin, and not PS, stimulates GTP turnover (Francy *et al.*, 2017). However, this was attributed to the cardiolipin-Drp1 filament specifically positioning GTPase domains in an orientation that facilitated catalytically active G-dimers that were not formed in PS-Drp1 filaments. Conversely, ETE lipids do not stimulate BDLP nucleotide turnover (Low & Löwe, 2006), yet tight catalytically active G-dimers were observed in $BDLP_{GMPPNP}$ (Figure 33).

In summary, the PLiMAP and co-sedimentation assays demonstrated that BDLP exhibits high nucleotide-independent affinity for anionic lipids, specifically high PG-content liposomes. Whereas BDLP requires GMPPNP-binding and self-assembly to mediate strong ETE liposome binding. ETE liposomes have a lower anionic lipid content.

#### 4.2.4.1 Cryo-EM Structure of GMPPNP-bound BDLP Filaments on PG Liposome Templates

To elucidate the mechanism by which PG liposomes might stimulate GTPase turnover, I visualised GMPPNP-bound filaments self-assembled onto PG liposome templates by cryo-EM. Summed 2D Fourier transforms of helical segments, aligned by 2D class averaging, were analysed to index the filament lattice (Figure 36A). This analysis indicated that filaments were homogenous with only a single helical lattice present in the sample. Key Bessel orders were assigned to a left-handed 12-start helical family, and a right-handed 6-start helical family, demonstrating that the filament also possessed C6 centrosymmetric symmetry (Figure 36B). Consequently, the 6-start helical family constituted the fundamental repeat that intersected all lattice points, and the helical rise and twist of this family, 17.8 Å and 21.5° respectively, were utilised to refine a filament map to a 7.8 Å overall resolution, using the IHRSR gold-standard FSC approach with BLUSH regularisation (Figure 36C).

The outer filament diameter (530 Å) and lumen diameter (117 Å) were larger than the $BDLP_{GMPPNP}$ filament, indicating reduced constriction of the underlying bilayer. PG and PC are both cylindrical lipids, whereas the ETE liposomes contained approximately 75% PE, which is a slightly conical lipid that can undergo Lm-hexII phase transitions at temperatures around 8 °C (Toombes *et al.*, 2002). Therefore, the ETE liposomes were composed of more fluid bilayers and were more amenable to higher curvature, whereas the PG liposomes were more rigid and would have been less readily deformed into high curvature. This may explain the reduced bilayer constriction in the BDLP-PG liposome filament. The increased diameter may

also explain the different helical lattice. Compared to the left-handed 10-start helical family of $BDLP_{GMPPNP,}$ the BDLP-PG liposome helical lattice maintained the $BDLP_{GMPPNP}$ ultrastructural interactions by incorporating ~20 more subunits per turn in the left-handed 12-start helical family. Similarly, the right-handed 6-start helical family incorporated ~0.9 more subunits per turn. In summary, the BDLP-PG liposome filament constricted the bilayer to a lesser extent and exhibited a subtly different helical lattice to maintain the helical ultrastructure in a larger, less constricted, filament diameter.

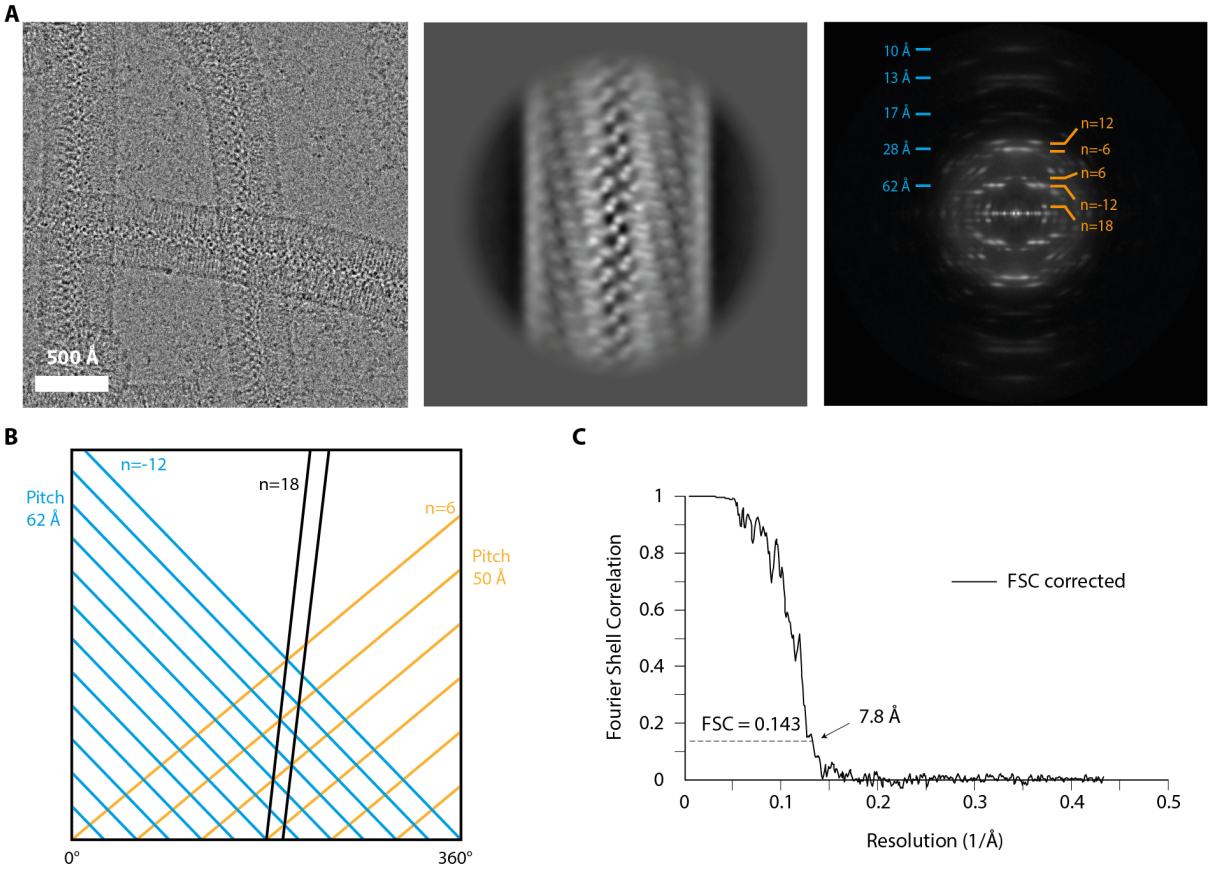


**Figure 36. GMPPNP-bound BDLP-PG Liposome Filament Lattice Indexing and FSC Curve.** **A,** Representative cryo-EM micrograph of filaments, a 2D class average and a summed Fourier transform of the Fourier transforms of filament segments aligned to the 2D class average. Indexing of key Bessel orders is shown. **B,** 2D representation of the helical lattice showing the arrangement of key Bessel orders. **C,** Helical refinement FSC curve.

In accordance with the $BDLP_{GMPPNP}$ map, local resolution estimates indicated high resolution and structural order in the peripheral regions of the BDLP-PG liposome map where the

GTPase domains were situated, and lower resolution and increased flexibility towards the central regions of the map where the membrane interface was located (Figure 37A). These observations further suggested that BDLP formed filaments with robust lateral GTPase domain contacts and comparatively weaker lateral contacts at the membrane interface when GMPPNP-bound. The map resolution was insufficient to facilitate *de novo* model construction; however, the $BDLP_{GMPPNP}$ dimer was fitted into the filament map using Phenix (Liebschner *et al.*, 2019), which reported a map-model cross correlation of 0.699.

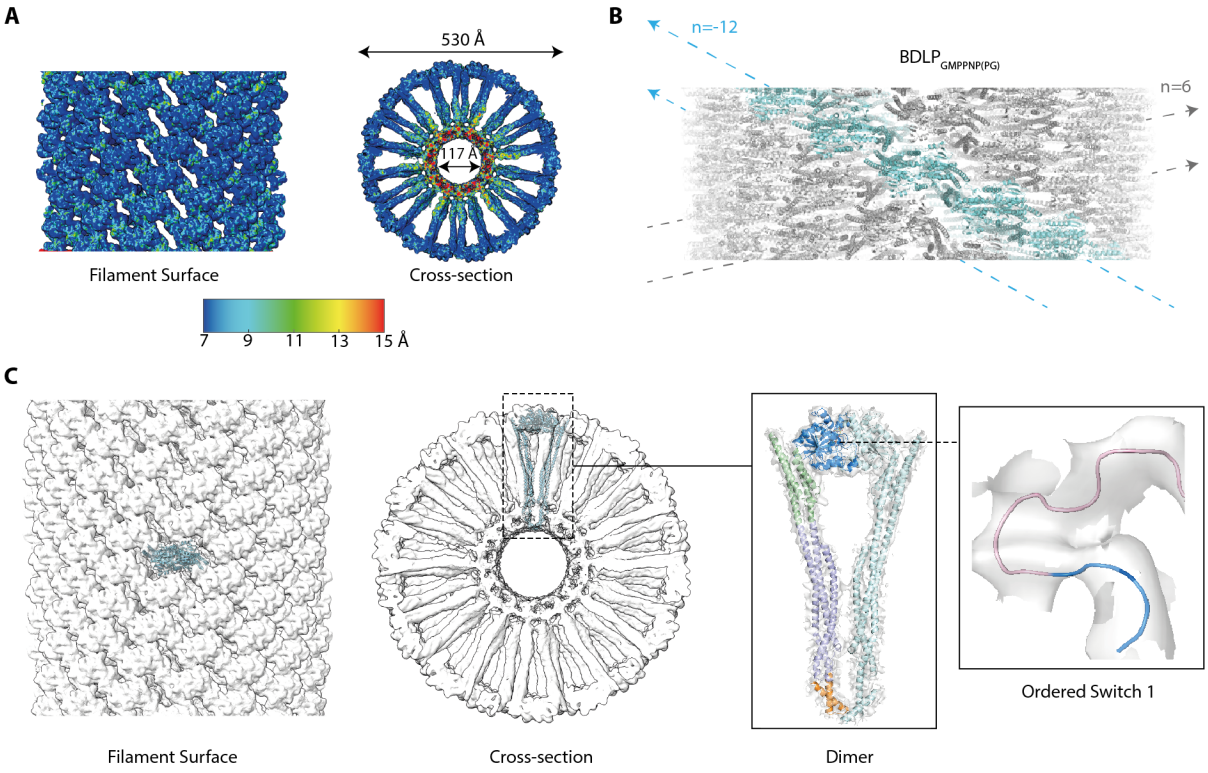


**Figure 37. $BDLP_{GMPPNP(PG)}$ Map and Model.**
The helical ultrastructure of $BDLP_{GMPPNP}$ and $BDLP_{GMPPNP(PG)}$ are equivalent, despite the larger filament diameter of $BDLP_{GMPPNP(PG)}$. **A,** Filament map coloured by local resolution estimates. **B,** $BDLP_{GMPPNP(PG)}$ filament model indicating key helical families. A left handed helical rung is coloured cyan. **C,** Filament map showing fit of a $BDLP_{GMPPNP(PG)}$ dimer and density supporting a tight G-dimer interface, including an ordered switch 1.

Helical parameters were applied to the $BDLP_{GMPPNP}$ dimer fit into the BDLP-PG liposome filament map to construct a helical model, termed $BDLP_{GMPPNP(PG)}$ (Figure 37B). Consistent with $BDLP_{GMPPNP}$, supporting density was observed for an overall open conformation, a closed

hinge 2 with a H13 helix break, an open two-helix bundle hinge 1, a three-helix bundle trunk, and an extended two-helix MBD below the trunk extending to the filament lumen (Figure 37C). The tight G-dimer interface and an ordered switch 1 motif were also preserved. Therefore, given the resolution to which the map was refined, the specific mechanism by which PG increases nucleotide turnover could not be elucidated. Overall, with only subtle lattice changes to accommodate a larger diameter filament, $BDLP_{GMPPNP}$ and $BDLP_{GMPPNP(PG)}$ were demonstrated to be equivalent structures, and $BDLP_{GMPPNP}$ remained a valid model for understanding the GTP-bound self-assembled and lipid-constricting BDLP structure.

### 4.2.5 A MBD Mutant can Tubulate PG Liposomes but cannot Achieve Tight Constriction

The previously predicted paddle was validated by Low *et al.*, 2009 using two mutants: F583E and a double L576E/L577E mutant. Both mutants inhibited ETE lipid binding and constriction. Given I demonstrated that the $BDLP_{GMPPNP}$ structure membrane interfacing was mediated by the newly assigned MBD and not the paddle, I analysed the position of these residues to understand why they were essential for membrane binding. All three residues were positioned within the bilayer on $H20_{\beta}$ of the $BDLP_{GMPPNP}$ MBD (Figure 38A). To ascertain whether the same MBD mutations also affected PG liposome binding, $BDLP_{F583E}$ was purified and analysed by co-sedimentation assay with ETE and PG liposomes. Consistent with previous results (Low *et al.*, 2009), $BDLP_{F583E}$ did not efficiently bind ETE liposomes, even when nucleotide-bound (Figure 38B). Additionally, whereas wild-type BDLP efficiently bound PG liposomes in the apo and GDP-bound states (Figure 35C), $BDLP_{F583E}$ did not (Figure 38B). Strikingly, when GMPPNP-bound, a significant proportion of $BDLP_{F583E}$ bound PG liposomes and co-sedimented in the pellet.

To ascertain whether this binding was accompanied by self-assembly into helical polymers, $BDLP_{F583E}$ was incubated with PG liposomes and GMPPNP under the same conditions used to produce the wild-type filament sample. A control sample of PG liposomes exhibited similar morphology under NS-EM to the ETE liposomes (Figure 38C). NS-EM analysis of the GMPPNP- and PG liposome-bound $BDLP_{F583E}$ sample revealed that this mutant was capable of tubulating PG liposomes and self-assembling into a loosely ordered filament (Figure 38D). Filaments varied in size, indicating significant flexibility and loose ordering. Furthermore, all filaments possessed significantly larger diameters (~750-800 Å) than the $BDMLP_{GMPPNP(PG)}$ assembly,

suggesting that phenylalanine-583 is a crucial residue for membrane constriction, potentially required by the MBD to fully penetrate and disrupt the bilayer. $BDLP_{F583E}$ filaments did not form tight lattices; however, similar to the $BDLP_{GMPPNP}$ assembly, hinge 1 open conformations and self-assembled left-handed helical rungs were identified, indicating that back-to-back self-assembly of G-dimers still occurred. Fourier space analysis indicated the filaments had a 100 Å repeat, which was attributed to these rungs. In the more constricted wild-type filament, the left-handed rungs repeat every 62 Å (Figure 36B). Collectively, these results suggested that full insertion of the MBD into the bilayer, mediated by large hydrophobic residues such as phenylalanine-583, is necessary for tight self-assembly of a membrane-constricting helical BDLP lattice.

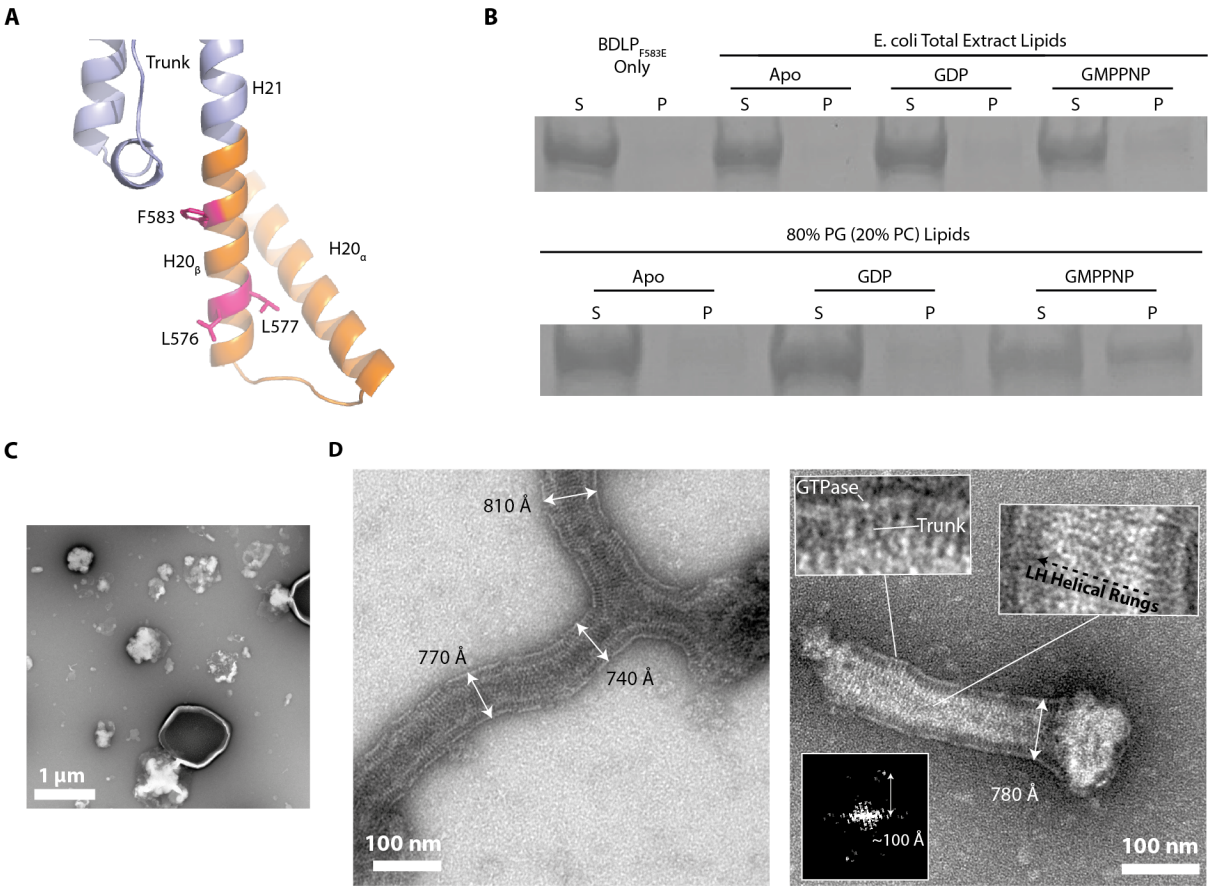


**Figure 38. $BDLP_{F583E}$ Membrane Binding and Constriction.**
Mutation of the MBD prevents tight binding and constriction of liposomes. **A,** $BDLP_{GMPPNP}$ structure highlighting positioning of key hydrophobic residues (pink) in the MBD that are essential for efficient ETE liposome binding. **B,** SDS-PAGE analysis of a $BDLP_{F583E}$-liposome co-sedimentation assay, stained with Coomassie. $BDLP_{F583E}$ has poor affinity for liposomes and was mainly found in the supernatant (S), but somewhat co-pelleted (P) with PG liposomes when GMPPNP-bound. **C,** NS-EM micrograph of PG liposomes. **D,** NS-EM analysis of GMPPNP-bound $BDLP_{F583E}$ self-assembled on PG

liposome templates, which the mutant was unable to fully constrict. Zoom panels highlight the open overall structure, left handed helical rungs and the 100 Å repeat of these rungs measured in Fourier space.

## 4.3 Discussion

This chapter demonstrated that BDLP was specifically upregulated in *N. punctiforme* hormogonia and was expressed as part of a four-gene operon under control of the hormogonium-specific sigma factors SigC and SigJ. Within hormogonia, BDLP formed cytoplasmic partitioned zones, potentially via liquid-liquid phase separation. Ordered structures reminiscent of BDLP decorated thylakoids and hexII nanoparticles, that remodelled from Lm phase thylakoid membranes. Collectively, these results suggested a putative and novel role for a bacterial DRP in mediating and maintaining stable lipid phase-changes, although direct evidence of BDLP mediating this change was not observed. Additionally, cryo-EM reconstructions of GMPPNP-bound BDLP protein-lipid filaments revealed for the first time the BDLP filament ultrastructure and how a tight G-dimer interface and GTP coordination position catalytic residues to mediate catalysis. The filament structure also elucidated how BDLP interfaces with membrane via a two-helix MBD that penetrates both leaflets of the bilayer, with implications for the predicted membrane interfaces of the mitofusins and Fzo.

### 4.3.1 A Putative Novel Bacterial DRP Function

BDLP being non-essential and its specific upregulation and role in hormogonia (Figure 26 & Figure 28A) demonstrated a specialised role of a bacterial DRP in development of a specific morphology and life cycle stage. This is not unique to *N. punctiforme* and BDLP, as the bacterial DRPs stDynA and stDynB are expressed under the control of a sporulation-specific transcriptional regulator with a role in stabilising the Z-ring during sporulation cell division (Schlimpert *et al.*, 2017). Similarly, the *E. coli* DRP CrfC is involved in cell cycle progression as it is required for chromosome equipartitioning during replication (Taniguchi *et al.*, 2019). Given the complex life cycles of many cyanobacteria that involve morphological changes and require membrane remodelling events (Risser, 2023), specific roles for cyanobacterial DRPs under control of life-cycle specific gene regulation factors, may be a broadly conserved characteristic. In addition to BDLP and BDLP2 the *N. punctiforme* genome encodes two DRPs at distinct genome loci (Npun_R1152 & Npun_F0558) (Bohuszewicz, Liu & Low, 2016).

Whether these DRPs have specialised roles in other life cycle stages is an exciting possibility that remains to be determined. In general, the hormogonium specific expression of BDLP highlighted the divergent and specific roles of a bacterial DRP.

Multi-DRP operons are found in numerous bacterial species (Bohuszewicz, Liu & Low, 2016). Consistent with this observation, transcriptomic analysis revealed that BDLP and BDLP2 were under the control of the same TSS (Figure 26A). During hormogonium development, BDLP expression was significantly higher than BDLP2 expression (Figure 26), suggesting functional redundancy that may explain why deletion of either gene was non-essential, nor affected colony morphology. As hormogonia represent the motile form of *N. punctiforme*, it was anticipated that BDLP or BDLP2 deletion might have affected colony morphology, had their individual role in hormogonium development been critical to motility. Whether BDLP2 can compensate for BDLP deletions or possesses another specific role in hormogonia remains to be understood. Bacterial DRPs that exist as pairs, such as cjDLP1 and cjDLP2 or LeoA (a BDLP homologue) and LeoBC, are fusogenic DRPs and require their partner dynamins to function (Liu, Noel & Low, 2018; Michie *et al.*, 2014). Indeed, heterotetramer formation is required for the cjDLPs to tether membranes in trans. Although IniA, also a BDLP homologue, displays low-level fission activity *in vitro*, its partner DRP (IniC) may be required to enhance its membrane remodelling activity and for its *in vivo* function (Wang *et al.*, 2019). Additionally, both Mfn1 and Mfn2 are essential for OMM fusion (Chen *et al.*, 2003). Membrane remodelling helical co-polymers are functionally significant in the equally ancient and conserved ESCRT-III family in archaea and eukaryotes (Pfitzner *et al.*, 2020), although co-polymers have yet to be identified in bacteria (Liu *et al.*, 2021b). Whether bacterial DRP pairs like BDLP and BDLP2 or the mitofusins form co-polymers to constrict and remodel membrane remains unresolved.

Notwithstanding this, the present chapter demonstrated that BDLP, and not BDLP2, expression was significantly upregulated in hormogonia (Figure 26). Moreover, BDLP-GFP overexpression was associated with remodelling of thylakoids into hexII nanoparticles (Figure 2), suggesting that BDLP2 might not be requisite for BDLP function *in vivo*. Furthermore, BDLP self-assembly onto membrane templates was sufficient to induce catalytically active G-dimers (Figure 33), and PG liposomes were capable of stimulating nucleotide turnover (Figure 260D), indicating that BDLP-BDLP2 interactions are not essential for self-assembly, membrane constriction or to stimulate GTPase activity. It is, however,

noteworthy that Mfn1 and Mfn2 can form tight homo-G-dimers, as well as hetero-G-dimers (Qi *et al.*, 2016; Li *et al.*, 2019). Low-level BDLP2 expression may be required for an alternative function during hormogonium development or thylakoid remodelling, such as targeting BDLP to specific thylakoid regions. Alternatively, gradual accumulation of BDLP2 or expression induced by a yet unidentified regulatory network might be necessary for the depolymerisation of BDLP coats that remain on hexII nanoparticles and thylakoids (Figure 28B & Figure 28C). Alphafold predicts BDLP2 in a $BDLP_{GMPPNP}$-like hinge 1 open conformation (Varadi *et al.*, 2024), with a two-helix MBD equivalent below the trunk and loosely ordered residues connecting the trunk and MBD, suggesting that BDLP2 interfaces with membrane in a BDLP-like manner (Figure 39A). BDLP2 also possesses an additional C-terminal domain, which the InterPro database predicts as a DnaJ domain (Paysan-Lafosse *et al.*, 2023). DnaJ domains activate the ATPase activity of Hsp70 chaperones (Qiu *et al.*, 2006), and therefore membrane-bound BDLP2 might be involved in recruiting chaperones to the membranes it binds, potentially to facilitate disassembly or conformational changes of BDLP membrane decorations or as part of a distinct BDLP2 function.

Although BDLP expression significantly exceeded BDLP2 expression, the short 108 amino acid coding sequence upstream of BDLP (Npun_R6514) exhibited comparable expression levels in hormogonia (Figure 1A), suggesting a significant role in hormogonium development. Npun_R6514 possesses an Alphafold-predicted two-helix arrangement with helices connected by a flexible linker, and the C-terminal helix is predicted as trans-membrane and the N-terminal helix as cytoplasmic by the TMHMM server (Figure 39B) (Krogh *et al.*, 2001; Varadi *et al.*, 2024). Consequently, Npun_R6514 may function as a membrane-anchored recruiter or activator of BDLP. Alphafold predictions of a BDLP-Npun_R6514 dimer indicate interactions between Npun_R6514 and the GTPase and trunk domains (Figure 39C). As it was demonstrated that BDLP can bind membranes in the apo state (Figure 35), such interactions may enable R6514 to inhibit GTP binding and/or self-assembly. Alternatively, they may prevent membrane binding. Both inhibitory actions would provide a mechanism to impede BDLP-mediated membrane remodelling at specific membranes, or temporally regulate BDLP activity. In conclusion, while the role of Npun_R6514 and its potential interaction with BDLP were not established, expression data suggested a hormogonium-specific function, potentially involved in BDLP regulation.

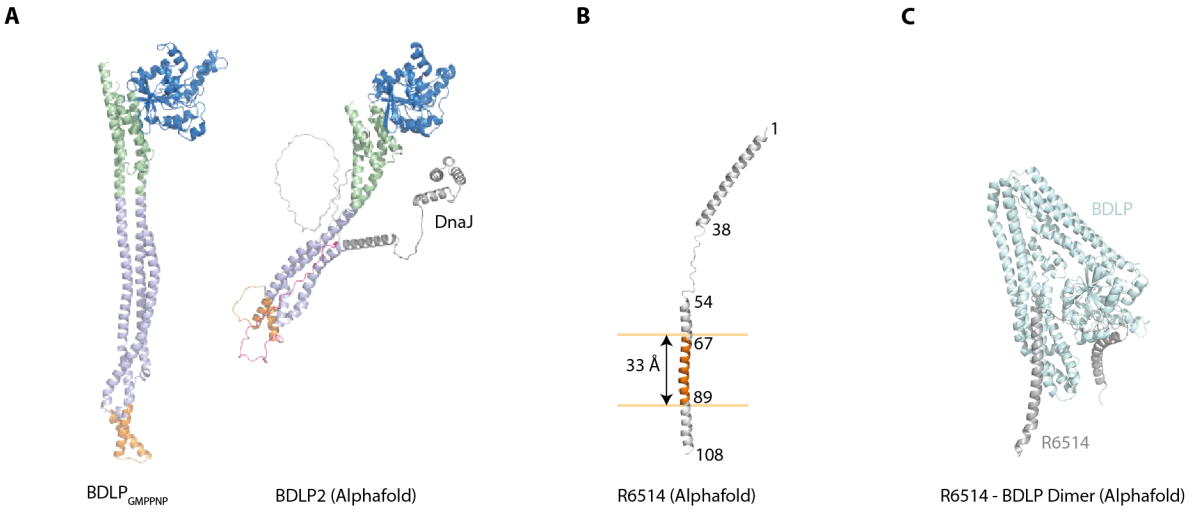


**Figure 39. Structural Predictions of Proteins in the BDLP Operon.**
**A,** BDLP$_{GMPPNP}$ and BDLP2 Alphafold prediction (Varadi *et al.*, 2024) coloured by domain. The BDLP2 C-terminal DnaJ domain is coloured grey. **B,** Alphafold prediction of Npun_R6514 structure. Orange residues represent the TMHMM predicted transmembrane domain. **C,** BDLP-Npun_R6514 dimer structure predicted by Alphafold (Jumper *et al.*, 2021). BDLP = cyan, R6514 = grey.

Cryo-CLEM analysis of hormogonia indicated that BDLP formed partitioned zones around BDLP-decorated hexII nanoparticles, which excluded cellular matter such as glycogen granules and ribosomes from the region. This was reminiscent of liquid-liquid phase separation, and such a phenomenon has been observed for dynamin 1, MxA and Drp1 (Imoto *et al.*, 2022; Davis *et al.*, 2019; Posey *et al.*, 2023), suggesting that the ability to undergo LLPS may be a conserved DSF feature. LLPS is frequently mediated by intrinsically disordered protein regions (Boeynaems *et al.*, 2018). In the BDLP$_{GMPPNP}$ structure residues 498-543 that joined H18 and the MBD were also disordered. Notably, these residues sit in a region between the trunk and MBD akin to the variable domain of Drp1, which is proposed to be disordered and mediate LLPS (Posey *et al.*, 2023). Furthermore, biomolecular condensates of dynamin 1, Drp1, and MxA have been proposed as crucial for rapid self-assembly when required (Imoto *et al.*, 2022; Davis *et al.*, 2019; Posey *et al.*, 2023); however, the reason for BDLP forming putative biomolecular condensates following thylakoid remodelling has not been established in this study. Given we observed BDLP-like decorations on the surface of hexII nanoparticles (Figure 28), biomolecular condensates may represent a mechanism for maintaining BDLP in

close association with hexII nanoparticles to prevent spontaneous lipid phase transitions back into the Lm phase.

The upregulation of BDLP, downregulation of genes associated with cylindrical lipid synthesis, and upregulation of genes associated with MGDG synthesis suggested a concerted effort in hormogonia to remodel thylakoid membranes into hexII nanoparticles, and a likely role of BDLP in mediating the phase change (Figure 28A). BDLP decorations of both thylakoids and hexII nanoparticles (Figure 28) further suggested BDLP was involved in this phase transition. However, it is also possible that BDLP was required for sequestering spontaneously formed hexII nanoparticles by decorating them, such that they could not spontaneously transition back into the Lm phase. Spontaneous phase changes could be promoted by the upregulation of MGDG synthesis and down regulation of cylindrical lipid synthesis in hormogonia (van Eerden *et al.*, 2015). However, the ability of BDLP to penetrate the bilayer and induce extreme lipid curvature suggests it may play a more active role (Figure 32B). Furthermore, the filament-forming Drp1 is able to at least transiently induce bilayer rafts of cardiolipin to transition into the hexII phase (Stepanyants *et al.*, 2015; Rochon *et al.*, 2024).

Long BDLP filaments were not observed *in vivo*, unlike those seen *in vitro* and used for cryo-EM reconstruction (Figure 30). Under native cell conditions, BDLP may only forms short helical collars, as is the case for dynamin 1, which only requires a few helical turns to mediate fission in *in silico* simulations (Pannuzzo, McDargh & Deserno, 2018), but can form extensive ordered filaments i*n vitro* (Jimah *et al.*, 2024). Additionally, more physiological lipid mixtures lead to shorter dynamin 1 filaments and are required for fission (Pucadyil & Schmid, 2008). Overall, these data suggested BDLP remodels thylakoid membranes into decorated hexII nanoparticles; however, the ability of BDLP to mediate phase changes remains to be directly proven. As hexII nanoparticles were observed in a BDLP-GFP overexpression strain, the extent to which TMs are remodelled into hexII nanoparticles in wild-type hormogonia remains to be elucidated.

### 4.3.2 BDLP Filament Ultrastructure Insights

To produce a sample of BDLP protein-lipid filaments suitable for cryo-EM structure determination, extensive optimisation was necessary to mitigate aggregation of filaments and untubulated liposomes (Figure 30). Filament aggregation may have been induced by

sub-optimal *in vitro* conditions but could also suggest that BDLP filaments possess inherent adhesive properties, potentially representing a means of tethering of tubulated membranes in trans, applicable to mitofusin-mediated membrane fusion. Nonetheless, a sample of more dispersed and linear filaments was obtained and utilised to reconstruct the $BDLP_{GMPPNP}$ filament map.

To reconstruct the filament map, revised helical parameters were required (Figure 31). The updated parameters represented a subtle lattice shift relative to the previously reported helical parameters; key Bessel orders represented 6- and 10-start helical families compared to the previously reported 7- and 11-start families (Low *et al.*, 2009). Technological limitations and the consequent lower resolution data acquired in 2009 would have obscured any observable differences in map quality of maps reconstructed with either set of helical parameters, and only with the advent of the 'resolution revolution' (Kühlbrandt, 2014) was the accurate Bessel order indexing achieved in this study. The significantly improved map quality and resolution in this investigation.

Alongside the higher local resolution of the outer regions of the filament map where the GTPase domains were situated (Figure 32B) and the presence of G-dimers in solution (Low & Löwe, 2006), the tight G-dimer interfaces of $BDLP_{GMPPNP}$ (Figure 33C) suggested that the G-dimer interface was the primary assembly interface of BDLP filaments, which polymerised via back-to-back association of G-dimers into helical rungs. NS-EM analysis of F583E mutants corroborated this, as GMPPNP-bound $BDLP_{F583E}$ filaments were unable to achieve tight constriction, but still demonstrated back-to-back association of G-dimers into left-handed helical rungs (Figure 14D). The back-to-back association of G-dimers within helical rungs across both neck and trunk domain longitudinal parallel interfaces was consistent with the back-to-back association of cjDLP2 within heterotetramers (Liu, Noel & Low, 2018), but contrasted with classical dynamin-like helical polymers and the trunk interfaces they form in a diagonal arrangement. This further highlights the diversity and functional tuning of polymerisation interfaces in the DSF. This observation is also relevant to potential mechanisms of mitofusin polymerisation and contradicts the controversial anti-parallel association of neck domain helices proposed to mediate mitofusin trans membrane tethering (Koshiba *et al.*, 2004).

For the first time, the $BDLP_{GMPPNP}$ structure provided insights into the BDLP catalytic mechanism, including the formation of a tight G-dimer interface and how BDLP coordinates GTP. The tight G-dimer interface positioned conserved catalytic motifs to coordinate both a charge-compensating magnesium ion and GMPPNP in an orientation primed for catalysis (Figure 33D & Figure 33E), confirming that BDLP hydrolyses GTP via a conserved DSF catalytic mechanism (Daumke & Praefcke, 2016). Notably, the charge compensating magnesium ion was coordinated by an ordered switch 1, which was disordered in GDP-bound BDLP. This is consistent with GTP-bound IniA and GDP.$BeF_3$-bound Mfn1 (Wang *et al.*, 2019; Yan *et al.*, 2018) and the DSF in general (Daumke & Praefcke, 2016). Given the canonical GMPPNP coordination and tight G-domain interface of $BDLP_{GMPPNP}$, it was unexpected that only PG liposomes, and not the ETE liposomes used as templates for $BDLP_{GMPPNP}$ filaments, were able to increase GTP turnover (Figure 35D). Furthermore, the overall architecture of $BDLP_{GMPPNP(PG)}$ and ordered switch 1 conformation were analogous to $BDLP_{GMPPNP}$. Elucidation of the membrane-bound BDLP G-dimer interface and active site arrangement during the transition state and post GTP-hydrolysis, or the membrane-bound apo BDLP structure, would provide insight into how specific lipids stimulate GTP turnover. In summary, the $BDLP_{GMPPNP}$ structure revealed how a tight G-dimer interface and GTP coordination prime the G-dimer for catalysis.

The $BDLP_{GMPPNP}$ structure also revealed how hinge 2 closing facilitated a tight G-dimer interface and hinge 1 opening enabled an extended conformation to promote helical polymerisation and membrane constriction (Figure 34). The mechanism by which these conformational changes were induced, whether through nucleotide or lipid binding or a combination thereof, remains unclear. However, the capacity of IniA and Fzo to bind membrane in an apo and overall closed conformation (Wang *et al.*, 2019; De Vecchis *et al.*, 2017) and the ability of BDLP to bind PG liposomes in the absence of nucleotide (Figure 35), potentially in an overall closed conformation, suggest that GTP binding plays the most significant role. An understanding of the apo membrane-bound BDLP arrangement would confirm this assertion.

The BDLP hinge 2 closed conformation in the presence of GMPPNP was consistent with Mfn1 (Yan *et al.*, 2018). To achieve a hinge 2 closed conformation in $BDLP_{GMPPNP}$, a H13 helix break was necessary (Figure 34B). Similar rearrangements are observed in Mfn1, wherein H6 undergoes the same rearrangement (Yan *et al.*, 2018), and in dynamin 1 an analogous flexible

helix and rearrangements also mediate hinge 2 closing and opening (Faelber *et al.*, 2011; Kong *et al.*, 2018). However, dynamin 1-like DRPs exhibit a hinge 2 closed conformation in the apo or GDP-bound states, whereas BDLP- or mitofusin-like DRPs exhibit the same conformation when GTP analogue-bound. For BDLP, it is possible that the nucleotide state is primarily responsible for mediating hinge 1 opening via release of GTPase-trunk contacts, and subsequent polymerisation forces the closed hinge 2 conformation required for tight G-dimerisation within the filament. Conversely, in dynamin 1 filaments for which a hinge 1 closed conformation has not been observed, hinge 2 conformation is directly modulated by GTP hydrolysis to drive power-strokes and rung sliding between trans-rung G-dimers to achieve super-constriction (Ganichkin *et al.*, 2021). In $BDLP_{GMPPNP}$, G-dimers form within rungs preventing a similar power-stroke mechanism of rung sliding and constriction. Therefore, the role of nucleotide hydrolysis in BDLP filaments remains unclear and may be required for depolymerisation or another as-yet-unresolved mechanism of membrane remodelling, perhaps required for Lm-HexII phase transitions.

### 4.3.3 The Novel BDLP Membrane Binding Domain might help Identify Membrane Binding Domains of other DRPs.

A significant question addressed in this work was how BDLP interfaces with membrane. The $BDLP_{GMPPNP}$ structure revealed that, rather than the outer leaflet-contacting paddle, BDLP interfaced with membrane via rearrangements of H20 to form a two-helix MBD below the trunk that spanned both bilayer leaflets (Figure 34D). A notable consequence of this was the formation of a continuous helix between the MBD, trunk and neck domains, offering a potential mechanism for allosteric communication between the distal GTPase-associated neck domain and the membrane interface.

Crucially, the two-helix MBD was virtually identical to the *in silico* simulated two-helix membrane interface that allows Fzo to interface with membrane in a hinge 1 closed conformation (De Vecchis *et al.*, 2017), suggesting BDLP may also be able to interface with membrane in a hinge 1 closed conformation. This observation has broader implications for the mitofusin membrane interface, as both mitofusins are predicted to have two transmembrane helices in an analogous position (Cohen & Tareste, 2018). The $BDLP_{GMPPNP}$ membrane interface contradicts recent suggestions that the mitofusins adopt an in-out topology, whereby a single transmembrane helix traverses the OMM such that the equivalent

of H21 (trunk) and H22 (neck) of BDLP protrude into the mitochondrial inter-membrane space (Figure 40) (Mattie *et al.*, 2018). The stable four-helix neck domain bundles of mitofusin crystal structures also support mitofusins adopting a BDLP-like membrane conformation that spans the bilayer but does not cross it (Qi *et al.*, 2016; Li *et al.*, 2019).

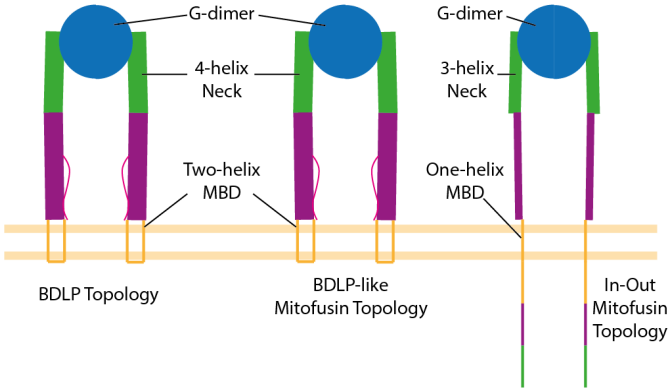


**Figure 40. Proposed Mitofusin Topologies.**
The proposed mitofusin in-out topology (Mattie *et al.*, 2018), where the mitofusins protrude into the inter-membrane space of mitochondria, is inconsistent with the membrane-bound BDLP structures presented in this study.

The BDLP MBD, which was not identified by hydropathy plots, may also facilitate the identification of membrane interfaces of DRPs that bioinformatic approaches have thus far failed to assign a membrane interface to, such as synDLP (Figure 41A & Figure 41B) (Gewehr *et al.*, 2023). Additionally, these results suggest that DRPs such as IniA, which have been assigned a predicted paddle-like membrane interface, may in fact interface with membrane via a BDLP-like MBD (Wang *et al.*, 2019). The predicted paddle and crystal structure-derived conformation of the trunk tip may still hold relevance for the initial stages of BDLP membrane sensing and binding, before refolding of H20 to stably bind the membrane with a two-helix MBD.

The BDLP MBD is also consistent with the conserved DSF feature of distinct membrane-interacting domains situated beyond the trunk tip, such as the dynamin 1 PH domain, Opa1 four-helix paddle, Mgm1 lipid-interacting stalk, or cjDLP2 two-strand β-sheet (Figure 41C) (Mehrotra, Nichols & Ramachandran, 2014; Yan *et al.*, 2020; Liu, Noel & Low, 2018). However,

a distinctive characteristic of the $BDLP_{GMPPNP}$ MBD is the occupation of both bilayer leaflets. Filament reconstructions of dynamin 1, Opa1 and related DRPs indicate embedding exclusively into the outer leaflet to disrupt the bilayer and induce curvature (Faelber *et al.*, 2019; von der Malsburg *et al.*, 2023; Nyenhuis *et al.*, 2023; Zhang *et al.*, 2020a; Rochon *et al.*, 2024; Kalia *et al.*, 2018; Liu *et al.*, 2021a; Jimah *et al.*, 2024). Consequently, the mitofusin- and BDLP-like MBD may be adapted to a unique mechanism of membrane remodelling.

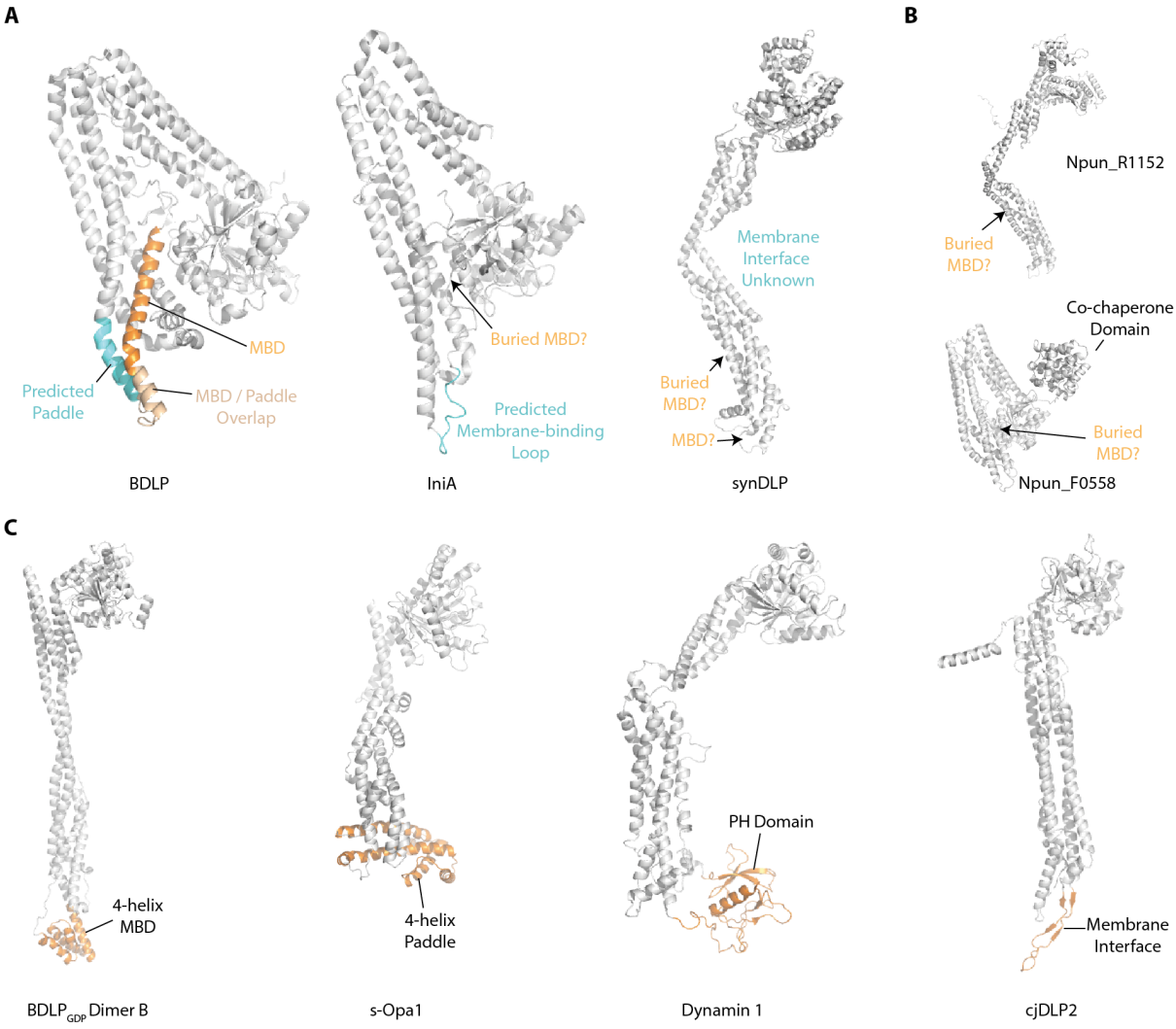


**Figure 41. DSF Conserved Membrane Interface Features.**
**A,** Left: BDLP crystal structure (PDB: 2J68) coloured with the previously predicted paddle (cyan) and cryo-EM determined MBD (orange). Overlapping regions also highlighted. Middle: IniA crystal stricture (PDB: 6J72). Cyan = proposed membrane interface. Note the similarity to BDLP indicating it may also possess a BDLP-like buried MBD. Right: cryo-EM structure of synDLP (PDB: 9EM7), for which no membrane binding domain has been determined, structurally or by bioinformatic analyses. **B,** Alphafold predicted structures of *N. punctiforme* DRPs, Npun_R1152 and Npun_F0558, with suggested buried BDLP-like MBDs highlighted, particularly relevant for Npun_F0558 which is predicted with a BDLP-like

structure. **C,** Comparison of membrane interfaces (orange) of $BDLP_{GDP}$ Dimer B, s-Opa1 (PDB: 8EF7), dynamin 1 (PDB: 6DLU), and cjDLP2 (PDB: 5OWV).

A BDLP MBD affinity for high PG-content liposomes was also demonstrated (Figure 35). Given that PG and PC share similar cylindrical shapes and BDLP exhibited a lower affinity for high PC content liposomes and ETE liposomes (with lower anionic lipid content), the BDLP lipid affinity assays suggested that the lipid preference was related to lipid charge rather than shape. A similar distinction between preference for negative charge over conical lipid shape had been demonstrated in Mgm1 (Yan *et al.*, 2020). More broadly, membrane binding domains of different DRPs also confer specificity for certain lipids. For instance, Drp1 binds cardiolipin and synDLP demonstrates a preference for negatively charged lipids (Francy *et al.*, 2017; Gewehr *et al.*, 2023). Furthermore, analogous to PG and not ETE liposomes stimulating BDLP GTP turnover, the dynamin 1 PH domain can bind negatively charged lipids, but only PI(4,5)P2 stimulates GTPase activity (Ford & Chappie, 2019).

Overall, the identification of the BDLP MBD has implications for understanding how mitofusins interface with membranes and demonstrates the conserved DSF principle of a distinct membrane binding domain that confers high affinity for specific lipids.

### 4.3.4 Conclusions and Outstanding Questions

This chapter has provided novel insights into the function and mechanism of BDLP-mediated membrane remodelling. The specific upregulation of BDLP during hormogonium development in *N. punctiforme* suggests a specialised role in this motile life cycle stage. Cryo-CLEM revealed BDLP's association with remodelled thylakoid membranes in the form of hexII nanoparticles, indicating a potential role in mediating stable lipid phase transitions. The high-resolution cryo-EM structure of $BDLP_{GMPPNP}$ filaments elucidated a novel two-helix membrane binding domain spanning both bilayer leaflets and the mechanism of GTP coordination and catalysis via a tight G-dimer interface. Furthermore, BDLP exhibited high affinity for anionic lipids, specifically PG, which stimulated its GTPase activity.

These findings raise several important questions. (1) The role of GTP hydrolysis in BDLP-mediated membrane remodelling, and how the membrane-bound GDP-bound state differs structurally and functionally from the GMPPNP-bound state. (2) Whether BDLP can directly

induce stable lipid phase transitions from the lamellar to hexII phase, and if so, the underlying mechanism. (3) Given the stimulation of GTPase activity by PG lipids, the influence of lipid composition on BDLP's membrane remodelling activity. Addressing these questions will provide a more comprehensive understanding of BDLP's mechanism and its potential role in regulating thylakoid membrane dynamics during hormogonium development. These insights may shed light on the broader mechanisms of membrane remodelling by bacterial DRPs and their eukaryotic homologues, particularly the mitofusins.

# Chapter 5: GDP-Bound BDLP Filament Structure

## 5.1 Introduction and Aims

The dynamin superfamily (DSF) of GTPases plays crucial roles in membrane remodelling across all domains of life (Jimah & Hinshaw, 2019). While eukaryotic dynamins and dynamin-related proteins (DRPs) often have well-defined roles in membrane fission or fusion, bacterial DRPs exhibit more diverse functions that are less well characterised (Bohuszewicz, Liu & Low, 2016). Chapter 4 explored the structure and function of bacterial dynamin-like protein (BDLP) from the cyanobacterium *Nostoc punctiforme*, revealing its specific upregulation during hormogonium development and its putative association with the remodelling of thylakoid membranes into inverse hexagonal (HexII) phase nanoparticles. The high-resolution cryo-EM structure of the GMPPNP-bound BDLP filament provided insights into its helical ultrastructure, nucleotide coordination and catalytic mechanism, and membrane binding mechanism. However, several key questions remained unanswered, particularly regarding the role of GTP hydrolysis in BDLP-mediated membrane remodelling and the direct involvement of BDLP in mediating stable lipid phase changes.

This chapter aims to address these unresolved questions by investigating the structure and function of GDP-bound BDLP filaments. While Chapter 4 demonstrated that BDLP can effectively bind phosphatidylglycerol (PG) liposomes in both apo and GDP-bound states, the structural basis for this interaction and its functional implications remained unclear. Furthermore, the mechanism by which GTP hydrolysis might drive membrane remodelling and potentially facilitate lipid phase transitions was not fully elucidated.

The study of GDP-bound BDLP filaments is particularly relevant given the complex roles of nucleotide state in DSF-mediated membrane remodelling. In classical dynamins, GTP hydrolysis drives conformational changes that lead to membrane fission (Antonny *et al.*, 2016). However, the mechanisms of membrane remodelling by bacterial DRPs and mitofusins are less well understood. By comparing the structures of GMPPNP- and GDP-bound BDLP

filaments, this chapter aims to provide new insights into how nucleotide state influences the architecture and membrane interface of these membrane-remodelling machines.

Additionally, while Chapter 4 provided evidence for BDLP's association with HexII nanoparticles in hormogonia, direct proof of BDLP's ability to mediate stable lipid phase changes was not obtained. This chapter seeks to address this gap by investigating whether BDLP alone is sufficient to induce and stabilise lipid phase transitions *in vitro*. Such findings would have significant implications for our understanding of how bacterial DRPs contribute to membrane dynamics and potentially regulate cellular processes through modulation of lipid phases.

Using cryo-EM reconstructions of GDP-bound filaments and exploration of BDLP-mediated remodelling of liposomes *in vitro*, this chapter aims to provide a more comprehensive understanding of BDLP's mechanism of action, its role in membrane remodelling, and its potential function in regulating thylakoid membrane dynamics during hormogonium development in *N. punctiforme*. These insights may also shed light on the broader mechanisms of membrane remodelling by bacterial DRPs and their eukaryotic homologues, particularly the mitofusins.

## 5.2 Results and Analysis

### 5.2.1 A GDP-Bound BDLP Filament Reveals Additional Residues that Displace Lipids from the Bilayer

In Chapter 4, the capacity of BDLP to efficiently bind PG liposomes in the apo and GDP-bound states was demonstrated. This observation contrasted with the affinity of GDP-bound BDLP for ETE liposomes, to which BDLP can only weakly bind and assemble upon as disordered flexible filaments (Low & Löwe, 2006). This finding suggested that PG liposomes represent a valuable tool for elucidating how nucleotide hydrolysis affects the membrane-bound BDLP conformation and the role of nucleotide hydrolysis in BDLP-mediated thylakoid remodelling.

#### 5.2.1.1 BDLP can tubulate PG liposomes when GDP-bound

To investigate the impact of nucleotide hydrolysis on the membrane-bound BDLP structure, GDP-bound or apo BDLP was incubated with PG liposomes under identical conditions previously utilised to generate GMPPNP-bound BDLP protein-lipid filaments. NS-EM analysis

of the apo sample revealed that BDLP did not constrict liposomes or form any discernible ordered decorations (Figure 42A), despite efficiently binding these liposomes (Figure 35). In contrast, GDP-bound BDLP formed extensive ordered filaments on PG liposomes reminiscent of the $BDLP_{GMPPNP}$ assembly (Figure 42B). Collectively, these observations suggested that the presence of anionic membranes alone is sufficient for BDLP membrane tethering, likely in an overall closed conformation that would still permit MBD bilayer penetration in an Fzo-like manner (Low & Löwe, 2006; De Vecchis *et al.*, 2017). Furthermore, these results indicated that self-assembly into helical polymers requires nucleotide binding to induce G-dimerisation, highlighting the G-dimer interface as the critical assembly interface of BDLP filaments.

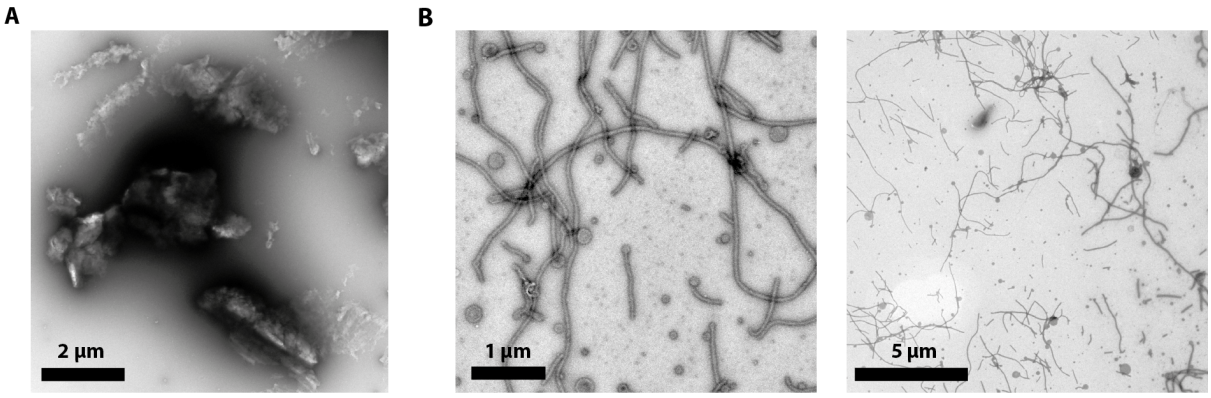


**Figure 42. NS-EM Analysis of PG Liposome-bound BDLP.**
**A,** Apo BDLP does not form ordered arrays on PG Liposomes. **B,** GDP-bound BDLP tubulates PG liposomes into long filaments.

### 5.2.1.2 Helical Reconstruction of a Super-constricted GDP-bound BDLP Filament

To understand the impact of nucleotide hydrolysis on the ultrastructure and membrane interface of BDLP protein-lipid filaments, GDP-bound BDLP-PG liposome filaments were vitrified via plunge freezing and visualised using cryo-EM. The GDP-bound BDLP filament diameter was 450 Å, which was significantly smaller than that of $BDLP_{GMPPNP(PG)}$ (530 Å), suggesting that nucleotide hydrolysis induces super-constriction of the filament. A minor population of thicker filaments was also present, and filaments exhibited the capacity to transition between thick and thin forms along their length (Figure 43A), suggesting conformational bistability within the filament when GDP-bound.

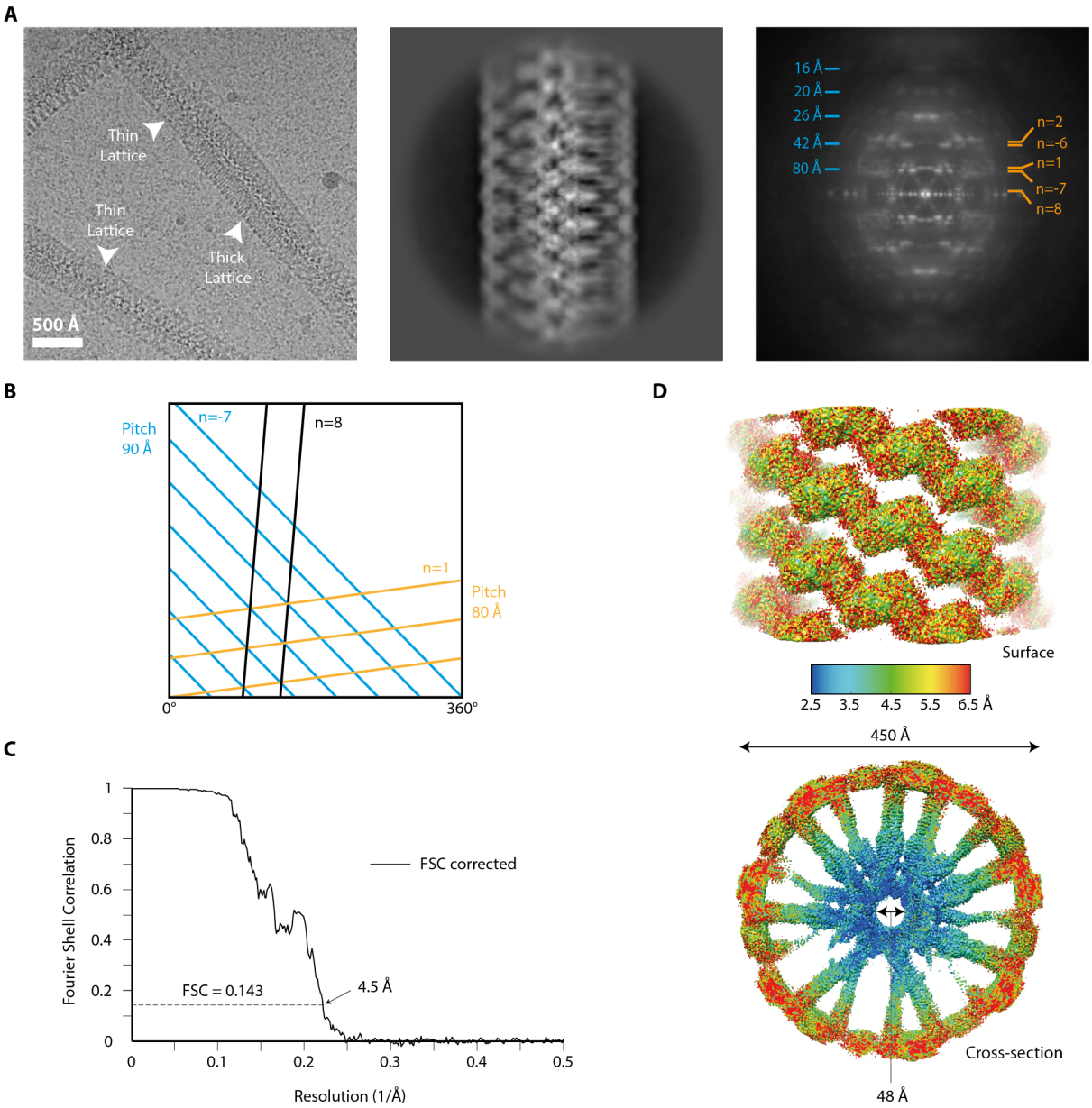


**Figure 43. BDLP$_{GDP}$ Filament Indexing and Reconstruction.**
**A,** Left: Representative cryo-EM micrograph of GDP-bound BDLP-PG liposome filaments, showing thick and thin lattices that can transition along the filament length. Middle: Thin filament 2D class average. Right: Summed Fourier transform of filaments aligned to the 2D class average, showing indexing of key Bessel orders. **B,** 2D representation of the filament lattice showing arrangement of key Bessel orders. **C,** FSC curve of the filament map. **D,** Filament map coloured by local resolution estimates and contoured at 3σ.

The filament coordinates were picked using crYOLO and the filaments were segmented into boxes which were sorted by 2D classification using RELION-5 (Wagner *et al.*, 2019; Burt *et al.*, 2024). As the 450 Å diameter filaments constituted the major lattice population, summed Fourier transforms of boxed segments of these filaments aligned by 2D classification were

analysed. This revealed that the thin filaments comprised a homogeneous population of a single helical lattice (Figure 43A). This lattice was indexed in Fourier space, and key Bessel orders were assigned to a left-handed 7-start helical family and a right-handed 1-start helical family that represented the fundamental repeat of the lattice (Figure 43B). Utilising a helical rise and twist of 3.47 Å and 94.9° that described the right-handed 1-start helical family, a cryo-EM map of the thin filament was refined to an overall resolution of 4.6 Å using the gold-standard FSC IHRSR approach with BLUSH regularisation (Figure 43C) (He & Scheres, 2017; Kimanius *et al.*, 2024). The inner lumen of the filament was constricted to a diameter of 48 Å, consistent with super-constriction of the underlying bilayer, and local resolution estimations indicated higher resolution and order at the inner regions of the map and lower resolution and flexibility at the outer regions (Figure 43D). In contrast to $BDLP_{GMPPNP}$, these findings suggested strong lateral contacts between the MBD and trunk domains, and weaker lateral contacts between the GTPase and neck domains. This indicated that GTP hydrolysis breaks lateral GTPase domain lateral contacts in favour of MBD domain lateral contacts.

#### 5.2.1.3 $BDLP_{GDP}$ Model Building and G-dimer Interface

To understand how nucleotide hydrolysis leads to a super-constricted filament, a model of GDP- and PG liposome-bound BDLP was built. The high local resolution and excellent side chain detail of the MBD and trunk facilitated *de novo* model building of the trunk and MBDs (Figure 44A). However, the GTPase and neck domains exhibited poor resolution. To address this, a focussed map of the asymmetric unit of the filament (a tetramer) was refined to an overall resolution of 5.5 Å (Figure 44B), which provided enhanced detail of the GTPase and neck domains. The resolution of the focussed map was insufficient for *de novo* model building; nevertheless, it permitted rigid-body fitting of the neck domain. Additionally, both the GDP-bound BDLP crystal structure and $BDLP_{GMPPNP}$ G-dimers were fitted into the map. This fitting suggested that a tight $BDLP_{GMPPNP}$-like G-dimer interface was maintained in the GDP-bound filament, as only the $BDLP_{GMPPNP}$ G-dimer correlated well with the density (Figure 44C). Furthermore, the resolution of the focussed refinement map was sufficient to resolve an ordered switch 1 – a key feature of the $BDLP_{GMPPNP}$ G-dimer that is not present in the GDP-bound BDLP crystal structure. The switch 1 density, although observable and indicating order, suggested the switch 1 conformation was not identical to $BDLP_{GMPPNP}$.

Therefore, I concluded that the overall structure of the G-dimer remained unchanged compared to $BDLP_{GMPPNP}$, and the $BDLP_{GMPPNP}$ G-dimer and neck domains were used as initial models that were refined in Phenix and ISOLDE (Liebschner *et al.*, 2019; Croll, 2018). A more detailed description of model construction can be found in Chapter 3 (Section 3.2.10.3.1). Overall, as the tight G-dimer interface was maintained, the map resolution in this region prevented elucidation of structural details to explain how the G-dimer active site differed to $BDLP_{GMPPNP}$ and therefore how nucleotide hydrolysis leads to super-constriction. The tetramer model was fitted into the filament map, and helical parameters were applied to construct a filament model, termed $BDLP_{GDP}$.

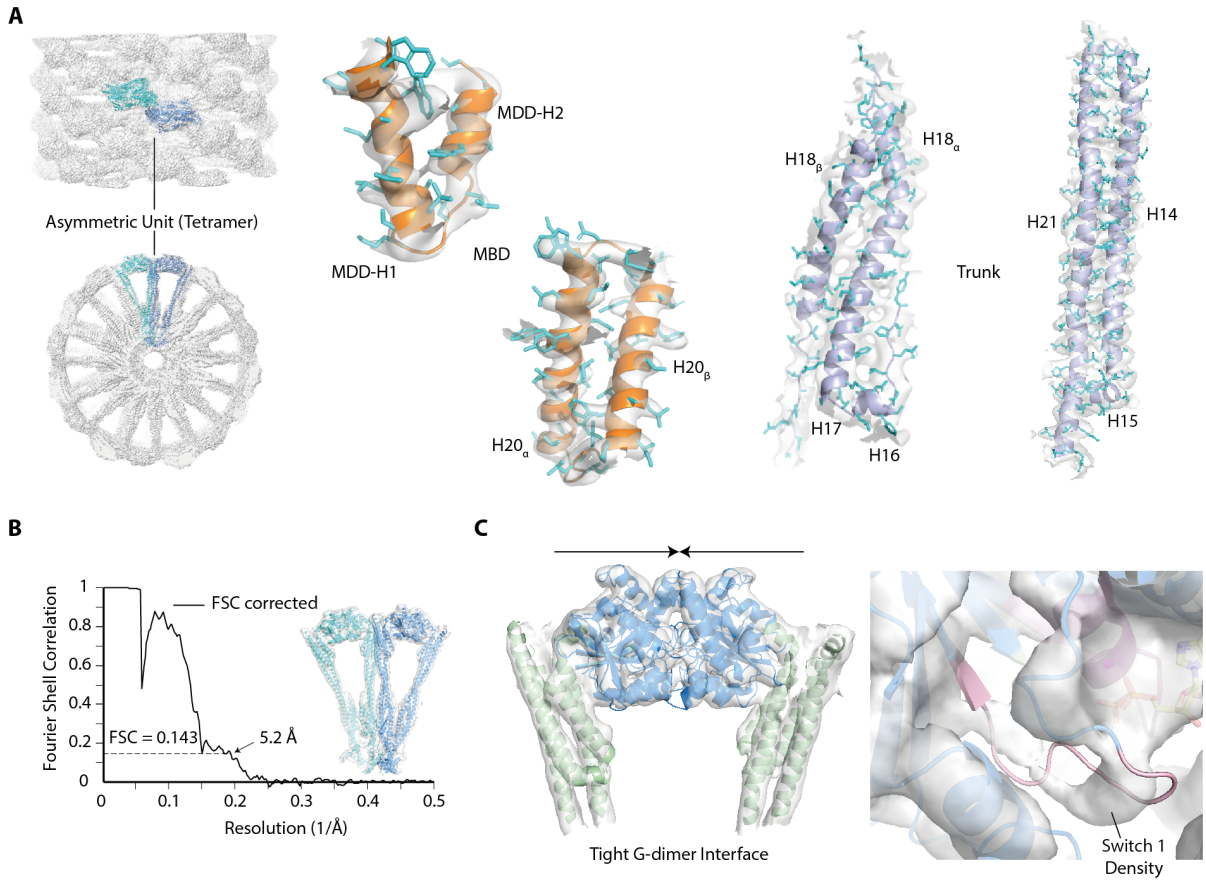


**Figure 44. $BDLP_{GDP}$ Model Building and Tetramer Focussed Refinement.**
**A,** The MBD and trunk were built into the filament map. Fit of the asymmetric unit (tetramer) model in the filament map (left) and MBD and trunk helices highlighted to demonstrate build quality. **B,** FSC curve of a refinement focussed on the central tetramer, with this map and model fit shown. **C,** Fit of the $BDLP_{GMPPNP}$ neck and GTPase domains into the GDP- and PG liposome-bound focussed tetramer map, shown for one dimer and highlighting the tight G-dimer interface that was maintained. Right panel highlights the ordered switch 1 density.

#### 5.2.1.4 Overall $BDLP_{GDP}$ Architecture

The $BDLP_{GDP}$ tetramer (asymmetric unit) comprised two distinct dimers, designated as Dimer A and Dimer B, which associated in a back-to-back arrangement (Figure 45A). Both dimers exhibited an overall structural configuration analogous to $BDLP_{GMPPNP}$ dimers, including the aforementioned tight G-dimer interface. Both dimers displayed broken H13 hinge 2 closed conformations, with $H13_{\alpha}$ oriented perpendicular to the neck and integrated into the GTPase domain. Furthermore, both dimers exhibited an open hinge 1 conformation and MBDs positioned below the trunk, spanning both leaflets of the bilayer. Dimer A and Dimer B associated back-to-back to form a tetramer via two interaction interfaces: one between adjacent neck and GTPase domains, and the other between trunk domains (Figure 45A).

#### 5.2.1.5 Nucleotide Hydrolysis Induces Trunk and MBD Conformational Changes

Given the overarching structural similarities between $BDLP_{GMPPNP}$ and $BDLP_{GDP}$, characterised by their open hinge 1, closed hinge 2 and tight G-dimer conformations, the trunk and MBDs were closely analysed to elucidate the structural changes $BDLP_{GDP}$ undergoes to generate a super-constricted filament. Alignment of $BDLP_{GMPPNP}$, Dimer A, and Dimer B monomers (anchored by their GTPase domains) revealed that neck domains were not affected by nucleotide state (Figure 45B). This suggested that hinge 2 flexibility is limited, and its conformation is unaffected by nucleotide hydrolysis within filaments. However, the $BDLP_{GDP}$ trunk underwent conformational changes and significant rotations about hinge 1. In comparison to the $BDLP_{GMPPNP}$ trunk, the trunk helices of Dimer A and Dimer B were rotated in opposite directions by 6° and 7°, respectively. The Dimer A trunk rotation did not affect the relative position of the MBD, which suggested this rotation facilitated trunk domain lateral contacts. Conversely, the 7° Dimer B trunk rotation was reflected in a 7° MBD displacement relative to the $BDLP_{GMPPNP}$ and Dimer A MBDs, suggesting this trunk rotation facilitated lateral MBD contacts. In the trunk domains of both $BDLP_{GDP}$ dimers, there was a helix break in H18 that created two anti-parallel helices ($H18_{\alpha}$ and $H18_{\beta}$) (Figure 45C). This helix break facilitated an increase in the membrane binding interface, mediated by residues 499-543 that connected $H18_{\beta}$ and $H20_{\alpha}$, herein termed the membrane displacement domain (MDD).

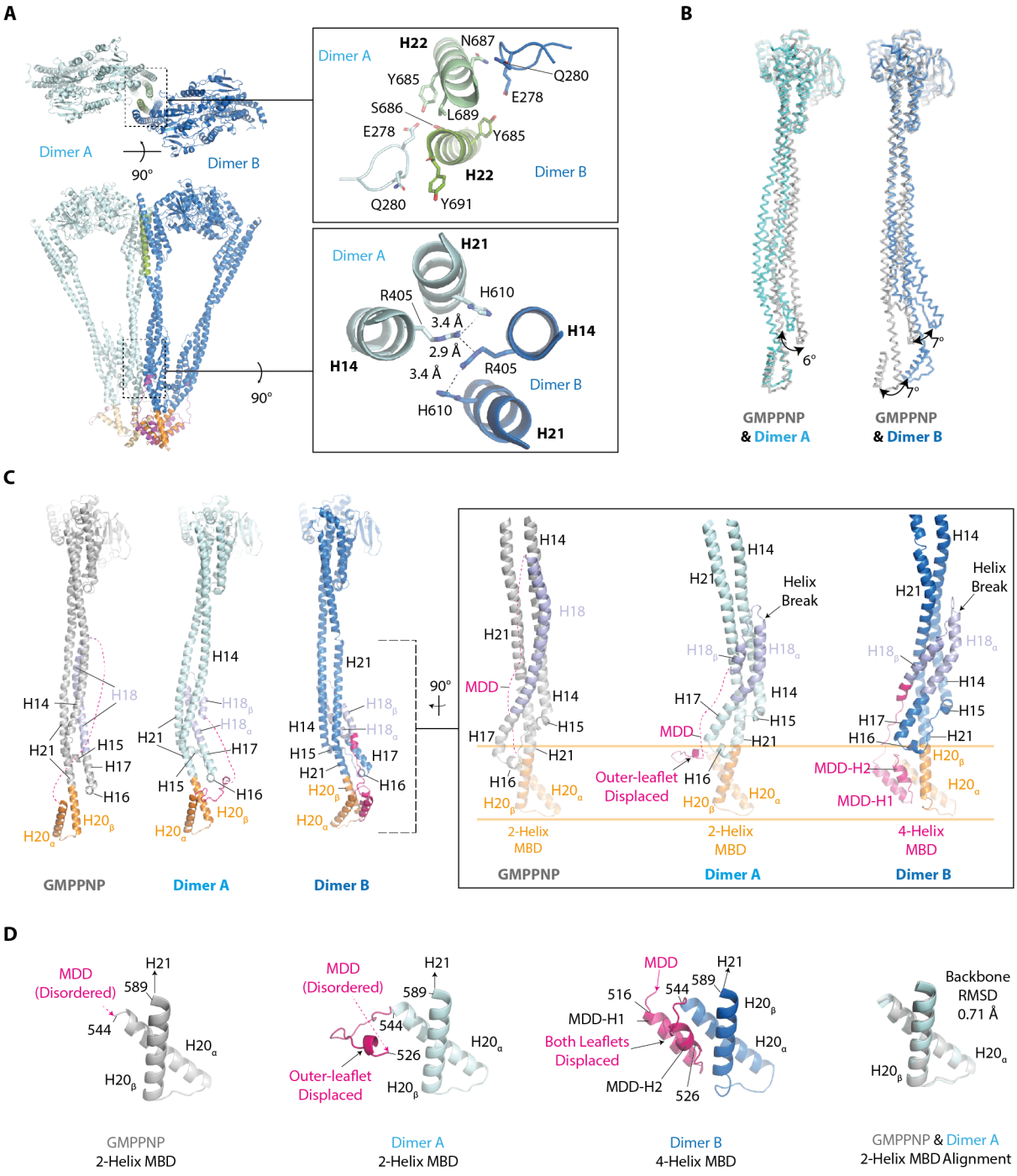


**Figure 45. GTP Hydrolysis-driven Trunk and MBD Conformational Changes.**
$BDLP_{GDP}$ trunk domain conformational changes allow folding of membrane displacement domain into the membrane. **A,** $BDLP_{GDP}$ tetramer formed by back-to-back association of two G-dimers – Dimer A (cyan) and Dimer B (dark blue). Zoom panels highlight back-to-back interaction interfaces. **B,** GTPase domain-anchored alignment of $BDLP_{GMPPNP}$ monomer (grey) with a Dimer A monomer (cyan) or Dimer B monomer (Dark Blue), highlighting relative rotations of the trunk. **C,** Cartoon representation of the monomers aligned in panel B. Zoom panel shows the unique trunk and MBD conformations of Dimer A and Dimer B, highlighting the H18 helix break and increase in the membrane-binding interface relative to $BDLP_{GMPPNP}$, facilitated by ordering of the membrane displacement domain (MDD) within the bilayer. Orange = MBD, pink = MDD. Orange lines indicate rough position of the bilayer **D,** $BDLP_{GDP}$ has more extensive MBDs. Comparison of the $BDLP_{GMPPNP}$ and $BDLP_{GDP}$ Dimer A and Dimer B MBDs. Far right: alignment of the Dimer A (cyan) and $BDLP_{GMPPNP}$ (grey) two-helix MBDs.

In the $BDLP_{GMPPNP}$ structure the MDD was disordered. In the $BDLP_{GDP}$ structure, Dimer A and Dimer B adopted two distinct MDD conformations (Figure 45D). The Dimer A MDD disrupted outer-leaflet lipids via residues 526-543, whereas the Dimer B MDD formed two transmembrane helices (residues 516-543) that inserted across both bilayer leaflets and associated with the $H20_{\alpha}$-$H20_{\beta}$ two-helix MBD to form a four-helix MBD (MDD-H1, MDD-H2, $H20_{\alpha}$ and $H20_{\beta}$). It is noteworthy that the Dimer A MDD residues connecting H18 and serine-526 were disordered, whilst the Dimer B MDD residues connecting H18 and glycine-516 formed an ordered connecting loop. This observation suggested that the four-helix MBD in Dimer B represented the maximal BDLP membrane binding unit, as no disordered residues remained to penetrate the membrane further. The two-helix MBD ($H20_{\alpha}$ and $H20_{\beta}$) was present in all lipid-bound BDLP structures, and the two-helix MBDs of $BDLP_{GMPPNP}$ and Dimer A aligned precisely with a backbone RMSD of 0.71 Å (Figure 45G). This indicated that the two-helix MBD constituted the minimal BDLP membrane binding unit, consistent with the Fzo and mitofusin two trans-membrane helices (De Vecchis *et al.*, 2017). In summary, the $BDLP_{GDP}$ structure revealed that nucleotide hydrolysis induces trunk conformational changes that facilitate an increase in the membrane interface beyond the $BDLP_{GMPPNP}$ two-helix MBD, mediated by the ordering of disordered MDD residues within the membrane.

### 5.2.2 Comparison of $BDLP_{GDP}$ and $BDLP_{GMPPNP}$ Filament Architectures Reveals that GTP Hydrolysis Breaks Lateral GTPase Domain Contacts

The super-constricted $BDLP_{GDP}$ filament exhibited markedly different local resolution estimations, indicating that nucleotide state determines whether lateral contacts are strong between the GTPase domains or MBDs. Given that the $BDLP_{GDP}$ trunk and MBDs demonstrated significant rotations (Figure 45), it was postulated that the formation of strong MBD and trunk lateral contacts, in lieu of strong lateral GTPase domain contacts, constitutes a key mechanism of super-constriction and membrane remodelling. To investigate this hypothesis, the filament architectures of $BDLP_{GMPPNP}$ and $BDLP_{GDP}$ were compared (Figure 46A). Both filaments exhibited left-handed helical rungs, with these fundamental repeats comprising back-to-back associations of $BDLP_{GMPPNP}$ dimers or $BDLP_{GDP}$ tetramers. The rungs corresponded to the left-handed 10- and 7-start helical repeats of the $BDLP_{GMPPNP}$ and $BDLP_{GDP}$ filaments, respectively. In both filaments, the intra-rung back-to-back interactions

between asymmetric units were mediated by neck domain H22 packing, while $BDLP_{GMPPNP}$ dimers also interacted through hydrophobic packing between $H20_{\alpha}$ MBD helices (Figure 46B).

Notably, $BDLP_{GMPPNP}$ demonstrated strong lateral GTPase domain associations between rungs along the filament axis, whereas $BDLP_{GDP}$ lateral GTPase domain interactions between rungs were entirely disrupted, resulting in rungs functioning as independent polymeric units at the GTPase and neck domain level (Figure 46A). This observation was consistent with the lower local resolution estimates and increased flexibility observed in the peripheral regions of the $BDLP_{GDP}$ filament map. It also suggested a rung-pivoting mechanism for achieving super-constriction upon GTP hydrolysis. The $BDLP_{GMPPNP}$ inter-rung GTPase domain interactions were facilitated by parallel-displaced π-stacking interactions between adjacent tyrosine-137 residues on H4 (Figure 46C).

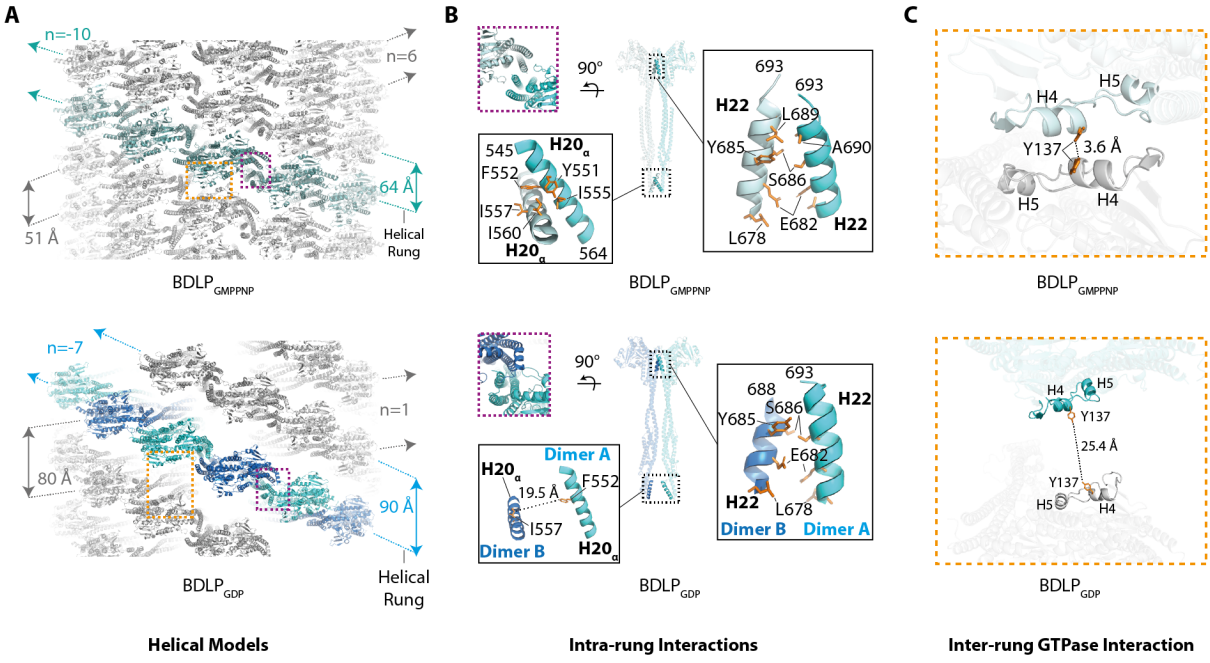


**Figure 46. Architecture of the $BDLP_{GMPPNP}$ and $BDLP_{GDP}$ Filaments.**
Nucleotide hydrolysis breaks a Y137 inter-rung pi-stacking interaction, causing separation of rungs at the GTPase domain level. **A,** $BDLP_{GMPPNP}$ (top) and $BDLP_{GDP}$ (bottom) helical filament models annotated with key helical repeats. Left-handed 10-start ($BDLP_{GMPPNP}$) and 7- start ($BDLP_{GDP}$) helical rungs are highlighted in blue. For $BDLP_{GDP}$, Dimer A subunits within the rung are coloured cyan, and Dimer B subunits are dark blue. Purple boxes highlight intra-rung interactions between asymmetric units and orange boxes highlight inter-rung interactions. **B**, Intra-rung back-to-back interactions between dimers ($BDLP_{GMPPNP}$ – top), and tetramers ($BDLP_{GDP}$ – bottom). These interactions correspond to the purple boxes highlighted in panel A. **C**, Inter-rung π-stacking interactions between tyrosine-137 residues in $BDLP_{GMPPNP}$ (top) are broken in $BDLP_{GDP}$ (bottom). This interaction is represented by the orange boxes in panel A.

To understand the influence of GTP hydrolysis on this π-stacking interaction, the positions of tyrosine-137 and H4 were compared to the positions of key catalytic motifs in the G-dimer. H4 was connected via a short loop to H5, the position of which was stabilised by interactions with switch 2 and, in trans across the G-dimer interface, H9 (Figure 47A). When compared to the loose off-membrane G-dimer, H9 is significantly displaced to contribute to contribute to the tight G-dimer interface (Figure 33E). Therefore, both these stabilising interactions are susceptible to influence by nucleotide state, G-dimerisation, and the catalytic cycle. Moreover, switch 1 residues that formed a hydrophobic network with the H4-H5 connecting loop neighboured the conserved magnesium-coordinating threonine-103 residue (Figure 47B). In $BDLP_{GDP}$, the tight G-dimer interface is maintained, and ordered switch 1 density is observed (Figure 44C). Additionally, the $BDLP_{GDP}$ density suggests no significant shift in the positioning of H4 relative to its position in $BDLP_{GMPPNP}$. The limited $BDLP_{GDP}$ G-dimer resolution therefore precludes a comprehensive understanding of the direct mechanism by which GTP hydrolysis could influence the positioning of H4. However, it is plausible that subtle shifts in the key catalytic motifs, particularly those observed in switch 1 (Figure 44D), may suffice to destabilise inter-rung tyrosine-137 interactions. The interaction network between H4-H5 and switch 1 is disrupted in the apo state (Low & Löwe, 2006), demonstrating both the capacity to disrupt the network of interactions that positions tyrosine-137 and the conformational flexibility of switch 1 in response to nucleotide state.

In summary, left-handed helical rungs were observed to be a stable assembly of $BDLP_{GMPPNP}$ and $BDLP_{GDP}$. In $BDLP_{GMPPNP}$, rungs were stapled together by an inter-rung π-stacking of tyrosine-137 residues, and this interaction was disrupted in $BDLP_{GDP}$, resulting in rung separation. Tyrosine-137 is situated in proximity to residues that form direct interactions with conserved catalytic motifs, and this may represent a mechanism by which GTP hydrolysis mediates the disruption of inter-rung GTPase domain contacts.

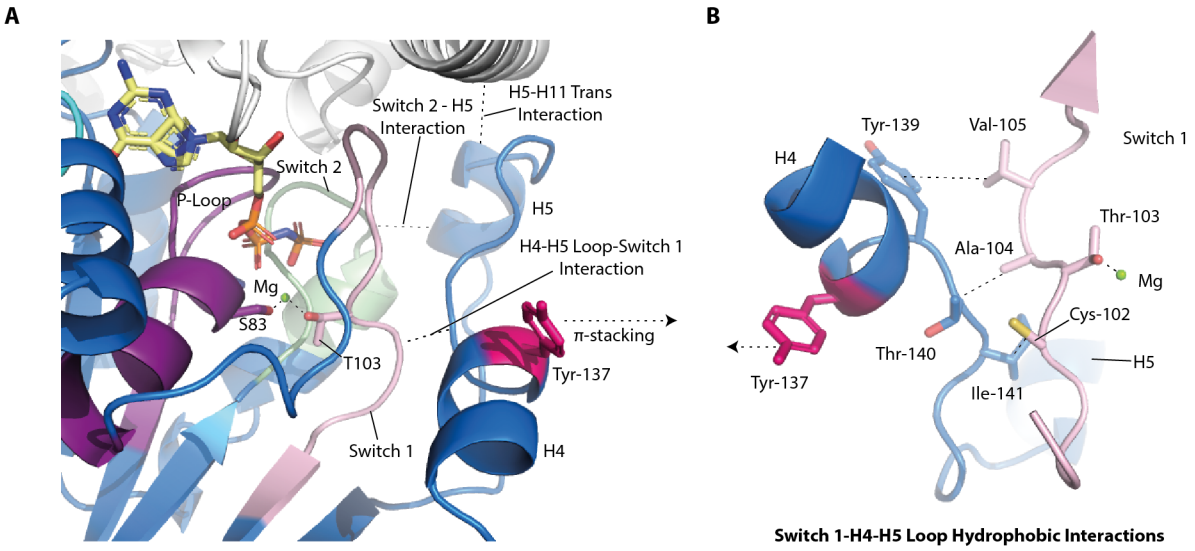


**Figure 47. Positioning of Conserved Catalytic Motifs in the BDLP$_{GMPPNP}$ G-dimer Relative to Tyrosine-137.**
**A,** BDLP$_{GMPPNP}$ model, showcasing interactions between H5 and the H4-H5 connecting loop and the conserved catalytic motifs. Tyrosine-137 (pink) is proximal to these interactions. **B,** Hydrophobic interactions between switch 1 and the H4-H5 connecting loop, proximal to tyrosine-137.

### 5.2.3 Nucleotide Hydrolysis Drives Membrane Displacement by Increasing Inter-rung MBD Contacts

The expanded BDLP$_{GDP}$ membrane interface and the higher local resolution estimates in this region suggested that the GTPase domain rung separation and trunk and MBD conformational changes resulted in extensive lateral contacts between MBDs. This also suggested a rung-pivoting mechanism to achieve super-constriction, whereby nucleotide hydrolysis drives increased contacts between MBDs to displace lipids and allow tighter constriction. To understand how MBD lateral contacts were formed and facilitated super-constriction, the helical architecture of the BDLP$_{GMPPNP}$ and BDLP$_{GDP}$ MBDs were compared. In both filaments, lateral interactions between the bilayer-spanning MBDs resulted in the membrane interface region being predominantly composed of protein, indicating significant lipid displacement from the bilayer. However, upon examination of the filament lumen surface, right-handed helical channels devoid of protein density at the membrane interface were observed (Figure 48A & Figure 48B). The fundamental building blocks of these helical channels were the gaps between MBDs of individual G-dimers. Within the helical lattice, the inter-rung alignment of these basic units formed the helical channels, which followed the right-handed 6-start (BDLP$_{GMPPNP}$) or 1-start (BDLP$_{GDP}$) helical repeats. Additionally, the helical channels were lined

with hydrophobic sidechains (Figure 48C & Figure 48D). This observation suggested that whilst lipid density was not observed within the filament maps, loosely ordered lipids were accommodated by the hydrophobic helical channels, herein termed the lipid channels (LCs).

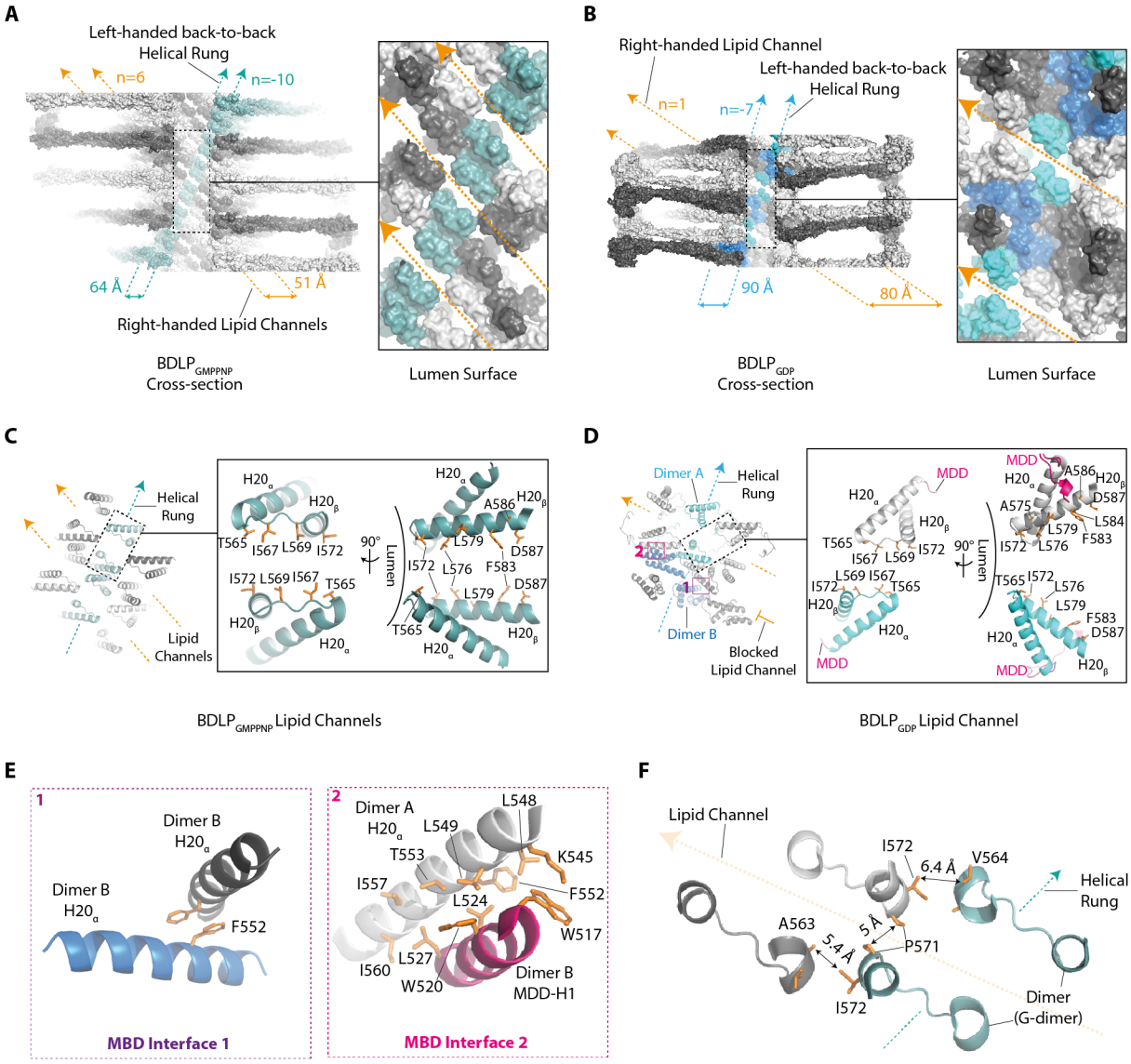


**Figure 48. MBD Helical Architecture and Lipid Channel Formation.**
Hydrophobic helical channels are formed at the lumen surface of BDLP filaments. **A-B,** Surface representation of the BDLP$_{GMPPNP}$ (**A**) and BDLP$_{GDP}$ (**B**) filament cross-section. Zoom panels highlight the lumen surface. Orange arrows indicate the right-handed 6- or 1-start helical repeats that the lipid channels follow. **A,** Teal highlights a left-handed 10-start helical rung. **B,** Blue highlights a left-handed 7-start helical rung, with Dimer A coloured cyan and Dimer B coloured dark blue. **C-D,** Lumen surface from panels A and B shown in cartoon representation. Zoom panels highlight the helices and hydrophobic residues that line the lipid channels. **C,** Each dimer of BDLP$_{GMPPNP}$ contributes to a lipid channel. **D,** Dimer B MBD arrangement blocks lipid channel formation in BDLP$_{GDP}$, such that only Dimer A contributes to lipid channel formation. **E,** Two BDLP$_{GDP}$ key MBD interfaces that allow tight MBD packing. Interfaces 1 and 2 are highlighted in panel D by purple and pink boxes respectively. **F,**

$BDLP_{GMPPNP}$ MBDs are loosely packed, and do not form tight inter-rung hydrophobic packing interactions.

$BDLP_{GDP}$ displaced significantly more lipids from the membrane than $BDLP_{GMPPNP}$. Whilst each $BDLP_{GMPPNP}$ dimer contributed to the formation of a LC between its MBDs (Figure 48C), $BDLP_{GDP}$ only formed a LC between Dimer A MBDs and not Dimer B MBDs (Figure 48D). The formation of a LC between Dimer B MBDs was prevented by the $BDLP_{GDP}$ trunk and MBD rotations, which resulted in tight inter-rung lateral contacts between Dimer B MBDs, thereby excluding lipids from the region. Two primary interfaces contributed to the strong lateral MBD contacts in $BDLP_{GDP}$ (Figure 48E). Firstly, a π-stacking interaction was formed between adjacent Dimer B H20 helices, which explained why $BDLP_{GDP}$ did not exhibit the intra-rung MBD contacts between $H20_{\alpha}$ helices observed in $BDLP_{GMPPNP}$ (Figure 46B). Secondly, inter-rung contacts between Dimer B and Dimer A were facilitated by hydrophobic packing of MDD-H1 (Dimer B) against $H20_{\alpha}$ (Dimer A). This interaction would not have been possible had the Dimer B MDD not rearranged to form additional transmembrane helices and a four-helix MBD. In contrast, MBDs did not strongly interact in the $BDLP_{GMPPNP}$ filament, consistent with the lower local resolution in this area and its minimal two-helix MBDs. Indeed, hydrophobic sidechains at the inter-rung MBD interfaces of $BDLP_{GMPPNP}$ were spaced at least 5 Å apart, suggesting weak interactions only (Figure 48F). Collectively, this analysis indicated that MBD positioning, and the helical architecture, were determined by inter-rung interactions between MBDs in $BDLP_{GDP}$ and by inter-rung GTPase domain interactions in $BDLP_{GMPPNP}$. The $BDLP_{GDP}$ trunk conformational changes and MBD expansion (mediated by ordering of MDD residues in the membrane) facilitated extensive MBD contacts that allowed $BDLP_{GDP}$ to displace more lipids from the bilayer to achieve greater membrane constriction.

To understand why lipids were confined to helical channels and the mechanistic function of the LCs, the properties of the LCs were analysed. Analysis of the surface potential of the $BDLP_{GMPPNP}$ LC revealed large neutral patches mediated by the hydrophobic side chains that lined the channel, which could preferentially interact with lipid acyl chains (Figure 49A). Moreover, the lumen-distal end of the channel surface was coated with a negatively charged patch, providing evidence that the LCs accommodated only inner leaflet lipids. Additionally, the lumen-exposed surface of the channel exhibited small positively charged pockets, which

may serve as sites of anionic outer-leaflet lipid head group coordination. Small angle x-ray and neutron scattering data suggests that a single PG molecule occupies ~1200 $Å^3$ volume in fluid bilayers at 30 °C (Pan *et al.*, 2012). Assuming a cylindrical PG shape, this would equate to a cylinder with a diameter of ~9 Å and length of ~18.5 Å (Figure 49B). To determine the number of lipids accommodated by the LC, the dimensions of the $BDLP_{GMPPNP}$ LCs were analysed. The lumen-proximal end of the channel exhibited a width of 10-11 Å, suggesting that one PG lipid could be accommodated across its width (Figure 49C). Opposing phenylalanine-583 residues functioned as 'caps' to the lipid channel, situated below the negatively charged patches and 25 Å from the lumen surface. This demonstrated that only inner-leaflet lipids were accommodated by the LCs, revealing how BDLP achieved tight bilayer constriction by complete disruption of the outer leaflet.

The $BDLP_{GMPPNP}$ LC geometry was subsequently compared the $BDLP_{GDP}$ LC geometry. The $BDLP_{GDP}$ LC exhibited similar surface potential characteristics (Figure 49D). However, its dimensions differed significantly. Notably, one unit of the LC was formed by inter-rung alignment of MBDs from neighbouring G-dimers. In $BDLP_{GMPPNP}$, one unit of the LC was formed by MBDs of the same G-dimer. Consequently, at the lumen surface, the $BDLP_{GDP}$ LC width ranged from 12 Å to 19 Å, indicating that certain LC regions could potentially accommodate a second PG molecule across its width (Figure 49E). Moreover, the height of the phenylalanine-583 caps was reduced to 19 Å. This reduction was caused by tilting of opposing MBDs that lined the LC, which additionally resulted in a conical LC shape with a lumen-distal width of up to 45 Å.

In conclusion, two principal alterations in the LC geometry are induced by GTP hydrolysis. Firstly, nucleotide hydrolysis diminishes the LC abundance within the filament. In $BDLP_{GMPPNP}$, each G-dimer contributes to a LC, and at any point along the filament axis there were 6 identical LCs that followed the right-handed 6-start helical repeat. In $BDLP_{GDP}$, tight MBD lateral contacts resulted in only a single LC being present at any point along the filament axis, which followed the 1-start helical repeat. This facilitated reduced the lipid-content in the $BDLP_{GDP}$ filament to achieve super-constriction.

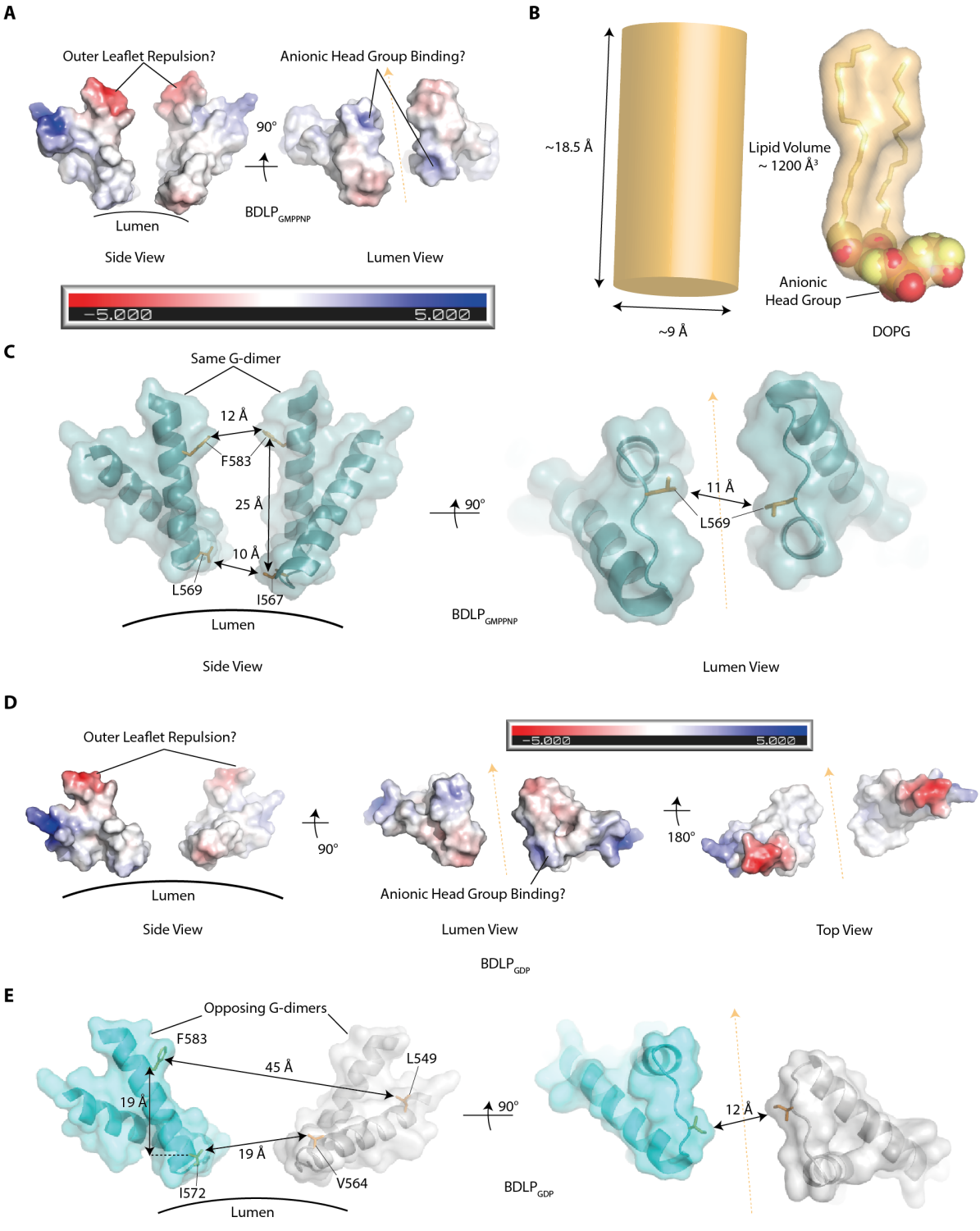


**Figure 49. Lipid Channel Surface Potential and Geometry.**
Nucleotide hydrolysis drives changes in the hydrophobic lipid channel geometry at the filament lumen. **A,** A single BDLP$_{GMPPNP}$ LC unit in surface representation coloured by surface potential. White = neutral (hydrophobic), red = negative charge, blue = positive charge. **B,** Rough dimensions of a PG lipid with 'cylindrical' shape. **C,** Dimensions of the BDLP$_{GMPPNP}$ LC. **D,** Surface potential of a single BDLP$_{GDP}$ LC unit, formed by inter-rung alignment of opposing MBDs. **E,** BDLP$_{GDP}$ LC dimensions and 'conical' shape.

Secondly, GTP hydrolysis induced a change in the shape of the LC. In $BDLP_{GMPPNP}$, the LC geometry suggested it was capable of accommodating approximately one lipid across its width, with a shape complimentary to cylindrical-shaped lipids such as PG. In $BDLP_{GDP}$, the LC may have been capable of accommodating up to two lipid head groups across its width. Furthermore, the region of the LC with hydrophobic acyl chain-interacting patches exhibited an expanded width and reduced height relative to $BDLP_{GMPPNP}$. This suggested that the $BDLP_{GDP}$ LC may have a preference for negative-curvature, hexII phase-favouring, inner leaflet lipids based on its shape – a potential mechanism for increasing the ratio of hexII phase favouring lipids within the filament. Alternatively, the shape of the $BDLP_{GDP}$ LC may force cylindrical lipids to arrange into a high negative curvature configuration or compel cylindrical lipids into a conical shape - a phenomenon that occurs in simulations of cylindrical lipids within hexII phase arrays (Ramezanpour & Tieleman, 2022). Overall, GTP hydrolysis-induced changes in LC geometry, potentially favouring or inducing negative curvature lipid shapes, is consistent with the observation of BDLP-associated remodelling of thylakoids into BDLP-decorated hexII nanoparticles in hormogonia (Figure 27).

#### 5.2.3.1 Lateral Contacts in $BDLP_{GMPPNP}$ are Consistent with those of $BDLP_{GMPPNP(PG)}$

I formed the $BDLP_{GDP}$ filaments on PG liposome templates and the $BDLP_{GMPPNP}$ filaments on ETE liposome templates. To confirm that the LC geometry changes and GTPase rung separation were a direct consequence of nucleotide state change and not a result of lipid composition differences, the helical architecture of $BDLP_{GMPPNP(PG)}$ was also analysed. Consistent with $BDLP_{GMPPNP}$, left-handed helical rungs of back-to-back interacting G-dimers were held together by a tyrosine-137 π-stacking interaction (Figure 50A). The interaction distance was slightly larger at 4.3 Å, compared to 3.6 Å in $BDLP_{GMPPNP}$, suggesting a weaker interaction that may be more readily disrupted by nucleotide hydrolysis. Furthermore, $BDLP_{GMPPNP(PG)}$ exhibited alignment of MBDs in a similar arrangement to $BDLP_{GMPPNP}$ to form helical channels that followed the right-handed 6-start helical repeat (Figure 50B). As the $BDLP_{GMPPNP}$ dimer was utilised to construct the $BDLP_{GMPPNP(PG)}$ helical filament and fit with high correlation into the filament map, it was inferred that the same hydrophobic residues lined the LC and the LC dimensions also remained constant. Overall, analysis of $BDLP_{GMPPNP(PG)}$ confirmed that nucleotide hydrolysis drives GTPase domain rung separation and MBD lateral contact formation to facilitate lipid displacement and alterations in LC geometry.

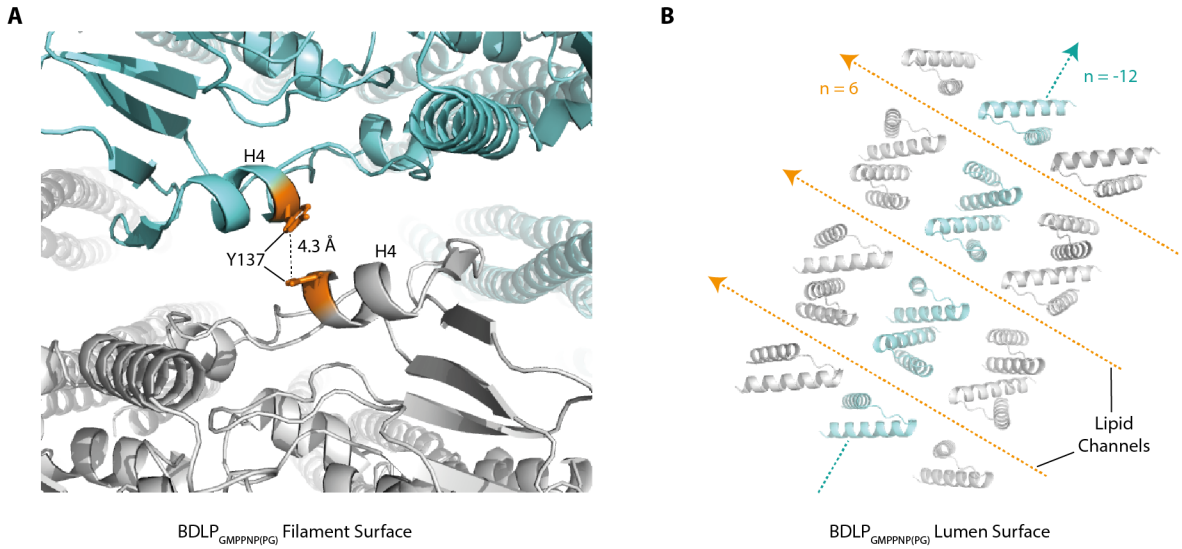


**Figure 50. BDLP$_{GMPPNP(PG)}$ Filament Architecture.**
The BDLP$_{GMPPNP(PG)}$ filament architecture reveals inter-rung interactions and lipid channel formation characteristic of BDLP$_{GMPPNP}$. **A,** Cartoon representation of the BDLP$_{GMPPNP(PG)}$ filament focussing on the inter-rung $\pi$-stacking interaction between adjacent tyrosine-137 residues (orange). **B,** Cartoon representation of the filament viewed from the lumen surface, showing parallel LCs following the right-handed 6-start helical repeat.

## 5.2.4 Thick GDP-bound BDLP Filaments Represent Intermediate States

### 5.2.4.1 Cryo-EM Reconstruction of Thick GDP-bound BDLP Filaments

Given that a population of thicker filaments was present in the PG liposome- and GDP-bound BDLP filament sample, these filaments were analysed to investigate conformational flexibility in GDP-bound filaments, understand what conformational changes are maintained across super-constricted and less-constricted GDP-bound filaments, and to elucidate potential mechanisms of BDLP-mediated thylakoid remodelling. Thick filament segments were sorted by 2D classification. This revealed that this minor population of filaments could be further sub-divided into 'thick' and 'extra-thick' filament lattices, herein termed BDLP$_{GDP(L2)}$ and BDLP$_{GDP(L3)}$ respectively.

### 5.2.4.2 BDLP$_{GDP(L2)}$ Reconstruction

BDLP$_{GDP(L2)}$ filament segments that represented the 'thick' lattice population were aligned by 2D classification and the sum of their Fourier transforms was indexed to elucidate the filament lattice (Figure 51A). Multiple indexing possibilities were evaluated and utilised to reconstruct filament maps, with a single set of parameters yielding the highest resolution

reconstruction with the most distinct map details. These parameters described a filament lattice with a primary right-handed 4-start helical family and left-handed 15-start helical family (Figure 51B). The lattice also exhibited a fundamental 1-start helical family which intersected all lattice points and possessed a rise and twist of 3.47 Å and 94.9°. These helical parameters were utilised to refine a filament map to an overall resolution of 9 Å using the gold-standard FSC IHRSR approach with BLUSH regularisation (Figure 51C).

The $BDLP_{GDP(L2)}$ filament exhibited a diameter of 500 Å and a lumen diameter of 95 Å (Figure 51D). In comparison to the $BDLP_{GMPPNP(PG)}$ filament, this observation suggested that the bilayer was constricted to a similar extent in both filaments and significantly less constricted than in the $BDLP_{GDP}$ filament. Despite a comparable lumen diameter to $BDLP_{GMPPNP(PG)}$, the overall filament diameter was smaller, indicating that nucleotide hydrolysis induces rearrangements that prepare BDLP filaments for super-constriction. The $BDLP_{GDP(L2)}$ map also revealed that G-dimers were arranged in a similar configuration to other BDLP filaments, with G-dimers associating back-to-back in a hinge 1 open conformation to form left-handed helical rungs that followed the 15-start helical family (Figure 51E). Moreover, alignment of MBDs between rungs produced right-handed LCs that followed the right-handed 4-start helical family.

Consistent with $BDLP_{GDP}$, the $BDLP_{GDP(L2)}$ map demonstrated separation of helical rungs, with an absence of inter-rung tyrosine-137 π-stacking interactions. This observation provided additional evidence that GTP hydrolysis drives the separation of filament rungs by disrupting this interaction. However, at the GTPase and neck domain level, novel interfaces between rungs were formed by connections between opposing neck and GTPase domains, which potentially prevented $BDLP_{GDP(L2)}$ from achieving super-constriction. Upon close examination of the trunk region of the map, a H18 break was observed, consistent with the $BDLP_{GDP}$ structure (Figure 51F). This further suggested that the H18 helix break is induced by GTP hydrolysis and primes the MDD residues for membrane displacement.

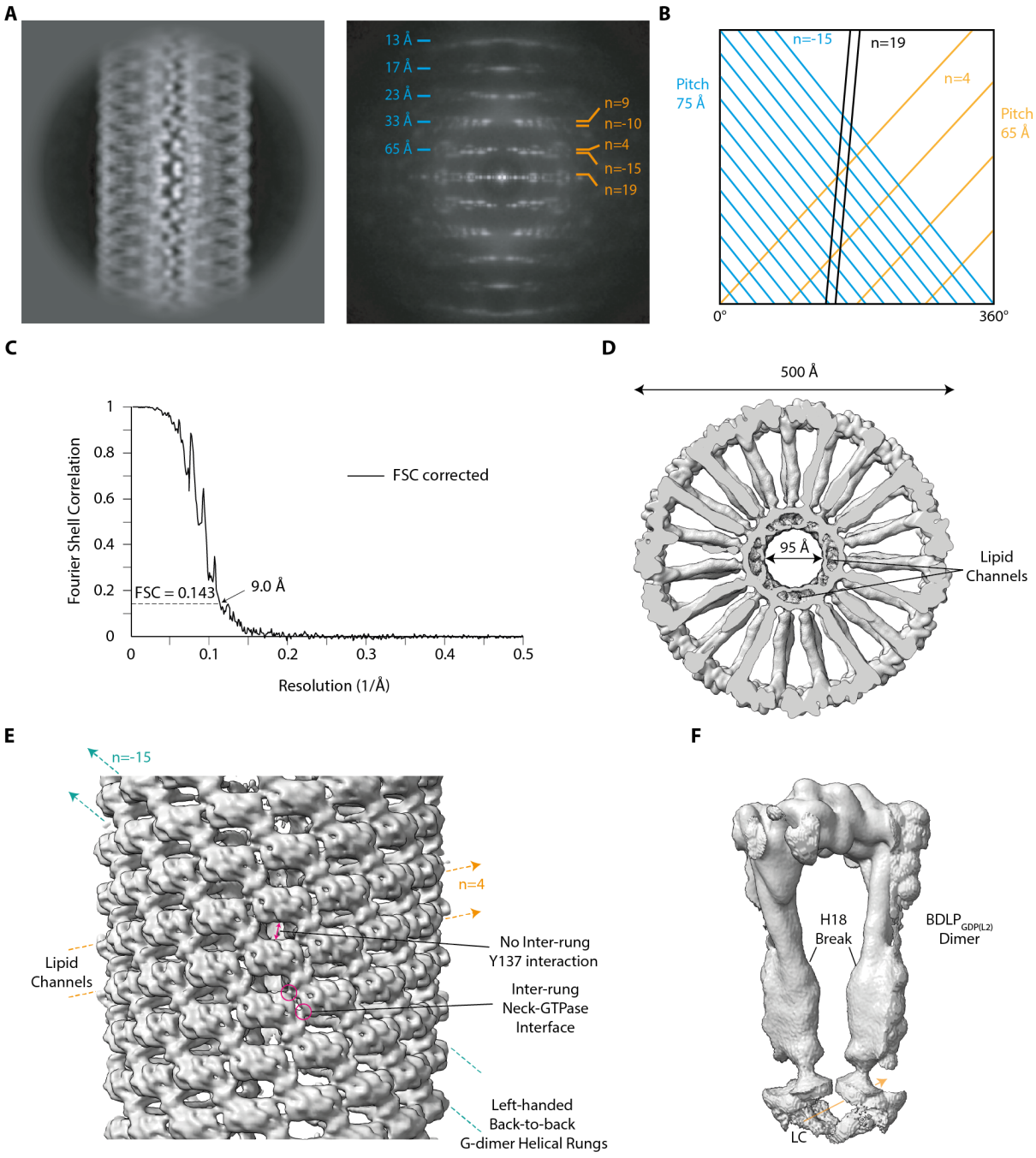


**Figure 51. BDLP$_{GDP(L2)}$ Indexing and Filament Map.**
**A,** 2D Class average of BDLP$_{GDP(L2)}$ filament segments and a summed Fourier transform of filaments segments aligned to the 2D class average, with indexing of key Bessel orders shown. **B,** 2D representation of the filament lattice showing arrangement of key Bessel orders. **C,** FSC curve of the final filament map. **D,** Cross-section of the filament map. **E,** Surface view of the filament map showing arrangement of G-dimers, annotated with key helical families. **F,** Section of the filament map focussing on a single G-dimer.

Overall, BDLP$_{GDP(L2)}$ represented an intermediate state between the BDLP$_{GMPPNP}$ and super-constricted BDLP$_{GDP}$ filaments, wherein the key tyrosine-137-mediated inter-rung

interactions were disrupted alongside a H18 helix break, but tight MBD interactions and super-constriction in a $BDLP_{GDP}$-like manner were not achieved.

#### 5.2.4.3 $BDLP_{GDP(L3)}$ Reconstruction

$BDLP_{GDP(L3)}$ filament segments representing the 'extra-thick' lattice population were aligned through 2D classification, and the sum of their Fourier transforms was indexed to elucidate the filament lattice (Figure 52A). Multiple indexing possibilities were evaluated and utilised to reconstruct filament maps, with a single set of parameters yielding the highest resolution reconstruction with the most distinct map details. These parameters described a filament lattice with a primary left-handed 3-start and 9-start helical families and a right-handed 6-start helical family (Figure 52B). This also indicated that $BDLP_{GDP(L3)}$ exhibited C3 centrosymmetric symmetry. Consequently, the left-handed 3-start helical family represented the fundamental helical repeat which intersected all lattice points, and its helical rise and twist of 20.6 Å and -37.8° were used to refine a filament map using the gold-standard FSC IHRSR approach with BLUSH regularisation. Despite only 1440 segments contributing to the final reconstruction, the $BDLP_{GDP(L3)}$ map refined to an overall resolution of 8.7 Å (Figure 52C).

The $BDLP_{GDP(L3)}$ filament exhibited a 535 Å diameter and a 120 Å lumen diameter (Figure 52D), suggesting significantly reduced bilayer constriction, akin to the $BDLP_{GMPPNP(PG)}$ filament and lumen diameters. Similar to $BDLP_{GDP(L2)}$, G-dimers were arranged by back-to-back association into left-handed helical rungs that followed the 9-start helical family, inter-rung tyrosine-137 interactions were disrupted, and inter-rung interfaces between neck and GTPase domains were formed (Figure 52E). These observations further supported the hypothesis that the thicker GDP-bound BDLP-PG liposome filaments represented an intermediate state between $BDLP_{GMPPNP}$ and $BDLP_{GDP}$.

Notably, the LCs formed by inter-rung alignment of MBDs followed the 3-start left-handed helical family. This is in stark contrast to the other BDLP helical assemblies, in which the LCs follow right-handed helical repeats. The helical lattice indicated that the asymmetric unit of the filament was a tetramer, analogous to the tetramers that formed helical rungs in the super-constricted $BDLP_{GDP}$ filament. In contrast to the $BDLP_{GDP}$ tetramer, the $BDLP_{GDP(L3)}$ tetramer formed LCs between MBDs of both the G-dimers of which it was comprised (Figure 52F).

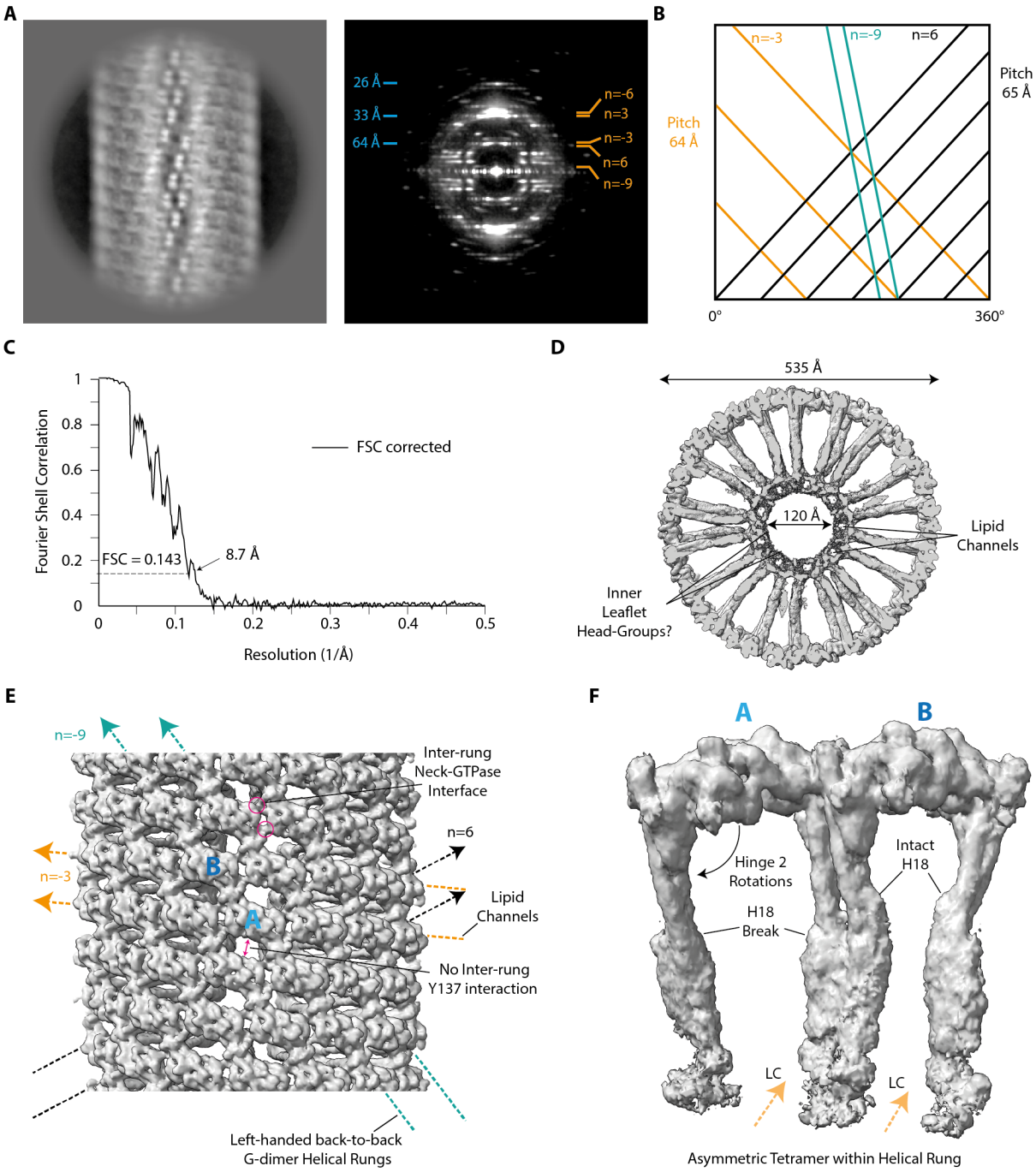


**Figure 52. BDLP$_{GDP(L3)}$ Indexing and Filament Map.**
**A,** 2D Class average of BDLP$_{GDP(L3)}$ filament segments and a summed Fourier transform of filaments segments aligned to the 2D class average, with indexing of key Bessel orders shown. **B,** 2D representation of the filament lattice showing arrangement of key Bessel orders. **C,** FSC curve of the final filament map. **D,** Cross-section of the filament map. **E,** Surface view of the filament map showing arrangement of G-dimers, annotated with key helical families. A and B indicate alternating dimers that form the asymmetric unit (tetramer) of the helical rungs and filament. **F,** Section of the filament map focussing on a single tetramer.

To understand the distinguishing features of each dimer within the tetramer, the filament map was subjected to detailed analysis, revealing several key differences (Figure 52F). Within each tetramer, one G-dimer exhibited a broken H18 conformation, while the other did not. Furthermore, the dimer displaying the broken H18 conformation also presented a more open hinge 2 conformation. Collectively, these observations substantiated the hypothesis that the thick GDP-bound filaments represented an intermediate state, demonstrating nucleotide-state-mediated rung separation, H18 flexibility to prime the MDD for bilayer penetration and lipid displacement, and tetramers composed of asymmetric dimers mediated by hinge and trunk flexibility, but not super-constriction and extensive lateral MBD contacts.

### 5.2.5 Comparison of $BDLP_{GDP(L2)}$ and $BDLP_{GDP(L3)}$ with $BDLP_{GMPPNP}$ and $BDLP_{GDP}$

#### 5.2.5.1 Rigid-body Fitting to Generate $BDLP_{GDP(L2)}$ and $BDLP_{GDP(L3)}$ Models

The resolution of the $BDLP_{GDP(L2)}$ and $BDLP_{GDP(L3)}$ filament maps did not support *de novo* model building. However, rigid bodies of the G-dimer, neck, and trunk domains from $BDLP_{GMPPNP}$ and $BDLP_{GDP}$ were individually fitted into the filament maps for comparison with these structures and to elucidate the filament ultrastructure of the thicker GDP-bound filaments. The details of this are described in the following sections. Overall, a model of the $BDLP_{GDP(L2)}$ dimer comprised the $BDLP_{GMPPNP}$ G-dimer, and the $BDLP_{GDP}$ Dimer B neck, trunk and MBDs, with the MDD residues removed. The unique dimers that formed the $BDLP_{GDP(L3)}$ tetramer were constructed separately. The first dimer, designated Dimer A2, comprised the $BDLP_{GMPPNP}$ G-dimer and neck domains, and the $BDLP_{GDP}$ Dimer B trunk and MBDs. The second dimer, designated Dimer B2, comprised the $BDLP_{GMPPNP}$ G-dimer, neck, trunk and MBDs.

#### 5.2.5.2 G-Dimer Interface

To ascertain whether a tight G-dimer interface was maintained in the thick GDP-bound filaments, the $BDLP_{GMPPNP}$ and GDP-bound BDLP crystal structure G-dimers were fitted into the $BDLP_{GDP(L2)}$ and $BDLP_{GDP(L3)}$ filament maps. This fitting indicated that these filaments also maintained a tight G-dimer interface, as only the $BDLP_{GMPPNP}$ dimer correlated well with the filament maps (Figure 53A), further suggesting that a tight G-dimer interface was necessary for maintaining membrane-bound helical assemblies. However, in comparison to $BDLP_{GDP}$ (Figure 44C), density supporting an ordered switch 1 was not observed (Figure 53B). This

further emphasised switch 1 as a key mediator of GTP-hydrolysis-driven changes in filament architecture.

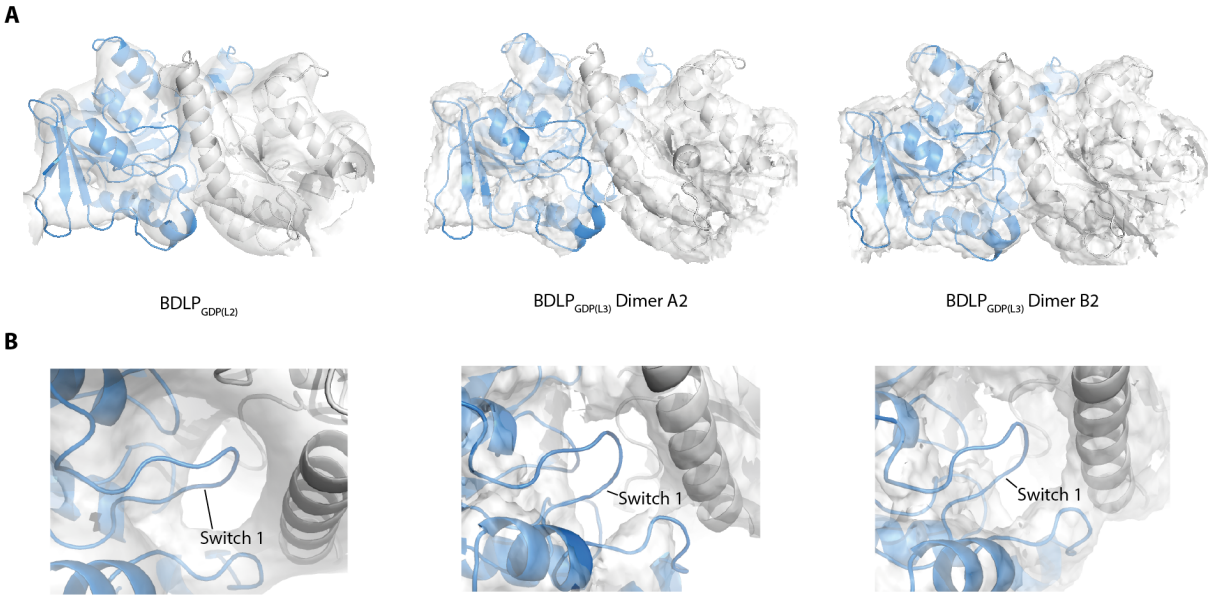


**Figure 53. Thick GDP-bound BDLP Filament G-Dimer Interface Analysis.**
**A,** $BDLP_{GMPPNP}$ G-dimer fit into the $BDLP_{GDP(L2)}$ and $BDLP_{GDP(L3)}$ filament maps. **B,** Zoom panels highlighting the absence of ordered switch 1 density in each map.

### 5.2.5.3 Hinge 2

Hinge 2 flexibility is a conserved DSF feature (Daumke & Praefcke, 2016). Indeed, between the BDLP structure observed by x-ray crystallography (Low & Löwe, 2006) and $BDLP_{GMPPNP}$, significant hinge 2 closing was necessary to form tight G-dimers within helical filaments. However, comparison of $BDLP_{GMPPNP}$ and $BDLP_{GDP}$ suggested that once tight G-dimers were formed in a helical lattice, hinge 2 conformation remained unaffected by nucleotide state (Figure 45B). To understand whether nucleotide hydrolysis can actually affect hinge 2 conformation within BDLP filaments, the hinge 2 conformations of $BDLP_{GDP(L2)}$ and $BDLP_{GDP(L3)}$ were also analysed.

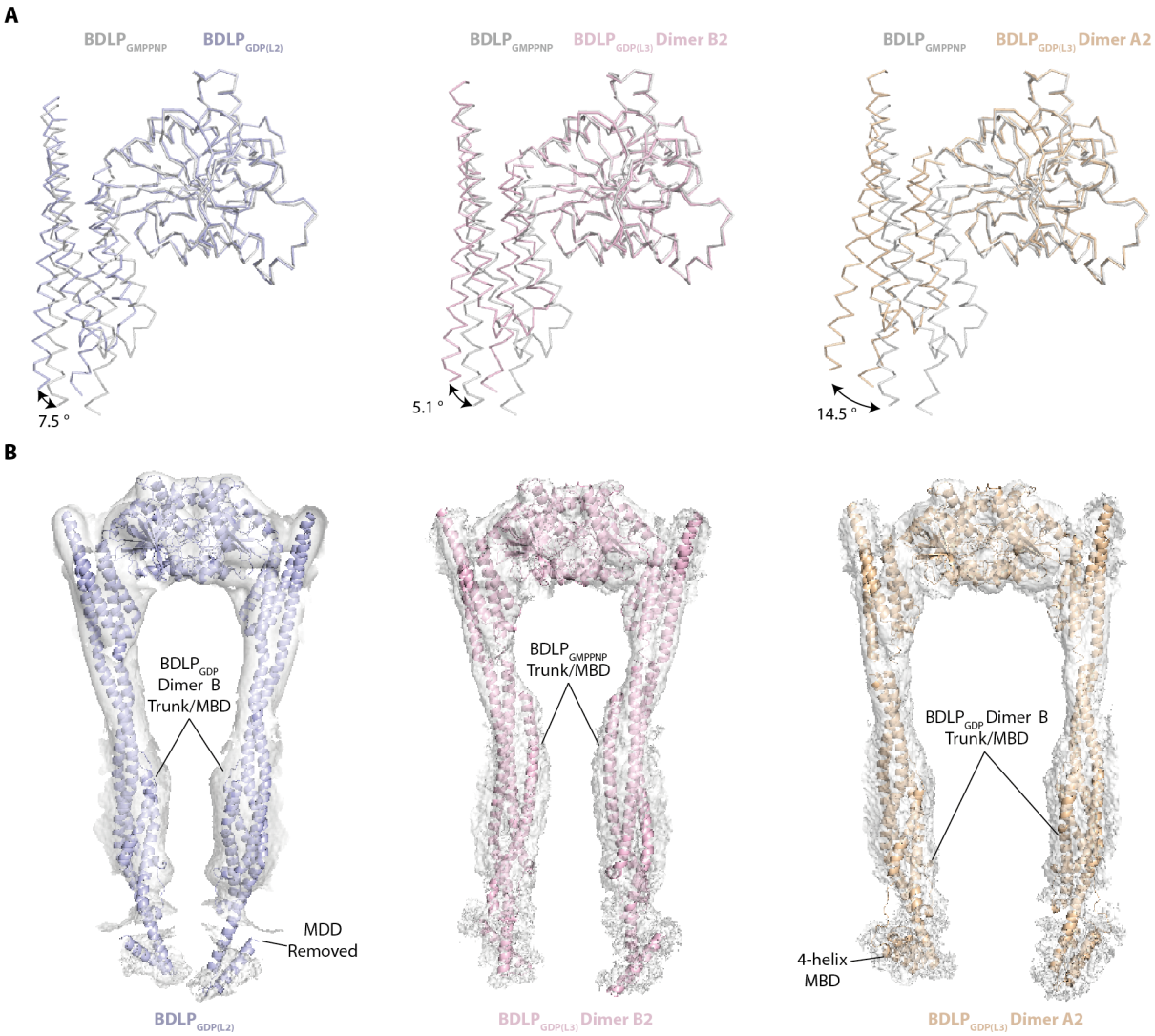
A
BDLP GMPPNP
BDLP GDP(L2)
7.5 °
BDLP GMPPNP
BDLP GDP(L3) Dimer B2
5.1 °
BDLP GMPPNP
BDLP GDP(L3) Dimer A2
14.5 °
B
BDLP GDP Dimer B Trunk/MBD
MDD Removed
BDLP GDP(L2)
BDLP GMPPNP Trunk/MBD
BDLP GDP(L3) Dimer B2
BDLP GDP Dimer B Trunk/MBD
4-helix MBD
BDLP GDP(L3) Dimer A2
C
BDLP GMPPNP
BDLP GDP(L2)
2 °
BDLP GMPPNP
BDLP GDP(L3) Dimer B2
4.5 °
BDLP GMPPNP
BDLP GDP(L3) Dimer A2
7.8 °

**Figure 54. $BDLP_{GDP(L2)}$ and $BDLP_{GDP(L3)}$ Neck, Trunk and MBD Conformations.**
**A,** Alignment of $BDLP_{GDP(L2)}$ (blue), $BDLP_{GDP(L3)}$ Dimer B2 (pink) or Dimer A2 (gold) monomers with $BDLP_{GMPPNP}$ (grey) anchored on their GTPase domains, highlighting hinge 2 opening within these lattices. **B,** Fit of dimer models of $BDLP_{GDP(L2)}$ and $BDLP_{GDP(L3)}$ into the filament map. **C,** Alignment of $BDLP_{GDP(L2)}$, $BDLP_{GDP(L3)}$ Dimer B2 or Dimer A2 monomers with $BDLP_{GMPPNP}$ anchored on their GTPase domains, highlighting rotations about hinge 1 that displace the trunk and MBDs of $BDLP_{GDP(L2)}$ and $BDLP_{GDP(L3)}$ relative to the $BDLP_{GMPPNP}$ trunk and MBDs.

Rigid bodies of the $BDLP_{GMPPNP}$ neck were fitted into the filament maps in addition to the G-dimers to construct a model of hinge 2 conformation in $BDLP_{GDP(L2)}$ and $BDLP_{GDP(L3)}$. Alignment of these models with $BDLP_{GMPPNP}$, anchored on their GTPase domains, revealed that partial hinge 2 opening occurred in the formation of the thicker GDP-bound filaments (Figure 54A). The most substantial opening occurred in Dimer A2 ($BDLP_{GDP(L3)}$), in which hinge 2 rotated 14.5° away from the GTPase domain. Hinge 2 opening in Dimer B2 and the $BDLP_{GDP(L2)}$ dimer was less pronounced. Overall, this analysis demonstrated hinge 2 conformational flexibility within membrane-bound filaments of BDLP, a conserved feature of other DSF filament assemblies (von der Malsburg *et al.*, 2023; Nyenhuis *et al.*, 2023).

#### 5.2.5.4 Trunk and MBDs

To construct a complete model of the $BDLP_{GDP(L2)}$ and $BDLP_{GDP(L3)}$ dimers, combined trunk and MBDs from $BDLP_{GMPPNP}$ and $BDLP_{GDP}$ were fitted into the filament maps (Figure 54B). From this fitting, only a single trunk-MBD variant exhibited good correlation with the filament map for each dimer. For $BDLP_{GDP(L2)}$, given the broken H18 features of the map, the Dimer A and Dimer B trunk-MBD models ($BDLP_{GDP}$) were evaluated. Only the Dimer B model fitted with good correlation into the map and was consequently used to model this region. Given the absence of density to support a four-helix MBD, the MDD residues were removed. For Dimer B2 ($BDLP_{GDP(L3)}$), the intact H18 indicated a $BDLP_{GMPPNP}$-like trunk conformation. Fitting of the $BDLP_{GMPPNP}$ trunk-MBD model into the map corroborated this and was used to complete the Dimer B2 model. However, Dimer A2 displayed a disrupted H18 conformation, so again the $BDLP_{GDP}$ Dimer A and Dimer B trunk-MBD models were fitted into the map, and only the Dimer B model fitted adequately into the density and was therefore used to complete the model. The density also supported a four-helix MBD. Overall, rigid-body fitting into the $BDLP_{GDP(L2)}$ and $BDLP_{GDP(L3)}$ densities revealed that the conformational diversity observed in $BDLP_{GMPPNP}$ and $BDLP_{GDP}$ was reflected in the thicker GDP-bound filaments. Furthermore, this

fitting also highlighted the conformational flexibility of H18 and the capacity of MDD residues to penetrate the membrane and form an expanded MBD, even when super constriction and full separation of helical rungs at the GTPase domain level were not observed.

To understand whether the hinge 1 rotational flexibility observed in $BDLP_{GDP}$ that resulted in trunk domain and MBD displacement was characteristic of $BDLP_{GDP(L2)}$ and $BDLP_{GDP(L3)}$, their monomers aligned to a $BDLP_{GMPPNP}$ monomer, anchored via their GTPase domains. This alignment revealed both trunk and MBD displacement relative to $BDLP_{GMPPNP}$ in all models (Figure 54C). This finding emphasised that hinge 1 rotational flexibility was crucial for the formation of diverse helical assemblies to accommodate trunk-trunk and MBD-MBD interfaces. Furthermore, this observation suggested that the trunk domain and MBD displacement in $BDLP_{GDP}$ Dimer B, which occurred in an opposite relative direction (Figure 45B), was unique and necessary for the extensive lateral MBD contacts and super-constriction in $BDLP_{GDP}$.

In conclusion, rigid body fitting into the $BDLP_{GDP(L2)}$ and $BDLP_{GDP(L3)}$ filament maps underscored the significance of hinge 1 and hinge 2 conformational flexibility in facilitating the formation of diverse BDLP helical assemblies. The conformational flexibility of H18 and MDD residues was also demonstrated by $BDLP_{GDP(L2)}$ and $BDLP_{GDP(L3)}$. Owing to the low resolution of the filament maps, whether subtle conformational changes occurred in $BDLP_{GDP(L2)}$ and $BDLP_{GDP(L3)}$ could not be determined, although overall the domain architectures were consistent with $BDLP_{GMPPNP}$ and $BDLP_{GDP}$.

#### 5.2.5.5 Lipid Channel Geometry

To understand the impact of the novel $BDLP_{GDP(L2)}$ and $BDLP_{GDP(L3)}$ helical assemblies on the membrane interface and LC geometries, helical models were generated by applying the helical parameters to the asymmetric unit models generated by rigid body fitting. The helical $BDLP_{GDP(L2)}$ model indicated that the novel inter-rung GTPase-neck domain interfaces were likely mediated by interactions between the β3-β4 connecting loop (GTPase domain) and H1 (neck domain) (Figure 55A). As β4 is connected and proximal to H4, which is intimately associated with switch 1 (Figure 47), this inter-rung interaction may also be modulated by the active site and switch 1 conformations in response to nucleotide hydrolysis. Analysis of the $BDLP_{GDP(L2)}$ lumen surface demonstrated that $BDLP_{GDP(L2)}$ forms helical LCs that follow the

right-handed 4-start helical family (Figure 55B), in a manner analogous to $BDLP_{GMPPNP}$. This observation suggested that $BDLP_{GDP(L2)}$ might function as an intermediate state between $BDLP_{GMPPNP}$ and $BDLP_{GDP}$ during GTP hydrolysis, wherein tyrosine-137 inter-rung interactions and H18 are disrupted, whilst weak inter-rung interfaces are still maintained and the $BDLP_{GMPPNP}$ LC geometry is preserved.

The $BDLP_{GDP(L3)}$ helical model also demonstrated that inter-rung GTPase-neck domain interfaces were mediated by the same helices and loops (Figure 55C). However, analysis of the lumen surface revealed significantly different LC geometry, with LCs up to 50 Å wide following the left-handed 3-start helical repeat (Figure 55D). The $BDLP_{GDP(L3)}$ LCs were formed by inter-rung Dimer A2-Dimer B2 interfaces between MBDs. In this configuration, the MBD residues that lined the LCs differed from the canonical residues that lined $BDLP_{GMPPNP}$ and $BDLP_{GDP}$ LCs. The LC surfaces comprised both charged and hydrophobic patches, suggesting weaker protein-lipid interfaces, consistent with the reduced bilayer constriction and lipid displacement of $BDLP_{GDP(L3)}$. Furthermore, the canonical inter-rung alignment of MBD helices that forms LCs in $BDLP_{GMPPNP}$ and $BDLP_{GDP}$ was also present in $BDLP_{GDP(L3)}$, but this alignment occurred orthogonal to the LCs, as indicated by the pink arrows in Figure 55D. This observation suggested that lipids may not have been exclusively confined to the helical LCs of $BDLP_{GDP(L3)}$, again aligning with a reduced ability to displace lipids and constrict the bilayer. Overall, the LC geometry of $BDLP_{GDP(L3)}$ differed significantly from other GMPPNP- and GDP-bound BDLP filaments.

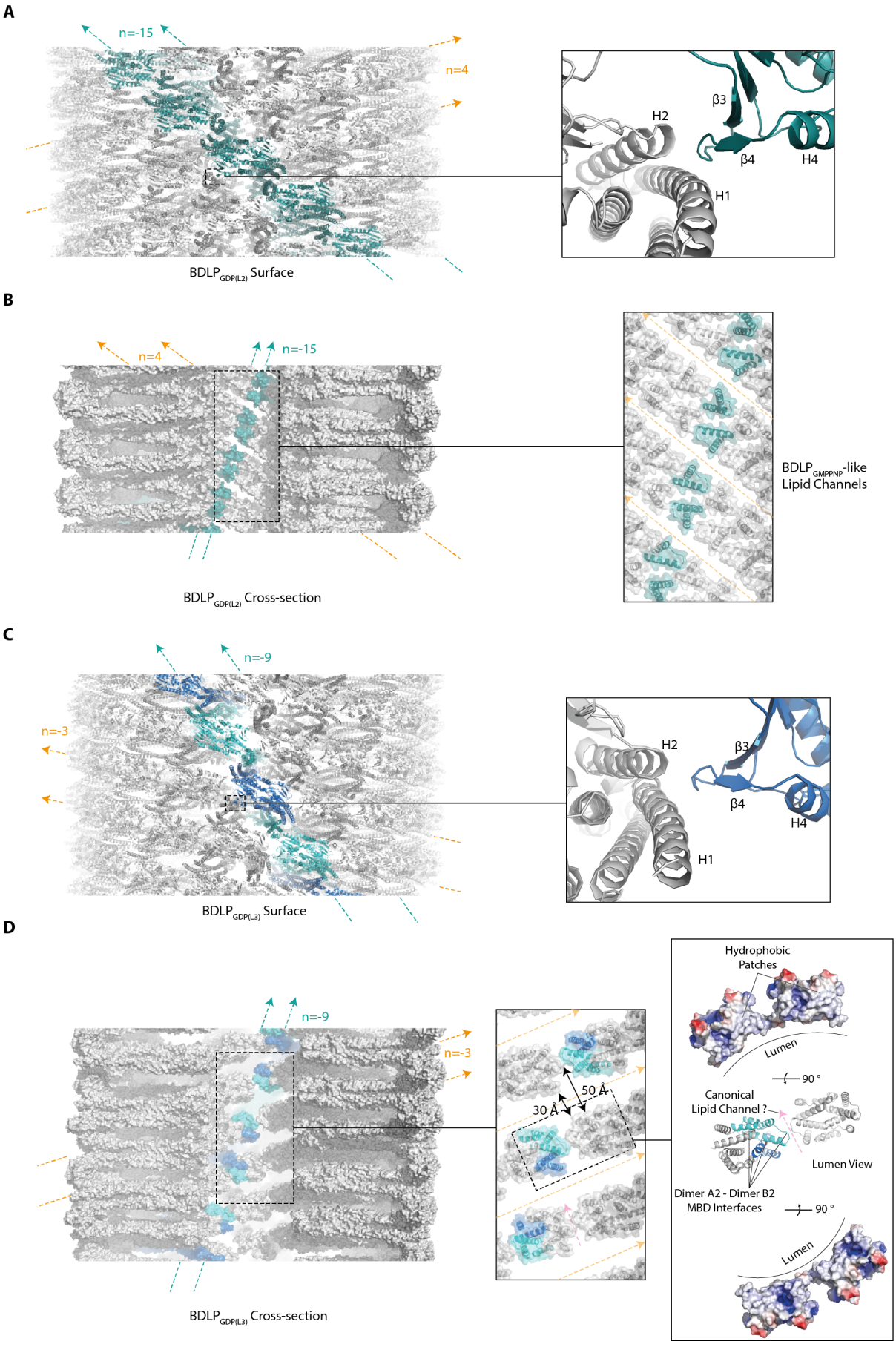
A
n=-15
n=4
β3
H2
β4
H4
H1
BDLP GDP(L2) Surface
B
n=4
n=-15
BDLP GMPPNP-like
Lipid Channels
BDLP GDP(L2) Cross-section
C
n=-9
n=-3
H2
β3
β4
H4
H1
BDLP GDP(L3) Surface
D
n=-9
n=-3
50 Å
30 Å
Hydrophobic
Patches
Lumen
90 °
Canonical
Lipid Channel ?
Lumen View
Dimer A2 - Dimer B2
MBD Interfaces
90 °
Lumen
BDLP GDP(L3) Cross-section

**Figure 55. $BDLP_{GDP(L2)}$ and $BDLP_{GDP(L3)}$ Helical Models and Lipid Channels.**
**A,** $BDLP_{GDP(L2)}$ helical model. A left-handed helical rung formed by back-to-back association of G-dimers is highlighted in blue. Zoom panel indicates the novel inter-rung GTPase-neck domain interface likely mediated by a H1-β3-β4 connecting loop interaction. **B,** $BDLP_{GDP(L2)}$ cross section surface. The zoom panel highlights the lumen surface and lipid channels, that form in a $BDLP_{GMPPNP}$-like manner. **C,** $BDLP_{GDP(L3)}$ helical model. A left-handed helical rung formed by back-to-back association of tetramers is highlighted in blue, with Dimer A2 coloured in cyan and Dimer B2 coloured in dark blue. Zoom panel indicates the same inter-rung GTPase-neck domain interaction as panel A. **D,** $BDLP_{GDP(L3)}$ cross section surface. Zoom panel (middle) highlights the novel large left-handed helical channels formed by inter-rung MBD interactions. Zoom panel (right) focusses on the MBD helices that form novel inter-rung interfaces. The surface potential of MBD residues lining the helical channels is shown, blue = positive charge, red = negative charge, white = neutral/hydrophobic. The pink arrows represent a potential canonical lipid channel connecting the larger lipid channel rungs.

### 5.2.6 BDLP Filaments Induce a Lamellar to HexII Lipid Phase Transition *in vitro*.

In Chapter 4, an association of BDLP with remodelling of TMs into hexII nanoparticles during hormogonium development was established with evidence from cryo-CLEM and transcriptomic data. However, direct evidence of BDLP remodelling thylakoids was not observed. The analysis of helical architectures in this chapter revealed that BDLP self-assembly onto membrane templates displaced the outer-leaflet lipids and confined the inner-leaflet lipids to helical LCs. Furthermore, the super-constricted GDP-bound filament ($BDLP_{GDP}$) suggested GTP hydrolysis drives increased membrane constriction and lipid displacement, confining lipids to just a single helical LC. To determine the self-assembly into super-constricting helical filaments and confinement of inner-leaflet lipids to a single LC is relevant to BDLP-mediated phase transitions, the ability of BDLP filaments to remodel Lm phase bilayers into hexII phase ordered arrays *in vitro* was investigated.

As *N. punctiforme* TMs contain a high proportion of hexII-favouring MGDG, PG liposomes were supplemented with MGDG replacing a proportion of PG. Various ratios of MGDG and PG were examined, and only lower MGDG proportions were deemed suitable, as higher MGDG content lipid mixtures were not readily dissolved in aqueous buffer. Therefore, the final MGDG liposomes utilised in *in vitro* assays comprised 20% MGDG, 20% PC and 60% PG. NS-EM analysis revealed that BDLP was capable of tubulating both these liposomes and control liposomes containing 40% PC and 60% PG in the presence of GMPPNP, and no tubulation was observed in the absence of nucleotide (Figure 56). This suggested BDLP interactions with 60% PG liposomes were equivalent to the interactions with the (80%) PG liposomes used for cryo-EM reconstructions of the BDLP protein-lipid filaments.

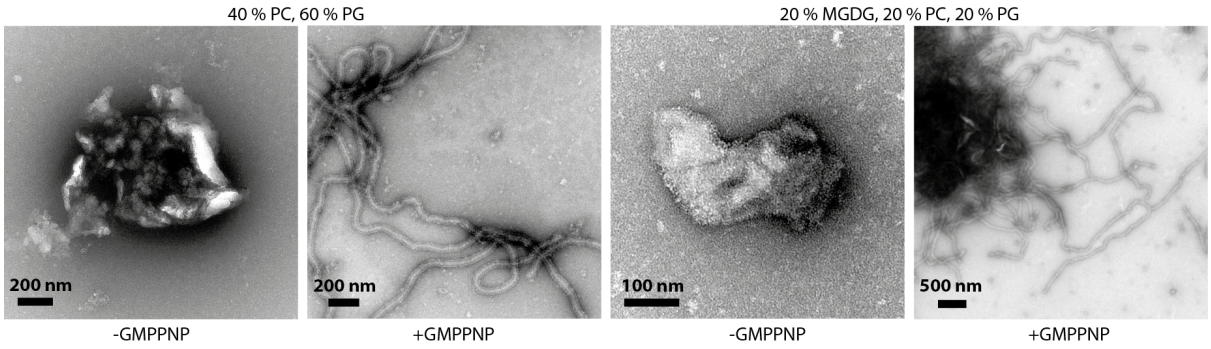


**Figure 56. NS-EM Analysis of BDLP Interactions with MGDG-containing Liposomes.**
BDLP can tubulate MGDG-containing liposomes. 1 mg/mL liposomes incubated with 30 μM BDLP with or without 4 mM GMPPNP. Liposome compositions are indicated above the micrographs.

To investigate the capacity of BDLP to remodel Lm phase liposomes into hexII phase ordered arrays, MGDG liposomes were incubated with BDLP and GTP, and subsequently, samples were applied to grids and vitrified via plunge-freezing. The samples were examined by cryo-ET, and tomograms were reconstructed. Furthermore, control tomograms of samples containing liposomes incubated with GTP under identical conditions, but in the absence of BDLP, were reconstructed. As anticipated, unilamellar and some multilamellar vesicles (MLVs) exhibiting an overall globular morphology were observed in the control samples (Figure 57A).

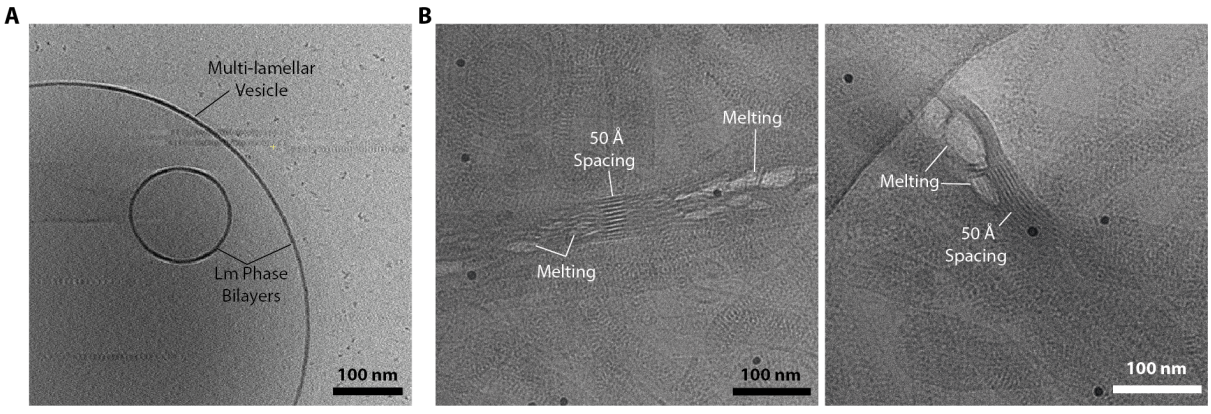


**Figure 57. Cryo-ET Analysis of BDLP-mediated Remodelling of MGDG Liposomes.**
BDLP tubulates liposomes and produces ordered and dose-sensitive lipid arrays, **A,** Slice through a tomogram of an MGDG multilamellar vesicle incubated with GTP in the absence of BDLP. **B,** Raw cryo-EM micrographs of a single tilt-series image collected after a total electron dose of 4.7 $e^-/A^2$. Sample

contains BDLP incubated with MGDG liposomes and GTP. The indicated ordered lipid arrays have a regular ~50 Å spacing.

Both dispersed BDLP protein-lipid filaments and bundles of aggregated filaments and liposomes were observed in the GTP-BDLP-MGDG liposome samples. Tomograms were targeted at regions of thicker ice, where aggregated bundles of BDLP filaments were observed to elucidate whether lipid phase changes occurred in these regions. During acquisition of tomogram tilt series, regular arrays with a ~50 Å spacing were observed in individual images at the 0° initial tilt angle, reminiscent of the side-views of hexII nanoparticles observed in hormogonia. However, for the majority of tomograms acquired, despite the thick ice, the regions containing ordered arrays melted after just a few images were collected: often after total electron doses of 4-8 $e^-/Å^2$ (Figure 57B). The sensitivity of the ordered arrays to electron dose suggested they possessed significant order akin to a hexII phase lattice, as samples with densely packed ordered arrays are typically more susceptible to radiation damage by inelastic scattering (Shi & Huang, 2022). Although why these ordered arrays melted and the hexII nanoparticles in hormogonia samples did not was unclear, and could indicate the *in vitro* conditions increased the order of the arrays.

To elucidate whether BDLP was remodelling MGDG liposomes into the ordered arrays and whether this represented the hexII phase, a 'brute-force' approach was followed, wherein a total of 50 tomograms were collected to obtain tomograms of the ordered arrays where sample melting was not observed. Whereas within most tomograms a melting effect was observed after relatively low electron doses were applied, two tomograms containing less extensive ordered arrays were acquired without sample melting. The less extensive ordered arrays suggested these tomograms captured an earlier stage of liposome remodelling.

Several features within the tomograms exhibited striking similarities to the tomograms of *in vivo* BDLP-associated hexII nanoparticles. BDLP was observed tubulating and decorating liposomes. The bilayer decorations had dimensions consistent with an overall open BDLP conformation, with a membrane binding domain spanning both leaflets (Figure 58A). Fourier space analysis of the BDLP-tubulated liposomes indicated a repeat of ~60 Å (Figure 58B), consistent with the helical pitch of left-handed helical rungs of BDLP filaments. Filament

diameters varied (Figure 58C), suggesting conformational bistabliity of filaments, consistent with the diverse BDLP helical assemblies identified in this work. Importantly, several filaments had diameters equivalent to the super-constricted state, confirming self-assembly, and GTP binding and hydrolysis, can induce bilayer super-constriction.

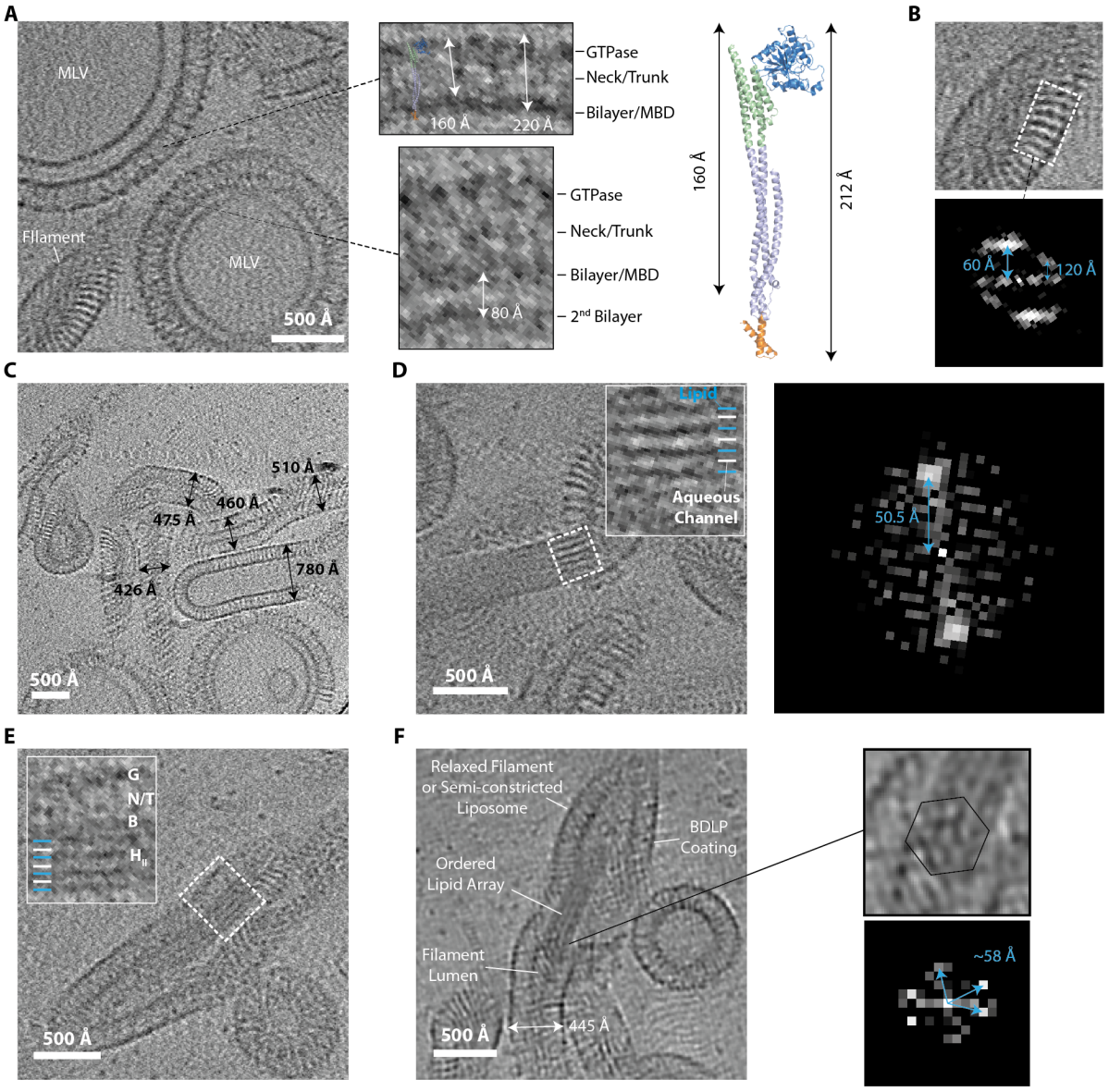


**Figure 58. Analysis of BDLP-generated Ordered Lipid Arrays.**
Tomograms of MGDG liposome samples incubated with BDLP and GTP contain ordered tubular lipid arrays reminiscent of the hexII phase. **A,** Tomogram slice showing BDLP decoration of lipid surfaces and an angled cross-section section through a filament. MLV = multilamellar vesicle. Zoom panels highlight the membrane decoration dimensions that match the BDLP extended open conformation (top) and the separation distance between stacked bilayers within the MLV. A cartoon representation of $BDLP_{GMPPNP}$ is shown for comparison. **B,** Fourier space analysis of the filament cross-section from panel A, indicating a repeat distance of BDLP rungs ~60 Å. **C,** Tomogram slice showing filament width diversity, indicating varying levels of constriction. Many filaments have diameters similar to the $BDLP_{GDP}$

super-constricted state (450 Å). **D,** Tomogram slice showing ordered lipid arrays. Zoom panel annotates the lipid layers (blue) and aqueous channel layers (white). Fourier space analysis indicates the lamellae have a spacing of 50.5 Å **E,** Tomogram slice showing BDLP bound to the side of ordered lipid arrays. Zoom panel: blue and white bars represent lipid and aqueous channel layers respectively. G = GTPase domain layer, N/T = neck/trunk, B = Bilayer, $H_{II}$ = ordered arrays / hexII phase lipids. **F,** Tomogram slice showing ordered lipid array within a filament lumen. The array appears to have a hexagonal arrangement, with Fourier space analysis indicating a ~58 Å hexagonal spacing, suggestive of the hexII phase.

Reconstructed tomograms also contained tightly packed tubular arrays (Figure 58D). The arrays were reminiscent of side views of *in vivo* hexII nanoparticles, and Fourier space analysis indicated a lateral repeat orthogonal to the longitudinal tubular axis of 50.5 Å (Figure 58D). The tubular arrays extended long distances (>1000 Å) and ran parallel with the longitudinal axes of the tubes. If the ordered arrays represented BDLP assembly spacings, a helical arrangement circumventing the longitudinal axis would have been expected. BDLP was observed coating the arrays (Figure 58E), reminiscent of BDLP coating hexII nanoparticles *in vivo*. Collectively, these observations confirmed the ordered arrays were not attributable to BDLP density, but were MGDG liposomes remodelled into tubular arrays.

The closest observed packing of bilayers within MLVs was ~80 Å (Figure 58A), indicating that the 50.5 Å lateral spacing of the ordered lipid arrays likely did not represent stacked Lm phase bilayers. Given the striking similarity of the *in vitro* lipid arrays to tubular hexII phase array side views observed within hormogonia (Figure 27) and in other cryo-EM and cryo-ET studies (Pattipeiluhu *et al.*, 2024; Kirchhoff *et al.*, 2007), efforts were undertaken to confirm a hexagonal arrangement of the tubular arrays. As the thin layer of vitrified sample was prepared by blotting, BDLP filaments were positioned relatively flat on the grids. The tubular lipid arrays also lay flat on the grids and were observed confined to the interior of decorated and semi-constricted liposomes or potentially the lumens of relaxed filaments (Figure 58F). Consequently, given the missing wedge of tomogram data collection (Wiedemann & Heckel, 2024), 'end-on' views of the lipid arrays were frequently stretched or absent. In contrast, 'end-on' views of the hexII nanoparticles were readily observed in the tomograms of hormogonia, as they were positioned in random orientation distributions within the cryo-FIB-milled lamellae.

Nevertheless, some putative 'end-on' views of the lipid arrays were observed, which appeared to adopt a hexagonal arrangement, consistent with BDLP remodelling Lm phase liposomes into ordered hexII phase tubes (Figure 58F). Fourier space analysis indicated these views were not entirely orthogonal to the longitudinal axis of the arrays; however, the analysis indicated a putative hexagonal repeat of ~58 Å. This suggested a more tightly packed hexII phase structure than that observed within hormogonia, which could be attributed to the *in vitro* conditions, and the hydration, lipid composition, and temperature dependence of hexII phase hexagonal spacing (Bratek *et al.*, 2019). Alternatively, the tubular lipid arrays might represent an inter-lamellar attachment (ILA) lipid phase, which is an intermediate observed during Lm-hexII phase transitions (Siegel, Green & Talmon, 1994). However, they demonstrated more visual consistency with hexII phase tubular arrays overall. In conclusion, cryo-ET visualisation of BDLP-mediated MGDG liposome remodelling revealed that BDLP was capable of remodelling Lm phase liposomes into ordered lipid arrays, which were likely hexII phase tubular structures.

An unresolved question pertained to how the helical LC and increased bilayer constriction of super-constricted BDLP filaments resulted in the remodelling of MGDG liposomes into putative hexII tubular arrays. Analysis of the tomograms revealed that lipid arrays emerged from the ends of super-constricted filaments (Figure 59). Up to eight filaments appeared to contribute to the central lipid array, and distinct examples of merging of tubular lipid arrays from two separate filament ends were observed. The lipid array was confined to the lumen of a BDLP-decorated semi-constricted liposome. It remained unclear whether this arose from relaxation of constricted BDLP filaments or was the central nucleating liposome for several filaments. The deposition of putative hexII tubular arrays within the liposome lumen was consistent with the observation of BDLP decorating hexII nanoparticles in hormogonia. The association of the putative hexII tubular arrays with the ends of filaments suggested that the confinement of inner leaflet lipids to the LC favoured spontaneous arrangement of lipids at the filament ends into the putative hexII arrays. Whether this process involved (1) relaxation of the filament to liberate lipids or (2) active displacement of lipids from the filament ends driven by filament super-constriction is undetermined.

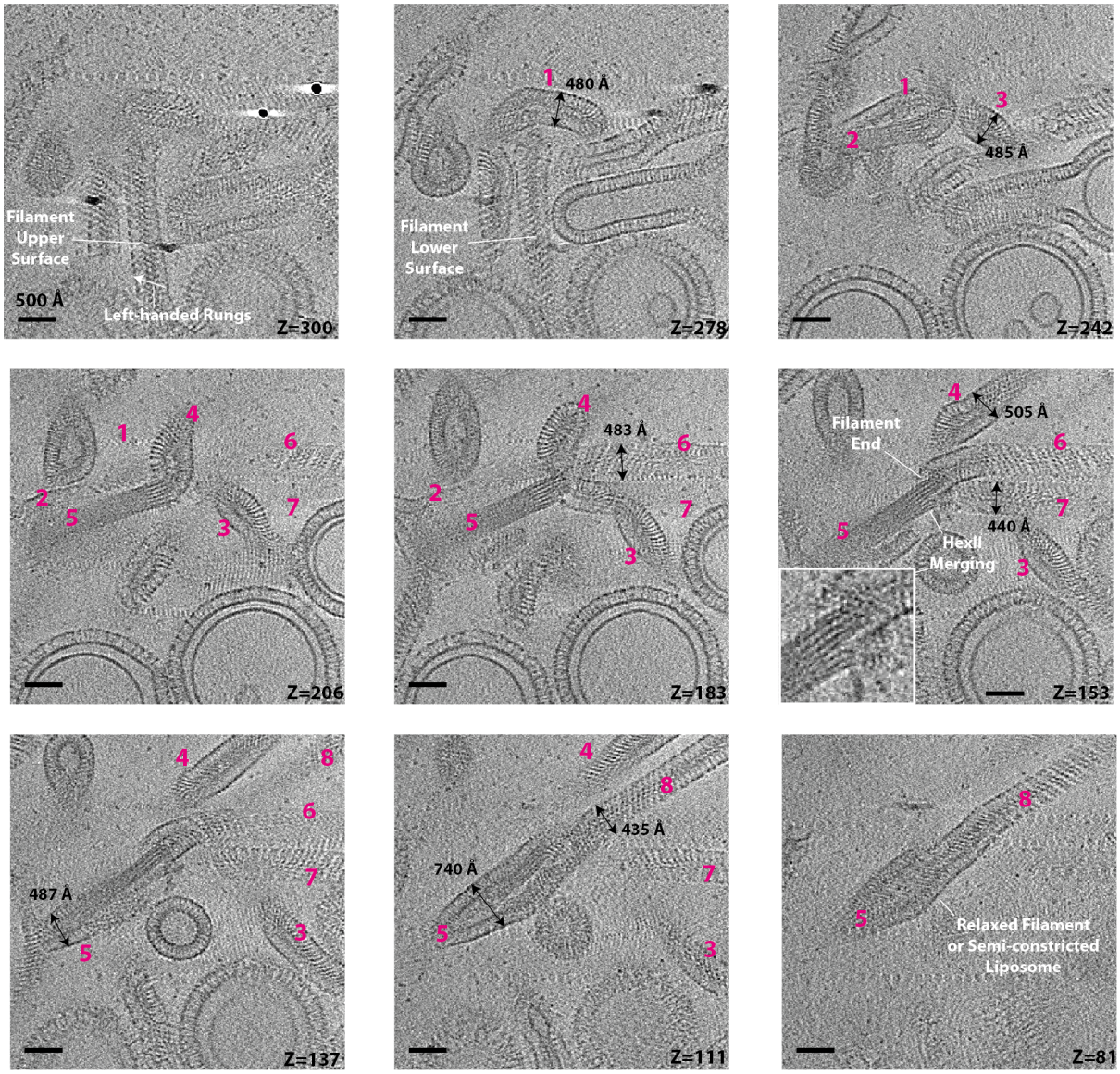


**Figure 59. Multiple Super-Constricted BDLP Filaments Contributing to Ordered Lipid Arrays.** Slices through a tomogram with descending Z-height (left-to-right, top-to-bottom). Multiple super-constricted filaments combine to form the ordered lipid array within the lumen of a relaxed filament or semi-constricted liposome. Pink numbers highlight individual tubes associated with the ordered lipid array.

Additionally, two potential mechanisms for remodelling of Lm phase bilayers into hexII-like tubular arrays were indicated by these results. Firstly, a displacement model whereby the LC geometry achieved remodelling through the displacement of Lm phase-favouring cylindrical lipids (PG and PC), leaving only hexII phase-favouring MGDG lipids within the LCs. Secondly, a lipid-arrangement model, whereby the LC arranged both MGDG and the cylindrical lipids such that they adopted high negative curvature similar to lipids within the ordered arrays.

Tomograms of 60% PG (40% PC) liposomes lacking MGDG, incubated with BDLP and GTP under the same conditions, exhibited no evidence of lipid remodelling into ordered arrays (Figure 60). However, they demonstrated super-constricted filaments and bilayer decorations.

Whether the absence MGDG meant BDLP was unable to mediate phase changes via a cylindrical-lipid displacement mechanism was not clear. BDLP may have mediated phase changes of 20% MGDG liposomes into non-bilayer lipid arrays that also contained PG and PC lipids via a lipid-arrangement mechanism, during which the phase change was stabilised or promoted by the presence of MGDG. Without MGDG BDLP may have been unable to efficiently configure PG and PC into phase change-favouring arrangements. Furthermore, fewer filament and liposome bundles or aggregates (where hexII-like structures were observed in the MGDG liposome samples) were observed in the 60% PG samples, and regions of undecorated bilayer were also noted. This suggested the reaction conditions were not optimal for processing of 60% PG liposomes to the point of phase-change. *N. punctiforme* thylakoids, to which BDLP was associated with in hormogonia, also contain > 50% MGDG, therefore extensive cylindrical lipid displacement is likely not required to actively remodel TMs into hexII nanoparticles. Moreover, under physiological conditions, simulated MGDG hexII arrays adopt a hexagonal spacing of 87-97 Å (Bratek *et al.*, 2019), significantly larger than the ~58 Å spacing observed here (Figure 58F), suggesting the lipid arrays were not solely comprised of MGDG, contradicting a lipid displacement model. Consistent with a lipid-arrangement model, PG within thylakoids that spontaneously undergo lipid polymorphism into hexII phase structures, is able to proportionally transition to the hexII phase alongside MGDG (van Eerden *et al.*, 2015).

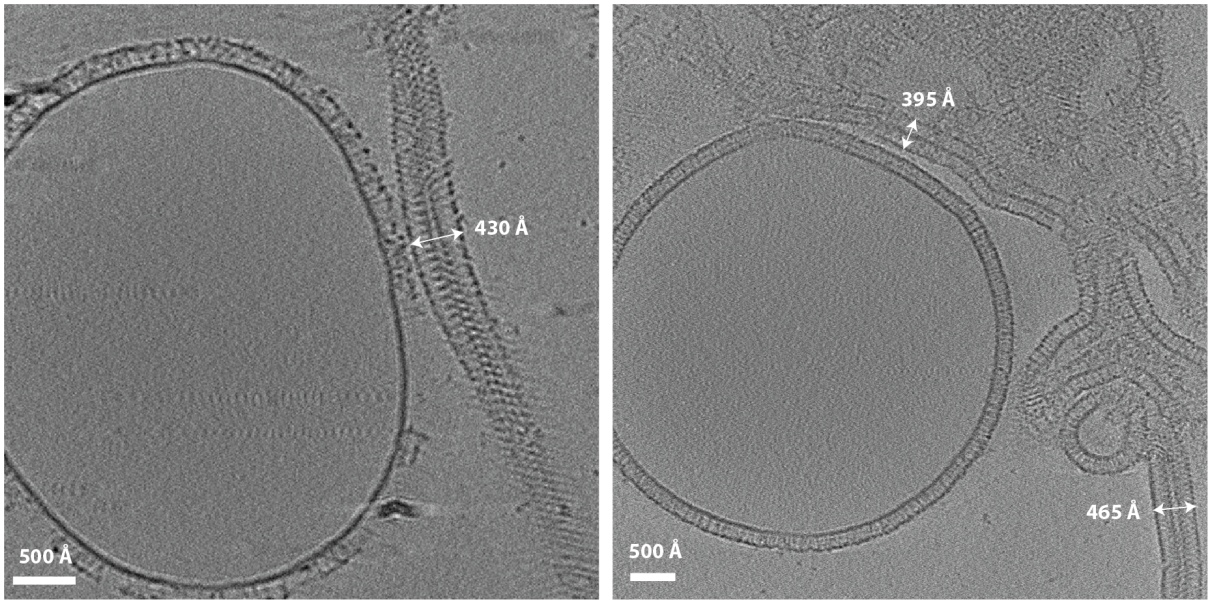


**Figure 60. BDLP-mediated Remodelling of Liposomes Lacking MGDG.**
Slices through tomograms of 60% PG (40% PC) liposomes incubated with BDLP and GTP.

In conclusion, cryo-ET revealed that multiple super-constricted BDLP filaments combined to deposit putative hexII phase lipid arrays from their filament ends within BDLP-decorated liposomes, providing functional relevance to the BDLP helical filament structures determined in this study.

## 5.3 Discussion

This chapter examined the role of GTP hydrolysis in BDLP-mediated membrane remodelling. The $BDLP_{GDP}$ filament structure revealed, for the first time, that BDLP can maintain a helical arrangement and tight G-dimer interface when GDP-bound and adopt a super-constricted state. However, the mechanism by which GTP hydrolysis drives BDLP super-constriction differs significantly from the dynamin 1 rung-sliding power stroke model (Liu *et al.*, 2021a), with increased constriction driven by rung pivoting mechanism. This involves rearrangements that increase the volume of the membrane binding domains and alter the filament lateral contacts to displace lipids from the bilayer, coupled with helical arrangements that restrict lipids to a single lipid channel. A minor population of less constricted GDP-bound filaments revealed both the most fundamental differences between GMPPNP- and GDP-bound BDLP protein-lipid filaments as well as potential intermediate states between $BDLP_{GMPPNP}$ and

$BDLP_{GDP}$ during a mechanistic cycle that leads to super-constriction. Cryo-ET analysis of BDLP-mediated membrane remodelling demonstrated, for the first time, the capacity of a DSF member to mediate stable lipid phase changes.

### 5.3.1 The Role of Nucleotide in BDLP-mediated Membrane Remodelling

The role of GTP hydrolysis in DSF-mediated membrane remodelling is inconsistent, with apparently contradictory effects on hinge 2 conformation observed for classical- and mitofusin-like DRPs (Anand, Eschenburg & Reubold, 2016; Rennie *et al.*, 2014; Yan *et al.*, 2018). In dynamin 1-mediated membrane constriction, GTP hydrolysis facilitates power-strokes that drive rung sliding and filament constriction, ultimately resulting in a super-constricted two-start filament architecture post GTP-hydrolysis (Jimah *et al.*, 2024). Previously, the overall closed BDLP conformations in apo and GDP-bound BDLP crystal structures, where the predicted paddle was concealed within the molecule, and overall open conformations in the membrane constricting GMPPNP-bound BDLP filaments, suggested that nucleotide hydrolysis induced BDLP filament depolymerisation to release the underlying destabilised membrane (Low & Löwe, 2006; Low *et al.*, 2009). However, the $BDLP_{GDP}$ filament structure presented here has revealed that, in a manner somewhat analogous to dynamin 1, GTP hydrolysis drives filament rearrangements to achieve super-constriction (Figure 43D), albeit through markedly different mechanisms.

#### 5.3.1.1 From Membrane-binding to Super-constriction

NS-EM analysis demonstrated that membrane-bound BDLP does not form ordered arrays in the apo state, but does form self-assembled decorations and tubulates liposomes in a helical assembly when nucleotide-bound (Figure 42). Furthermore G-dimers and left-handed rungs of back-to-back associated G-dimers were the stable assembly units of both GMPPNP- and GDP-bound BDLP protein-lipid filaments (Figure 46 & Figure 42). This confirmed that nucleotide binding is the primary driver of self-assembly, promoting G-dimer formation. Given the simulated ability of Fzo to bind membrane in an overall closed conformation (De Vecchis *et al.*, 2017), these observations also suggest that nucleotide binding and G-dimerisation, rather than membrane binding, drives conformational changes, including hinge 1 opening, that facilitate self-assembly of BDLP helical filaments.

As discussed in Chapter 4, the fundamental filament interface of tight G-dimers within $BDLP_{GMPNP}$ rungs, which has also now been demonstrated as stable within $BDLP_{GDP}$ rungs (Figure 44C), precludes a dynamin 1-like rung sliding power stroke mechanism that involves breaking and re-forming of inter-rung G-dimers to achieve super constriction. The $BDLP_{GDP}$ structure has demonstrated that super-constriction is instead achieved via a rung-pivoting mechanism; GTP hydrolysis disrupts lateral GTPase domain contacts, specifically an inter-rung tyrosine-137 π-stacking interaction, in favour of strong lateral inter-rung MBD contacts to displace lipids and achieve tighter constriction. The $BDLP_{GDP(L2)}$ and $BDLP_{GDP(L3)}$ filaments corroborated this finding as, despite not achieving super constriction, they demonstrated that GDP-bound BDLP filaments do not form inter-rung lateral tyrosine-137 contacts. The BDLP filament structures suggest a mechanism for how GTP hydrolysis breaks lateral tyrosine-137 contacts: GTP hydrolysis causes active site rearrangements, specifically rearrangements of switch 1, which is ordered in $BDLP_{GMPPNP}$, and disordered in the GDP-bound crystal structure and $BDLP_{GDP(L2)}$ and $BDLP_{GDP(L3)}$ (Figure 53B), and seemingly adopts a slightly different conformation in $BDLP_{GDP}$ (Figure 44C). The proximity of switch 1 to H4 and tyrosine-137 suggests switch 1 conformational changes help break lateral $\pi$-stacking interactions (Figure 47). The rung-pivoting mechanism of bilayer constriction is also driven by formation of a tight MBD lattice. Forming membrane-interfacing domain lateral contacts in membrane-constricting filaments is a conserved feature of DSF helical polymers, as demonstrated by s-Mgm1 and dynamin 1 structures (Faelber *et al.*, 2019; Jimah *et al.*, 2024). However, given the differing mechanisms of super-constriction, these contacts are not formed at the expense of GTPase domain lateral contacts. In conclusion, GTP hydrolysis drives BDLP protein-lipid filament super-constriction by providing the energy to disrupt lateral GTPase domain contacts to allow rung-pivoting and formation of lateral MBD contacts that displace lipids.

Previously, the closing of hinge 1 and opening of hinge 2 upon GTP hydrolysis, as evidenced by the GDP-bound BDLP crystal structure (Low & Löwe, 2006), was proposed as a mechanism for depolymerisation and BDLP releasing membrane. However, the $BDLP_{GDP}$ structure demonstrated that BDLP can form stable polymers when GDP-bound, with tight G-dimer interfaces and a closed hinge 2 and open hinge 1 conformation (Figure 45A). Furthermore, $BDLP_{GDP(L2)}$ and $BDLP_{GDP(L3)}$ both exhibited largely equivalent hinge conformations (Figure 54B).

The membrane and hexII nanoparticle BDLP decorations observed in hormogonia (Figure 28) and *in vitro* (Figure 58A) suggest that BDLP remains stably membrane bound until an external factor mediates GDP release or depolymerises BDLP coatomers and filaments. Consequently, a significant question raised by these results is how does BDLP depolymerise and release the membrane? It is possible that BDLP2, potentially through recruitment of DnaK chaperones via its DnaJ domain, acts to depolymerise BDLP assemblies. The eukaryotic DnaK homologue Hsp70 has been demonstrated to depolymerise clathrin assemblies on endocytic vesicles (Sousa *et al.*, 2016), therefore chaperone-mediated depolymerisation of membrane remodelling scaffolds is not unprecedented. Alternatively, another factor, expressed during vegetative cell development once the hormogonium life cycle stage terminates (Risser, 2023), may mediate GDP release or BDLP depolymerisation or both. The interaction of DRPs with regulatory factors is not unprecedented, as exemplified by regulatory interactions between dynamin 1 and BAR-domain proteins or Drp1 with the mitochondrial surface receptor Mid49 (Kalia *et al.*, 2018; Zerihun, Sukumaran & Qvit, 2023; Daumke, Roux & Haucke, 2014).

The overall open conformation of GDP-bound BDLP within filaments casts doubt on the physiological relevance of the overall closed (hinge 1 closed, hinge 2 open) conformation of apo and GDP-bound BDLP crystal structures (Low & Löwe, 2006). It is unclear whether this conformation exists in solution or was induced by crystal packing. Indeed, LeoA, a BDLP homologue, was crystallised in an open conformation in the apo state (Michie *et al.*, 2014). The same doubt it applicable to the reported Mfn1 and Mfn2 hinge 2 open conformations (Yan *et al.*, 2018; Li *et al.*, 2019). However, overall closed conformations have been demonstrated for other DSF members. The cmDmn1 closed structure was validated in solution, and IniA was crystallised in a closed conformation and demonstrated nucleotide dependent oligomeric state changes in solution (Wang *et al.*, 2019; Bohuszewicz & Low, 2018). Therefore, it is likely that a closed BDLP conformation is present in solution, and also when membrane bound in the apo state, like Fzo (De Vecchis *et al.*, 2017). Nevertheless, the mechanisms by which nucleotide is released and how BDLP transitions from an open, membrane-bound conformation to a closed conformation or off-membrane state are unknown.

An unresolved question presented in Chapter 4 was why PG liposomes, and not ETE liposomes, stimulate GTP turnover, despite filaments formed on either template exhibiting

similar arrangements and identical tight G-dimer interfaces and ordered switch 1 (and presumably active site) conformations. In this chapter, the capacity of stable GDP-bound filaments to form on PG liposome templates was demonstrated (Figure 42), and stable super-constricted filaments post GTP hydrolysis were also observed (Figure 58C). This phenomenon does not occur on ETE liposome templates, to which BDLP only weakly binds when GDP-bound (Figure 35C). This observation suggests that in filaments formed on ETE liposomes, GTP hydrolysis would lead to disassembly and membrane release. Crucially, this would involve loss of a tight G-dimer interface and likely formation of a closed BDLP conformation that does not promote self-assembly. Conversely, following GTP hydrolysis in filaments formed on PG liposome templates, BDLP remains assembled in an open conformation. The open self-assembled conformation of BDLP may promote self-assembly of additional BDLP protomers to form longer filaments, and therefore promote GTP binding with a tight G-dimer interface that is catalytically active, thus increasing the observed GTPase activity *in vitro*. In summary, the ability of BDLP to remain bound to PG liposomes post-hydrolysis may explain why lipid-stimulated GTP turnover is observed in the presence of PG liposomes.

#### 5.3.1.2 Intermediate States

The minor population of thicker GDP-bound BDLP filaments observed in this study, $BDLP_{GDP(L2)}$ and $BDLP_{GDP(L3)}$, exhibited several intermediate features between the $BDLP_{GMPPNP}$ and $BDLP_{GDP}$ structures. The $BDLP_{GDP(L2)}$ and $BDLP_{GDP(L3)}$ filament diameters were 500 Å and 535 Å respectively (Figure 51D & Figure 52D), comparable to the 530 Å $BDLP_{GMPPNP(PG)}$ filament diameter. The 95 Å and 120 Å lumen diameters ($BDLP_{GDP(L2)}$ and $BDLP_{GDP(L3)}$ respectively) suggested similar or slightly increased membrane constriction relative to the $BDLP_{GMPPNP(PG)}$ 117 Å lumen diameter, but not $BDLPG_{GDP}$-like super-constriction. It remains unclear whether these filaments formed by relaxation of super-constricted filaments or were unable to achieve super-constriction, given they did not benefit from energy released by GTP hydrolysis. Nevertheless, they demonstrated several intermediate features that elucidated potential mechanisms for how BDLP might achieve super-constriction. $BDLP_{GDP(L3)}$ demonstrated how, in rungs not stably held together by inter-rung GTPase interactions, asymmetric back-to-back tetramers can form within rungs (Figure 54). Tetramer asymmetry is required by $BDLP_{GDP}$ to form tight inter-rung MBD contacts and a 1-start LC.

Additionally, $BDLP_{GDP(L3)}$ exhibited both broken and intact H18 conformations (Figure 52F), indicating a delicate equilibrium exists for the H18 conformation. The equilibrium is shifted in favour of a broken conformation in GDP-bound filaments with weaker or disrupted inter-rung GTPase domain associations. And in GMPPNP-bound filaments with tight inter-rung GTPase domain associations, the equilibrium is shifted in favour of an intact H18. H18 breaks prime MDD residues to interact with and disrupt the membrane to increase lipid displacement and consequently membrane constriction (Figure 45C). The weak neck-GTPase domain contacts in $BDLP_{GDP(L3)}$ (Figure 55C) may explain why super-constriction was not achieved, as the H18 conformational equilibrium may have been less shifted in favour of H18 breaks as a result of these contacts. Consequently, $BDLP_{GDP(L3)}$ was restricted in its ability to disrupt the membrane via MDD residues. In the fully rung-separated $BDLP_{GDP}$ filament, the equilibrium is shifted in strong favour of H18 breaks allowing the MDD to disrupt the membrane to a greater extent.

$BDLP_{GDP(L2)}$ possessed a broken H18 conformation, but only a two-helix MBD (Figure 54B). This observation suggested that an H18 helix break first allows more MDD residues to interact with the membrane before folding to expand the MBD. It is possible that the weak inter-rung neck-GTPase domain contacts of $BDLP_{GDP(L2)}$ prevented the full pivot mechanism-based formation of extensive lateral MBD contacts that facilitate the folding of MDD residues into the membrane, as observed in $BDLP_{GDP}$ (Figure 45 & Figure 46). The ubiquitous H18 helix breaks of $BDLP_{GDP(L2)}$ would have allowed more MDD residues to interact with the membrane, which, whilst disordered, may have still contributed to bilayer disruption that enabled $BDLP_{GDP(L2)}$ to achieve greater membrane constriction than $BDLP_{GDP(L3)}$ and $BDLP_{GMPPNP(PG)}$ (both of which demonstrated more intact H18 conformations, and consequently reduced ability for MDD residues to disrupt the membrane).

$BDLP_{GDP(L2)}$ and $BDLP_{GDP(L3)}$ also exhibited disordered switch 1 conformations (Figure 53B) that were not observed in $BDLP_{GDP}$ (Figure 44C). This corroborated a mechanism for the disruption of tyrosine-137 inter-rung contacts driven by GTP hydrolysis and subsequent switch 1 conformational changes. Both filaments also demonstrated hinges 1 and 2 conformational flexibility (Figure 54), and the overall filament diversity presented in this study illustrates flexibility of the filament interfaces. Both hinge and interface flexibility are conserved features of DSF filaments demonstrated in dynamin 1 and s-Opa1 filaments (Liu *et al.*, 2021a; von der Malsburg *et al.*, 2023). In summary, the minor population of $BDLP_{GDP(L2)}$ and $BDLP_{GDP(L3)}$

filaments provided insights into the role of GTP hydrolysis in BDLP-mediated membrane remodelling. Specifically, they corroborated a mechanism for GTP-hydrolysis driving rung-separation at the GTPase domain level which promotes H18 helix breaks to facilitate lipid displacement and increased membrane constriction.

### 5.3.2 A Conserved Membrane Displacement Mechanism?

A remarkable feature of $BDLP_{GDP}$ was the near-complete displacement of lipids from the filament, with the membrane interface being predominantly composed of protein (Figure 43D & Figure 44A). Disruption of bilayer outer leaflet appears to be a conserved mechanism for achieving membrane constriction (Liu *et al.*, 2021a; Jimah *et al.*, 2024), although the extensive lipid displacement observed in this study is thus far unique to the BDLP protein-lipid filaments. It has also been demonstrated that the paddles of s-Opa1 filaments insert into and lift lipids from the outer leaflet to disrupt the bilayer and enhance constriction (von der Malsburg *et al.*, 2023).

Recent research has demonstrated that a minimal construct of Mfn1 comprising the heptad repeat region 1 (HR1) can mediate fusion of vesicles via bilayer disruption, but requires membrane packing defects to allow its insertion into the bilayer (Daste *et al.*, 2018; Vlieghe *et al.*, 2023). Notably, the HR1 domain corresponds to the neck and trunk domain regions of BDLP between the GTPase and MBD ($H13_{\beta}$-H19), and membrane disruption by HR1 was specifically attributed to its C-terminus (Daste *et al.*, 2018) – a region corresponding to the BDLP MDD (Figure 45C & Figure 45D). Therefore, the MDD rearrangements in $BDLP_{GDP}$, which allow membrane interaction and disruption, provide a mechanistic insight into how the mitofusins fuse OMMs, as proposed by the model in Figure 61.

The minimal two-helix MBD identified in $BDLP_{GMPPNP}$ represents the initial BDLP membrane interface, and is analogous to the two transmembrane helices proposed to facilitate membrane binding by the mitofusins. Membrane binding by the two-helix MBD induces packing defects in the membrane; in the extreme case of BDLP, the helical arrangement of two-helix MBDs creates a 6-start right-handed helical LC of inner leaflet lipids (Figure 50B). Membrane binding by the two mitofusin transmembrane helices in an analogous manner would also create packing defects that would allow the C-terminal region of HR1 to disrupt the membrane (Vlieghe *et al.*, 2023). Bilayer penetration and disruption by the BDLP MDD,

which in the case of Dimer B involves formation of a four-helix MBD (Figure 45C & Figure 45D), indicate how the C-terminal region of HR1 might disrupt the bilayer to achieve fusion (Daste *et al.*, 2018). In summary, the mechanism revealed by $BDLP_{GDP,}$ of increased bilayer displacement and disruption by the MDD, provides mechanistic insights into how the mitofusins achieve fusion through disruption of the bilayer. However, it remains to be established whether the mitofusins can also form BDLP-like helical assemblies.

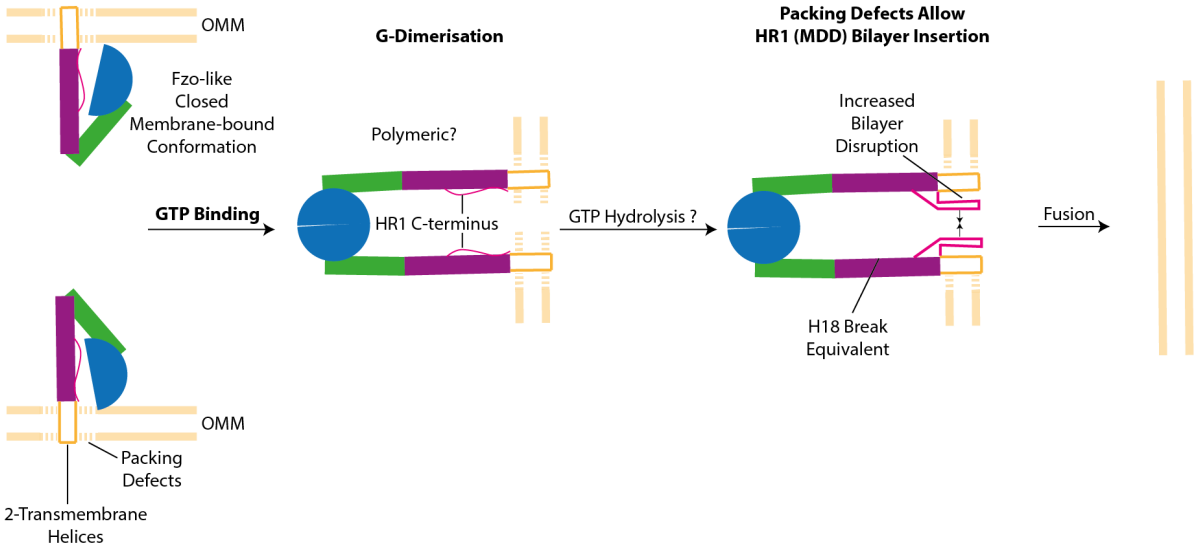


**Figure 61. Model for Mitofusin-mediated Membrane Fusion.**
Mitofusins bind the membrane via two trans-membrane helices in a Fzo/BDLP-like manner. The two-helix bundle induces membrane packing defects. GTP binding allows transition to an open conformation and G-dimerisation, which tethers membranes in trans. Packing defects in the trans-tethered membranes allow the C-terminal end of HR1 (equivalent to the BDLP MDD) to penetrate and disrupt the bilayer. This may be aided by GTP hydrolysis and, subsequently, a helix-break in the BDLP H18 equivalent. The disrupted bilayers held in close proximity are primed to undergo fusion.

### 5.3.3 Structural Comparisons Reveal MBD Conservation Across the Mitofusin-like Dynamin Clade

Despite the mitofusins being the closest BDLP homologues, they share only approximately 30% sequence homology with BDLP (Low & Löwe, 2006). This demonstrates the remarkable structural convergence of low shared homology but related sequences within the DSF. In general, facilitated by advancements in structural biology and structural prediction tools such as Alphafold (Jumper *et al.*, 2021), structural homology of distantly or seemingly unrelated sequences is emerging as a key indicator of protein function. For instance, the archaeallum

and bacterial flagellar filament have converged on related structures that enable them to form analogous filaments that facilitate reversible motility (Kreutzberger *et al.*, 2022).

To this end, the BDLP sequence was aligned with the sequences of the mitofusins, Fzo, and IniA (Figure 63A) (Sievers *et al.*, 2011), and the sequence positions that aligned with the BDLP MBD and MDD were correlated with their experimentally-determined or Alphafold-predicted structures (Figure 63B), to understand the conservation of the membrane displacement mechanism observed for BDLP (Wang *et al.*, 2019; Varadi *et al.*, 2024).

This analysis revealed that the MDD and MBD were conserved features of IniA, the mitofusins and Fzo. The IniA crystal structure demonstrated how the MBD and MDD were located within the core of the overall folded conformation, analogous to the BDLP crystal structures (Figure 63B). The mitofusins and Fzo were predicted in an overall open conformation, with MBD helices positioned below the trunk, analogous to the BDLP structure within filaments. All structures exhibited a broken H18 equivalent conformation, with residues that aligned with the start of the BDLP MDD observed at the helix break location. Consequently, the predicted MDD residues are positioned to facilitate bilayer disruption in addition to the transmembrane helices (MBD). This suggests the BDLP MDD is a conserved feature of mitofusin-like DRPs that mediates membrane disruption in addition to the established transmembrane helices. Although the predicted MDD and MBD helices of the mitofusins and Fzo did not form a helical bundle like $BDLP_{GDP}$ Dimer B, it is noteworthy that these predictions were conducted in the absence of lateral helical contacts and lipids that likely helped to order the $BDLP_{GDP}$ MDDs. In conclusion, the BDLP mechanism of membrane disruption appears to be conserved throughout the mitofusin-like DRPs, and consequently, this study provides insight into the mechanism by which mitofusins disrupt the bilayer to achieve fusion.

Given that structural homology demonstrated a conserved mechanism of membrane disruption, an investigation was conducted to determine whether structural homology could also identify other mitofusin-like DRPs across the three domains of life. The recent deposition of Alphafold-predicted structures for all known coding sequences has facilitated the development of rapid algorithms such as Foldseek and AlphaFind, which can identify

structural homology irrespective of sequence conservation (Varadi *et al.*, 2024; Procházka *et al.*, 2024; van Kempen *et al.*, 2024). Comparison of both the open and closed BDLP conformations with predicted protein structures within the Alphafold database using these tools revealed that mitofusin-like DRPs, and likely the MDD mechanism of membrane disruption, are conserved across all three domains of life (Figure 62).

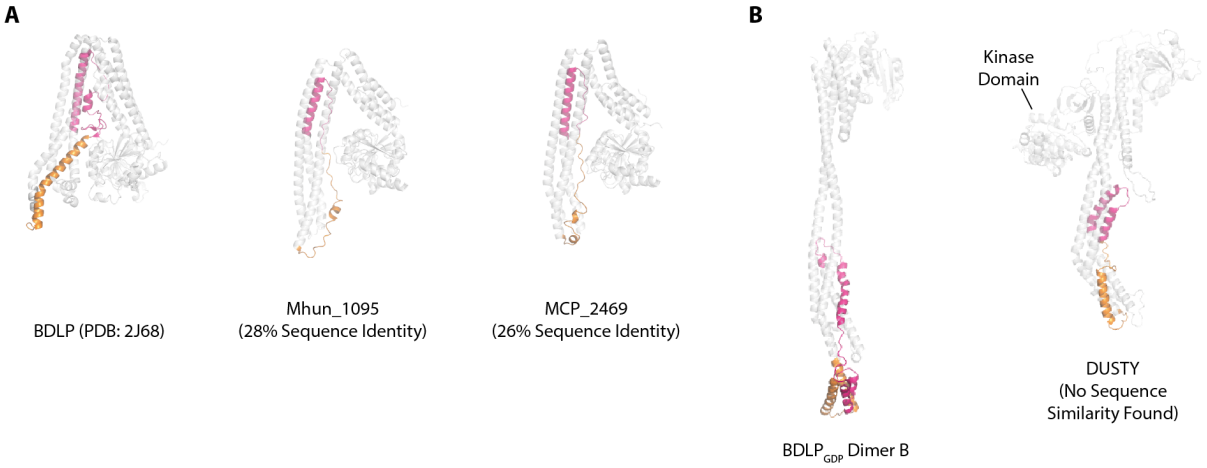


**Figure 62. BDLP Homologues Identified by Structural Homology.**
**A,** GDP-bound BDLP crystal structure, coloured by MBD (orange) and MDD (pink). Also, Alphafold predictions of archaeal BDLP-like genes from *Methanospirillum hungatei* JF-1 (gene name: Mhun_1095) and *Methanocella paludicola* (MCP_2469), with estimated MBD and MDD coloured based on structural homology with BDLP. **B,** $BDLP_{GDP}$ Dimer B coloured by MBD and MDD. Also, Alphafold prediction of DUSTY (human) structure (gene name: DSTYK), coloured by estimated MBD and MDD based on structural homology with BDLP.

Various archaeal mitofusin-like homologues were identified, some in a BDLP closed conformation (Figure 62A). Archaea exhibit diverse and complex morphologies (van Wolferen *et al.*, 2022), and consequently, archaeal DRPs may contribute to the development and maintenance of these structures. Analysis of the mitofusin-like DRPs from *Methanospirillum hungatei* JF-1 (Mhun_1095) and *Methanocella paludicola* (MCP_2469) indicated that both possessed active P-loops with a conserved terminal serine, suggesting a capacity to bind and hydrolyse GTP. Mhun_1095 and MCP_2469 shared only 28% and 26% sequence identity with BDLP respectively. However, their structural homology with BDLP suggests they are capable of binding and disrupting bilayers via a MBD and MDD (Figure 62A), emphasising the BDLP mechanism of bilayer displacement as an ancient mode of membrane binding and disruption. The question of whether archaeal dynamins share the conserved abilities of self-assembly

and membrane constriction remains to be elucidated, although the structural homology with BDLP suggests they likely possess this feature. Mhun_1095 is encoded alongside another BDLP homologue Mhun_1096 in the genome, analogous to many bacterial DRPs that exist as DRP pairs, including BDLP (Bohuszewicz, Liu & Low, 2016).

AlphaFind, Foldseek and Foldseek cluster analyses (Barrio-Hernandez *et al.*, 2023) also identified several eukaryotic GTPases that have not previously been discussed as DSF members. For instance, SLIP GTPases, although annotated in InterPro with dynamin-like domains (Paysan-Lafosse *et al.*, 2023), are recognised as nucleus-localised GTPases involved in replication and implicated in certain cancer-types (Richter *et al.*, 2009). Predicted structures of SLIP GTPases exhibited striking structural homology with BDLP, often predicted in a closed conformation. Furthermore, several BDLP homologues with additional C-terminal kinase domains were identified. Of particular interest, the human dual-serine-threonine kinase (DUSTY) protein is not annotated with dynamin-like domains by InterPro. Using the default BLAST settings (Zhang *et al.*, 2000), no sequence similarity between BDLP and DUSTY was identified. However, Alphafold structural prediction demonstrated that DUSTY arranges with canonical DSF domain architecture, specifically in an open BDLP-like conformation with a closed BDLP-like trunk conformation (Figure 62B). This structural prediction also suggested that DUSTY might possess a conserved BDLP-like method of membrane binding and disruption via MBDs and MDDs.

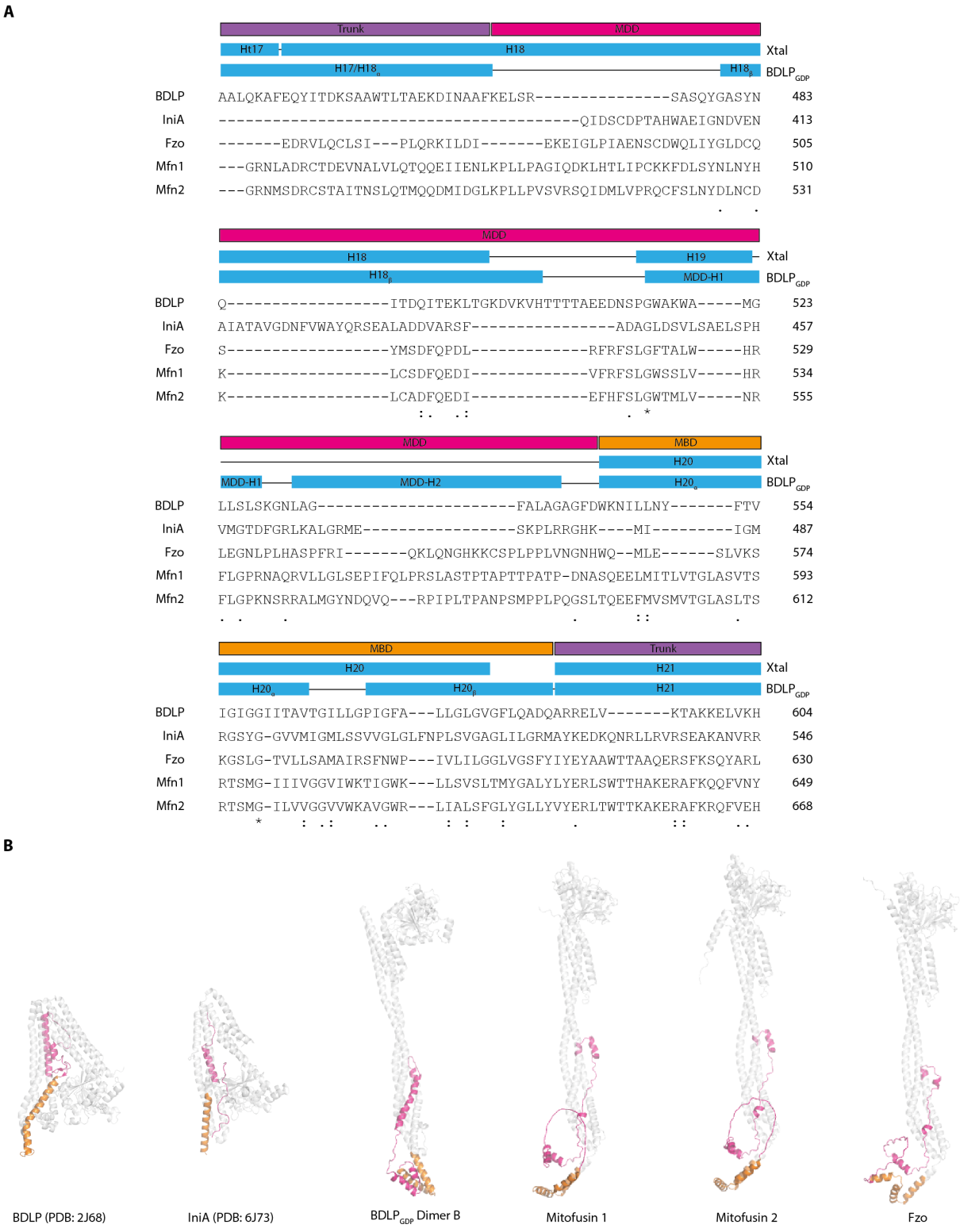


**Figure 63. Conservation of the BDLP MDD.**
**A,** Multiple sequence alignment of BDLP, IniA (*Mycobacterium smegmatis*), mitofusins 1 and 2 (human) and Fzo (*S. cerevisiae*). Shown are the sequence regions of the MDD, MBD and flanking regions. Domains are annotated and coloured with BDLP nomenclature from this study, and helices from the GDP-bound BDLP crystal structure (Xtal) and Dimer B structure ($BDLP_{GDP}$) are represented by blue boxes. * = identical residues, : = conserved substitutions, . = semi-conserved substitutions. **B,** Monomers of the GDP-bound BDLP and GTP-bound IniA crystal structures, $BDLP_{GDP}$ Dimer B cryo-

EM structure, and Mfn1, Mfn2, and Fzo Alphafold predictions (Varadi *et al.*, 2024). Coloured by sequence that aligned with the BDLP MDD (pink) and MBD (orange).

The DUSTY BDLP-like domains have predominantly been characterised as non-catalytic regions, and the kinase (ePK) domain is involved in complex signalling pathways that implicate DUSTY in lung cancer (Peng *et al.*, 2006; Zhong *et al.*, 2021a). DUSTY possesses an inactive P-loop, which suggests it may not be capable of binding and hydrolysing GTP; however, this functionality may be compensated for by the kinase domain. Alternatively, unlike canonical DSF members, GTPase activating proteins or guanine exchange factors may interact with DUSTY. To investigate this hypothesis, the DUSTY interactome was predicted using Human PPI (Zhang *et al.*, 2024), which suggested that a guanine exchange factor (rhoGEF11), which has demonstrated ability to bind the RhoA GTPase (Derewenda *et al.*, 2004), likely interacts with DUSTY. This would represent a novel method of DSF GTPase domain regulation, as it is currently postulated that all DSF members do not require GTPase activating proteins or guanine exchange factors (Praefcke & McMahon, 2004). This also raises significant questions regarding whether DUSTY can form canonical G-dimers and self-assemble into helical filaments. Although the homology with BDLP suggests a potential mechanism for membrane binding, whether DUSTY can constrict membrane is also a pertinent question. DUSTY knockouts affect lysosome biogenesis and vesicle trafficking (Sun *et al.*, 2020). Whether this is solely related to their role in signalling via the kinase domain or a putative membrane remodelling activity is also an intriguing area of inquiry.

In conclusion, structural comparisons with the Alphafold database have revealed broad conservation of BDLP structural features, particularly the MBD and MDD, across all three domains of life, suggesting that the mechanism of membrane disruption presented here is ancient and involved in myriad membrane remodelling events.

### 5.3.4 BDLP-mediated Lipid Phase Changes

Cryo-ET analysis in this chapter demonstrated, for the first time, the capacity of DRP to facilitate stable lipid phase changes (Figure 57 & Figure 58). The *in vitro* conditions used, and the dose-sensitivity of ordered arrays (Figure 57), constrained data acquisition to what are likely the earliest stages of membrane remodelling into alternative phases. The ordered

tubular structures of lipid arrays and potential end-on views (Figure 58) suggested that BDLP was capable of remodelling Lm phase liposomes into hexII phase arrays with long-range order. The putative hexII phase arrays appeared to emerge from the ends of multiple super-constricted filaments. The lipid arrays were also confined to the interior of a BDLP-decorated semi-constricted liposome. In Chapter 4, cryo-CLEM analysis of hormogonia indicated that BDLP remained bound to hexII nanoparticles (Figure 28). Despite Drp1 being seemingly able to bind transient hexII phase structures (Stepanyants *et al.*, 2015), this observation elucidates how BDLP was likely bound to hexII nanoparticle-encasing liposomes to form decorations observed in hormogonia. However, spontaneous transition of the encasing liposomes to the hexII phase in later stages of membrane remodelling cannot be excluded.

The emergence of putative hexII phase lipids from the filament ends (Figure 59) validated the super-constricted $BDLP_{GDP}$ filament as a physiologically relevant membrane remodelling BDLP assembly. Furthermore, this suggested that the bilayer disruption and confinement of inner leaflet lipids to the 1-start LC (Figure 48) represents the mechanism by which BDLP filaments remodel lipids into a configuration that promotes phase changes. It is possible that the geometry of the $BDLP_{GDP}$ 1-start LC (which corresponds to a more conical lipid shape compared to the cylindrical lipid-accommodating $BDLP_{GMPPNP}$ LCs (Figure 49)), arranges inner leaflet lipids in a configuration that promotes spontaneous adoption of the hexII phase at the filament ends. Within tomograms, filament diameters smaller than the super-constricted $BDLP_{GDP}$ filament diameter (450 Å) were observed, including in the PG liposome control sample (Figure 60). This observation suggested that in the presence of GTP, additional constriction beyond that of the $BDLP_{GDP}$ structure occurs, representing an unresolved mechanistic step. This extra constriction might induce displacement of lipids from the LC from the filament termini and may involve further ordering of the Dimer A MDDs to adopt a more Dimer B MDD-like conformation (Figure 45D). Future sub-tomogram averaging, or single particle analysis, may provide further mechanistic insight.

### 5.3.5 Conclusions

This chapter has elucidated the role of GTP hydrolysis in BDLP-mediated membrane remodelling, revealing a novel mechanism of membrane super-constriction. This process confines lipids to a single lipid channel with geometry favouring hexII phase-like lipid

arrangements. Cryo-ET analysis confirmed BDLP's capacity to remodel lamellar phase liposomes into ordered lipid arrays, likely representing hexII phase structures.

These findings have broader implications for understanding DSF function. The identification of a conserved membrane displacement domain (MDD) across mitofusin-like dynamins suggests a shared mechanism for bilayer disruption, potentially elucidating details of mitofusin-mediated fusion. Moreover, the study revealed structural homology between BDLP and previously unrecognised dynamin-like proteins, including in archaea and eukaryotic proteins such as DUSTY, indicating an ancient and widely conserved membrane remodelling mechanism.

Outstanding questions remain regarding the precise mechanistic details of lipid release from BDLP filaments, the extent of hexII nanoparticle formation in wild-type hormogonia, and how BDLP disassembles from membranes. Future protein-lipid simulations could provide additional insights into lipid channel interactions. Nonetheless, this study has advanced understanding of DRP-mediated membrane remodelling and lipid phase transitions, with implications for the mitofusins in particular.

# Chapter 6: Discussion

The research presented in this thesis used biochemical, cryo-EM and cryo-ET analyses to elucidate the *in vivo* role of BDLP during hormogonium development of *N. punctiforme,* specifically in the remodelling of thylakoid membranes into BDLP-decorated hexII nanoparticles. Furthermore, structural and mechanistic insights into BDLP-mediated thylakoid remodelling were revealed. The mode of BDLP self-assembly and membrane binding also has broader implications for mechanisms of mitofusin-mediated mitochondrial outer membrane fusion. This chapter synthesises the findings of Chapter 4 and Chapter 5 into models explicating how and why BDLP remodels thylakoids into hexII nanoparticles. The primary objective of this study was to investigate the most fundamental conserved mechanisms of membrane remodelling in the DSF. Consequently, the conserved DSF principles demonstrated by BDLP are also discussed.

## 6.1 The Inverse-hexagonal Phase in *N. punctiforme* hormogonia

It has been proposed that cyanobacterial DRPs may contribute to thylakoid biogenesis and maintenance (Jilly *et al.*, 2018). However, the ESCRT-III homologue Vipp1 possesses well-established mechanisms of membrane repair and fusion, and specific thylakoid remodelling activity of Vipp1 has been demonstrated (Naskar *et al.*, 2023; Gupta *et al.*, 2021). Consequently, an alternative non-redundant role for cyanobacterial DRPs may exist. Chapter 4 demonstrated that in hormogonia, both the BDLP gene and MGDG synthesis genes were upregulated, whereas genes involved in the synthesis of cylindrical, Lm phase-favouring lipids were downregulated. Furthermore, BDLP-decorated hexII nanoparticles appeared to undergo liquid-liquid phase separation into partitioned zones alongside BDLP. These findings suggested a gene regulation-driven process during hormogonium development to sequester and maintain thylakoid lipids in hexII nanoparticles. Hormogonia exhibit significantly reduced photosynthetic activity and are primarily dedicated to motility (Risser, 2023); hence, the majority of thylakoid membranes become redundant in hormogonia. Sequestering thylakoids may serve functions in (1) providing reserves of thylakoid lipids for future thylakoid biogenesis when hormogonia differentiate into vegetative photosynthetic filaments, and (2) in mediating regulation of lateral pressure in the remaining thylakoid membranes.

Lipid synthesis incurs a substantial energetic cost, exceeding that of protein synthesis relative to the cell mass of bacteria (Ortega-Arzola, Higgins & Cockell, 2024; Mahmoudabadi *et al.*, 2019). Consequently, the sequestration of thylakoid lipids in hexII nanoparticles when they are not required, protected and stabilised by LLPS and BDLP decorations, negates the energy demands of lipid degradation and synthesis by storing lipids for future use. Moreover, during differentiation into vegetative cells, depolymerisation of the BDLP coatomers would facilitate rapid reorganisation of hexII nanoparticles into thylakoids via a spontaneous phase transition (Guéguen & Maréchal, 2022), particularly in the presence of large amounts of newly synthesised photosynthetic machinery (Simidjiev *et al.*, 2000; Garab *et al.*, 2022). This process would enable cells to reinitiate photosynthetic activity more rapidly than if thylakoids were rebuilt via lipid synthesis. Additionally, cyanobacteria and *N. punctiforme* modify their lipid composition in response to various stress conditions (Kobayashi *et al.*, 2024; Mikhaylenko, Skorokhod & Kholodny, 1998). The lipids sequestered in hexII nanoparticles would reflect the lipid composition of cells during the early stages of hormogonium development. This would provide a lipid source, compositionally unaffected by potential stresses experienced in the hormogonium life-cycle stage, for biogenesis of thylakoids in the development of post-hormogonium vegetative cells.

Photosynthesis is not completely abolished in hormogonia (Campbell & Meeks, 1989). The remaining thylakoids and photosynthetic machinery in hormogonia must maintain a protein-lipid ratio and biophysical properties that enable efficient photosynthesis. Photosystem II activity is regulated by the lateral pressure within the bilayer, which is turn determined by the lipid volume and composition (Tietz *et al.*, 2015; Garab *et al.*, 2022; Kirchhoff *et al.*, 2007). Controlled and stable BDLP-mediated remodelling of thylakoids and the removal of lipids, including a potentially disproportionate amount of MGDG, may provide a mechanism to regulate or enhance photosynthetic activity in hormogonia that frequently exist in low-light conditions (Risser, 2023). Overall, BDLP-mediated thylakoid phase changes may offer a means of photosystem regulation and energy-efficient thylakoid degradation and biogenesis in hormogonia.

## 6.2 Potential Applications for BDLP-mediated Phase Changes in Drug Delivery

Non-bilayer lipid phases, in particular the cubic and hexII phases, are of particular interest for delivery of small molecule drugs (Chen, Ma & Gui, 2014; Almsherqi, Margadant & Deng, 2010; Chavda *et al.*, 2023). The contained and protected aqueous channels of lipid nanoparticles of either phase provide a protective environment to harbour small molecules. The hexII phase in particular offers increased resistance to pancreatic lipolysis, generally provides a mechanism of slower release of small molecules, is not cytotoxic, and has been shown to improve the bioavailability of various drugs (Chen, Ma & Gui, 2014; Chavda *et al.*, 2023). Considerable efforts have been made to create hexII phase drug carriers that are stable under physiological conditions (Chen, Ma & Gui, 2014; Chavda *et al.*, 2023). For example, for the stable delivery and prolonged release of breast cancer treatment drugs (Salata, Malagó & Lopes, 2022). BDLP-mediated remodelling of lipids into the hexII phase may prove useful for formation of coated and protected hexII nanoparticles typically larger than the small hexII hexasomes currently used for drug delivery (Chavda *et al.*, 2023). Additionally, BDLP hexII nanoparticle coatomers may prove a useful means for targeted delivery, with modifications of the external BDLP coat to facilitate binding to specific receptors.

## 6.3 A model for BDLP-mediated Lipid Phase Changes

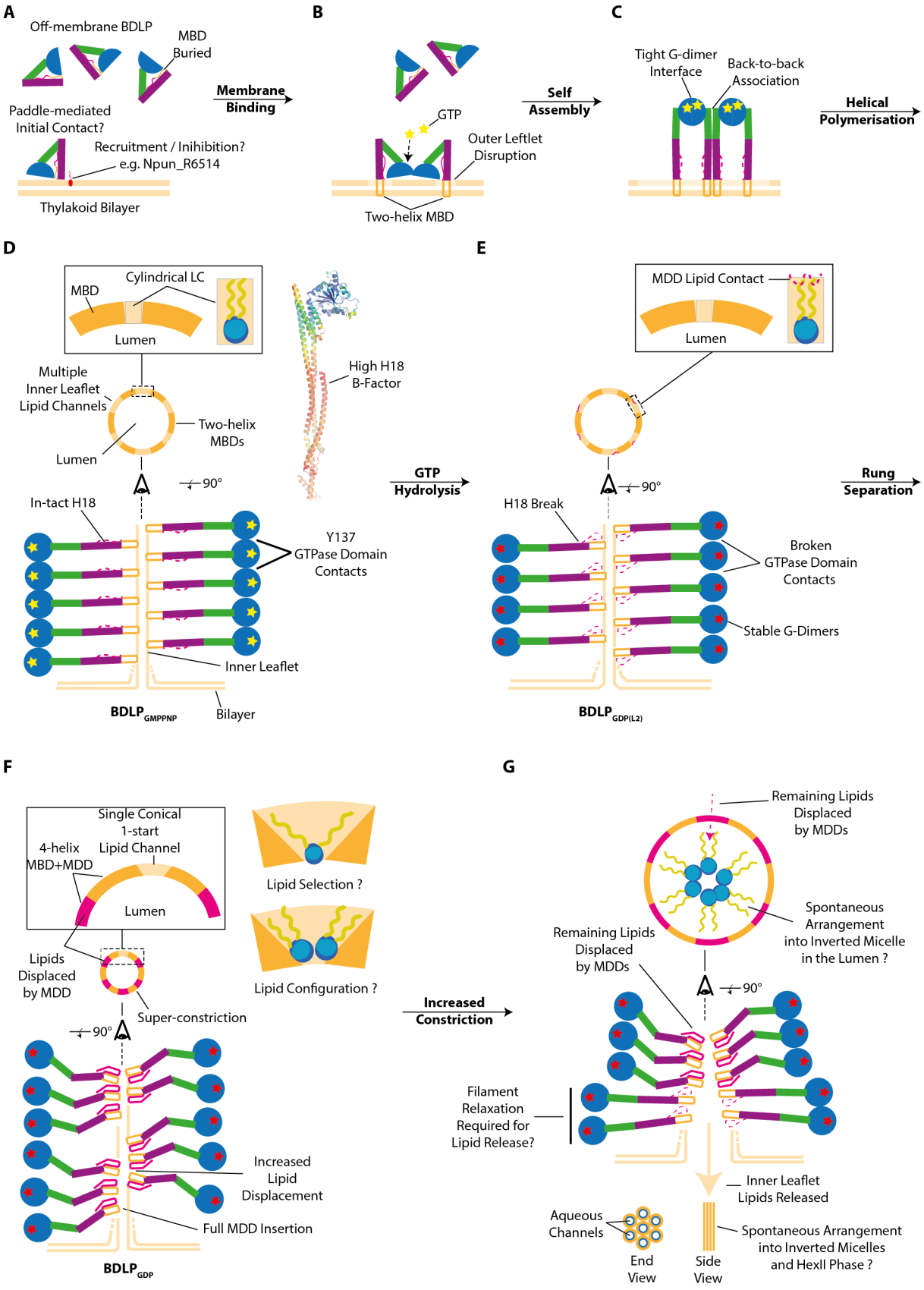


**Figure 64. Model of BDLP-Mediated Lipid Phase Changes.**

**A,** Apo BDLP is in a closed conformation (hinge 1 closed, hinge 2 open). Additional factors or the trunk tip (paddle) may mediate initial membrane contact and recruitment of BDLP to the membrane. **B,** BDLP binds membrane via reorganisation of H20 into a two-helix bundle, likely maintaining an overall closed conformation. **C,** GTP binding allows tight G-dimer interfaces to form, and BDLP transitions to an overall open conformation. G-dimers self-assemble on membrane in a back-to-back arrangement. **D,** Continued self-assembly leads to helical polymerisation on the membrane. The outer leaflet is displaced from the filament, and inner leaflet lipids are confined to helical lipid channels. Inter-rung GTPase domain contacts are formed within the filament. **E,** GTP hydrolysis breaks inter-rung GTPase domain contacts, facilitating a H18 helix break, which allows MDD residues to contact lipids in the helical channels. **F,** Complete rung separation on the GTPase and neck domain level facilitates or is driven by MDD folding within the lipid channels to create strong lateral MBD contacts. MDD ordering within the lipid channels also displaces more lipids from the filament, facilitating super-constriction. Only one lipid channel remains in this filament and has a shape complimentary to conical shaped lipids or lipids arranged with high negative curvature. **G,** Increased constriction may further displace lipids from the lipid channel into the filament lumen. Lipids may spontaneously adopt an inverted micelle (hexII) configuration within the filament lumen, or when released from the filament. This may require a relaxation of the filament from the super-constricted state.

The GMPPNP- and GDP-bound BDLP protein-lipid filament structures presented in Chapter 4 and Chapter 5 provided critical insights into how BDLP self-assembles, hydrolyses GTP, super-constricts the membrane and organises lipids. Based on these insights, a model of how BDLP mediates lipid phase changes is proposed in Figure 64.

In the off-membrane apo state, BDLP adopts a hinge 1 closed, hinge 2 open, overall closed conformation (Figure 64A) (Low & Löwe, 2006). The previously assigned paddle at the trunk tip may still hold relevance for mediating the initial membrane contacts and packing defects in the outer leaflet. Alternatively, additional factors such as the BDLP operon encoded Npun_R6514 might be involved in the recruitment of BDLP to the membrane, or involved in inhibiting membrane binding or self-assembly. Membrane binding is mediated by refolding of H20 to form a two-helix MBD which penetrates both bilayer leaflets below the trunk (Figure 64B), leading to bilayer packing defects. Given the simulated ability of Fzo to interface with membrane in a closed conformation (De Vecchis *et al.*, 2017), and the ability of apo BDLP to bind PG liposomes without forming ordered assemblies, it is likely that BDLP can bind membrane in a closed conformation. Subsequent GTP binding is therefore likely the trigger for hinge 1 opening and hinge 2 closing, allowing tight G-dimers to form (Figure 64C). The overall open conformation allows back-to-back association of G-dimers into nascent helical rungs. As membrane-bound G-dimers associate, the bilayer is further destabilised by the local concentration of membrane insertions leading to curvature induction, as evidenced in this study by the ability of $BDLP_{F583E}$ to semi-constrict liposomes with loosely packed helical rungs

whilst not fully disrupting the bilayer. Continued self-assembly and inter-rung association of G-dimers via tyrosine-137 π-stacking interactions leads to polymerisation of a helical filament (Figure 64D) – $BDLP_{GMPPNP}$.

Within the GTP-bound helical filament, lipids are confined to helical lipid channels. The outer leaflet is displaced from the filament by negative charge above the phenylalanine-583 cap, and only inner leaflet lipids are accommodated within the lipid channels. The lipid channels possess vertical walls, providing a surface shape complementary to cylindrical shaped lipids such as PG. Furthermore, H18 remains intact in the GTP-bound filament, preventing the MDD from contacting lipids. However, the high H18 B-factor suggests it is flexible and primed to undergo conformational change. The tight G-dimer interfaces prime BDLP for catalysis by positioning of conserved catalytic residues and motifs.

GTP hydrolysis changes the switch 1 conformation, and consequently disrupts the inter-rung tyrosine-137 interactions on the proximal H4, which breaks inter-rung GTPase domain contacts. This shifts the H18 conformational equilibrium, leading to H18 helix breaks (Figure 64E). The H18 break allows MDD residues to contact the lipids within the helical lipid channels. However, if inter-rung neck-GTPase domain contacts persist, as in $BDLP_{GDP(L2)}$, increased MBD lateral contacts cannot be formed. Complete separation of rungs at the neck and GTPase domain level allows a pivoting action of rungs, and formation of strong lateral MBD contacts, facilitated by the folding of the MDD into the lipid channels, where in the case of Dimer B it forms a two-helix bundle, creating a four-helix MBD that displaces all lipids from the channel (Figure 64F). Alternatively, the folding of the MDD into the lipid channels and consequent strong lateral MBD contacts may provide the energy required to disrupt neck-GTPase domain contacts – in other words, allow a transition from a $BDLP_{GDP(L2)}$ to $BDLP_{GDP}$ filament structure in a rung-pivoting action. Increased lipid disruption and displacement by the MDD facilitates the super-constriction observed in $BDLP_{GDP}$. The lipid displacement and helical rearrangements result in the confinement of remaining lipids within the filament to a single 1-start helical lipid channel. The lipid channel shape is also altered, with slanted hydrophobic surfaces, that might (1) selectively accommodate only conical shaped lipids or (2) force cylindrical lipids into a hexII-like high negative curvature configuration.

The displacement of outer leaflet lipids is crucial for mediating lipid phase transitions – only inner leaflet lipids in a high negative curvature configuration remain within the super-constricted filament. The release of these lipids from the lipid channels allows spontaneous arrangement of these lipids into inverted micelles either (1) in the filament lumen or (2) when released from the filament within the thylakoid lumen. An additional final constriction and lipid displacement may also occur (as observed by cryo-ET), to further displace lipids from the 1-start channel observed in $BDLP_{GDP}$. Both models (1) and (2) rely on the BDLP-driven arrangement of inner leaflet lipids that promoted spontaneous arrangement into inverted micelles.

## 6.4 Conserved Principles of DSF-mediated Membrane Remodelling

This study of BDLP has illuminated several conserved principles of DSF-mediated membrane remodelling. A fundamental feature is nucleotide-dependent self-assembly, with GTP binding facilitating tight G-dimer formation and subsequent polymerisation into helical filaments. This mirrors the behaviour of other DSF members such as dynamin 1 and mitofusins, but demonstrates differences in the primary oligomerisation interfaces of different filaments – G-dimers in BDLP filaments, diagonal trunk interfaces in dynamin 1-like filaments (Liu *et al.*, 2021a). The BDLP two-helix membrane binding domain demonstrates a conserved mechanism of bilayer penetration, analogous to the predicted transmembrane helices of mitofusins and Fzo (De Vecchis *et al.*, 2017), and more broadly analogous to the distinct membrane binding domains situated below the trunk in DSF filaments (von der Malsburg *et al.*, 2023; Jimah *et al.*, 2024).

The tight G-dimer interface observed in $BDLP_{GMPPNP}$ illustrates the conserved mechanism of assembly-stimulated GTP hydrolysis within the DSF, with catalytic residues positioned for efficient hydrolysis (Daumke & Praefcke, 2016). BDLP exhibits significant conformational flexibility about two conserved hinges in response to nucleotide state and membrane binding, crucial for transitions between closed cytosolic and open membrane-bound states as well as membrane remodelling. Additionally, the diverse BDLP filamentous assemblies demonstrate filament interface flexibility. These flexibilities are a shared feature across the DSF, enabling diverse functions (Ford & Chappie, 2019).

The BDLP preference for anionic lipids, particularly PG, mirrors the lipid specificity observed in other DSF members, such as the cardiolipin preference of Drp1 (Francy *et al.*, 2017). The ability of BDLP to displace lipids from the bilayer, particularly in its super-constricted GDP-bound state, reflects a conserved mechanism of membrane remodelling within the DSF. This displacement is crucial for inducing membrane curvature and facilitating fission or fusion events (von der Malsburg *et al.*, 2023; Liu *et al.*, 2021a; Jimah *et al.*, 2024). However. the near-complete lipid displacement from BDLP filaments is thus far unique to BDLP. In general, generating high curvature membranes is requisite for fission, fusion and hexII formation. HexII arrays can also form from elongation of fusion pores (Marrink & Mark, 2004). Consequently, the evolutionary transition from DSF-mediated fission and fusion to the regulation of lipid phase transitions (or the reverse) may have been a relatively facile adaptation.

The specific upregulation of BDLP during hormogonium development highlights a somewhat conserved principle of lifecycle-dependent regulation of DSF proteins, as seen with mitofusins in mitochondrial dynamics during cell division (Chen, Zhao & Li, 2023), and in stDynA and stDynB in sporulation (Schlimpert *et al.*, 2017). BDLP's genomic proximity to BDLP2 reflects the common occurrence of dynamin pairs or multi-dynamin operons in bacteria, suggesting potential functional interactions or redundancy (Bohuszewicz, Liu & Low, 2016). The observation of putative BDLP-associated liquid-liquid phase separation in hormogonia aligns with recent findings of LLPS in other DSF members, such as dynamin 1, suggesting a conserved mechanism for localised concentration of these proteins (Imoto *et al.*, 2022).

These conserved principles, revealed through the study of BDLP, provide valuable insights into the fundamental mechanisms of membrane constriction, disruption, and remodelling across the DSF, from bacteria to eukaryotes, and highlight the ancient origins and functional adaptations of these crucial membrane-remodelling machines throughout evolution.

## 6.5 Final Remarks

This study has significantly advanced our understanding of BDLP-mediated membrane remodelling and its role in cyanobacterial biology. However, several questions remain to be addressed in future research. The precise mechanistic details of lipid release from BDLP filaments and the formation of hexII nanoparticles warrant further investigation. The extent of hexII nanoparticle formation in wild-type hormogonia, as opposed to the BDLP-GFP

overexpression strain, remains to be determined, alongside the precise role of hexII nanoparticles in hormogonia. Additionally, the mechanism by which BDLP disassembles from membranes and potentially returns to its soluble state is yet to be elucidated. Future studies could benefit from protein-lipid simulations to provide additional insights into lipid channel interactions and the dynamics of lipid phase transitions. Such simulations could help bridge the gap between our structural understanding and the observed biochemical effects.

This work has further highlighted the diverse functions of bacterial DRPs compared to their eukaryotic counterparts. While eukaryotic DSF members often have well-defined roles in membrane fission or fusion, BDLP demonstrates a novel function in mediating stable lipid phase transitions. This diversity in bacterial DRP functions, now including lipid phase modulation, underscores the adaptability of these ancient proteins and their roles in various and potentially unresolved cellular processes.

In conclusion, this study not only provides critical insights into BDLP's mechanism and function but also opens new avenues for understanding membrane dynamics and remodelling in bacteria and cellular life in general. The potential applications of BDLP-mediated hexII nanoparticle formation in drug delivery systems present an exciting prospect for translating these fundamental biological insights into practical applications. As we continue to unravel the complexities of membrane remodelling across all domains of life, the study of bacterial DRPs like BDLP will undoubtedly play a crucial role in deepening our understanding of these essential cellular processes.

# References


Acehan, D., Malhotra, A., Xu, Y., Ren, M., et al. (2011a) Cardiolipin Affects the Supramolecular Organization of ATP Synthase in Mitochondria. *Biophysical Journal*. [Online] 100 (9), 2184–2192. Available from: doi:https://doi.org/10.1016/j.bpj.2011.03.031.

Acehan, D., Vaz, F., Houtkooper, R.H., James, J., et al. (2011b) Cardiac and Skeletal Muscle Defects in a Mouse Model of Human Barth Syndrome*. *Journal of Biological Chemistry*. [Online] 286 (2), 899–908. Available from: doi:https://doi.org/10.1074/jbc.M110.171439.

Aebi, U. & Pollard, T.D. (1987) A glow discharge unit to render electron microscope grids and other surfaces hydrophilic. *Journal of electron microscopy technique*. [Online] 7 (1), 29–33. Available from: doi:10.1002/jemt.1060070104.

Afzal, N., Lederer, W.J., Jafri, M.S. & Mannella, C.A. (2021) Effect of crista morphology on mitochondrial ATP output: A computational study. *Current Research in Physiology*. [Online] 4, 163–176. Available from: doi:https://doi.org/10.1016/j.crphys.2021.03.005.

Agulleiro, J.I. & Fernandez, J.J. (2011) Fast tomographic reconstruction on multicore computers. *Bioinformatics*. [Online] 27 (4), 582–583. Available from: doi:10.1093/bioinformatics/btq692.

Albers, S.-V. & Meyer, B.H. (2011) The archaeal cell envelope. *Nature Reviews Microbiology*. [Online] 9 (6), 414–426. Available from: doi:10.1038/nrmicro2576.

Alexander, C., Votruba, M., Pesch, U.E., Thiselton, D.L., et al. (2000) OPA1, encoding a dynamin-related GTPase, is mutated in autosomal dominant optic atrophy linked to chromosome 3q28. *Nature genetics*. [Online] 26 (2), 211–215. Available from: doi:10.1038/79944.

Almsherqi, Z.A., Margadant, F. & Deng, Y. (2010) The Cubic 'Faces' of Biomembranes. *Advances in planar lipid bilayers and liposomes*. [Online] 12, 79–99. Available from: doi:10.1016/B978-0-12-381266-7.00004-3.

Almsherqi, Z.A., McLachlan, C.S., Mossop, P., Knoops, K., et al. (2005) Direct template matching reveals a host subcellular membrane gyroid cubic structure that is associated with SARS virus. *Redox Report*. [Online] 10 (3), 167–171. Available from: doi:10.1179/135100005X57373.

Alonso Y Adell, M., Migliano, S.M. & Teis, D. (2016) ESCRT-III and Vps4: a dynamic multipurpose tool for membrane budding and scission. *The FEBS Journal*. [Online] 283 (18), 3288–3302. Available from: doi:https://doi.org/10.1111/febs.13688.

Altamura, E., Milano, F., Tangorra, R.R., Trotta, M., et al. (2017) Highly Oriented Photosynthetic Reaction Centers Generate a Proton Gradient in Synthetic Protocells. *Proceedings of the National Academy of Sciences*. [Online] 114 (15), 3837–3842. Available from: doi:10.1073/pnas.1617593114.

Alvarez, F.J.D., He, S., Perilla, J.R., Jang, S., et al. (2017) CryoEM structure of MxB reveals a novel oligomerization interface critical for HIV restriction. *Science advances*. [Online] 3 (9), e1701264. Available from: doi:10.1126/sciadv.1701264.

Amann, S.J., Keihsler, D., Bodrug, T., Brown, N.G., et al. (2023) Frozen in time: analyzing molecular dynamics with time-resolved cryo-EM. *Structure (London, England : 1993)*. [Online] 31 (1), 4–19. Available from: doi:10.1016/j.str.2022.11.014.

Anand, R., Eschenburg, S. & Reubold, T.F. (2016) Crystal structure of the GTPase domain and the bundle signalling element of dynamin in the GDP state. *Biochemical and biophysical research communications*. [Online] 469 (1), 76–80. Available from:

doi:10.1016/j.bbrc.2015.11.074.
Anand, R., Kondadi, A.K., Meisterknecht, J., Golombek, M., et al. (2020) MIC26 and MIC27 cooperate to regulate cardiolipin levels and the landscape of OXPHOS complexes. *Life science alliance*. [Online] 3 (10). Available from: doi:10.26508/lsa.202000711.
Anand, R., Wai, T., Baker, M.J., Kladt, N., et al. (2014) The i-AAA protease YME1L and OMA1 cleave OPA1 to balance mitochondrial fusion and fission. *The Journal of cell biology*. [Online] 204 (6), 919–929. Available from: doi:10.1083/jcb.201308006.
Antonny, B., Burd, C., De Camilli, P., Chen, E., et al. (2016) Membrane fission by dynamin: what we know and what we need to know. *The EMBO Journal*. [Online] 35 (21), 2270–2284. Available from: doi:https://doi.org/10.15252/embj.201694613.
Armbruster, M., Messa, M., Ferguson, S.M., De Camilli, P., et al. (2013) Dynamin phosphorylation controls optimization of endocytosis for brief action potential bursts Graeme Davis (ed.). *eLife*. [Online] 2, e00845. Available from: doi:10.7554/eLife.00845.
Armstrong, R.E., Hayes, P.K. & Walsby, A.E. (1983) Gas Vacuole Formation in Hormogonia of Nostoc muscorum. *Microbiology*. [Online] 129 (2), 263–270. Available from: doi:https://doi.org/10.1099/00221287-129-2-263.
Atilla-Gokcumen, G.E., Muro, E., Relat-Goberna, J., Sasse, S., et al. (2014) Dividing cells regulate their lipid composition and localization. *Cell*. [Online] 156 (3), 428–439. Available from: doi:10.1016/j.cell.2013.12.015.
Babl, L., Merino-Salomón, A., Kanwa, N. & Schwille, P. (2022) Membrane mediated phase separation of the bacterial nucleoid occlusion protein Noc. *Scientific Reports*. [Online] 12 (1), 17949. Available from: doi:10.1038/s41598-022-22680-5.
Bai, L., You, Q., Jain, B.K., Duan, H.D., et al. (2020) Transport mechanism of P4 ATPase phosphatidylcholine flippases Christopher G Burd, Vivek Malhotra, & Christopher G Burd (eds.). *eLife*. [Online] 9, e62163. Available from: doi:10.7554/eLife.62163.
Bai, S., Chen, T. & Deng, X. (2018) Guanylate-Binding Protein 1 Promotes Migration and Invasion of Human Periodontal Ligament Stem Cells. *Stem cells international*. [Online] 2018, 6082956. Available from: doi:10.1155/2018/6082956.
Bailey, S., Walters, R.G., Jansson, S. & Horton, P. (2001) Acclimation of Arabidopsis thaliana to the light environment: the existence of separate low light and high light responses. *Planta*. [Online] 213 (5), 794–801. Available from: doi:10.1007/s004250100556.
Banani, S.F., Lee, H.O., Hyman, A.A. & Rosen, M.K. (2017) Biomolecular condensates: organizers of cellular biochemistry. *Nature reviews. Molecular cell biology*. [Online] 18 (5), 285–298. Available from: doi:10.1038/nrm.2017.7.
Barrio-Hernandez, I., Yeo, J., Jänes, J., Mirdita, M., et al. (2023) Clustering predicted structures at the scale of the known protein universe. *Nature*. [Online] 622 (7983), 637–645. Available from: doi:10.1038/s41586-023-06510-w.
Basanta, B., Hirschi, M.M., Grotjahn, D.A. & Lander, G.C. (2022) A case for glycerol as an acceptable additive for single-particle cryoEM samples. *Acta crystallographica. Section D, Structural biology*. [Online] 78 (Pt 1), 124–135. Available from: doi:10.1107/S2059798321012110.
Bashkirov, P. V, Akimov, S.A., Evseev, A.I., Schmid, S.L., et al. (2008) GTPase Cycle of Dynamin Is Coupled to Membrane Squeeze and Release, Leading to Spontaneous Fission. *Cell*. [Online] 135 (7), 1276–1286. Available from: doi:https://doi.org/10.1016/j.cell.2008.11.028.
Basu Ball, W., Neff, J.K. & Gohil, V.M. (2018) The role of nonbilayer phospholipids in mitochondrial structure and function. *FEBS letters*. [Online] 592 (8), 1273–1290.

Available from: doi:10.1002/1873-3468.12887.
Basu, K., Lajoie, D., Aumentado-Armstrong, T., Chen, J., et al. (2017) Molecular mechanism of DRP1 assembly studied in vitro by cryo-electron microscopy. *PloS one*. [Online] 12 (6), e0179397. Available from: doi:10.1371/journal.pone.0179397.
Bean, B.P. (2007) The action potential in mammalian central neurons. *Nature Reviews Neuroscience*. [Online] 8 (6), 451–465. Available from: doi:10.1038/nrn2148.
Becker, N.A., Peters, J.P., Maher, L.J. 3rd & Lionberger, T.A. (2013) Mechanism of promoter repression by Lac repressor-DNA loops. *Nucleic acids research*. [Online] 41 (1), 156–166. Available from: doi:10.1093/nar/gks1011.
Benador, I.Y., Veliova, M., Mahdaviani, K., Petcherski, A., et al. (2018) Mitochondria Bound to Lipid Droplets Have Unique Bioenergetics, Composition, and Dynamics that Support Lipid Droplet Expansion. *Cell metabolism*. [Online] 27 (4), 869-885.e6. Available from: doi:10.1016/j.cmet.2018.03.003.
Bepler, T., Kelley, K., Noble, A.J. & Berger, B. (2020) Topaz-Denoise: general deep denoising models for cryoEM and cryoET. *Nature Communications*. [Online] 11 (1), 5208. Available from: doi:10.1038/s41467-020-18952-1.
Bepler, T., Morin, A., Rapp, M., Brasch, J., et al. (2019) Positive-unlabeled convolutional neural networks for particle picking in cryo-electron micrographs. *Nature Methods*. [Online] 16 (11), 1153–1160. Available from: doi:10.1038/s41592-019-0575-8.
Berger, C., Premaraj, N., Ravelli, R.B.G., Knoops, K., et al. (2023) Cryo-electron tomography on focused ion beam lamellae transforms structural cell biology. *Nature Methods*. [Online] 20 (4), 499–511. Available from: doi:10.1038/s41592-023-01783-5.
Bevers, E.M. & Williamson, P.L. (2016) Getting to the Outer Leaflet: Physiology of Phosphatidylserine Exposure at the Plasma Membrane. *Physiological reviews*. [Online] 96 (2), 605–645. Available from: doi:10.1152/physrev.00020.2015.
Bhatti, J.S., Kaur, S., Mishra, J., Dibbanti, H., et al. (2023) Targeting dynamin-related protein-1 as a potential therapeutic approach for mitochondrial dysfunction in Alzheimer's disease. *Biochimica et Biophysica Acta (BBA) - Molecular Basis of Disease*. [Online] 1869 (7), 166798. Available from: doi:https://doi.org/10.1016/j.bbadis.2023.166798.
Bishop, R.E. (2014) Emerging roles for anionic non-bilayer phospholipids in fortifying the outer membrane permeability barrier. *Journal of bacteriology*. [Online] 196 (18), 3209–3213. Available from: doi:10.1128/JB.02043-14.
den Blaauwen, T., Hamoen, L.W. & Levin, P.A. (2017) The divisome at 25: the road ahead. *Current opinion in microbiology*. [Online] 36, 85–94. Available from: doi:10.1016/j.mib.2017.01.007.
Boeynaems, S., Alberti, S., Fawzi, N.L., Mittag, T., et al. (2018) Protein Phase Separation: A New Phase in Cell Biology. *Trends in cell biology*. [Online] 28 (6), 420–435. Available from: doi:10.1016/j.tcb.2018.02.004.
Bohuszewicz, O., Liu, J. & Low, H.H. (2016) Membrane remodelling in bacteria. *Journal of Structural Biology*. [Online] 196 (1), 3–14. Available from: doi:https://doi.org/10.1016/j.jsb.2016.05.010.
Bohuszewicz, O. & Low, H.H. (2018) Structure of a mitochondrial fission dynamin in the closed conformation. *Nature structural & molecular biology*. [Online] 25 (8), 722–731. Available from: doi:10.1038/s41594-018-0097-6.
Botelho, A.V., Huber, T., Sakmar, T.P. & Brown, M.F. (2006) Curvature and hydrophobic forces drive oligomerization and modulate activity of rhodopsin in membranes. *Biophysical journal*. [Online] 91 (12), 4464–4477. Available from: doi:10.1529/biophysj.106.082776.

Böttinger, L., Horvath, S.E., Kleinschroth, T., Hunte, C., et al. (2012) Phosphatidylethanolamine and Cardiolipin Differentially Affect the Stability of Mitochondrial Respiratory Chain Supercomplexes. *Journal of Molecular Biology*. [Online] 423 (5), 677–686. Available from: doi:https://doi.org/10.1016/j.jmb.2012.09.001.

Boye, T.L., Maeda, K., Pezeshkian, W., Sønder, S.L., et al. (2017) Annexin A4 and A6 induce membrane curvature and constriction during cell membrane repair. *Nature Communications*. [Online] 8 (1), 1623. Available from: doi:10.1038/s41467-017-01743-6.

Bradford, M.M. (1976) A rapid and sensitive method for the quantitation of microgram quantities of protein utilizing the principle of protein-dye binding. *Analytical Biochemistry*. [Online] 72 (1), 248–254. Available from: doi:https://doi.org/10.1016/0003-2697(76)90527-3.

Bramkamp, M. & Lopez, D. (2015) Exploring the existence of lipid rafts in bacteria. *Microbiology and molecular biology reviews : MMBR*. [Online] 79 (1), 81–100. Available from: doi:10.1128/MMBR.00036-14.

Brandner, A., De Vecchis, D., Baaden, M., Cohen, M.M., et al. (2019) Physics-based oligomeric models of the yeast mitofusin Fzo1 at the molecular scale in the context of membrane docking. *Mitochondrion*. [Online] 49, 234–244. Available from: doi:https://doi.org/10.1016/j.mito.2019.06.010.

Brandt, T., Cavellini, L., Kuhlbrandt, W. & Cohen, M.M. (2016) A mitofusin-dependent docking ring complex triggers mitochondrial fusion in vitro. *eLife*. [Online] 5. Available from: doi:10.7554/eLife.14618.

Bratek, L., Markiewicz, M., Baczynski, K., Jalocha-Bratek, J., et al. (2019) Inverse hexagonal phase of poly-unsaturated monogalactolipid: A computer model and analysis. *Journal of Molecular Liquids*. [Online] 290, 111189. Available from: doi:https://doi.org/10.1016/j.molliq.2019.111189.

Braverman, N.E. & Moser, A.B. (2012) Functions of plasmalogen lipids in health and disease. *Biochimica et Biophysica Acta (BBA) - Molecular Basis of Disease*. [Online] 1822 (9), 1442–1452. Available from: doi:https://doi.org/10.1016/j.bbadis.2012.05.008.

Brilot, A.F., Chen, J.Z., Cheng, A., Pan, J., et al. (2012) Beam-induced motion of vitrified specimen on holey carbon film. *Journal of Structural Biology*. [Online] 177 (3), 630–637. Available from: doi:https://doi.org/10.1016/j.jsb.2012.02.003.

van den Brink-van der Laan, E., Antoinette Killian, J. & de Kruijff, B. (2004) Nonbilayer lipids affect peripheral and integral membrane proteins via changes in the lateral pressure profile. *Biochimica et Biophysica Acta (BBA) - Biomembranes*. [Online] 1666 (1), 275–288. Available from: doi:https://doi.org/10.1016/j.bbamem.2004.06.010.

Brites, P., Waterham, H.R. & Wanders, R.J.A. (2004) Functions and biosynthesis of plasmalogens in health and disease. *Biochimica et biophysica acta*. [Online] 1636 (2–3), 219–231. Available from: doi:10.1016/j.bbalip.2003.12.010.

Brown, M.F. (2012) Curvature forces in membrane lipid-protein interactions. *Biochemistry*. [Online] 51 (49), 9782–9795. Available from: doi:10.1021/bi301332v.

Brown, S., Santa Maria, J.P.J. & Walker, S. (2013) Wall teichoic acids of gram-positive bacteria. *Annual review of microbiology*. [Online] 67, 313–336. Available from: doi:10.1146/annurev-micro-092412-155620.

Bryce, S., Stolzer, M., Crosby, D., Yang, R., et al. (2023) Human atlastin-3 is a constitutive ER membrane fusion catalyst. *The Journal of cell biology*. [Online] 222 (7). Available from: doi:10.1083/jcb.202211021.

Buchholz, T.-O., Krull, A., Shahidi, R., Pigino, G., et al. (2019) Chapter 13 - Content-aware image restoration for electron microscopy. In: Thomas Müller-Reichert & Gaia B T - Methods in Cell Biology Pigino (eds.). *Three-Dimensional Electron Microscopy*. [Online]. Academic Press. pp. 277–289. Available from: doi:https://doi.org/10.1016/bs.mcb.2019.05.001.

Bürmann, F., Ebert, N., van Baarle, S. & Bramkamp, M. (2011) A bacterial dynamin-like protein mediating nucleotide-independent membrane fusion. *Molecular microbiology*. [Online] 79 (5), 1294–1304. Available from: doi:10.1111/j.1365-2958.2011.07523.x.

Burt, A., Toader, B., Warshamanage, R., von Kügelgen, A., et al. (2024) An image processing pipeline for electron cryo-tomography in RELION-5. *bioRxiv*. [Online] 2024.04.26.591129. Available from: doi:10.1101/2024.04.26.591129.

Caffrey, M. (2015) A comprehensive review of the lipid cubic phase or in meso method for crystallizing membrane and soluble proteins and complexes. *Acta crystallographica. Section F, Structural biology communications*. [Online] 71 (Pt 1), 3–18. Available from: doi:10.1107/S2053230X14026843.

Caforio, A. & Driessen, A.J.M. (2017) Archaeal phospholipids: Structural properties and biosynthesis. *Biochimica et Biophysica Acta (BBA) - Molecular and Cell Biology of Lipids*. [Online] 1862 (11), 1325–1339. Available from: doi:https://doi.org/10.1016/j.bbalip.2016.12.006.

Cai, Y.P. & Wolk, C.P. (1990) Use of a conditionally lethal gene in Anabaena sp. strain PCC 7120 to select for double recombinants and to entrap insertion sequences. *Journal of bacteriology*. [Online] 172 (6), 3138–3145. Available from: doi:10.1128/jb.172.6.3138-3145.1990.

Cail, R.C., Shirazinejad, C.R. & Drubin, D.G. (2022) Induced nanoscale membrane curvature bypasses the essential endocytic function of clathrin. *The Journal of cell biology*. [Online] 221 (7). Available from: doi:10.1083/jcb.202109013.

Campbell, E.L. & Meeks, J.C. (1989) Characteristics of Hormogonia Formation by Symbiotic Nostoc spp. in Response to the Presence of Anthoceros punctatus or Its Extracellular Products. *Applied and environmental microbiology*. [Online] 55 (1), 125–131. Available from: doi:10.1128/aem.55.1.125-131.1989.

Campbell, E.L., Summers, M.L., Christman, H., Martin, M.E., et al. (2007) Global gene expression patterns of Nostoc punctiforme in steady-state dinitrogen-grown heterocyst-containing cultures and at single time points during the differentiation of akinetes and hormogonia. *Journal of bacteriology*. [Online] 189 (14), 5247–5256. Available from: doi:10.1128/JB.00360-07.

Campbell, M.G., Cheng, A., Brilot, A.F., Moeller, A., et al. (2012) Movies of ice-embedded particles enhance resolution in electron cryo-microscopy. *Structure (London, England : 1993)*. [Online] 20 (11), 1823–1828. Available from: doi:10.1016/j.str.2012.08.026.

Cao, H., Krueger, E.W., Chen, J., Drizyte-Miller, K., et al. (2020) The anti-viral dynamin family member MxB participates in mitochondrial integrity. *Nature Communications*. [Online] 11 (1), 1048. Available from: doi:10.1038/s41467-020-14727-w.

Cao, Y.-L., Meng, S., Chen, Y., Feng, J.-X., et al. (2017) MFN1 structures reveal nucleotide-triggered dimerization critical for mitochondrial fusion. *Nature*. [Online] 542 (7641), 372–376. Available from: doi:10.1038/nature21077.

Cardona, T. (2018) Early Archean origin of heterodimeric Photosystem I. *Heliyon*. [Online] 4 (3), e00548. Available from: doi:10.1016/j.heliyon.2018.e00548.

Cardona, T., Battchikova, N., Agervald, Å., Zhang, P., et al. (2007) Isolation and characterization of thylakoid membranes from the filamentous cyanobacterium Nostoc

punctiforme. *Physiologia Plantarum*. [Online] 131 (4), 622–634. Available from: doi:https://doi.org/10.1111/j.1399-3054.2007.00982.x.

Cardona, T., Sánchez-Baracaldo, P., Rutherford, A.W. & Larkum, A.W. (2019) Early Archean origin of Photosystem II. *Geobiology*. [Online] 17 (2), 127–150. Available from: doi:10.1111/gbi.12322.

Carlton, J.G. & Baum, B. (2023) Roles of ESCRT-III polymers in cell division across the tree of life. *Current Opinion in Cell Biology*. [Online] 85, 102274. Available from: doi:https://doi.org/10.1016/j.ceb.2023.102274.

Chappie, J.S., Acharya, S., Leonard, M., Schmid, S.L., et al. (2010) G domain dimerization controls dynamin's assembly-stimulated GTPase activity. *Nature*. [Online] 465 (7297), 435–440. Available from: doi:10.1038/nature09032.

Chappie, J.S., Mears, J.A., Fang, S., Leonard, M., et al. (2011) A pseudoatomic model of the dynamin polymer identifies a hydrolysis-dependent powerstroke. *Cell*. [Online] 147 (1), 209–222. Available from: doi:10.1016/j.cell.2011.09.003.

Chavda, V.P., Dyawanapelly, S., Dawre, S., Ferreira-Faria, I., et al. (2023) Lyotropic liquid crystalline phases: Drug delivery and biomedical applications. *International Journal of Pharmaceutics*. [Online] 647, 123546. Available from: doi:https://doi.org/10.1016/j.ijpharm.2023.123546.

Chen, H., Detmer, S.A., Ewald, A.J., Griffin, E.E., et al. (2003) Mitofusins Mfn1 and Mfn2 coordinately regulate mitochondrial fusion and are essential for embryonic development. *The Journal of cell biology*. [Online] 160 (2), 189–200. Available from: doi:10.1083/jcb.200211046.

Chen, J., Noble, A.J., Kang, J.Y. & Darst, S.A. (2019) Eliminating effects of particle adsorption to the air/water interface in single-particle cryo-electron microscopy: Bacterial RNA polymerase and CHAPSO. *Journal of structural biology: X*. [Online] 1. Available from: doi:10.1016/j.yjsbx.2019.100005.

Chen, W., Zhao, H. & Li, Y. (2023) Mitochondrial dynamics in health and disease: mechanisms and potential targets. *Signal Transduction and Targeted Therapy*. [Online] 8 (1), 333. Available from: doi:10.1038/s41392-023-01547-9.

Chen, Y., Ma, P. & Gui, S. (2014) Cubic and Hexagonal Liquid Crystals as Drug Delivery Systems. *BioMed Research International*. [Online] 2014 (1), 815981. Available from: doi:https://doi.org/10.1155/2014/815981.

Chen, Y., Zhang, L., Graf, L., Yu, B., et al. (2017) Conformational dynamics of dynamin-like MxA revealed by single-molecule FRET. *Nature Communications*. [Online] 8 (1), 15744. Available from: doi:10.1038/ncomms15744.

Chen, Z. & Rand, R.P. (1997) The influence of cholesterol on phospholipid membrane curvature and bending elasticity. *Biophysical journal*. [Online] 73 (1), 267–276. Available from: doi:10.1016/S0006-3495(97)78067-6.

Cheng, X., Chen, K., Dong, B., Yang, M., et al. (2021) Dynamin-dependent vesicle twist at the final stage of clathrin-mediated endocytosis. *Nature cell biology*. [Online] 23 (8), 859–869. Available from: doi:10.1038/s41556-021-00713-x.

Cheng, X. & Smith, J.C. (2019) Biological Membrane Organization and Cellular Signaling. *Chemical Reviews*. [Online] 119 (9), 5849–5880. Available from: doi:10.1021/acs.chemrev.8b00439.

Cheng, Y. (2018) Single-particle cryo-EM—How did it get here and where will it go. *Science*. [Online] 361 (6405), 876–880. Available from: doi:10.1126/science.aat4346.

Chernomordik, L. V & Kozlov, M.M. (2008) Mechanics of membrane fusion. *Nature structural*

*& molecular biology*. [Online] 15 (7), 675–683. Available from: doi:10.1038/nsmb.1455.
Cho, Y.W., Gonzales, A., Harwood, T. V, Huynh, J., et al. (2017) Dynamic localization of HmpF regulates type IV pilus activity and directional motility in the filamentous cyanobacterium Nostoc punctiforme. *Molecular microbiology*. [Online] 106 (2), 252–265. Available from: doi:10.1111/mmi.13761.
Choudhary, V., Golani, G., Joshi, A.S., Cottier, S., et al. (2018) Architecture of Lipid Droplets in Endoplasmic Reticulum Is Determined by Phospholipid Intrinsic Curvature. *Current biology : CB*. [Online] 28 (6), 915-926.e9. Available from: doi:10.1016/j.cub.2018.02.020.
Chua, E.Y.D., Mendez, J.H., Rapp, M., Ilca, S.L., et al. (2022) Better, Faster, Cheaper: Recent Advances in Cryo-Electron Microscopy. *Annual review of biochemistry*. [Online] 91, 1–32. Available from: doi:10.1146/annurev-biochem-032620-110705.
Ciarlo, L., Manganelli, V., Garofalo, T., Matarrese, P., et al. (2010) Association of fission proteins with mitochondrial raft-like domains. *Cell Death & Differentiation*. [Online] 17 (6), 1047–1058. Available from: doi:10.1038/cdd.2009.208.
Claret Fernández, L., Mesman, R. & van Niftrik, L. (2020) *The Anammoxosome Organelle: The Power Plant of Anaerobic Ammonium-Oxidizing (Anammox) Bacteria BT - Bacterial Organelles and Organelle-like Inclusions*. In: Dieter Jendrossek (ed.). [Online]. Cham, Springer International Publishing. pp. 107–123. Available from: doi:10.1007/978-3-030-60173-7_5.
Cogliati, S., Frezza, C., Soriano, M.E., Varanita, T., et al. (2013) Mitochondrial cristae shape determines respiratory chain supercomplexes assembly and respiratory efficiency. *Cell*. [Online] 155 (1), 160–171. Available from: doi:10.1016/j.cell.2013.08.032.
Cohen, M.M. & Tareste, D. (2018) Recent insights into the structure and function of Mitofusins in mitochondrial fusion. *F1000Research*. [Online] 7, F1000 Faculty Rev-1983. Available from: doi:10.12688/f1000research.16629.1.
Colosimo, R., Warren, F.J., Edwards, C.H., Ryden, P., et al. (2021) Comparison of the behavior of fungal and plant cell wall during gastrointestinal digestion and resulting health effects: A review. *Trends in Food Science & Technology*. [Online] 110, 132–141. Available from: doi:https://doi.org/10.1016/j.tifs.2021.02.001.
Connor, O.M., Matta, S.K. & Friedman, J.R. (2023) Completion of mitochondrial division requires the intermembrane space protein Mdi1/Atg44. *Journal of Cell Biology*. [Online] 222 (10), e202303147. Available from: doi:10.1083/jcb.202303147.
Croll, T.I. (2018) ISOLDE: a physically realistic environment for model building into low-resolution electron-density maps. *Acta crystallographica. Section D, Structural biology*. [Online] 74 (Pt 6), 519–530. Available from: doi:10.1107/S2059798318002425.
Crosby, D. & Lee, T.H. (2022) Membrane fusion by Drosophila atlastin does not require GTP hydrolysis. *Molecular Biology of the Cell*. [Online] 33 (14), br23. Available from: doi:10.1091/mbc.E22-05-0164.
Cullis, P.R. & De Kruijff, B. (1979) Lipid polymorphism and the functional roles of lipids in biological membranes. *Biochimica et Biophysica Acta (BBA) - Reviews on Biomembranes*. [Online] 559 (4), 399–420. Available from: doi:https://doi.org/10.1016/0304-4157(79)90012-1.
Czub, J. & Baginski, M. (2006) Comparative Molecular Dynamics Study of Lipid Membranes Containing Cholesterol and Ergosterol. *Biophysical Journal*. [Online] 90 (7), 2368–2382. Available from: doi:https://doi.org/10.1529/biophysj.105.072801.
Dai, M., Dong, Z., Xu, K. & Zhang, Q.C. (2023) CryoRes: Local Resolution Estimation of Cryo-EM Density Maps by Deep Learning. *Journal of Molecular Biology*. [Online] 435 (9),

168059. Available from: doi:https://doi.org/10.1016/j.jmb.2023.168059.
Dal Negro, L. & Boriskina, S. V (2012) Deterministic aperiodic nanostructures for photonics and plasmonics applications. *Laser & Photonics Reviews*. [Online] 6 (2), 178–218. Available from: doi:https://doi.org/10.1002/lpor.201000046.
Danev, R. & Baumeister, W. (2016) Cryo-EM single particle analysis with the Volta phase plate Sjors H W Scheres (ed.). *eLife*. [Online] 5, e13046. Available from: doi:10.7554/eLife.13046.
Danev, R., Buijsse, B., Khoshouei, M., Plitzko, J.M., et al. (2014) Volta potential phase plate for in-focus phase contrast transmission electron microscopy. *Proceedings of the National Academy of Sciences of the United States of America*. [Online] 111 (44), 15635–15640. Available from: doi:10.1073/pnas.1418377111.
Daste, F., Sauvanet, C., Bavdek, A., Baye, J., et al. (2018) The heptad repeat domain 1 of Mitofusin has membrane destabilization function in mitochondrial fusion. *EMBO reports*. [Online] 19 (6). Available from: doi:10.15252/embr.201643637.
Daumke, O., Lundmark, R., Vallis, Y., Martens, S., et al. (2007) Architectural and mechanistic insights into an EHD ATPase involved in membrane remodelling. *Nature*. [Online] 449 (7164), 923–927. Available from: doi:10.1038/nature06173.
Daumke, O. & Praefcke, G.J.K. (2016) Invited review: Mechanisms of GTP hydrolysis and conformational transitions in the dynamin superfamily. *Biopolymers*. [Online] 105 (8), 580–593. Available from: doi:https://doi.org/10.1002/bip.22855.
Daumke, O., Roux, A. & Haucke, V. (2014) BAR Domain Scaffolds in Dynamin-Mediated Membrane Fission. *Cell*. [Online] 156 (5), 882–892. Available from: doi:https://doi.org/10.1016/j.cell.2014.02.017.
Davies, K.M., Anselmi, C., Wittig, I., Faraldo-Gómez, J.D., et al. (2012) Structure of the yeast F1Fo-ATP synthase dimer and its role in shaping the mitochondrial cristae. *Proceedings of the National Academy of Sciences of the United States of America*. [Online] 109 (34), 13602–13607. Available from: doi:10.1073/pnas.1204593109.
Davis, D., Yuan, H., Liang, F.-X., Yang, Y.-M., et al. (2019) Human Antiviral Protein MxA Forms Novel Metastable Membraneless Cytoplasmic Condensates Exhibiting Rapid Reversible Tonicity-Driven Phase Transitions. *Journal of virology*. [Online] 93 (22). Available from: doi:10.1128/JVI.01014-19.
Davis, M.W. & Jorgensen, E.M. (2022) ApE, A Plasmid Editor: A Freely Available DNA Manipulation and Visualization Program. *Frontiers in bioinformatics*. [Online] 2, 818619. Available from: doi:10.3389/fbinf.2022.818619.
Demé, B., Cataye, C., Block, M.A., Maréchal, E., et al. (2014) Contribution of galactoglycerolipids to the 3-dimensional architecture of thylakoids. *FASEB journal : official publication of the Federation of American Societies for Experimental Biology*. [Online] 28 (8), 3373–3383. Available from: doi:10.1096/fj.13-247395.
Demurtas, D., Guichard, P., Martiel, I., Mezzenga, R., et al. (2015) Direct visualization of dispersed lipid bicontinuous cubic phases by cryo-electron tomography. *Nature Communications*. [Online] 6 (1), 8915. Available from: doi:10.1038/ncomms9915.
Deng, Y. & Almsherqi, Z.A. (2015) Evolution of cubic membranes as antioxidant defence system. *Interface focus*. [Online] 5 (4), 20150012. Available from: doi:10.1098/rsfs.2015.0012.
Deng, Y., Almsherqi, Z.A., Ng, M.M.L. & Kohlwein, S.D. (2010) Do viruses subvert cholesterol homeostasis to induce host cubic membranes? *Trends in cell biology*. [Online] 20 (7), 371–379. Available from: doi:10.1016/j.tcb.2010.04.001.

Deng, Y., Almsherqi, Z.A., Shui, G., Wenk, M.R., et al. (2009) Docosapentaenoic acid (DPA) is a critical determinant of cubic membrane formation in amoeba Chaos mitochondria. *The FASEB Journal*. [Online] 23 (9), 2866–2871. Available from: doi:https://doi.org/10.1096/fj.09-130435.

Deng, Y., Kohlwein, S.D. & Mannella, C.A. (2002) Fasting induces cyanide-resistant respiration and oxidative stress in the amoeba Chaos carolinensis: implications for the cubic structural transition in mitochondrial membranes. *Protoplasma*. [Online] 219 (3–4), 160–167. Available from: doi:10.1007/s007090200017.

Denisov, I.G. & Sligar, S.G. (2016) Nanodiscs for structural and functional studies of membrane proteins. *Nature Structural & Molecular Biology*. [Online] 23 (6), 481–486. Available from: doi:10.1038/nsmb.3195.

Deolal, P., Scholz, J., Ren, K., Bragulat-Teixidor, H., et al. (2024) Sculpting nuclear envelope identity from the endoplasmic reticulum during the cell cycle. *Nucleus (Austin, Tex.)*. [Online] 15 (1), 2299632. Available from: doi:10.1080/19491034.2023.2299632.

Derewenda, U., Oleksy, A., Stevenson, A.S., Korczynska, J., et al. (2004) The crystal structure of RhoA in complex with the DH/PH fragment of PDZRhoGEF, an activator of the Ca(2+) sensitization pathway in smooth muscle. *Structure (London, England : 1993)*. [Online] 12 (11), 1955–1965. Available from: doi:10.1016/j.str.2004.09.003.

Diaz, R., Rice, W.J. & Stokes, D.L. (2010) Fourier-Bessel reconstruction of helical assemblies. *Methods in enzymology*. [Online] 482, 131–165. Available from: doi:10.1016/S0076-6879(10)82005-1.

Dickerson, J.L., Lu, P.-H., Hristov, D., Dunin-Borkowski, R.E., et al. (2022) Imaging biological macromolecules in thick specimens: The role of inelastic scattering in cryoEM. *Ultramicroscopy*. [Online] 237, 113510. Available from: doi:https://doi.org/10.1016/j.ultramic.2022.113510.

Dlouhý, O., Javornik, U., Zsiros, O., Šket, P., et al. (2021a) Lipid Polymorphism of the Subchloroplast—Granum and Stroma Thylakoid Membrane—Particles. I. 31P-NMR Spectroscopy. *Cells*. 10 (22354).

Dlouhý, O., Karlický, V., Arshad, R., Zsiros, O., et al. (2021b) Lipid Polymorphism of the Subchloroplast-Granum and Stroma Thylakoid Membrane-Particles. II. Structure and Functions. *Cells*. [Online] 10 (9). Available from: doi:10.3390/cells10092363.

Dlouhý, O., Kurasová, I., Karlický, V., Javornik, U., et al. (2020) Modulation of non-bilayer lipid phases and the structure and functions of thylakoid membranes: effects on the water-soluble enzyme violaxanthin de-epoxidase. *Scientific Reports*. [Online] 10 (1), 11959. Available from: doi:10.1038/s41598-020-68854-x.

Dodge, J.T. & Phillips, G.B. (1967) Composition of phospholipids and of phospholipid fatty acids and aldehydes in human red cells. *Journal of Lipid Research*. [Online] 8 (6), 667–675. Available from: doi:https://doi.org/10.1016/S0022-2275(20)38890-8.

Domínguez-Escobar, J., Wolf, D., Fritz, G., Höfler, C., et al. (2014) Subcellular localization, interactions and dynamics of the phage-shock protein-like Lia response in Bacillus subtilis. *Molecular Microbiology*. [Online] 92 (4), 716–732. Available from: doi:https://doi.org/10.1111/mmi.12586.

Dotson, R.J., Smith, C.R., Bueche, K., Angles, G., et al. (2017) Influence of Cholesterol on the Oxygen Permeability of Membranes: Insight from Atomistic Simulations. *Biophysical journal*. [Online] 112 (11), 2336–2347. Available from: doi:10.1016/j.bpj.2017.04.046.

Del Dotto, V., Fogazza, M., Carelli, V., Rugolo, M., et al. (2018) Eight human OPA1 isoforms, long and short: What are they for? *Biochimica et biophysica acta. Bioenergetics*. [Online]

1859 (4), 263–269. Available from: doi:10.1016/j.bbabio.2018.01.005.
Drulyte, I., Johnson, R.M., Hesketh, E.L., Hurdiss, D.L., et al. (2018) Approaches to altering particle distributions in cryo-electron microscopy sample preparation. *Acta crystallographica. Section D, Structural biology*. [Online] 74 (Pt 6), 560–571. Available from: doi:10.1107/S2059798318006496.
Du, S. & Lutkenhaus, J. (2019) At the Heart of Bacterial Cytokinesis: The Z Ring. *Trends in microbiology*. [Online] 27 (9), 781–791. Available from: doi:10.1016/j.tim.2019.04.011.
Dubochet, J., Adrian, M., Chang, J.J., Homo, J.C., et al. (1988) Cryo-electron microscopy of vitrified specimens. *Q Rev Biophys*. [Online] 21 (2), 129–228. Available from: doi:10.1017/s0033583500004297.
Dubochet, J., Lepault, J., Freeman, R., Berriman, J.A., et al. (1982) Electron microscopy of frozen water and aqueous solutions. *Journal of Microscopy*. [Online] 128 (3), 219–237. Available from: doi:https://doi.org/10.1111/j.1365-2818.1982.tb04625.x.
Dudek, J., Cheng, I.-F., Balleininger, M., Vaz, F.M., et al. (2013) Cardiolipin deficiency affects respiratory chain function and organization in an induced pluripotent stem cell model of Barth syndrome. *Stem cell research*. [Online] 11 (2), 806–819. Available from: doi:10.1016/j.scr.2013.05.005.
Duong-Ly, K.C. & Gabelli, S.B. (2015) Affinity Purification of a Recombinant Protein Expressed as a Fusion with the Maltose-Binding Protein (MBP) Tag. *Methods in enzymology*. [Online] 559, 17–26. Available from: doi:10.1016/bs.mie.2014.11.004.
Dupuy, P., Gutierrez, C. & Neyrolles, O. (2023) Modulation of bacterial membrane proteins activity by clustering into plasma membrane nanodomains. *Molecular Microbiology*. [Online] 120 (4), 502–507. Available from: doi:https://doi.org/10.1111/mmi.15105.
Ebner, M., Puchkov, D., López-Ortega, O., Muthukottiappan, P., et al. (2023) Nutrient-regulated control of lysosome function by signaling lipid conversion. *Cell*. [Online] 186 (24), 5328-5346.e26. Available from: doi:https://doi.org/10.1016/j.cell.2023.09.027.
Edgar, R.C. (2004) MUSCLE: multiple sequence alignment with high accuracy and high throughput. *Nucleic acids research*. [Online] 32 (5), 1792–1797. Available from: doi:10.1093/nar/gkh340.
van Eerden, F.J., de Jong, D.H., de Vries, A.H., Wassenaar, T.A., et al. (2015) Characterization of thylakoid lipid membranes from cyanobacteria and higher plants by molecular dynamics simulations. *Biochimica et Biophysica Acta (BBA) - Biomembranes*. [Online] 1848 (6), 1319–1330. Available from: doi:https://doi.org/10.1016/j.bbamem.2015.02.025.
Egelman, E.H. (2000) A robust algorithm for the reconstruction of helical filaments using single-particle methods. *Ultramicroscopy*. [Online] 85 (4), 225–234. Available from: doi:https://doi.org/10.1016/S0304-3991(00)00062-0.
Emoto, K., Inadome, H., Kanaho, Y., Narumiya, S., et al. (2005) Local Change in Phospholipid Composition at the Cleavage Furrow Is Essential for Completion of Cytokinesis*. *Journal of Biological Chemistry*. [Online] 280 (45), 37901–37907. Available from: doi:https://doi.org/10.1074/jbc.M504282200.
Faelber, K., Dietrich, L., Noel, J.K., Wollweber, F., et al. (2019) Structure and assembly of the mitochondrial membrane remodelling GTPase Mgm1. *Nature*. [Online] 571 (7765), 429–433. Available from: doi:10.1038/s41586-019-1372-3.
Faelber, K., Posor, Y., Gao, S., Held, M., et al. (2011) Crystal structure of nucleotide-free dynamin. *Nature*. [Online] 477 (7366), 556–560. Available from: doi:10.1038/nature10369.

Fan, F., Wu, Y., Hara, M., Rizk, A., et al. (2021a) Dynamin deficiency causes insulin secretion failure and hyperglycemia. *Proceedings of the National Academy of Sciences of the United States of America*. [Online] 118 (32). Available from: doi:10.1073/pnas.2021764118.

Fan, H., Wang, B., Zhang, Y., Zhu, Y., et al. (2021b) A cryo-electron microscopy support film formed by 2D crystals of hydrophobin HFBI. *Nature Communications*. [Online] 12 (1), 7257. Available from: doi:10.1038/s41467-021-27596-8.

Fan, Z.-A., Tsang, K.-Y., Chen, S.-H. & Chen, Y.-F. (2016) Revisit the Correlation between the Elastic Mechanics and Fusion of Lipid Membranes. *Scientific Reports*. [Online] 6 (1), 31470. Available from: doi:10.1038/srep31470.

Faruqi, A.R. & Henderson, R. (2007) Electronic detectors for electron microscopy. *Current Opinion in Structural Biology*. [Online] 17 (5), 549–555. Available from: doi:https://doi.org/10.1016/j.sbi.2007.08.014.

Feng, X., Fu, Z., Kaledhonkar, S., Jia, Y., et al. (2017) A Fast and Effective Microfluidic Spraying-Plunging Method for High-Resolution Single-Particle Cryo-EM. *Structure (London, England : 1993)*. [Online] 25 (4), 663-670.e3. Available from: doi:10.1016/j.str.2017.02.005.

Fenton, A.R., Jongens, T.A. & Holzbaur, E.L.F. (2021) Mitochondrial dynamics: Shaping and remodeling an organelle network. *Current Opinion in Cell Biology*. [Online] 68, 28–36. Available from: doi:https://doi.org/10.1016/j.ceb.2020.08.014.

Fernandez-Gimenez, E., Carazo, J.M. & Sorzano, C.O.S. (2023) Local defocus estimation in single particle analysis in cryo-electron microscopy. *Journal of Structural Biology*. [Online] 215 (4), 108030. Available from: doi:https://doi.org/10.1016/j.jsb.2023.108030.

Findinier, J., Delevoye, C. & Cohen, M.M. (2019) The dynamin-like protein Fzl promotes thylakoid fusion and resistance to light stress in Chlamydomonas reinhardtii. *PLOS Genetics*. 15 (3), e1008047.

Fischetti, V.A. (2019) Surface Proteins on Gram-Positive Bacteria. *Microbiology spectrum*. [Online] 7 (4). Available from: doi:10.1128/microbiolspec.GPP3-0012-2018.

Fong, W.-K., Hanley, T. & Boyd, B.J. (2009) Stimuli responsive liquid crystals provide 'on-demand' drug delivery in vitro and in vivo. *Journal of controlled release : official journal of the Controlled Release Society*. [Online] 135 (3), 218–226. Available from: doi:10.1016/j.jconrel.2009.01.009.

Fonseca, T.B., Sánchez-Guerrero, Á., Milosevic, I. & Raimundo, N. (2019) Mitochondrial fission requires DRP1 but not dynamins. *Nature*. [Online] 570 (7761), E34–E42. Available from: doi:10.1038/s41586-019-1296-y.

Ford, M.G.J. & Chappie, J.S. (2019) The structural biology of the dynamin-related proteins: New insights into a diverse, multitalented family. *Traffic*. [Online] 20 (10), 717–740. Available from: doi:https://doi.org/10.1111/tra.12676.

Francy, C.A., Clinton, R.W., Fröhlich, C., Murphy, C., et al. (2017) Cryo-EM Studies of Drp1 Reveal Cardiolipin Interactions that Activate the Helical Oligomer. *Scientific reports*. [Online] 7 (1), 10744. Available from: doi:10.1038/s41598-017-11008-3.

Frank, J. (2006a) 15Electron Microscopy of Macromolecular Assemblies Joachim Frank (ed.). *Three-Dimensional Electron Microscopy of Macromolecular Assemblies: Visualization of Biological Molecules in Their Native State*. [Online]. p.0. Available from: doi:10.1093/acprof:oso/9780195182187.003.0002.

Frank, J. (2006b) 193Three-Dimensional Reconstruction Joachim Frank (ed.). *Three-Dimensional Electron Microscopy of Macromolecular Assemblies: Visualization of*

*Biological Molecules in Their Native State*. [Online]. p.0. Available from: doi:10.1093/acprof:oso/9780195182187.003.0005.

Frank, J. (2006c) 1Introduction Joachim Frank (ed.). *Three-Dimensional Electron Microscopy of Macromolecular Assemblies: Visualization of Biological Molecules in Their Native State*. [Online]. p.0. Available from: doi:10.1093/acprof:oso/9780195182187.003.0001.

Frank, J. (2006d) 71Two-Dimensional Averaging Techniques Joachim Frank (ed.). *Three-Dimensional Electron Microscopy of Macromolecular Assemblies: Visualization of Biological Molecules in Their Native State*. [Online]. p.0. Available from: doi:10.1093/acprof:oso/9780195182187.003.0003.

Frank, S., Gaume, B., Bergmann-Leitner, E.S., Leitner, W.W., et al. (2001) The role of dynamin-related protein 1, a mediator of mitochondrial fission, in apoptosis. *Developmental cell*. [Online] 1 (4), 515–525. Available from: doi:10.1016/s1534-5807(01)00055-7.

Franklin, R.E. & Gosling, R.G. (1953) Evidence for 2-Chain Helix in Crystalline Structure of Sodium Deoxyribonucleate. *Nature*. [Online] 172 (4369), 156–157. Available from: doi:10.1038/172156a0.

Freundlich, M.M. (1963) Origin of the Electron Microscope. *Science*. [Online] 142 (3589), 185–188. Available from: doi:10.1126/science.142.3589.185.

Frewein, M., Kollmitzer, B., Heftberger, P. & Pabst, G. (2016) Lateral pressure-mediated protein partitioning into liquid-ordered/liquid-disordered domains. *Soft matter*. [Online] 12 (13), 3189–3195. Available from: doi:10.1039/c6sm00042h.

Frey, T.G., Renken, C.W. & Perkins, G.A. (2002) Insight into mitochondrial structure and function from electron tomography. *Biochimica et Biophysica Acta (BBA) - Bioenergetics*. [Online] 1555 (1), 196–203. Available from: doi:https://doi.org/10.1016/S0005-2728(02)00278-5.

Fribourgh, J.L., Nguyen, H.C., Matreyek, K.A., Alvarez, F.J.D., et al. (2014) Structural insight into HIV-1 restriction by MxB. *Cell host & microbe*. [Online] 16 (5), 627–638. Available from: doi:10.1016/j.chom.2014.09.021.

Friedman, J.R., Mourier, A., Yamada, J., McCaffery, J.M., et al. (2015) MICOS coordinates with respiratory complexes and lipids to establish mitochondrial inner membrane architecture. *eLife*. [Online] 4. Available from: doi:10.7554/eLife.07739.

Frohlich, C., Grabiger, S., Schwefel, D., Faelber, K., et al. (2013) Structural insights into oligomerization and mitochondrial remodelling of dynamin 1-like protein. *The EMBO journal*. [Online] 32 (9), 1280–1292. Available from: doi:10.1038/emboj.2013.74.

Fry, M.Y., Navarro, P.P., Hakim, P., Ananda, V.Y., et al. (2024) In situ architecture of Opa1-dependent mitochondrial cristae remodeling. *The EMBO Journal*. [Online] 43 (3), 391–413. Available from: doi:https://doi.org/10.1038/s44318-024-00027-2.

Fu, C., Donovan, W.P., Shikapwashya-Hasser, O., Ye, X., et al. (2014) Hot Fusion: an efficient method to clone multiple DNA fragments as well as inverted repeats without ligase. *PloS one*. [Online] 9 (12), e115318. Available from: doi:10.1371/journal.pone.0115318.

Fujiwara, I., Vavylonis, D. & Pollard, T.D. (2007) Polymerization kinetics of ADP- and ADP-Pi-actin determined by fluorescence microscopy. *Proceedings of the National Academy of Sciences*. [Online] 104 (21), 8827–8832. Available from: doi:10.1073/pnas.0702510104.

Fukuda, T., Furukawa, K., Maruyama, T., Yamashita, S., et al. (2023) The mitochondrial intermembrane space protein mitofissin drives mitochondrial fission required for mitophagy. *Molecular Cell*. [Online] 83 (12), 2045-2058.e9. Available from: doi:https://doi.org/10.1016/j.molcel.2023.04.022.

Fuller, N. & Rand, R.P. (2001) The influence of lysolipids on the spontaneous curvature and

bending elasticity of phospholipid membranes. *Biophysical journal*. [Online] 81 (1), 243–254. Available from: doi:10.1016/S0006-3495(01)75695-0.

Gallagher-Jones, M., Glynn, C., Boyer, D.R., Martynowycz, M.W., et al. (2018) Sub-ångström cryo-EM structure of a prion protofibril reveals a polar clasp. *Nature structural & molecular biology*. [Online] 25 (2), 131–134. Available from: doi:10.1038/s41594-017-0018-0.

Galli, V., Sebastian, R., Moutel, S., Ecard, J., et al. (2017) Uncoupling of dynamin polymerization and GTPase activity revealed by the conformation-specific nanobody dynab Christien Merrifield (ed.). *eLife*. [Online] 6, e25197. Available from: doi:10.7554/eLife.25197.

Gambelli, L., Isupov, M.N. & Daum, B. (2022) Escaping the symmetry trap in helical reconstruction. *Faraday discussions*. [Online] Available from: doi:10.1039/d2fd00051b.

Gambelli, L., McLaren, M., Conners, R., Sanders, K., et al. (2024) Structure of the two-component S-layer of the archaeon Sulfolobus acidocaldarius Han Remaut, Volker Dötsch, & Han Remaut (eds.). *eLife*. [Online] 13, e84617. Available from: doi:10.7554/eLife.84617.

Ganichkin, O.M., Vancraenenbroeck, R., Rosenblum, G., Hofmann, H., et al. (2021) Quantification and demonstration of the collective constriction-by-ratchet mechanism in the dynamin molecular motor. *Proceedings of the National Academy of Sciences*. [Online] 118 (28), e2101144118. Available from: doi:10.1073/pnas.2101144118.

Gao, H., Sage, T.L. & Osteryoung, K.W. (2006) FZL, an FZO-like protein in plants, is a determinant of thylakoid and chloroplast morphology. *Proceedings of the National Academy of Sciences of the United States of America*. [Online] 103 (17), 6759–6764. Available from: doi:10.1073/pnas.0507287103.

Gao, S. & Hu, J. (2021) Mitochondrial Fusion: The Machineries In and Out. *Trends in Cell Biology*. [Online] 31 (1), 62–74. Available from: doi:https://doi.org/10.1016/j.tcb.2020.09.008.

Gao, S., von der Malsburg, A., Paeschke, S., Behlke, J., et al. (2010) Structural basis of oligomerization in the stalk region of dynamin-like MxA. *Nature*. [Online] 465 (7297), 502–506. Available from: doi:10.1038/nature08972.

Gao, S., von der Malsburg, A., Dick, A., Faelber, K., et al. (2011) Structure of Myxovirus Resistance Protein A Reveals Intra- and Intermolecular Domain Interactions Required for the Antiviral Function. *Immunity*. [Online] 35 (4), 514–525. Available from: doi:https://doi.org/10.1016/j.immuni.2011.07.012.

Garab, G., Lohner, K., Laggner, P. & Farkas, T. (2000) Self-regulation of the lipid content of membranes by non-bilayer lipids: a hypothesis. *Trends in Plant Science*. [Online] 5 (11), 489–494. Available from: doi:https://doi.org/10.1016/S1360-1385(00)01767-2.

Garab, G., Yaguzhinsky, L.S., Dlouhý, O., Nesterov, S. V, et al. (2022) Structural and functional roles of non-bilayer lipid phases of chloroplast thylakoid membranes and mitochondrial inner membranes. *Progress in Lipid Research*. [Online] 86, 101163. Available from: doi:https://doi.org/10.1016/j.plipres.2022.101163.

García-Fernández, E., Koch, G., Wagner, R.M., Fekete, A., et al. (2017) Membrane Microdomain Disassembly Inhibits MRSA Antibiotic Resistance. *Cell*. [Online] 171 (6), 1354-1367.e20. Available from: doi:https://doi.org/10.1016/j.cell.2017.10.012.

Gatti, P., Schiavon, C., Cicero, J., Manor, U., et al. (2024) Mitochondria- and ER-associated actin are required for mitochondrial fusion. *bioRxiv : the preprint server for biology*. [Online] Available from: doi:10.1101/2023.06.13.544768.

Ge, Y., Shi, X., Boopathy, S., McDonald, J., et al. (2020) Two forms of Opa1 cooperate to complete fusion of the mitochondrial inner-membrane. *eLife*. [Online] 9. Available from: doi:10.7554/eLife.50973.

Gemmer, M., Chaillet, M.L., van Loenhout, J., Cuevas Arenas, R., et al. (2023) Visualization of translation and protein biogenesis at the ER membrane. *Nature*. [Online] 614 (7946), 160–167. Available from: doi:10.1038/s41586-022-05638-5.

Gewehr, L., Junglas, B., Jilly, R., Franz, J., et al. (2023) SynDLP is a dynamin-like protein of Synechocystis sp. PCC 6803 with eukaryotic features. *Nature Communications*. [Online] 14 (1), 2156. Available from: doi:10.1038/s41467-023-37746-9.

Ghosh, A. & Spakowitz, A.J. (2024) Local changes in protein filament properties drive large-scale membrane transformations involved in endosome tethering and fusion. *Soft Matter*. [Online] Available from: doi:10.1039/D4SM00299G.

Giacomello, M., Pyakurel, A., Glytsou, C. & Scorrano, L. (2020) The cell biology of mitochondrial membrane dynamics. *Nature Reviews Molecular Cell Biology*. [Online] 21 (4), 204–224. Available from: doi:10.1038/s41580-020-0210-7.

Gibson, D.G., Young, L., Chuang, R.-Y., Venter, J.C., et al. (2009) Enzymatic assembly of DNA molecules up to several hundred kilobases. *Nature Methods*. [Online] 6 (5), 343–345. Available from: doi:10.1038/nmeth.1318.

Glaeser, R.M. (2016) How good can cryo-EM become? *Nature Methods*. [Online] 13 (1), 28–32. Available from: doi:10.1038/nmeth.3695.

Glaeser, R.M. (2018) Proteins, interfaces, and cryo-EM grids. *Current Opinion in Colloid & Interface Science*. [Online] 34, 1–8. Available from: doi:https://doi.org/10.1016/j.cocis.2017.12.009.

Glaeser, R.M. (2008) Retrospective: Radiation damage and its associated “Information Limitations”. *Journal of Structural Biology*. [Online] 163 (3), 271–276. Available from: doi:https://doi.org/10.1016/j.jsb.2008.06.001.

Glaeser, R.M., Downing, K., DeRosier, D., Chiu, W., et al. (2007) Electron Crystallography of Helical Structures Robert M Glaeser, Kenneth Downing, David DeRosier, Wah Chiu, et al. (eds.). *Electron Crystallography Of Biological Macromolecules*. [Online]. p.0. Available from: doi:10.1093/oso/9780195088717.003.0012.

Gomes, L.C., Di Benedetto, G. & Scorrano, L. (2011) During autophagy mitochondria elongate, are spared from degradation and sustain cell viability. *Nature cell biology*. [Online] 13 (5), 589–598. Available from: doi:10.1038/ncb2220.

Gonzalez, A., Riley, K.W., Harwood, T. V, Zuniga, E.G., et al. (2019) A Tripartite, Hierarchical Sigma Factor Cascade Promotes Hormogonium Development in the Filamentous Cyanobacterium Nostoc punctiforme. *mSphere*. [Online] 4 (3). Available from: doi:10.1128/mSphere.00231-19.

Goss, R. & Latowski, D. (2020) Lipid Dependence of Xanthophyll Cycling in Higher Plants and Algae. *Frontiers in Plant Science*. 11.

Goss, R., Lohr, M., Latowski, D., Grzyb, J., et al. (2005) Role of hexagonal structure-forming lipids in diadinoxanthin and violaxanthin solubilization and de-epoxidation. *Biochemistry*. [Online] 44 (10), 4028–4036. Available from: doi:10.1021/bi047464k.

Grant, T., Rohou, A. & Grigorieff, N. (2018) cisTEM, user-friendly software for single-particle image processing Edward H Egelman (ed.). *eLife*. [Online] 7, e35383. Available from: doi:10.7554/eLife.35383.

Grassucci, R.A., Taylor, D.J. & Frank, J. (2007) Preparation of macromolecular complexes for cryo-electron microscopy. *Nature Protocols*. [Online] 2 (12), 3239–3246. Available from:

doi:10.1038/nprot.2007.452.
Grigorieff, N. (2000) Resolution measurement in structures derived from single particles. *Acta crystallographica. Section D, Biological crystallography*. [Online] 56 (Pt 10), 1270–1277. Available from: doi:10.1107/s0907444900009549.
Gross, M., Cramton, S.E., Götz, F. & Peschel, A. (2001) Key role of teichoic acid net charge in Staphylococcus aureus colonization of artificial surfaces. *Infection and immunity*. [Online] 69 (5), 3423–3426. Available from: doi:10.1128/IAI.69.5.3423-3426.2001.
Gruszecki, W.I. & Strzałka, K. (2005) Carotenoids as modulators of lipid membrane physical properties. *Biochimica et biophysica acta*. [Online] 1740 (2), 108–115. Available from: doi:10.1016/j.bbadis.2004.11.015.
Guan, S., Zhao, L. & Peng, R. (2022) Mitochondrial Respiratory Chain Supercomplexes: From Structure to Function. *International journal of molecular sciences*. [Online] 23 (22). Available from: doi:10.3390/ijms232213880.
Guéguen, N. & Maréchal, E. (2022) Origin of cyanobacterial thylakoids via a non-vesicular glycolipid phase transition and their impact on the Great Oxygenation Event. *Journal of Experimental Botany*. [Online] 73 (9), 2721–2734. Available from: doi:10.1093/jxb/erab429.
Gupta, T.K., Klumpe, S., Gries, K., Heinz, S., et al. (2021) Structural basis for VIPP1 oligomerization and maintenance of thylakoid membrane integrity. *Cell*. [Online] 184 (14), 3643-3659.e23. Available from: doi:https://doi.org/10.1016/j.cell.2021.05.011.
Han, J., Pluhackova, K. & Böckmann, R.A. (2017) The Multifaceted Role of SNARE Proteins in Membrane Fusion. *Frontiers in physiology*. [Online] 8, 5. Available from: doi:10.3389/fphys.2017.00005.
Harayama, T. & Riezman, H. (2018) Understanding the diversity of membrane lipid composition. *Nature Reviews Molecular Cell Biology*. [Online] 19 (5), 281–296. Available from: doi:10.1038/nrm.2017.138.
Hayes, S., Schachtschabel, J., Mishkind, M., Munnik, T., et al. (2021) Hot topic: Thermosensing in plants. *Plant, Cell & Environment*. [Online] 44 (7), 2018–2033. Available from: doi:https://doi.org/10.1111/pce.13979.
Hayward, S.B. & Glaeser, R.M. (1979) Radiation damage of purple membrane at low temperature. *Ultramicroscopy*. [Online] 4 (2), 201–210. Available from: doi:https://doi.org/10.1016/S0304-3991(79)90211-0.
He, S. & Scheres, S.H.W. (2017) Helical reconstruction in RELION. *Journal of Structural Biology*. [Online] 198 (3), 163–176. Available from: doi:https://doi.org/10.1016/j.jsb.2017.02.003.
Van Heel, M. (1987) Angular reconstitution: A posteriori assignment of projection directions for 3D reconstruction. *Ultramicroscopy*. [Online] 21 (2), 111–123. Available from: doi:https://doi.org/10.1016/0304-3991(87)90078-7.
van Heel, M. & Frank, J. (1981) Use of multivariates statistics in analysing the images of biological macromolecules. *Ultramicroscopy*. [Online] 6 (1), 187–194. Available from: doi:https://doi.org/10.1016/S0304-3991(81)80197-0.
Henderson, R. (2013) Avoiding the pitfalls of single particle cryo-electron microscopy: Einstein from noise. *Proceedings of the National Academy of Sciences of the United States of America*. [Online] 110 (45), 18037–18041. Available from: doi:10.1073/pnas.1314449110.
Henderson, R. (2015) Overview and future of single particle electron cryomicroscopy. *Archives of Biochemistry and Biophysics*. [Online] 581, 19–24. Available from:

doi:https://doi.org/10.1016/j.abb.2015.02.036.
Henderson, R. (1995) The potential and limitations of neutrons, electrons and X-rays for atomic resolution microscopy of unstained biological molecules. *Quarterly Reviews of Biophysics*. [Online] 28 (2), 171–193. Available from: doi:DOI: 10.1017/S003358350000305X.
Hennig, R., Heidrich, J., Saur, M., Schmüser, L., et al. (2015) IM30 triggers membrane fusion in cyanobacteria and chloroplasts. *Nature communications*. [Online] 6, 7018. Available from: doi:10.1038/ncomms8018.
Hetherington, C. (2004) Aberration correction for TEM. *Materials Today*. [Online] 7 (12), 50–55. Available from: doi:https://doi.org/10.1016/S1369-7021(04)00571-1.
Hoppins, S. & Nunnari, J. (2009) The molecular mechanism of mitochondrial fusion. *Biochimica et Biophysica Acta (BBA) - Molecular Cell Research*. [Online] 1793 (1), 20–26. Available from: doi:https://doi.org/10.1016/j.bbamcr.2008.07.005.
Horvath, S.E. & Daum, G. (2013) Lipids of mitochondria. *Progress in Lipid Research*. [Online] 52 (4), 590–614. Available from: doi:https://doi.org/10.1016/j.plipres.2013.07.002.
Howley, E., Mangus, A., Williams, D. & Torres, C.I. (2023) Intracytoplasmic membranes develop in Geobacter sulfurreducens under thermodynamically limiting conditions. *npj Biofilms and Microbiomes*. [Online] 9 (1), 18. Available from: doi:10.1038/s41522-023-00384-6.
Hryc, C.F., Mallampalli, V.K.P.S., Bovshik, E.I., Azinas, S., et al. (2023) Structural insights into cardiolipin replacement by phosphatidylglycerol in a cardiolipin-lacking yeast respiratory supercomplex. *Nature Communications*. [Online] 14 (1), 2783. Available from: doi:10.1038/s41467-023-38441-5.
Hsu, F., Spannl, S., Ferguson, C., Hyman, A.A., et al. (2018) Rab5 and Alsin regulate stress-activated cytoprotective signaling on mitochondria. *eLife*. [Online] 7. Available from: doi:10.7554/eLife.32282.
Hu, C., Shu, L., Huang, X., Yu, J., et al. (2020) OPA1 and MICOS Regulate mitochondrial crista dynamics and formation. *Cell Death & Disease*. [Online] 11 (10), 940. Available from: doi:10.1038/s41419-020-03152-y.
Hu, J. & Rapoport, T.A. (2016) Fusion of the endoplasmic reticulum by membrane-bound GTPases. *Seminars in Cell & Developmental Biology*. [Online] 60, 105–111. Available from: doi:https://doi.org/10.1016/j.semcdb.2016.06.001.
Hu, M., Yu, H., Gu, K., Wang, Z., et al. (2018) A particle-filter framework for robust cryo-EM 3D reconstruction. *Nature methods*. [Online] 15 (12), 1083–1089. Available from: doi:10.1038/s41592-018-0223-8.
Hu, Y., Cheng, K., He, L., Zhang, X., et al. (2021) NMR-Based Methods for Protein Analysis. *Analytical Chemistry*. [Online] 93 (4), 1866–1879. Available from: doi:10.1021/acs.analchem.0c03830.
Huang, Y. & Gui, S. (2018) Factors affecting the structure of lyotropic liquid crystals and the correlation between structure and drug diffusion. *RSC Advances*. [Online] 8 (13), 6978–6987. Available from: doi:10.1039/C7RA12008G.
Huang, Z., Shen, L., Wang, W., Mao, Z., et al. (2021) Structure of photosystem I-LHCI-LHCII from the green alga Chlamydomonas reinhardtii in State 2. *Nature Communications*. [Online] 12 (1), 1100. Available from: doi:10.1038/s41467-021-21362-6.
Hughes, A.H., Hancock, I.C. & Baddiley, J. (1973) The function of teichoic acids in cation control in bacterial membranes. *The Biochemical journal*. [Online] 132 (1), 83–93. Available from: doi:10.1042/bj1320083.

Imoto, Y., Raychaudhuri, S., Ma, Y., Fenske, P., et al. (2022) Dynamin is primed at endocytic sites for ultrafast endocytosis. *Neuron*. [Online] 110 (17), 2815-2835.e13. Available from: doi:10.1016/j.neuron.2022.06.010.

Isik, O.A. & Cizmecioglu, O. (2023) *Rafting on the Plasma Membrane: Lipid Rafts in Signaling and Disease BT - Cell Biology and Translational Medicine, Volume 20: Organ Function, Maintenance, Repair in Health and Disease*. In: Kursad Turksen (ed.). [Online]. Cham, Springer Nature Switzerland. pp. 87–108. Available from: doi:10.1007/5584_2022_759.

Jahn, R., Cafiso, D.C. & Tamm, L.K. (2024) Mechanisms of SNARE proteins in membrane fusion. *Nature Reviews Molecular Cell Biology*. [Online] 25 (2), 101–118. Available from: doi:10.1038/s41580-023-00668-x.

Jamali, K., Käll, L., Zhang, R., Brown, A., et al. (2024) Automated model building and protein identification in cryo-EM maps. *Nature*. [Online] 628 (8007), 450–457. Available from: doi:10.1038/s41586-024-07215-4.

Jensen, G.J. (2021) *Grant Jensen Cryo-EM Lectures*. [Online]. 2021. YouTube. Available from: https://www.youtube.com/playlist?list=PLhiuGaXlZZenm7lu5qv_A59zEWkRKkBn5.

Ji, C., Du, S., Li, P., Zhu, Q., et al. (2019) Structural mechanism for guanylate-binding proteins (GBPs) targeting by the Shigella E3 ligase IpaH9.8. *PLoS pathogens*. [Online] 15 (6), e1007876. Available from: doi:10.1371/journal.ppat.1007876.

Jilly, R., Khan, N.Z., Aronsson, H. & Schneider, D. (2018) Dynamin-Like Proteins Are Potentially Involved in Membrane Dynamics within Chloroplasts and Cyanobacteria. *Frontiers in plant science*. [Online] 9, 206. Available from: doi:10.3389/fpls.2018.00206.

Jimah, J.R. & Hinshaw, J.E. (2019) Structural Insights into the Mechanism of Dynamin Superfamily Proteins. *Trends in cell biology*. [Online] 29 (3), 257–273. Available from: doi:10.1016/j.tcb.2018.11.003.

Jimah, J.R., Kundu, N., Stanton, A.E., Sochacki, K.A., et al. (2024) Cryo-EM structures of membrane-bound dynamin in a post-hydrolysis state primed for membrane fission. *Developmental Cell*. [Online] 59 (14), 1783-1793.e5. Available from: doi:https://doi.org/10.1016/j.devcel.2024.04.008.

Johnson, M.P. & Wientjes, E. (2020) The relevance of dynamic thylakoid organisation to photosynthetic regulation. *Biochimica et Biophysica Acta (BBA) - Bioenergetics*. [Online] 1861 (4), 148039. Available from: doi:https://doi.org/10.1016/j.bbabio.2019.06.011.

Jose, G.P., Gopan, S., Bhattacharyya, S. & Pucadyil, T.J. (2020) A facile, sensitive and quantitative membrane-binding assay for proteins. *Traffic (Copenhagen, Denmark)*. [Online] 21 (3), 297–305. Available from: doi:10.1111/tra.12719.

Jose, G.P. & Pucadyil, T.J. (2020) PLiMAP: Proximity-Based Labeling of Membrane-Associated Proteins. *Current protocols in protein science*. [Online] 101 (1), e110. Available from: doi:10.1002/cpps.110.

Joubert, F. & Puff, N. (2021) Mitochondrial Cristae Architecture and Functions: Lessons from Minimal Model Systems. *Membranes*. [Online] 11 (7). Available from: doi:10.3390/membranes11070465.

Jumper, J., Evans, R., Pritzel, A., Green, T., et al. (2021) Highly accurate protein structure prediction with AlphaFold. *Nature*. [Online] 596 (7873), 583–589. Available from: doi:10.1038/s41586-021-03819-2.

Junglas, B., Gewehr, L., Mernberger, L., Schönnenbeck, P., et al. (2024) Structural basis for GTPase activity and conformational changes of the bacterial dynamin-like protein SynDLP. *Cell Reports*. [Online] 43 (9). Available from: doi:10.1016/j.celrep.2024.114657.

Junglas, B., Huber, S.T., Heidler, T., Schlösser, L., et al. (2021) PspA adopts an ESCRT-III-like fold and remodels bacterial membranes. *Cell*. [Online] 184 (14), 3674-3688.e18. Available from: doi:10.1016/j.cell.2021.05.042.

Junglas, B. & Schneider, D. (2018) What is Vipp1 good for? *Molecular Microbiology*. [Online] 108 (1), 1–5. Available from: doi:https://doi.org/10.1111/mmi.13924.

Kaila, V.R.I. & Wikström, M. (2021) Architecture of bacterial respiratory chains. *Nature Reviews Microbiology*. [Online] 19 (5), 319–330. Available from: doi:10.1038/s41579-020-00486-4.

Kalb, R.C., Nyabuto, G.O., Morran, M.P., Maity, S., et al. (2024) The large GTPase Guanylate-Binding Protein-1 (GBP-1) promotes mitochondrial fission in glioblastoma. *bioRxiv*. [Online] 2024.05.08.593235. Available from: doi:10.1101/2024.05.08.593235.

Kalia, R., Wang, R.Y.-R., Yusuf, A., Thomas, P. V, et al. (2018) Structural basis of mitochondrial receptor binding and constriction by DRP1. *Nature*. [Online] 558 (7710), 401–405. Available from: doi:10.1038/s41586-018-0211-2.

Kameoka, S., Adachi, Y., Okamoto, K., Iijima, M., et al. (2018) Phosphatidic Acid and Cardiolipin Coordinate Mitochondrial Dynamics. *Trends in cell biology*. [Online] 28 (1), 67–76. Available from: doi:10.1016/j.tcb.2017.08.011.

Kamerkar, S.C., Kraus, F., Sharpe, A.J., Pucadyil, T.J., et al. (2018) Dynamin-related protein 1 has membrane constricting and severing abilities sufficient for mitochondrial and peroxisomal fission. *Nature Communications*. [Online] 9 (1), 5239. Available from: doi:10.1038/s41467-018-07543-w.

Kapust, R.B. & Waugh, D.S. (2000) Controlled Intracellular Processing of Fusion Proteins by TEV Protease. *Protein Expression and Purification*. [Online] 19 (2), 312–318. Available from: doi:https://doi.org/10.1006/prep.2000.1251.

Kastner, B., Fischer, N., Golas, M.M., Sander, B., et al. (2008) GraFix: sample preparation for single-particle electron cryomicroscopy. *Nature Methods*. [Online] 5 (1), 53–55. Available from: doi:10.1038/nmeth1139.

van Kempen, M., Kim, S.S., Tumescheit, C., Mirdita, M., et al. (2024) Fast and accurate protein structure search with Foldseek. *Nature Biotechnology*. [Online] 42 (2), 243–246. Available from: doi:10.1038/s41587-023-01773-0.

Khalifat, N., Fournier, J.-B., Angelova, M.I. & Puff, N. (2011) Lipid packing variations induced by pH in cardiolipin-containing bilayers: The driving force for the cristae-like shape instability. *Biochimica et Biophysica Acta (BBA) - Biomembranes*. [Online] 1808 (11), 2724–2733. Available from: doi:https://doi.org/10.1016/j.bbamem.2011.07.013.

Khamar, H.J., Breathwaite, E.K., Prasse, C.E., Fraley, E.R., et al. (2010) Multiple roles of soluble sugars in the establishment of Gunnera-Nostoc endosymbiosis. *Plant physiology*. [Online] 154 (3), 1381–1389. Available from: doi:10.1104/pp.110.162529.

Khayatan, B., Bains, D.K., Cheng, M.H., Cho, Y.W., et al. (2017) A Putative O-Linked β-N-Acetylglucosamine Transferase Is Essential for Hormogonium Development and Motility in the Filamentous Cyanobacterium Nostoc punctiforme. *Journal of bacteriology*. [Online] 199 (9). Available from: doi:10.1128/JB.00075-17.

Kimanius, D., Dong, L., Sharov, G., Nakane, T., et al. (2021) New tools for automated cryo-EM single-particle analysis in RELION-4.0. *The Biochemical journal*. [Online] 478 (24), 4169–4185. Available from: doi:10.1042/BCJ20210708.

Kimanius, D., Jamali, K., Wilkinson, M.E., Lövestam, S., et al. (2024) Data-driven regularization lowers the size barrier of cryo-EM structure determination. *Nature Methods*. [Online] Available from: doi:10.1038/s41592-024-02304-8.

Kirchhoff, H., Haase, W., Wegner, S., Danielsson, R., et al. (2007) Low-Light-Induced Formation of Semicrystalline Photosystem II Arrays in Higher Plant Chloroplasts. *Biochemistry*. [Online] 46 (39), 11169–11176. Available from: doi:10.1021/bi700748y.

Kirchhoff, H., Mukherjee, U. & Galla, H.-J. (2002) Molecular Architecture of the Thylakoid Membrane: Lipid Diffusion Space for Plastoquinone. *Biochemistry*. [Online] 41 (15), 4872–4882. Available from: doi:10.1021/bi011650y.

Klug, A. (1999) The tobacco mosaic virus particle: structure and assembly. *Philosophical transactions of the Royal Society of London. Series B, Biological sciences*. [Online] 354 (1383), 531–535. Available from: doi:10.1098/rstb.1999.0404.

Kobayashi, K. (2016) Role of membrane glycerolipids in photosynthesis, thylakoid biogenesis and chloroplast development. *Journal of plant research*. [Online] 129 (4), 565–580. Available from: doi:10.1007/s10265-016-0827-y.

Kobayashi, K., Jimbo, H., Nakamura, Y. & Wada, H. (2024) Biosynthesis of phosphatidylglycerol in photosynthetic organisms. *Progress in Lipid Research*. [Online] 93, 101266. Available from: doi:https://doi.org/10.1016/j.plipres.2023.101266.

Kobayashi, K., Yoshihara, A. & Kubota-Kawai, H. (2023) Evolutionary implications from lipids in membrane bilayers and photosynthetic complexes in cyanobacteria and chloroplasts. *The Journal of Biochemistry*. [Online] 174 (5), 399–408. Available from: doi:10.1093/jb/mvad058.

Kondadi, A.K., Anand, R., Hänsch, S., Urbach, J., et al. (2020) Cristae undergo continuous cycles of membrane remodelling in a MICOS‐dependent manner. *EMBO reports*. [Online] 21 (3), e49776. Available from: doi:https://doi.org/10.15252/embr.201949776.

Kong, D., Liu, R., Liu, J., Zhou, Q., et al. (2020) Cubic Membranes Formation in Synchronized Human Hepatocellular Carcinoma Cells Reveals a Possible Role as a Structural Antioxidant Defense System in Cell Cycle Progression. *Frontiers in Cell and Developmental Biology*. 8.

Kong, L., Sochacki, K.A., Wang, H., Fang, S., et al. (2018) Cryo-EM of the dynamin polymer assembled on lipid membrane. *Nature*. [Online] 560 (7717), 258–262. Available from: doi:10.1038/s41586-018-0378-6.

Korbie, D.J. & Mattick, J.S. (2008) Touchdown PCR for increased specificity and sensitivity in PCR amplification. *Nature Protocols*. [Online] 3 (9), 1452–1456. Available from: doi:10.1038/nprot.2008.133.

Korobova, F., Ramabhadran, V. & Higgs, H.N. (2013) An actin-dependent step in mitochondrial fission mediated by the ER-associated formin INF2. *Science (New York, N.Y.)*. [Online] 339 (6118), 464–467. Available from: doi:10.1126/science.1228360.

Koshiba, T., Detmer, S.A., Kaiser, J.T., Chen, H., et al. (2004) Structural Basis of Mitochondrial Tethering by Mitofusin Complexes. *Science*. [Online] 305 (5685), 858–862. Available from: doi:10.1126/science.1099793.

Kourkoutis, L.F., Plitzko, J.M. & Baumeister, W. (2012) Electron Microscopy of Biological Materials at the Nanometer Scale. *Annual Review of Materials Research*. [Online] 42 (Volume 42, 2012), 33–58. Available from: doi:https://doi.org/10.1146/annurev-matsci-070511-155004.

Kowalewska, Ł., Mazur, R., Suski, S., Garstka, M., et al. (2016) Three-Dimensional Visualization of the Tubular-Lamellar Transformation of the Internal Plastid Membrane Network during Runner Bean Chloroplast Biogenesis. *The Plant cell*. [Online] 28 (4), 875–891. Available from: doi:10.1105/tpc.15.01053.

Kreida, S. & Törnroth-Horsefield, S. (2015) Structural insights into aquaporin selectivity and

regulation. *Current Opinion in Structural Biology*. [Online] 33, 126–134. Available from: doi:https://doi.org/10.1016/j.sbi.2015.08.004.

Kremer, J.R., Mastronarde, D.N. & McIntosh, J.R. (1996) Computer visualization of three-dimensional image data using IMOD. *Journal of structural biology*. [Online] 116 (1), 71–76. Available from: doi:10.1006/jsbi.1996.0013.

Kreutzberger, M.A.B., Sonani, R.R., Liu, J., Chatterjee, S., et al. (2022) Convergent evolution in the supercoiling of prokaryotic flagellar filaments. *Cell*. [Online] 185 (19), 3487-3500.e14. Available from: doi:10.1016/j.cell.2022.08.009.

Krogh, A., Larsson, B., von Heijne, G. & Sonnhammer, E.L. (2001) Predicting transmembrane protein topology with a hidden Markov model: application to complete genomes. *Journal of molecular biology*. [Online] 305 (3), 567–580. Available from: doi:10.1006/jmbi.2000.4315.

de Kruijff, B. (1997) Biomembranes. Lipids beyond the bilayer. *Nature*. [Online]. 386 (6621) pp.129–130. Available from: doi:10.1038/386129a0.

Krypotou, E., Townsend, G.E., Gao, X., Tachiyama, S., et al. (2023) Bacteria require phase separation for fitness in the mammalian gut. *Science*. [Online] 379 (6637), 1149–1156. Available from: doi:10.1126/science.abn7229.

Kucukelbir, A., Sigworth, F.J. & Tagare, H.D. (2014) Quantifying the local resolution of cryo-EM density maps. *Nature Methods*. [Online] 11 (1), 63–65. Available from: doi:10.1038/nmeth.2727.

Kühlbrandt, W. (2014) The Resolution Revolution. *Science*. [Online] 343 (6178), 1443 LP – 1444. Available from: doi:10.1126/science.1251652.

Kumar, R., Islinger, M., Worthy, H., Carmichael, R., et al. (2024) The peroxisome: an update on mysteries 3.0. *Histochemistry and Cell Biology*. [Online] 161 (2), 99–132. Available from: doi:10.1007/s00418-023-02259-5.

Kutsch, M. & Coers, J. (2021) Human guanylate binding proteins: nanomachines orchestrating host defense. *The FEBS journal*. [Online] 288 (20), 5826–5849. Available from: doi:10.1111/febs.15662.

La, T.M., Tachibana, H., Li, S.-A., Abe, T., et al. (2020) Dynamin 1 is important for microtubule organization and stabilization in glomerular podocytes. *The FASEB Journal*. [Online] 34 (12), 16449–16463. Available from: doi:https://doi.org/10.1096/fj.202001240RR.

Langlois, R., Pallesen, J., Ash, J.T., Nam Ho, D., et al. (2014) Automated particle picking for low-contrast macromolecules in cryo-electron microscopy. *Journal of structural biology*. [Online] 186 (1), 1–7. Available from: doi:10.1016/j.jsb.2014.03.001.

Latowski, D., Akerlund, H.-E. & Strzałka, K. (2004) Violaxanthin de-epoxidase, the xanthophyll cycle enzyme, requires lipid inverted hexagonal structures for its activity. *Biochemistry*. [Online] 43 (15), 4417–4420. Available from: doi:10.1021/bi049652g.

Latychevskaia, T. (2017) Spatial coherence of electron beams from field emitters and its effect on the resolution of imaged objects. *Ultramicroscopy*. [Online] 175, 121–129. Available from: doi:https://doi.org/10.1016/j.ultramic.2016.11.008.

Laursen, S.P., Bowerman, S. & Luger, K. (2021) Archaea: The Final Frontier of Chromatin. *Journal of molecular biology*. [Online] 433 (6), 166791. Available from: doi:10.1016/j.jmb.2020.166791.

Lee, J.E., Westrate, L.M., Wu, H., Page, C., et al. (2016) Multiple dynamin family members collaborate to drive mitochondrial division. *Nature*. [Online] 540 (7631), 139–143. Available from: doi:10.1038/nature20555.

Levy, A., Grzadkowski, M., Poitevin, F., Vallese, F., et al. (2024) Revealing biomolecular

structure and motion with neural ab initio cryo-EM reconstruction. *bioRxiv : the preprint server for biology*. [Online] Available from: doi:10.1101/2024.05.30.596729.

Li, H., Wang, Z., Fang, X., Zeng, W., et al. (2022) Poroptosis: A form of cell death depending on plasma membrane nanopores formation. *iScience*. [Online] 25 (6), 104481. Available from: doi:10.1016/j.isci.2022.104481.

Li, X., Mooney, P., Zheng, S., Booth, C.R., et al. (2013) Electron counting and beam-induced motion correction enable near-atomic-resolution single-particle cryo-EM. *Nature Methods*. [Online] 10 (6), 584–590. Available from: doi:10.1038/nmeth.2472.

Li, Y.-J., Cao, Y.-L., Feng, J.-X., Qi, Y., et al. (2019) Structural insights of human mitofusin-2 into mitochondrial fusion and CMT2A onset. *Nature Communications*. [Online] 10 (1), 4914. Available from: doi:10.1038/s41467-019-12912-0.

Liebschner, D., Afonine, P. V, Baker, M.L., Bunkóczi, G., et al. (2019) Macromolecular structure determination using X-rays, neutrons and electrons: recent developments in Phenix. *Acta crystallographica. Section D, Structural biology*. [Online] 75 (Pt 10), 861–877. Available from: doi:10.1107/S2059798319011471.

Liko, I., Degiacomi, M.T., Mohammed, S., Yoshikawa, S., et al. (2016) Dimer interface of bovine cytochrome c oxidase is influenced by local posttranslational modifications and lipid binding. *Proceedings of the National Academy of Sciences of the United States of America*. [Online] 113 (29), 8230–8235. Available from: doi:10.1073/pnas.1600354113.

Lindberg, P., Lindblad, P. & Cournac, L. (2004) Gas exchange in the filamentous cyanobacterium Nostoc punctiforme strain ATCC 29133 and Its hydrogenase-deficient mutant strain NHM5. *Applied and environmental microbiology*. [Online] 70 (4), 2137–2145. Available from: doi:10.1128/AEM.70.4.2137-2145.2004.

Liu, J., Alvarez, F.J.D., Clare, D.K., Noel, J.K., et al. (2021a) CryoEM structure of the super-constricted two-start dynamin 1 filament. *Nature Communications*. [Online] 12 (1), 5393. Available from: doi:10.1038/s41467-021-25741-x.

Liu, J., Noel, J.K. & Low, H.H. (2018) Structural basis for membrane tethering by a bacterial dynamin-like pair. *Nature Communications*. [Online] 9 (1), 3345. Available from: doi:10.1038/s41467-018-05523-8.

Liu, J., Tassinari, M., Souza, D.P., Naskar, S., et al. (2021b) Bacterial Vipp1 and PspA are members of the ancient ESCRT-III membrane-remodeling superfamily. *Cell*. [Online] 184 (14), 3660-3673.e18. Available from: doi:https://doi.org/10.1016/j.cell.2021.05.041.

Liu, N. & Wang, H.-W. (2023) Better Cryo-EM Specimen Preparation: How to Deal with the Air–Water Interface? *Journal of Molecular Biology*. [Online] 435 (9), 167926. Available from: doi:https://doi.org/10.1016/j.jmb.2022.167926.

Lobo-Jarne, T. & Ugalde, C. (2018) Respiratory chain supercomplexes: Structures, function and biogenesis. *Seminars in cell & developmental biology*. [Online] 76, 179–190. Available from: doi:10.1016/j.semcdb.2017.07.021.

Lorent, J.H., Diaz-Rohrer, B., Lin, X., Spring, K., et al. (2017) Structural determinants and functional consequences of protein affinity for membrane rafts. *Nature Communications*. [Online] 8 (1), 1219. Available from: doi:10.1038/s41467-017-01328-3.

Lorent, J.H., Levental, K.R., Ganesan, L., Rivera-Longsworth, G., et al. (2020) Plasma membranes are asymmetric in lipid unsaturation, packing and protein shape. *Nature Chemical Biology*. [Online] 16 (6), 644–652. Available from: doi:10.1038/s41589-020-0529-6.

Low, H.H., Gubellini, F., Rivera-Calzada, A., Braun, N., et al. (2014) Structure of a type IV

secretion system. *Nature*. [Online] 508 (7497), 550–553. Available from: doi:10.1038/nature13081.

Low, H.H. & Löwe, J. (2006) A bacterial dynamin-like protein. *Nature*. [Online] 444 (7120), 766–769. Available from: doi:10.1038/nature05312.

Low, H.H., Sachse, C., Amos, L.A. & Löwe, J. (2009) Structure of a Bacterial Dynamin-like Protein Lipid Tube Provides a Mechanism For Assembly and Membrane Curving. *Cell*. [Online] 139 (7), 1342–1352. Available from: doi:https://doi.org/10.1016/j.cell.2009.11.003.

Lu, X., Luo, C., Wu, J., Deng, Y., et al. (2023) Ion channels and transporters regulate nutrient absorption in health and disease. *Journal of cellular and molecular medicine*. [Online] 27 (18), 2631–2642. Available from: doi:10.1111/jcmm.17853.

Mackenzie, J.M., Khromykh, A.A. & Parton, R.G. (2007) Cholesterol manipulation by West Nile virus perturbs the cellular immune response. *Cell host & microbe*. [Online] 2 (4), 229–239. Available from: doi:10.1016/j.chom.2007.09.003.

Mahajan, M., Bharambe, N., Shang, Y., Lu, B., et al. (2021) NMR identification of a conserved Drp1 cardiolipin-binding motif essential for stress-induced mitochondrial fission. *Proceedings of the National Academy of Sciences*. [Online] 118 (29), e2023079118. Available from: doi:10.1073/pnas.2023079118.

Mahmoudabadi, G., Phillips, R., Lynch, M. & Milo, R. (2019) Defining the Energetic Costs of Cellular Structures. *bioRxiv*. [Online] 666040. Available from: doi:10.1101/666040.

von der Malsburg, A., Abutbul-Ionita, I., Haller, O., Kochs, G., et al. (2011) Stalk Domain of the Dynamin-like MxA GTPase Protein Mediates Membrane Binding and Liposome Tubulation via the Unstructured L4 Loop*. *Journal of Biological Chemistry*. [Online] 286 (43), 37858–37865. Available from: doi:https://doi.org/10.1074/jbc.M111.249037.

von der Malsburg, A., Sapp, G.M., Zuccaro, K.E., von Appen, A., et al. (2023) Structural mechanism of mitochondrial membrane remodelling by human OPA1. *Nature*. [Online] 620 (7976), 1101–1108. Available from: doi:10.1038/s41586-023-06441-6.

Manni, M.M., Tiberti, M.L., Pagnotta, S., Barelli, H., et al. (2018) Acyl chain asymmetry and polyunsaturation of brain phospholipids facilitate membrane vesiculation without leakage Patricia Bassereau (ed.). *eLife*. [Online] 7, e34394. Available from: doi:10.7554/eLife.34394.

Mareš, J., Strunecký, O., Bučinská, L. & Wiedermannová, J. (2019) Evolutionary Patterns of Thylakoid Architecture in Cyanobacteria. *Frontiers in microbiology*. [Online] 10, 277. Available from: doi:10.3389/fmicb.2019.00277.

Marques, M.A., Purdy, M.D. & Yeager, M. (2019) CryoEM maps are full of potential. *Current opinion in structural biology*. [Online] 58, 214–223. Available from: doi:10.1016/j.sbi.2019.04.006.

Marrink, S.-J. & Mark, A.E. (2004) Molecular view of hexagonal phase formation in phospholipid membranes. *Biophysical journal*. [Online] 87 (6), 3894–3900. Available from: doi:10.1529/biophysj.104.048710.

Mathelié-Guinlet, M., Asmar, A.T., Collet, J.-F. & Dufrêne, Y.F. (2020) Lipoprotein Lpp regulates the mechanical properties of the E. coli cell envelope. *Nature Communications*. [Online] 11 (1), 1789. Available from: doi:10.1038/s41467-020-15489-1.

Matsuki, Y., Iwamoto, M. & Oiki, S. (2024) Asymmetric Lipid Bilayers and Potassium Channels Embedded Therein in the Contact Bubble Bilayer. *Methods in molecular biology (Clifton, N.J.)*. [Online] 2796, 1–21. Available from: doi:10.1007/978-1-0716-3818-7_1.

Mattie, S., Riemer, J., Wideman, J.G. & McBride, H.M. (2018) A new mitofusin topology places

the redox-regulated C terminus in the mitochondrial intermembrane space. *The Journal of cell biology*. [Online] 217 (2), 507–515. Available from: doi:10.1083/jcb.201611194.

Mazur, R., Mostowska, A., Szach, J., Gieczewska, K., et al. (2019) Galactolipid deficiency disturbs spatial arrangement of the thylakoid network in Arabidopsis thaliana plants. *Journal of experimental botany*. [Online] 70 (18), 4689–4704. Available from: doi:10.1093/jxb/erz219.

McMahon, H.T. & Boucrot, E. (2015) Membrane curvature at a glance. *Journal of cell science*. [Online] 128 (6), 1065–1070. Available from: doi:10.1242/jcs.114454.

McMullan, G., Chen, S., Henderson, R. & Faruqi, A.R. (2009) Detective quantum efficiency of electron area detectors in electron microscopy. *Ultramicroscopy*. [Online] 109 (9), 1126–1143. Available from: doi:https://doi.org/10.1016/j.ultramic.2009.04.002.

McMullan, G., Naydenova, K., Mihaylov, D., Yamashita, K., et al. (2023) Structure determination by cryoEM at 100 keV. *Proceedings of the National Academy of Sciences of the United States of America*. [Online] 120 (49), e2312905120. Available from: doi:10.1073/pnas.2312905120.

van Meer, G., Voelker, D.R. & Feigenson, G.W. (2008) Membrane lipids: where they are and how they behave. *Nature Reviews Molecular Cell Biology*. [Online] 9 (2), 112–124. Available from: doi:10.1038/nrm2330.

Mehrotra, N., Nichols, J. & Ramachandran, R. (2014) Alternate pleckstrin homology domain orientations regulate dynamin-catalyzed membrane fission. *Molecular biology of the cell*. [Online] 25 (6), 879–890. Available from: doi:10.1091/mbc.E13-09-0548.

Melo, A.A., Hegde, B.G., Shah, C., Larsson, E., et al. (2017) Structural insights into the activation mechanism of dynamin-like EHD ATPases. *Proceedings of the National Academy of Sciences*. [Online] 114 (22), 5629–5634. Available from: doi:10.1073/pnas.1614075114.

Melzak, K.A., Muth, M., Kirschhöfer, F., Brenner-Weiss, G., et al. (2020) Lipid ratios as a marker for red blood cell storage quality and as a possible explanation for donor gender differences in storage quality. *Vox Sanguinis*. [Online] 115 (8), 655–663. Available from: doi:https://doi.org/10.1111/vox.12924.

Meng, J. (2017) Distinct functions of dynamin isoforms in tumorigenesis and their potential as therapeutic targets in cancer. *Oncotarget*. [Online] 8 (25), 41701–41716. Available from: doi:10.18632/oncotarget.16678.

Meredith, S.A., Yoneda, T., Hancock, A.M., Connell, S.D., et al. (2021) Model Lipid Membranes Assembled from Natural Plant Thylakoids into 2D Microarray Patterns as a Platform to Assess the Organization and Photophysics of Light-Harvesting Proteins. *Small*. [Online] 17 (14), 2006608. Available from: doi:https://doi.org/10.1002/smll.202006608.

Merk, A., Bartesaghi, A., Banerjee, S., Falconieri, V., et al. (2016) Breaking Cryo-EM Resolution Barriers to Facilitate Drug Discovery. *Cell*. [Online] 165 (7), 1698–1707. Available from: doi:10.1016/j.cell.2016.05.040.

Michie, K.A., Boysen, A., Low, H.H., Møller-Jensen, J., et al. (2014) LeoA, B and C from enterotoxigenic Escherichia coli (ETEC) are bacterial dynamins. *PloS one*. [Online] 9 (9), e107211. Available from: doi:10.1371/journal.pone.0107211.

Mielich-Süss, B., Wagner, R.M., Mietrach, N., Hertlein, T., et al. (2017) Flotillin scaffold activity contributes to type VII secretion system assembly in Staphylococcus aureus. *PLOS Pathogens*. 13 (11), e1006728.

Mikhaylenko, N.F., Skorokhod, T.P. & Kholodny, N.G. (1998) *Membrane Lipid Composition of the Cyanobacteria Nostoc Punctiforme and Spirulina Platensis under Various Conditions*

*of Carbon Nutrition BT - Photosynthesis: Mechanisms and Effects: Volume I–V: Proceedings of the XIth International Congress on Photosynthe*. In: G Garab (ed.). [Online]. Dordrecht, Springer Netherlands. pp. 1831–1834. Available from: doi:10.1007/978-94-011-3953-3_428.

Miller, A.L. (2011) The contractile ring. *Current biology : CB*. [Online] 21 (24), R976-8. Available from: doi:10.1016/j.cub.2011.10.044.

Minagawa, J. (2011) State transitions—The molecular remodeling of photosynthetic supercomplexes that controls energy flow in the chloroplast. *Biochimica et Biophysica Acta (BBA) - Bioenergetics*. [Online] 1807 (8), 897–905. Available from: doi:https://doi.org/10.1016/j.bbabio.2010.11.005.

Morlot, S., Galli, V., Klein, M., Chiaruttini, N., et al. (2012) Membrane shape at the edge of the dynamin helix sets location and duration of the fission reaction. *Cell*. [Online] 151 (3), 619–629. Available from: doi:10.1016/j.cell.2012.09.017.

Muhammad, I., Shalmani, A., Ali, M., Yang, Q.-H., et al. (2021) Mechanisms Regulating the Dynamics of Photosynthesis Under Abiotic Stresses. *Frontiers in Plant Science*. 11.

Murai, T. (2012) The role of lipid rafts in cancer cell adhesion and migration. *International journal of cell biology*. [Online] 2012, 763283. Available from: doi:10.1155/2012/763283.

Murray, D.H., Jahnel, M., Lauer, J., Avellaneda, M.J., et al. (2016) An endosomal tether undergoes an entropic collapse to bring vesicles together. *Nature*. [Online] 537 (7618), 107–111. Available from: doi:10.1038/nature19326.

Murugova, T.N., Gordeliy, V.I., Kuklin, A.I., Solodovnikova, I.M., et al. (2007) Study of three-dimensionally ordered structures of intact mitochondria by small-angle neutron scattering. *Crystallography Reports*. [Online] 52 (3), 521–524. Available from: doi:10.1134/S1063774507030339.

Naba, A. (2024) Mechanisms of assembly and remodelling of the extracellular matrix. *Nature Reviews Molecular Cell Biology*. [Online] Available from: doi:10.1038/s41580-024-00767-3.

Nakane, T., Kimanius, D., Lindahl, E. & Scheres, S.H.W. (2018) Characterisation of molecular motions in cryo-EM single-particle data by multi-body refinement in RELION Axel T Brunger (ed.). *eLife*. [Online] 7, e36861. Available from: doi:10.7554/eLife.36861.

Nakane, T., Kotecha, A., Sente, A., McMullan, G., et al. (2020) Single-particle cryo-EM at atomic resolution. *bioRxiv*. [Online] 2020.05.22.110189. Available from: doi:10.1101/2020.05.22.110189.

Naskar, S., Merino, A., Espadas, J., Singh, J., et al. (2023) Mechanism for Vipp1 spiral formation, ring biogenesis and membrane repair. *bioRxiv*. [Online] 2023.09.26.559607. Available from: doi:10.1101/2023.09.26.559607.

Naydenova, K., Peet, M.J. & Russo, C.J. (2019) Multifunctional graphene supports for electron cryomicroscopy. *Proceedings of the National Academy of Sciences of the United States of America*. [Online] 116 (24), 11718–11724. Available from: doi:10.1073/pnas.1904766116.

Nesterov, S., Chesnokov, Y., Kamyshinsky, R., Panteleeva, A., et al. (2021) Ordered Clusters of the Complete Oxidative Phosphorylation System in Cardiac Mitochondria. *International journal of molecular sciences*. [Online] 22 (3). Available from: doi:10.3390/ijms22031462.

Nicolson, G.L. (2014) The Fluid-Mosaic Model of Membrane Structure: still relevant to understanding the structure, function and dynamics of biological membranes after more than 40 years. *Biochimica et biophysica acta*. [Online] 1838 (6), 1451–1466. Available from: doi:10.1016/j.bbamem.2013.10.019.

Noble, A.J., Wei, H., Dandey, V.P., Zhang, Z., et al. (2018) Reducing effects of particle adsorption to the air–water interface in cryo-EM. *Nature Methods*. [Online] 15 (10), 793–795. Available from: doi:10.1038/s41592-018-0139-3.

Nyenhuis, S.B., Wu, X., Strub, M.-P., Yim, Y.-I., et al. (2023) OPA1 helical structures give perspective to mitochondrial dysfunction. *Nature*. [Online] 620 (7976), 1109–1116. Available from: doi:10.1038/s41586-023-06462-1.

Nyquist, H. (1928) Certain Topics in Telegraph Transmission Theory. *Transactions of the American Institute of Electrical Engineers*. [Online] 47 (2), 617–644. Available from: doi:10.1109/T-AIEE.1928.5055024.

O'Sullivan, M.J. & Lindsay, A.J. (2020) The Endosomal Recycling Pathway-At the Crossroads of the Cell. *International journal of molecular sciences*. [Online] 21 (17). Available from: doi:10.3390/ijms21176074.

Ogawa, Y., Iwano, M., Shikanai, T. & Sakamoto, W. (2023) FZL, a dynamin-like protein localized to curved grana edges, is required for efficient photosynthetic electron transfer in Arabidopsis. *Frontiers in plant science*. [Online] 14, 1279699. Available from: doi:10.3389/fpls.2023.1279699.

Olmos, Y. (2022) The ESCRT Machinery: Remodeling, Repairing, and Sealing Membranes. *Membranes*. [Online] 12 (6). Available from: doi:10.3390/membranes12060633.

Oosawa, F. & Kasai, M. (1962) A theory of linear and helical aggregations of macromolecules. *Journal of Molecular Biology*. [Online] 4 (1), 10–21. Available from: doi:https://doi.org/10.1016/S0022-2836(62)80112-0.

Orlova, E. V. & Saibil, H.R. (2011) Structural Analysis of Macromolecular Assemblies by Electron Microscopy. *Chemical Reviews*. [Online] 111 (12), 7710–7748. Available from: doi:10.1021/cr100353t.

Ortega-Arzola, E., Higgins, P.M. & Cockell, C.S. (2024) The minimum energy required to build a cell. *Scientific Reports*. [Online] 14 (1), 5267. Available from: doi:10.1038/s41598-024-54303-6.

Osawa, M., Anderson, D.E. & Erickson, H.P. (2008) Reconstitution of Contractile FtsZ Rings in Liposomes. *Science*. [Online] 320 (5877), 792–794. Available from: doi:10.1126/science.1154520.

Ouweneel, A.B., Thomas, M.J. & Sorci-Thomas, M.G. (2020) The ins and outs of lipid rafts: functions in intracellular cholesterol homeostasis, microparticles, and cell membranes: Thematic Review Series: Biology of Lipid Rafts. *Journal of Lipid Research*. [Online] 61 (5), 676–686. Available from: doi:https://doi.org/10.1194/jlr.TR119000383.

Ozeir, M. & Cohen, M.M. (2022) From dynamin related proteins structures and oligomers to membrane fusion mediated by mitofusins. *Biochimica et Biophysica Acta (BBA) - Bioenergetics*. [Online] 1863 (8), 148913. Available from: doi:https://doi.org/10.1016/j.bbabio.2022.148913.

Palacios-Rápalo, S.N., De Jesús-González, L.A., Cordero-Rivera, C.D., Farfan-Morales, C.N., et al. (2021) Cholesterol-Rich Lipid Rafts as Platforms for SARS-CoV-2 Entry. *Frontiers in immunology*. [Online] 12, 796855. Available from: doi:10.3389/fimmu.2021.796855.

Pan, J., Heberle, F.A., Tristram-Nagle, S., Szymanski, M., et al. (2012) Molecular structures of fluid phase phosphatidylglycerol bilayers as determined by small angle neutron and X-ray scattering. *Biochimica et biophysica acta*. [Online] 1818 (9), 2135–2148. Available from: doi:10.1016/j.bbamem.2012.05.007.

Panja, S., Aich, P., Jana, B. & Basu, T. (2008) How does plasmid DNA penetrate cell membranes in artificial transformation process of Escherichia coli? *Molecular Membrane Biology*. 25,

411–422.
Panja, S., Saha, S., Jana, B. & Basu, T. (2006) Role of membrane potential on artificial transformation of E. coli with plasmid DNA. *Journal of biotechnology*. [Online] 127 (1), 14–20. Available from: doi:10.1016/j.jbiotec.2006.06.008.
Pannuzzo, M., McDargh, Z.A. & Deserno, M. (2018) The role of scaffold reshaping and disassembly in dynamin driven membrane fission Michael M Kozlov & Vivek Malhotra (eds.). *eLife*. [Online] 7, e39441. Available from: doi:10.7554/eLife.39441.
Papasergi-Scott, M.M., Pérez-Hernández, G., Batebi, H., Gao, Y., et al. (2024) Time-resolved cryo-EM of G-protein activation by a GPCR. *Nature*. [Online] 629 (8014), 1182–1191. Available from: doi:10.1038/s41586-024-07153-1.
Paradies, G., Paradies, V., De Benedictis, V., Ruggiero, F.M., et al. (2014) Functional role of cardiolipin in mitochondrial bioenergetics. *Biochimica et Biophysica Acta (BBA) - Bioenergetics*. [Online] 1837 (4), 408–417. Available from: doi:https://doi.org/10.1016/j.bbabio.2013.10.006.
Pasquina-Lemonche, L., Burns, J., Turner, R.D., Kumar, S., et al. (2020) The architecture of the Gram-positive bacterial cell wall. *Nature*. [Online] 582 (7811), 294–297. Available from: doi:10.1038/s41586-020-2236-6.
Passmore, L.A. & Russo, C.J. (2016) Specimen Preparation for High-Resolution Cryo-EM. *Methods in enzymology*. [Online] 579, 51–86. Available from: doi:10.1016/bs.mie.2016.04.011.
Pattipeiluhu, R., Zeng, Y., Hendrix, M.M.R.M., Voets, I.K., et al. (2024) Liquid crystalline inverted lipid phases encapsulating siRNA enhance lipid nanoparticle mediated transfection. *Nature Communications*. [Online] 15 (1), 1303. Available from: doi:10.1038/s41467-024-45666-5.
Pauling, L., Corey, R.B. & Branson, H.R. (1951) The structure of proteins; two hydrogen-bonded helical configurations of the polypeptide chain. *Proceedings of the National Academy of Sciences of the United States of America*. [Online] 37 (4), 205–211. Available from: doi:10.1073/pnas.37.4.205.
Paysan-Lafosse, T., Blum, M., Chuguransky, S., Grego, T., et al. (2023) InterPro in 2022. *Nucleic Acids Research*. [Online] 51 (D1), D418–D427. Available from: doi:10.1093/nar/gkac993.
Peet, M.J., Henderson, R. & Russo, C.J. (2019) The energy dependence of contrast and damage in electron cryomicroscopy of biological molecules. *Ultramicroscopy*. [Online] 203, 125–131. Available from: doi:10.1016/j.ultramic.2019.02.007.
Peng, J., Dong, W., Chen, Y., Mo, R., et al. (2006) Dusty protein kinases: primary structure, gene evolution, tissue specific expression and unique features of the catalytic domain. *Biochimica et biophysica acta*. [Online] 1759 (11–12), 562–572. Available from: doi:10.1016/j.bbaexp.2006.10.004.
Pettersen, E.F., Goddard, T.D., Huang, C.C., Couch, G.S., et al. (2004) UCSF Chimera--a visualization system for exploratory research and analysis. *Journal of computational chemistry*. [Online] 25 (13), 1605–1612. Available from: doi:10.1002/jcc.20084.
Petty, K.J. (1996) Metal-Chelate Affinity Chromatography. *Current Protocols in Molecular Biology*. [Online] 36 (1), 10.11.10-10.11.24. Available from: doi:https://doi.org/10.1002/0471142727.mb1011bs36.
Pfitzner, A.-K., Mercier, V., Jiang, X., Moser von Filseck, J., et al. (2020) An ESCRT-III Polymerization Sequence Drives Membrane Deformation and Fission. *Cell*. [Online] 182 (5), 1140-1155.e18. Available from: doi:10.1016/j.cell.2020.07.021.
Phillips, D.A., Zacharoff, L.A., Hampton, C.M., Chong, G.W., et al. (2021) A bacterial membrane

sculpting protein with BAR domain-like activity. *eLife*. [Online] 10. Available from: doi:10.7554/eLife.60049.

Pöhnl, M., Trollmann, M.F.W. & Böckmann, R.A. (2023) Nonuniversal impact of cholesterol on membranes mobility, curvature sensing and elasticity. *Nature Communications*. [Online] 14 (1), 8038. Available from: doi:10.1038/s41467-023-43892-x.

Pollard, T.D. & Borisy, G.G. (2003) Cellular Motility Driven by Assembly and Disassembly of Actin Filaments. *Cell*. [Online] 112 (4), 453–465. Available from: doi:https://doi.org/10.1016/S0092-8674(03)00120-X.

Poojari, C.S., Scherer, K.C. & Hub, J.S. (2021) Free energies of membrane stalk formation from a lipidomics perspective. *Nature Communications*. [Online] 12 (1), 6594. Available from: doi:10.1038/s41467-021-26924-2.

Posey, A.E., Ross, K.A., Bagheri, M., Lanum, E.N., et al. (2023) The variable domain from dynamin-related protein 1 promotes liquid–liquid phase separation that enhances its interaction with cardiolipin-containing membranes. *Protein Science*. [Online] 32 (11), e4787. Available from: doi:https://doi.org/10.1002/pro.4787.

Praefcke, G.J.K. & McMahon, H.T. (2004) The dynamin superfamily: universal membrane tubulation and fission molecules? *Nature Reviews Molecular Cell Biology*. [Online] 5 (2), 133–147. Available from: doi:10.1038/nrm1313.

Prakash, B., Praefcke, G.J.K., Renault, L., Wittinghofer, A., et al. (2000) Structure of human guanylate-binding protein 1 representing a unique class of GTP-binding proteins. *Nature*. [Online] 403 (6769), 567–571. Available from: doi:10.1038/35000617.

Prichard, K.L., O'Brien, N.S., Murcia, S.R., Baker, J.R., et al. (2022) Role of Clathrin and Dynamin in Clathrin Mediated Endocytosis/Synaptic Vesicle Recycling and Implications in Neurological Diseases. *Frontiers in Cellular Neuroscience*. 15.

Procházka, D., Slanináková, T., Olha, J., Rošinec, A., et al. (2024) AlphaFind: discover structure similarity across the proteome in AlphaFold DB. *Nucleic Acids Research*. [Online] 52 (W1), W182–W186. Available from: doi:10.1093/nar/gkae397.

Pucadyil, T.J. & Schmid, S.L. (2008) Real-time visualization of dynamin-catalyzed membrane fission and vesicle release. *Cell*. [Online] 135 (7), 1263–1275. Available from: doi:10.1016/j.cell.2008.11.020.

Punjani, A. & Fleet, D.J. (2023) 3DFlex: determining structure and motion of flexible proteins from cryo-EM. *Nature Methods*. [Online] 20 (6), 860–870. Available from: doi:10.1038/s41592-023-01853-8.

Punjani, A., Rubinstein, J.L., Fleet, D.J. & Brubaker, M.A. (2017) cryoSPARC: algorithms for rapid unsupervised cryo-EM structure determination. *Nature Methods*. [Online] 14 (3), 290–296. Available from: doi:10.1038/nmeth.4169.

Punjani, A., Zhang, H. & Fleet, D.J. (2020) Non-uniform refinement: adaptive regularization improves single-particle cryo-EM reconstruction. *Nature Methods*. [Online] 17 (12), 1214–1221. Available from: doi:10.1038/s41592-020-00990-8.

Qi, Y., Yan, L., Yu, C., Guo, X., et al. (2016) Structures of human mitofusin 1 provide insight into mitochondrial tethering. *Journal of Cell Biology*. [Online] 215 (5), 621–629. Available from: doi:10.1083/jcb.201609019.

Qiu, X.-B., Shao, Y.-M., Miao, S. & Wang, L. (2006) The diversity of the DnaJ/Hsp40 family, the crucial partners for Hsp70 chaperones. *Cellular and molecular life sciences : CMLS*. [Online] 63 (22), 2560–2570. Available from: doi:10.1007/s00018-006-6192-6.

Raetz, C.R. & Dowhan, W. (1990) Biosynthesis and function of phospholipids in Escherichia coli. *Journal of Biological Chemistry*. [Online] 265 (3), 1235–1238. Available from:

doi:https://doi.org/10.1016/S0021-9258(19)40001-X.
Raetz, C.R.H. & Whitfield, C. (2002) Lipopolysaccharide endotoxins. *Annual review of biochemistry*. [Online] 71, 635–700. Available from: doi:10.1146/annurev.biochem.71.110601.135414.
Rajput, S., Yao, S., Keizer, D.W., Sani, M.-A., et al. (2022) NMR spectroscopy of lipidic cubic phases. *Biophysical reviews*. [Online] 14 (1), 67–74. Available from: doi:10.1007/s12551-021-00900-y.
Ramachandran, R. & Schmid, S.L. (2018) The dynamin superfamily. *Current Biology*. [Online] 28 (8), R411–R416. Available from: doi:https://doi.org/10.1016/j.cub.2017.12.013.
Ramezanpour, M. & Tieleman, D.P. (2022) Computational Insights into the Role of Cholesterol in Inverted Hexagonal Phase Stabilization and Endosomal Drug Release. *Langmuir : the ACS journal of surfaces and colloids*. [Online] 38 (24), 7462–7471. Available from: doi:10.1021/acs.langmuir.2c00430.
Ramírez-Aportela, E., Mota, J., Conesa, P., Carazo, J.M., et al. (2019) DeepRes: a new deep-learning- and aspect-based local resolution method for electron-microscopy maps. *IUCrJ*. [Online] 6 (Pt 6), 1054–1063. Available from: doi:10.1107/S2052252519011692.
Ramírez-Aportela, E., Vilas, J.L., Glukhova, A., Melero, R., et al. (2020) Automatic local resolution-based sharpening of cryo-EM maps. *Bioinformatics*. [Online] 36 (3), 765–772. Available from: doi:10.1093/bioinformatics/btz671.
Ramlaul, K., Feng, Z., Canavan, C., de Martín Garrido, N., et al. (2023) A 3D-printed flow-cell for on-grid purification of electron microscopy samples directly from lysate. *Journal of Structural Biology*. [Online] 215 (3), 107999. Available from: doi:https://doi.org/10.1016/j.jsb.2023.107999.
Rast, A., Schaffer, M., Albert, S., Wan, W., et al. (2019) Biogenic regions of cyanobacterial thylakoids form contact sites with the plasma membrane. *Nature Plants*. [Online] 5 (4), 436–446. Available from: doi:10.1038/s41477-019-0399-7.
Renaud, J.-P., Chari, A., Ciferri, C., Liu, W., et al. (2018) Cryo-EM in drug discovery: achievements, limitations and prospects. *Nature Reviews Drug Discovery*. [Online] 17 (7), 471–492. Available from: doi:10.1038/nrd.2018.77.
Rennie, M.L., McKelvie, S.A., Bulloch, E.M.M. & Kingston, R.L. (2014) Transient Dimerization of Human MxA Promotes GTP Hydrolysis, Resulting in a Mechanical Power Stroke. *Structure*. [Online] 22 (10), 1433–1445. Available from: doi:https://doi.org/10.1016/j.str.2014.08.015.
Reubold, T.F., Faelber, K., Plattner, N., Posor, Y., et al. (2015) Crystal structure of the dynamin tetramer. *Nature*. [Online] 525 (7569), 404–408. Available from: doi:10.1038/nature14880.
Rexroth, S., Mullineaux, C.W., Ellinger, D., Sendtko, E., et al. (2011) The plasma membrane of the cyanobacterium Gloeobacter violaceus contains segregated bioenergetic domains. *The Plant cell*. [Online] 23 (6), 2379–2390. Available from: doi:10.1105/tpc.111.085779.
Richter, K., Brar, S., Ray, M., Pisitkun, P., et al. (2009) Speckled-like pattern in the germinal center (SLIP-GC), a nuclear GTPase expressed in activation-induced deaminase-expressing lymphomas and germinal center B cells. *The Journal of biological chemistry*. [Online] 284 (44), 30652–30661. Available from: doi:10.1074/jbc.M109.014506.
Risser, D.D. (2023) Hormogonium Development and Motility in Filamentous Cyanobacteria. *Applied and environmental microbiology*. [Online] 89 (6), e0039223. Available from: doi:10.1128/aem.00392-23.
Risser, D.D., Chew, W.G. & Meeks, J.C. (2014) Genetic characterization of the hmp locus, a

chemotaxis-like gene cluster that regulates hormogonium development and motility in Nostoc punctiforme. *Molecular microbiology*. [Online] 92 (2), 222–233. Available from: doi:10.1111/mmi.12552.

Risser, D.D. & Meeks, J.C. (2013) Comparative transcriptomics with a motility-deficient mutant leads to identification of a novel polysaccharide secretion system in Nostoc punctiforme. *Molecular microbiology*. [Online] 87 (4), 884–893. Available from: doi:10.1111/mmi.12138.

Risser, D.D., Wong, F.C.Y. & Meeks, J.C. (2012) Biased inheritance of the protein PatN frees vegetative cells to initiate patterned heterocyst differentiation. *Proceedings of the National Academy of Sciences*. [Online] 109 (38), 15342–15347. Available from: doi:10.1073/pnas.1207530109.

Rochon, K., Bauer, B.L., Roethler, N.A., Buckley, Y., et al. (2024) Structural basis for regulated assembly of the mitochondrial fission GTPase Drp1. *Nature Communications*. [Online] 15 (1), 1328. Available from: doi:10.1038/s41467-024-45524-4.

Rodríguez-García, R., Volkov, V.A., Chen, C.-Y., Katrukha, E.A., et al. (2020) Mechanisms of Motor-Independent Membrane Remodeling Driven by Dynamic Microtubules. *Current Biology*. [Online] 30 (6), 972-987.e12. Available from: doi:https://doi.org/10.1016/j.cub.2020.01.036.

Rohou, A. & Grigorieff, N. (2015) CTFFIND4: Fast and accurate defocus estimation from electron micrographs. *Journal of structural biology*. [Online] 192 (2), 216–221. Available from: doi:10.1016/j.jsb.2015.08.008.

Rosenthal, P.B. & Henderson, R. (2003) Optimal Determination of Particle Orientation, Absolute Hand, and Contrast Loss in Single-particle Electron Cryomicroscopy. *Journal of Molecular Biology*. [Online] 333 (4), 721–745. Available from: doi:https://doi.org/10.1016/j.jmb.2003.07.013.

De Rosier, D.J. & Klug, A. (1968) Reconstruction of Three Dimensional Structures from Electron Micrographs. *Nature*. [Online] 217 (5124), 130–134. Available from: doi:10.1038/217130a0.

Ruban, A. V (2016) Nonphotochemical Chlorophyll Fluorescence Quenching: Mechanism and Effectiveness in Protecting Plants from Photodamage. *Plant Physiology*. [Online] 170 (4), 1903–1916. Available from: doi:10.1104/pp.15.01935.

Ruskin, A.I., Yu, Z. & Grigorieff, N. (2013) Quantitative characterization of electron detectors for transmission electron microscopy. *Journal of structural biology*. [Online] 184 (3), 385–393. Available from: doi:10.1016/j.jsb.2013.10.016.

Russo, C.J. & Passmore, L.A. (2014) Electron microscopy: Ultrastable gold substrates for electron cryomicroscopy. *Science (New York, N.Y.)*. [Online] 346 (6215), 1377–1380. Available from: doi:10.1126/science.1259530.

Russo, C.J. & Passmore, L.A. (2016) Progress towards an optimal specimen support for electron cryomicroscopy. *Current Opinion in Structural Biology*. [Online] 37, 81–89. Available from: doi:https://doi.org/10.1016/j.sbi.2015.12.007.

Salata, G.C., Malagó, I.D. & Lopes, L.B. (2022) A Lipid-Based In Situ-Forming Hexagonal Phase for Prolonged Retention and Drug Release in the Breast Tissue. *AAPS PharmSciTech*. [Online] 23 (7), 260. Available from: doi:10.1208/s12249-022-02411-9.

Sasaki, Y., Kubota, R. & Minami, T. (2021) Molecular self-assembled chemosensors and their arrays. *Coordination Chemistry Reviews*. [Online] 429, 213607. Available from: doi:https://doi.org/10.1016/j.ccr.2020.213607.

Sato, N., Kamimura, R. & Tsuzuki, M. (2016) Dispensability of a sulfolipid for photoautotrophic

cell growth and photosynthesis in a marine cyanobacterium, Synechococcus sp. PCC 7002. *Biochemical and biophysical research communications*. [Online] 477 (4), 854–860. Available from: doi:10.1016/j.bbrc.2016.06.148.

Sawant, P., Eissenberger, K., Karier, L., Mascher, T., et al. (2016) A dynamin-like protein involved in bacterial cell membrane surveillance under environmental stress. *Environmental microbiology*. [Online] 18 (8), 2705–2720. Available from: doi:10.1111/1462-2920.13110.

Schaffer, M., Mahamid, J., Engel, B.D., Laugks, T., et al. (2017) Optimized cryo-focused ion beam sample preparation aimed at in situ structural studies of membrane proteins. *Journal of Structural Biology*. [Online] 197 (2), 73–82. Available from: doi:https://doi.org/10.1016/j.jsb.2016.07.010.

Scheffers, D.-J. & Pinho, M.G. (2005) Bacterial cell wall synthesis: new insights from localization studies. *Microbiology and molecular biology reviews : MMBR*. [Online] 69 (4), 585–607. Available from: doi:10.1128/MMBR.69.4.585-607.2005.

Scheres, S.H. (2014) Beam-induced motion correction for sub-megadalton cryo-EM particles. *eLife*. [Online] 3, e03665. Available from: doi:10.7554/eLife.03665.

Scheres, S.H.W. (2016) Processing of Structurally Heterogeneous Cryo-EM Data in RELION. *Methods in enzymology*. [Online] 579, 125–157. Available from: doi:10.1016/bs.mie.2016.04.012.

Scheres, S.H.W. (2012) RELION: implementation of a Bayesian approach to cryo-EM structure determination. *Journal of structural biology*. [Online] 180 (3), 519–530. Available from: doi:10.1016/j.jsb.2012.09.006.

Scheres, S.H.W. (2015) Semi-automated selection of cryo-EM particles in RELION-1.3. *Journal of Structural Biology*. [Online] 189 (2), 114–122. Available from: doi:https://doi.org/10.1016/j.jsb.2014.11.010.

Scheres, S.H.W. & Chen, S. (2012) Prevention of overfitting in cryo-EM structure determination. *Nature Methods*. [Online] 9 (9), 853–854. Available from: doi:10.1038/nmeth.2115.

Scheres, S.H.W., Gao, H., Valle, M., Herman, G.T., et al. (2007) Disentangling conformational states of macromolecules in 3D-EM through likelihood optimization. *Nature Methods*. [Online] 4 (1), 27–29. Available from: doi:10.1038/nmeth992.

Scheres, S.H.W., Valle, M., Nuñez, R., Sorzano, C.O.S., et al. (2005) Maximum-likelihood multi-reference refinement for electron microscopy images. *Journal of molecular biology*. [Online] 348 (1), 139–149. Available from: doi:10.1016/j.jmb.2005.02.031.

Schlame, M. (2021) Protein crowding in the inner mitochondrial membrane. *Biochimica et Biophysica Acta (BBA) - Bioenergetics*. [Online] 1862 (1), 148305. Available from: doi:https://doi.org/10.1016/j.bbabio.2020.148305.

Schlimpert, S., Wasserstrom, S., Chandra, G., Bibb, M.J., et al. (2017) Two dynamin-like proteins stabilize FtsZ rings during Streptomyces sporulation. *Proceedings of the National Academy of Sciences of the United States of America*. [Online] 114 (30), E6176–E6183. Available from: doi:10.1073/pnas.1704612114.

Schwab, J., Kimanius, D., Burt, A., Dendooven, T., et al. (2024) DynaMight: estimating molecular motions with improved reconstruction from cryo-EM images. *Nature Methods*. [Online] Available from: doi:10.1038/s41592-024-02377-5.

Schwarz, D.S. & Blower, M.D. (2016) The endoplasmic reticulum: structure, function and response to cellular signaling. *Cellular and molecular life sciences : CMLS*. [Online] 73 (1), 79–94. Available from: doi:10.1007/s00018-015-2052-6.

Schwechheimer, C. & Kuehn, M.J. (2015) Outer-membrane vesicles from Gram-negative bacteria: biogenesis and functions. *Nature Reviews Microbiology*. [Online] 13 (10), 605–619. Available from: doi:10.1038/nrmicro3525.

Semenova, G.A. (1999) The Relationship between the Transformation of Thylakoid Acyl Lipids and the Formation of Tubular Lipid Aggregates Visible on Fracture Faces. *Journal of Plant Physiology*. [Online] 155 (6), 669–677. Available from: doi:https://doi.org/10.1016/S0176-1617(99)80081-9.

Serwas, D., Akamatsu, M., Moayed, A., Vegesna, K., et al. (2022) Mechanistic insights into actin force generation during vesicle formation from cryo-electron tomography. *Developmental Cell*. [Online] 57 (9), 1132-1145.e5. Available from: doi:https://doi.org/10.1016/j.devcel.2022.04.012.

Sexton, D.L., Burgold, S., Schertel, A. & Tocheva, E.I. (2022) Super-resolution confocal cryo-CLEM with cryo-FIB milling for in situ imaging of Deinococcus radiodurans. *Current Research in Structural Biology*. [Online] 4, 1–9. Available from: doi:https://doi.org/10.1016/j.crstbi.2021.12.001.

Sezgin, E., Levental, I., Mayor, S. & Eggeling, C. (2017) The mystery of membrane organization: composition, regulation and roles of lipid rafts. *Nature Reviews Molecular Cell Biology*. [Online] 18 (6), 361–374. Available from: doi:10.1038/nrm.2017.16.

Shambhavi, G., Kumar, C.P. & Manjula, R. (2021) Peptidoglycan: Structure, Synthesis, and Regulation. *EcoSal Plus*. [Online] 9 (2). Available from: doi:10.1128/ecosalplus.ESP-0010-2020.

Shatsky, M., Hall, R.J., Brenner, S.E. & Glaeser, R.M. (2009) A method for the alignment of heterogeneous macromolecules from electron microscopy. *Journal of structural biology*. [Online] 166 (1), 67–78. Available from: doi:10.1016/j.jsb.2008.12.008.

Shi, D. & Huang, R. (2022) Analysis and comparison of electron radiation damage assessments in Cryo-EM by single particle analysis and micro-crystal electron diffraction. *Frontiers in molecular biosciences*. [Online] 9, 988928. Available from: doi:10.3389/fmolb.2022.988928.

Shi, L., Yang, C., Zhang, M., Li, K., et al. (2024) Dissecting the mechanism of atlastin-mediated homotypic membrane fusion at the single-molecule level. *Nature Communications*. [Online] 15 (1), 2488. Available from: doi:10.1038/s41467-024-46919-z.

Shi, X., Chen, M., Yu, Z., Bell, J.M., et al. (2019) In situ structure and assembly of the multidrug efflux pump AcrAB-TolC. *Nature Communications*. [Online] 10 (1), 2635. Available from: doi:10.1038/s41467-019-10512-6.

Shinji, H., Sasaki, N., Hamim, I., Itoh, Y., et al. (2023) Dynamin-related protein 2 interacts with the membrane-associated methyltransferase domain of plantago asiatica mosaic virus replicase and promotes viral replication. *Virus Research*. [Online] 331, 199128. Available from: doi:https://doi.org/10.1016/j.virusres.2023.199128.

Siegel, D.P., Green, W.J. & Talmon, Y. (1994) The mechanism of lamellar-to-inverted hexagonal phase transitions: a study using temperature-jump cryo-electron microscopy. *Biophysical Journal*. [Online] 66 (2, Part 1), 402–414. Available from: doi:https://doi.org/10.1016/S0006-3495(94)80790-8.

Sievers, F., Wilm, A., Dineen, D., Gibson, T.J., et al. (2011) Fast, scalable generation of high-quality protein multiple sequence alignments using Clustal Omega. *Molecular systems biology*. [Online] 7, 539. Available from: doi:10.1038/msb.2011.75.

Sigworth, F.J. (1998) A Maximum-Likelihood Approach to Single-Particle Image Refinement. *Journal of Structural Biology*. [Online] 122 (3), 328–339. Available from:

doi:https://doi.org/10.1006/jsbi.1998.4014.
Sigworth, F.J. (2015) Principles of cryo-EM single-particle image processing. *Microscopy*. [Online] 65 (1), 57–67. Available from: doi:10.1093/jmicro/dfv370.
Silhavy, T.J., Kahne, D. & Walker, S. (2010) The bacterial cell envelope. *Cold Spring Harbor perspectives in biology*. [Online] 2 (5), a000414. Available from: doi:10.1101/cshperspect.a000414.
Simidjiev, I., Stoylova, S., Amenitsch, H., Jávorfi, T., et al. (2000) Self-assembly of large, ordered lamellae from non-bilayer lipids and integral membrane proteins in vitro. *Proceedings of the National Academy of Sciences*. [Online] 97 (4), 1473–1476. Available from: doi:10.1073/pnas.97.4.1473.
Simunovic, M., Evergren, E., Callan-Jones, A. & Bassereau, P. (2019) Curving Cells Inside and Out: Roles of BAR Domain Proteins in Membrane Shaping and Its Cellular Implications. *Annual Review of Cell and Developmental Biology*. [Online] 35 (Volume 35, 2019), 111–129. Available from: doi:https://doi.org/10.1146/annurev-cellbio-100617-060558.
Singaravelu, K., Nelson, C., Bakowski, D., de Brito, O.M., et al. (2011) Mitofusin 2 regulates STIM1 migration from the Ca2+ store to the plasma membrane in cells with depolarized mitochondria. *The Journal of biological chemistry*. [Online] 286 (14), 12189–12201. Available from: doi:10.1074/jbc.M110.174029.
Singer, S.J. & Nicolson, G.L. (1972) The fluid mosaic model of the structure of cell membranes. *Science (New York, N.Y.)*. [Online] 175 (4023), 720–731. Available from: doi:10.1126/science.175.4023.720.
Sohlenkamp, C. & Geiger, O. (2016) Bacterial membrane lipids: diversity in structures and pathways. *FEMS Microbiology Reviews*. [Online] 40 (1), 133–159. Available from: doi:10.1093/femsre/fuv008.
Song, Q., Hu, Y., Yin, A., Wang, H., et al. (2022) DNA Holliday Junction: History, Regulation and Bioactivity. *International journal of molecular sciences*. [Online] 23 (17). Available from: doi:10.3390/ijms23179730.
Sousa, R., Liao, H.-S., Cuéllar, J., Jin, S., et al. (2016) Clathrin-coat disassembly illuminates the mechanisms of Hsp70 force generation. *Nature Structural & Molecular Biology*. [Online] 23 (9), 821–829. Available from: doi:10.1038/nsmb.3272.
Splitt, S.D. & Risser, D.D. (2016) The non-metabolizable sucrose analog sucralose is a potent inhibitor of hormogonium differentiation in the filamentous cyanobacterium Nostoc punctiforme. *Archives of microbiology*. [Online] 198 (2), 137–147. Available from: doi:10.1007/s00203-015-1171-7.
Stachowiak, J.C., Schmid, E.M., Ryan, C.J., Ann, H.S., et al. (2012) Membrane bending by protein–protein crowding. *Nature Cell Biology*. [Online] 14 (9), 944–949. Available from: doi:10.1038/ncb2561.
Stepanyants, N., Macdonald, P.J., Francy, C.A., Mears, J.A., et al. (2015) Cardiolipin's propensity for phase transition and its reorganization by dynamin-related protein 1 form a basis for mitochondrial membrane fission. *Molecular biology of the cell*. [Online] 26 (17), 3104–3116. Available from: doi:10.1091/mbc.E15-06-0330.
Stowell, M.H.B., Marks, B., Wigge, P. & McMahon, H.T. (1999) Nucleotide-dependent conformational changes in dynamin: evidence for a mechanochemical molecular spring. *Nature Cell Biology*. [Online] 1 (1), 27–32. Available from: doi:10.1038/8997.
Strelak, D., Jiménez-Moreno, A., Vilas, J.L., Ramírez-Aportela, E., et al. (2021) Advances in Xmipp for Cryo-Electron Microscopy: From Xmipp to Scipion. *Molecules (Basel, Switzerland)*. [Online] 26 (20). Available from: doi:10.3390/molecules26206224.

Studier, F.W. & Moffatt, B.A. (1986) Use of bacteriophage T7 RNA polymerase to direct selective high-level expression of cloned genes. *Journal of Molecular Biology*. [Online] 189 (1), 113–130. Available from: doi:https://doi.org/10.1016/0022-2836(86)90385-2.

Subbotin, V. & Fiksel, G. (2023) Exploring the Lipid World Hypothesis: A Novel Scenario of Self-Sustained Darwinian Evolution of the Liposomes. *Astrobiology*. [Online] 23 (3), 344–357. Available from: doi:10.1089/ast.2021.0161.

Sun, C., Gonzalez, B. & Jiang, W. (2022) Helical Indexing in Real Space. *Scientific Reports*. [Online] 12 (1), 8162. Available from: doi:10.1038/s41598-022-11382-7.

Sun, M., Azumaya, C.M., Tse, E., Bulkley, D.P., et al. (2021) Practical considerations for using K3 cameras in CDS mode for high-resolution and high-throughput single particle cryo-EM. *Journal of Structural Biology*. [Online] 213 (3), 107745. Available from: doi:https://doi.org/10.1016/j.jsb.2021.107745.

Sun, X., Zhou, Y., Zhang, R., Wang, Z., et al. (2020) Dstyk mutation leads to congenital scoliosis-like vertebral malformations in zebrafish via dysregulated mTORC1/TFEB pathway. *Nature Communications*. [Online] 11 (1), 479. Available from: doi:10.1038/s41467-019-14169-z.

Sundborger, A.C., Fang, S., Heymann, J.A., Ray, P., et al. (2014) A dynamin mutant defines a superconstricted prefission state. *Cell reports*. [Online] 8 (3), 734–742. Available from: doi:10.1016/j.celrep.2014.06.054.

Svitkina, T. (2018) The Actin Cytoskeleton and Actin-Based Motility. *Cold Spring Harbor perspectives in biology*. [Online] 10 (1). Available from: doi:10.1101/cshperspect.a018267.

Szilágyi, A., Selstam, E. & Åkerlund, H.-E. (2008) Laurdan fluorescence spectroscopy in the thylakoid bilayer: The effect of violaxanthin to zeaxanthin conversion on the galactolipid dominated lipid environment. *Biochimica et Biophysica Acta (BBA) - Biomembranes*. [Online] 1778 (1), 348–355. Available from: doi:https://doi.org/10.1016/j.bbamem.2007.10.006.

Szule, J.A., Fuller, N.L. & Rand, P.R. (2002) The Effects of Acyl Chain Length and Saturation of Diacylglycerols and Phosphatidylcholines on Membrane Monolayer Curvature. *Biophysical Journal*. [Online] 83 (2), 977–984. Available from: doi:https://doi.org/10.1016/S0006-3495(02)75223-5.

Taguchi, N., Ishihara, N., Jofuku, A., Oka, T., et al. (2007) Mitotic phosphorylation of dynamin-related GTPase Drp1 participates in mitochondrial fission. *The Journal of biological chemistry*. [Online] 282 (15), 11521–11529. Available from: doi:10.1074/jbc.M607279200.

Tamura, K., Stecher, G. & Kumar, S. (2021) MEGA11: Molecular Evolutionary Genetics Analysis Version 11. *Molecular Biology and Evolution*. [Online] 38 (7), 3022–3027. Available from: doi:10.1093/molbev/msab120.

Taniguchi, S., Kasho, K., Ozaki, S. & Katayama, T. (2019) Escherichia coli CrfC Protein, a Nucleoid Partition Factor, Localizes to Nucleoid Poles via the Activities of Specific Nucleoid-Associated Proteins. *Frontiers in microbiology*. [Online] 10, 72. Available from: doi:10.3389/fmicb.2019.00072.

Tegunov, D. & Cramer, P. (2019) Real-time cryo-electron microscopy data preprocessing with Warp. *Nature methods*. [Online] 16 (11), 1146–1152. Available from: doi:10.1038/s41592-019-0580-y.

Tenchov, B.G., MacDonald, R.C. & Siegel, D.P. (2006) Cubic Phases in Phosphatidylcholine-Cholesterol Mixtures: Cholesterol as Membrane "Fusogen". *Biophysical Journal*. [Online]

91 (7), 2508–2516. Available from: doi:https://doi.org/10.1529/biophysj.106.083766.
Tetsch, L. & Jung, K. (2009) How are signals transduced across the cytoplasmic membrane? Transport proteins as transmitter of information. *Amino acids*. [Online] 37 (3), 467–477. Available from: doi:10.1007/s00726-009-0235-x.
Thayer, S.S. & Björkman, O. (1990) Leaf Xanthophyll content and composition in sun and shade determined by HPLC. *Photosynthesis Research*. [Online] 23 (3), 331–343. Available from: doi:10.1007/BF00034864.
Thompson, R.F., Walker, M., Siebert, C.A., Muench, S.P., et al. (2016) An introduction to sample preparation and imaging by cryo-electron microscopy for structural biology. *Methods*. [Online] 100, 3–15. Available from: doi:https://doi.org/10.1016/j.ymeth.2016.02.017.
Tietz, S., Leuenberger, M., Höhner, R., Olson, A.H., et al. (2020) A proteoliposome-based system reveals how lipids control photosynthetic light harvesting. *Journal of Biological Chemistry*. [Online] 295 (7), 1857–1866. Available from: doi:https://doi.org/10.1074/jbc.RA119.011707.
Tietz, S., Puthiyaveetil, S., Enlow, H.M., Yarbrough, R., et al. (2015) Functional Implications of Photosystem II Crystal Formation in Photosynthetic Membranes*. *Journal of Biological Chemistry*. [Online] 290 (22), 14091–14106. Available from: doi:https://doi.org/10.1074/jbc.M114.619841.
Timofeev, V. & Samygina, V. (2023) Protein Crystallography: Achievements and Challenges. *Crystals*. [Online]. 13 (1). Available from: doi:10.3390/cryst13010071.
Tivol, W.F., Briegel, A. & Jensen, G.J. (2008) An improved cryogen for plunge freezing. *Microscopy and microanalysis : the official journal of Microscopy Society of America, Microbeam Analysis Society, Microscopical Society of Canada*. [Online] 14 (5), 375–379. Available from: doi:10.1017/S1431927608080781.
Toader, B., Sigworth, F.J. & Lederman, R.R. (2023) Methods for Cryo-EM Single Particle Reconstruction of Macromolecules Having Continuous Heterogeneity. *Journal of molecular biology*. [Online] 435 (9), 168020. Available from: doi:10.1016/j.jmb.2023.168020.
Toombes, G.E.S., Finnefrock, A.C., Tate, M.W. & Gruner, S.M. (2002) Determination of Lα–HII Phase Transition Temperature for 1,2-Dioleoyl-sn-Glycero-3-Phosphatidylethanolamine. *Biophysical Journal*. [Online] 82 (5), 2504–2510. Available from: doi:https://doi.org/10.1016/S0006-3495(02)75593-8.
Toyoshima, C. & Unwin, N. (1988) Contrast transfer for frozen-hydrated specimens: Determination from pairs of defocused images. *Ultramicroscopy*. [Online] 25 (4), 279–291. Available from: doi:https://doi.org/10.1016/0304-3991(88)90003-4.
Trochet, D. & Bitoun, M. (2021) A review of Dynamin 2 involvement in cancers highlights a promising therapeutic target. *Journal of Experimental & Clinical Cancer Research*. [Online] 40 (1), 238. Available from: doi:10.1186/s13046-021-02045-y.
Tsvetkova, N.M., Horváth, I., Török, Z., Wolkers, W.F., et al. (2002) Small heat-shock proteins regulate membrane lipid polymorphism. *Proceedings of the National Academy of Sciences*. [Online] 99 (21), 13504–13509. Available from: doi:10.1073/pnas.192468399.
Tuijtel, M.W., Koster, A.J., Jakobs, S., Faas, F.G.A., et al. (2019) Correlative cryo super-resolution light and electron microscopy on mammalian cells using fluorescent proteins. *Scientific Reports*. [Online] 9 (1), 1369. Available from: doi:10.1038/s41598-018-37728-8.
Tyska, M.J. & Warshaw, D.M. (2002) The myosin power stroke. *Cell Motility*. [Online] 51 (1),

1–15. Available from: doi:https://doi.org/10.1002/cm.10014.
Uebe, R. & Schüler, D. (2016) Magnetosome biogenesis in magnetotactic bacteria. *Nature Reviews Microbiology*. [Online] 14 (10), 621–637. Available from: doi:10.1038/nrmicro.2016.99.
Varadi, M., Bertoni, D., Magana, P., Paramval, U., et al. (2024) AlphaFold Protein Structure Database in 2024: providing structure coverage for over 214 million protein sequences. *Nucleic acids research*. [Online] 52 (D1), D368–D375. Available from: doi:10.1093/nar/gkad1011.
Varlakhanova, N. V, Alvarez, F.J.D., Brady, T.M., Tornabene, B.A., et al. (2018) Structures of the fungal dynamin-related protein Vps1 reveal a unique, open helical architecture. *The Journal of cell biology*. [Online] 217 (10), 3608–3624. Available from: doi:10.1083/jcb.201712021.
De Vecchis, D., Cavellini, L., Baaden, M., Hénin, J., et al. (2017) A membrane-inserted structural model of the yeast mitofusin Fzo1. *Scientific Reports*. [Online] 7 (1), 10217. Available from: doi:10.1038/s41598-017-10687-2.
Venugopal, H., Mobbs, J., Taveneau, C., Fox, D.R., et al. (2024) Obtaining high-resolution cryo-EM structures using a common LaB6, 120-keV electron microscope equipped with a sub 200-keV optimised direct electron detector. *bioRxiv*. [Online] 2024.05.26.595910. Available from: doi:10.1101/2024.05.26.595910.
Vereb, G., Szöllősi, J., Matkó, J., Nagy, P., et al. (2003) Dynamic, yet structured: The cell membrane three decades after the Singer–Nicolson model. *Proceedings of the National Academy of Sciences*. [Online] 100 (14), 8053–8058. Available from: doi:10.1073/pnas.1332550100.
Vestal, D.J. & Jeyaratnam, J.A. (2011) The guanylate-binding proteins: emerging insights into the biochemical properties and functions of this family of large interferon-induced guanosine triphosphatase. *Journal of interferon & cytokine research : the official journal of the International Society for Interferon and Cytokine Research*. [Online] 31 (1), 89–97. Available from: doi:10.1089/jir.2010.0102.
Vilas, J.L., Gómez-Blanco, J., Conesa, P., Melero, R., et al. (2018) MonoRes: Automatic and Accurate Estimation of Local Resolution for Electron Microscopy Maps. *Structure*. [Online] 26 (2), 337-344.e4. Available from: doi:https://doi.org/10.1016/j.str.2017.12.018.
Villa, E., Schaffer, M., Plitzko, J.M. & Baumeister, W. (2013) Opening windows into the cell: focused-ion-beam milling for cryo-electron tomography. *Current Opinion in Structural Biology*. [Online] 23 (5), 771–777. Available from: doi:https://doi.org/10.1016/j.sbi.2013.08.006.
Vlieghe, A., Niort, K., Fumat, H., Guigner, J.-M., et al. (2023) Role of Lipids and Divalent Cations in Membrane Fusion Mediated by the Heptad Repeat Domain 1 of Mitofusin. *Biomolecules*. [Online] 13 (9). Available from: doi:10.3390/biom13091341.
Vollmer, W., Blanot, D. & De Pedro, M.A. (2008) Peptidoglycan structure and architecture. *FEMS Microbiology Reviews*. [Online] 32 (2), 149–167. Available from: doi:10.1111/j.1574-6976.2007.00094.x.
Vulović, M., Ravelli, R.B.G., van Vliet, L.J., Koster, A.J., et al. (2013) Image formation modeling in cryo-electron microscopy. *Journal of Structural Biology*. [Online] 183 (1), 19–32. Available from: doi:https://doi.org/10.1016/j.jsb.2013.05.008.
Wade, R.H. (1992) A brief look at imaging and contrast transfer. *Ultramicroscopy*. [Online] 46 (1), 145–156. Available from: doi:https://doi.org/10.1016/0304-3991(92)90011-8.

Wadsten-Hindrichsen, P., Bender, J., Unga, J. & Engström, S. (2007) Aqueous self-assembly of phytantriol in ternary systems: effect of monoolein, distearoylphosphatidylglycerol and three water-miscible solvents. *Journal of colloid and interface science*. [Online] 315 (2), 701–713. Available from: doi:10.1016/j.jcis.2007.07.011.

Wagner, F.R., Watanabe, R., Schampers, R., Singh, D., et al. (2020) Preparing samples from whole cells using focused-ion-beam milling for cryo-electron tomography. *Nature Protocols*. [Online] 15 (6), 2041–2070. Available from: doi:10.1038/s41596-020-0320-x.

Wagner, T., Merino, F., Stabrin, M., Moriya, T., et al. (2019) SPHIRE-crYOLO is a fast and accurate fully automated particle picker for cryo-EM. *Communications Biology*. [Online] 2 (1), 218. Available from: doi:10.1038/s42003-019-0437-z.

Wang, B., Zhang, L., Dai, T., Qin, Z., et al. (2021) Liquid–liquid phase separation in human health and diseases. *Signal Transduction and Targeted Therapy*. [Online] 6 (1), 290. Available from: doi:10.1038/s41392-021-00678-1.

Wang, C., Chen, Y., Hu, S. & Liu, X. (2023) Insights into the function of ESCRT and its role in enveloped virus infection. *Frontiers in Microbiology*. [Online] 14. Available from: doi:10.3389/fmicb.2023.1261651.

Wang, H.-W. & Wang, J.-W. (2017) How cryo-electron microscopy and X-ray crystallography complement each other. *Protein science : a publication of the Protein Society*. [Online] 26 (1), 32–39. Available from: doi:10.1002/pro.3022.

Wang, M., Guo, X., Yang, X., Zhang, B., et al. (2019) Mycobacterial dynamin-like protein IniA mediates membrane fission. *Nature Communications*. [Online] 10 (1), 3906. Available from: doi:10.1038/s41467-019-11860-z.

Warecki, B., Ling, X., Bast, I. & Sullivan, W. (2020) ESCRT-III-mediated membrane fusion drives chromosome fragments through nuclear envelope channels. *The Journal of cell biology*. [Online] 219 (3). Available from: doi:10.1083/jcb.201905091.

Watson, J.D. & Crick, F.H.C. (1953) Molecular Structure of Nucleic Acids: A Structure for Deoxyribose Nucleic Acid. *Nature*. [Online] 171 (4356), 737–738. Available from: doi:10.1038/171737a0.

Wei, H., Dandey, V.P., Zhang, Z., Raczkowski, A., et al. (2018) Optimizing “self-wicking” nanowire grids. *Journal of Structural Biology*. [Online] 202 (2), 170–174. Available from: doi:https://doi.org/10.1016/j.jsb.2018.01.001.

Weismehl, M., Chu, X., Kutsch, M., Lauterjung, P., et al. (2024) Structural insights into the activation mechanism of antimicrobial GBP1. *The EMBO journal*. [Online] 43 (4), 615–636. Available from: doi:10.1038/s44318-023-00023-y.

Welc, R., Luchowski, R., Kluczyk, D., Zubik-Duda, M., et al. (2021) Mechanisms shaping the synergism of zeaxanthin and PsbS in photoprotective energy dissipation in the photosynthetic apparatus of plants. *The Plant Journal*. [Online] 107 (2), 418–433. Available from: doi:https://doi.org/10.1111/tpj.15297.

Wenger, J., Klinglmayr, E., Fröhlich, C., Eibl, C., et al. (2013) Functional mapping of human dynamin-1-like GTPase domain based on x-ray structure analyses. *PloS one*. [Online] 8 (8), e71835. Available from: doi:10.1371/journal.pone.0071835.

Wiedemann, S. & Heckel, R. (2024) A deep learning method for simultaneous denoising and missing wedge reconstruction in cryogenic electron tomography. *Nature Communications*. [Online] 15 (1), 8255. Available from: doi:10.1038/s41467-024-51438-y.

Wiedemann, S. & Heckel, R. (2023) A Deep Learning Method for Simultaneous Denoising and Missing Wedge Reconstruction in Cryogenic Electron Tomography. *ArXiv*. abs/2311.0.

Wikström, M., Xie, J., Bogdanov, M., Mileykovskaya, E., et al. (2004) Monoglucosyldiacylglycerol, a foreign lipid, can substitute for phosphatidylethanolamine in essential membrane-associated functions in Escherichia coli. *The Journal of biological chemistry*. [Online] 279 (11), 10484–10493. Available from: doi:10.1074/jbc.M310183200.

Williams, D.B. & Carter, C.B. (2009a) *Amplitude Contrast BT - Transmission Electron Microscopy: A Textbook for Materials Science*. In: David B Williams & C Barry Carter (eds.). [Online]. Boston, MA, Springer US. pp. 371–388. Available from: doi:10.1007/978-0-387-76501-3_22.

Williams, D.B. & Carter, C.B. (2009b) Diffraction in TEM. In: *Transmission Electron Microscopy: A Textbook for Materials Science*. [Online]. Boston, MA, Springer US. pp. 197–209. Available from: doi:10.1007/978-0-387-76501-3_11.

Williams, D.B. & Carter, C.B. (2009c) *Elastic Scattering BT - Transmission Electron Microscopy: A Textbook for Materials Science*. In: David B Williams & C Barry Carter (eds.). [Online]. Boston, MA, Springer US. pp. 39–51. Available from: doi:10.1007/978-0-387-76501-3_3.

Williams, D.B. & Carter, C.B. (2009d) *Electron Sources BT - Transmission Electron Microscopy: A Textbook for Materials Science*. In: David B Williams & C Barry Carter (eds.). [Online]. Boston, MA, Springer US. pp. 73–89. Available from: doi:10.1007/978-0-387-76501-3_5.

Williams, D.B. & Carter, C.B. (2009e) *Inelastic Scattering and Beam Damage BT - Transmission Electron Microscopy: A Textbook for Materials Science*. In: David B Williams & C Barry Carter (eds.). [Online]. Boston, MA, Springer US. pp. 53–71. Available from: doi:10.1007/978-0-387-76501-3_4.

Williams, D.B. & Carter, C.B. (2009f) *Lenses, Apertures, and Resolution BT - Transmission Electron Microscopy: A Textbook for Materials Science*. In: David B Williams & C Barry Carter (eds.). [Online]. Boston, MA, Springer US. pp. 91–114. Available from: doi:10.1007/978-0-387-76501-3_6.

Williams, D.B. & Carter, C.B. (2009g) Phase-Contrast Images. In: *Transmission Electron Microscopy: A Textbook for Materials Science*. [Online]. Boston, MA, Springer US. pp. 389–405. Available from: doi:10.1007/978-0-387-76501-3_23.

Williams, D.B. & Carter, C.B. (2009h) *Pumps and Holders BT - Transmission Electron Microscopy: A Textbook for Materials Science*. In: David B Williams & C Barry Carter (eds.). [Online]. Boston, MA, Springer US. pp. 127–140. Available from: doi:10.1007/978-0-387-76501-3_8.

Williams, D.B. & Carter, C.B. (2009i) *Scattering and Diffraction BT - Transmission Electron Microscopy: A Textbook for Materials Science*. In: David B Williams & C Barry Carter (eds.). [Online]. Boston, MA, Springer US. pp. 23–38. Available from: doi:10.1007/978-0-387-76501-3_2.

Williams, D.B. & Carter, C.B. (2009j) The Instrument. In: *Transmission Electron Microscopy: A Textbook for Materials Science*. [Online]. Boston, MA, Springer US. pp. 141–171. Available from: doi:10.1007/978-0-387-76501-3_9.

Williams, D.B. & Carter, C.B. (2009k) *The Transmission Electron Microscope BT - Transmission Electron Microscopy: A Textbook for Materials Science*. In: David B Williams & C Barry Carter (eds.). [Online]. Boston, MA, Springer US. pp. 3–22. Available from: doi:10.1007/978-0-387-76501-3_1.

Williams, W.P., Brain, A.P.R. & Dominy, P.J. (1992) Induction of non-bilayer lipid phase separations in chloroplast thylakoid membranes by compatible co-solutes and its relation to therthermal stability of Photosystem II. *Biochimica et Biophysica Acta (BBA) -*

*Bioenergetics*. [Online] 1099 (2), 137–144. Available from: doi:https://doi.org/10.1016/0005-2728(92)90210-S.

Williamson, J.J. & Olmsted, P.D. (2018) Effects of Passive Phospholipid Flip-Flop and Asymmetric External Fields on Bilayer Phase Equilibria. *Biophysical Journal*. [Online] 115 (10), 1956–1965. Available from: doi:https://doi.org/10.1016/j.bpj.2018.10.003.

Witwinowski, J., Sartori-Rupp, A., Taib, N., Pende, N., et al. (2022) An ancient divide in outer membrane tethering systems in bacteria suggests a mechanism for the diderm-to-monoderm transition. *Nature Microbiology*. [Online] 7 (3), 411–422. Available from: doi:10.1038/s41564-022-01066-3.

Wolf, D.M., Segawa, M., Kondadi, A.K., Anand, R., et al. (2019) Individual cristae within the same mitochondrion display different membrane potentials and are functionally independent. *The EMBO journal*. [Online] 38 (22), e101056. Available from: doi:10.15252/embj.2018101056.

van Wolferen, M., Pulschen, A.A., Baum, B., Gribaldo, S., et al. (2022) The cell biology of archaea. *Nature Microbiology*. [Online] 7 (11), 1744–1755. Available from: doi:10.1038/s41564-022-01215-8.

Wrapp, D., Wang, N., Corbett, K.S., Goldsmith, J.A., et al. (2020) Cryo-EM structure of the 2019-nCoV spike in the prefusion conformation. *Science*. [Online] 367 (6483), 1260–1263. Available from: doi:10.1126/science.abb2507.

Wu, G., Cui, X., Chen, H., Renaud, J.B., et al. (2018) Dynamin-Like Proteins of Endocytosis in Plants Are Coopted by Potyviruses To Enhance Virus Infection. *Journal of virology*. [Online] 92 (23). Available from: doi:10.1128/JVI.01320-18.

Yan, L., Qi, Y., Huang, X., Yu, C., et al. (2018) Structural basis for GTP hydrolysis and conformational change of MFN1 in mediating membrane fusion. *Nature Structural & Molecular Biology*. [Online] 25 (3), 233–243. Available from: doi:10.1038/s41594-018-0034-8.

Yan, L., Qi, Y., Ricketson, D., Li, L., et al. (2020) Structural analysis of a trimeric assembly of the mitochondrial dynamin-like GTPase Mgm1. *Proceedings of the National Academy of Sciences*. [Online] 117 (8), 4061–4070. Available from: doi:10.1073/pnas.1919116117.

Yingxing, L., Xiao, C., Weili, Z., Kefan, F., et al. (2024) The metabolic slowdown caused by the deletion of pspA accelerates protein aggregation during stationary phase facilitating antibiotic persistence. *Antimicrobial Agents and Chemotherapy*. [Online] 68 (2), e00937-23. Available from: doi:10.1128/aac.00937-23.

Yu, C., Zhao, J., Yan, L., Qi, Y., et al. (2020) Structural insights into G domain dimerization and pathogenic mutation of OPA1. *The Journal of cell biology*. [Online] 219 (7). Available from: doi:10.1083/jcb.201907098.

Yuan, F., Alimohamadi, H., Bakka, B., Trementozzi, A.N., et al. (2021) Membrane bending by protein phase separation. *Proceedings of the National Academy of Sciences of the United States of America*. [Online] 118 (11). Available from: doi:10.1073/pnas.2017435118.

Zacharioudakis, E., Agianian, B., Kumar MV, V., Biris, N., et al. (2022) Modulating mitofusins to control mitochondrial function and signaling. *Nature Communications*. [Online] 13 (1), 3775. Available from: doi:10.1038/s41467-022-31324-1.

Zachs, T., Schertel, A., Medeiros, J., Weiss, G.L., et al. (2020) Fully automated, sequential focused ion beam milling for cryo-electron tomography. *eLife*. [Online] 9. Available from: doi:10.7554/eLife.52286.

Zerihun, M., Sukumaran, S. & Qvit, N. (2023) The Drp1-Mediated Mitochondrial Fission Protein Interactome as an Emerging Core Player in Mitochondrial Dynamics and

Cardiovascular Disease Therapy. *International journal of molecular sciences*. [Online] 24 (6). Available from: doi:10.3390/ijms24065785.

Zhan, T., Lv, W. & Deng, Y. (2017) Multilayer gyroid cubic membrane organization in green alga Zygnema. *Protoplasma*. [Online] 254 (5), 1923–1930. Available from: doi:10.1007/s00709-017-1083-2.

Zhang, D., Zhang, Y., Ma, J., Zhu, C., et al. (2020a) Cryo-EM structures of S-OPA1 reveal its interactions with membrane and changes upon nucleotide binding. *eLife*. [Online] 9. Available from: doi:10.7554/eLife.50294.

Zhang, J., Humphreys, I.R., Pei, J., Kim, J., et al. (2024) Computing the Human Interactome. *bioRxiv*. [Online] 2024.10.01.615885. Available from: doi:10.1101/2024.10.01.615885.

Zhang, K. (2016) Gctf: Real-time CTF determination and correction. *Journal of structural biology*. [Online] 193 (1), 1–12. Available from: doi:10.1016/j.jsb.2015.11.003.

Zhang, R., Lee, D.M., Jimah, J.R., Gerassimov, N., et al. (2020b) Dynamin regulates the dynamics and mechanical strength of the actin cytoskeleton as a multifilament actin-bundling protein. *Nature Cell Biology*. [Online] 22 (6), 674–688. Available from: doi:10.1038/s41556-020-0519-7.

Zhang, X. (2022) Python-based Helix Indexer: A graphical user interface program for finding symmetry of helical assembly through Fourier–Bessel indexing of electron microscopic data. *Protein Science*. [Online] 31 (1), 107–117. Available from: doi:https://doi.org/10.1002/pro.4186.

Zhang, X., Belousoff, M.J., Zhao, P., Kooistra, A.J., et al. (2020c) Differential GLP-1R Binding and Activation by Peptide and Non-peptide Agonists. *Molecular Cell*. [Online] 80 (3), 485-500.e7. Available from: doi:https://doi.org/10.1016/j.molcel.2020.09.020.

Zhang, X. & Hu, J. (2010) The Arabidopsis chloroplast division protein DYNAMIN-RELATED PROTEIN5B also mediates peroxisome division. *The Plant cell*. [Online] 22 (2), 431–442. Available from: doi:10.1105/tpc.109.071324.

Zhang, Z., Schwartz, S., Wagner, L. & Miller, W. (2000) A greedy algorithm for aligning DNA sequences. *Journal of computational biology : a journal of computational molecular cell biology*. [Online] 7 (1–2), 203–214. Available from: doi:10.1089/10665270050081478.

Zheng, S.Q., Palovcak, E., Armache, J.-P., Verba, K.A., et al. (2017) MotionCor2: anisotropic correction of beam-induced motion for improved cryo-electron microscopy. *Nature Methods*. [Online] 14 (4), 331–332. Available from: doi:10.1038/nmeth.4193.

Zhong, C., Chen, M., Chen, Y., Yao, F., et al. (2021a) Loss of DSTYK activates Wnt/β-catenin signaling and glycolysis in lung adenocarcinoma. *Cell Death & Disease*. [Online] 12 (12), 1122. Available from: doi:10.1038/s41419-021-04385-1.

Zhong, E.D., Bepler, T., Berger, B. & Davis, J.H. (2021b) CryoDRGN: reconstruction of heterogeneous cryo-EM structures using neural networks. *Nature Methods*. [Online] 18 (2), 176–185. Available from: doi:10.1038/s41592-020-01049-4.

Zhu, J., Penczek, P.A., Schröder, R. & Frank, J. (1997) Three-Dimensional Reconstruction with Contrast Transfer Function Correction from Energy-Filtered Cryoelectron Micrographs: Procedure and Application to the 70SEscherichia coliRibosome. *Journal of Structural Biology*. [Online] 118 (3), 197–219. Available from: doi:https://doi.org/10.1006/jsbi.1997.3845.

Zhu, S., Bradfield, C.J., Maminska, A., Park, E.-S., et al. (2024) Native architecture of a human GBP1 defense complex for cell-autonomous immunity to infection. *Science*. [Online] 383 (6686), eabm9903. Available from: doi:10.1126/science.abm9903.

Zhu, Y., Carragher, B., Glaeser, R.M., Fellmann, D., et al. (2004) Automatic particle selection:

results of a comparative study. *Journal of Structural Biology*. [Online] 145 (1), 3–14. Available from: doi:https://doi.org/10.1016/j.jsb.2003.09.033.

Zivanov, J., Nakane, T., Forsberg, B.O., Kimanius, D., et al. (2018) New tools for automated high-resolution cryo-EM structure determination in RELION-3. *eLife*. [Online] 7. Available from: doi:10.7554/eLife.42166.

Zivanov, J., Nakane, T. & Scheres, S.H.W. (2019) A Bayesian approach to beam-induced motion correction in cryo-EM single-particle analysis. *IUCrJ*. [Online] 6 (1), 5–17. Available from: doi:10.1107/S205225251801463X.

Zivanov, J., Nakane, T. & Scheres, S.H.W. (2020) Estimation of high-order aberrations and anisotropic magnification from cryo-EM data sets in RELION-3.1. *IUCrJ*. [Online] 7 (Pt 2), 253–267. Available from: doi:10.1107/S2052252520000081.

Ziviani, E., Tao, R.N. & Whitworth, A.J. (2010) Drosophila parkin requires PINK1 for mitochondrial translocation and ubiquitinates mitofusin. *Proceedings of the National Academy of Sciences of the United States of America*. [Online] 107 (11), 5018–5023. Available from: doi:10.1073/pnas.0913485107.

# Appendices

## Collaborator Methods

### PLiMAP and GTPase Activity Assay Methods

*These assays were performed and analysed by Keerti Singh and Thomas Pucadyil.*

**Liposome Preparation.** 1,2-Dioleoyl-sn-glycero-3-phosphocholine (DOPC) and 1,2-dioleolyl-sn-glycero-3-phosphatidylglycerol (DOPG) were obtained from Avanti Lipids. The bifunctional photoactivable fluorescent lipid probe, BODIPY-diazirine PE, was synthesized according to the protocols established by (Jose & Pucadyil, 2020) and (Jose *et al.*, 2020).

To prepare the liposomes, the lipids were aliquoted at desired ratios into a glass tube and dried under high vacuum for 3 hours to form a thin lipid film. Following the drying process, deionized water was added to the dried lipid film to achieve a final lipid concentration of 1 mM. The lipid suspension was then hydrated at 50 °C for 30 minutes, during which it was vortexed vigorously to ensure thorough mixing. The hydrated lipids were extruded through 100 nm pore size polycarbonate filters (Whatman), resulting in homogeneous lipid vesicles suitable for subsequent experiments.

**Proximity-based labelling of membrane-associated proteins (PLiMAP) assay.** PLiMAP assays were conducted as previously described (Jose et al., 2020; Jose and Pucadyil, 2020). Liposomes composed of increasing molar percentages of DOPG and 1 mol% BODIPY-diazirine PE were incubated with BDLP at a 100:1 lipid-to-protein molar ratio in a final volume of 30 µL. Samples were incubated in the dark at room temperature for 30 minutes and subsequently exposed to UV light (365 nm; UVP crosslinker CL-1000L) at an intensity of 200 mJ/cm² for 1 minute. Following UV exposure, samples were mixed with SDS-PAGE sample buffer, boiled, and resolved by SDS-PAGE. Gels were first imaged for BODIPY fluorescence using a Typhoon Biomolecular Imager (Amersham) and subsequently stained with Coomassie Brilliant Blue (CBB) to detect total protein.

To evaluate the effect of nucleotides on BDLP binding to DOPG liposomes, 1 mM of indicated nucleotide was added to the liposome-protein mixture (100:1 lipid-to-protein molar ratio),

and the PLiMAP assay was performed as described above. Binding data were fitted to a one-site binding isotherm using GraphPad Prism for analysis.

**GTPase Assay.** BDLP was centrifuged at 100,000 g to remove the protein aggregates before performing the GTPase assay. Liposomes were made with 1,2-Dioleoyl-sn-glycero-3-phosphocholine (DOPC; 20 Mol %) and 1,2-dioleolyl-sn-glycero-3-phosphatidylglycerol (DOPG; 80 Mol %) in 20mM HEPES pH 7.4 buffer and 150mM NaCl. BDLP (1μM) was mixed with 1 mM GTP (Jena Biosciences, Germany) in the presence or absence of liposomes (100uM) in 20mM HEPES pH 7.4 buffer with 150mM NaCl and 1mM MgCl2 and incubated at 37 °C. Aliquots were taken at regular intervals and quenched with 0.5mM EDTA. Inorganic phosphate released was assayed with the malachite green reagent (Kamerkar *et al.*, 2018).

## *N. punctiforme* Strain Construction and Analysis

*This work was carried out by Douglas Risser.*

**Strains and culture conditions.** For a detailed description of the strains used in this study, refer to Table 18. *N. punctiforme* ATCC 29133 and its derivatives were cultured in Allan and Arnon medium diluted four-fold (AA/4), without supplementation of fixed nitrogen, as previously described (Campbell *et al.*, 2007), with the exception that 4 and 10 mM sucralose was added to liquid and solid medium, respectively, to inhibit hormogonium formation (Splitt & Risser, 2016). For hormogonium induction for phenotypic analysis, the equivalent of 30 μg/ml chlorophyll-a (Chla) of cell material from cultures at a Chla concentration of 10-20 μg/ml was harvested at 2,000 g for 3 min, washed twice with AA/4 and resuspended in 2 ml of fresh AA/4 without sucralose. For selective growth, the medium was supplemented with 50 μg/ml neomycin. *Escherichia coli* cultures were grown in lysogeny broth (LB) for liquid cultures or LB supplemented with 1.5% (w/v) agar for plates. Selective growth medium was supplemented with 50 μg/ml kanamycin, 50 μg/ml ampicillin, and 15 μg/ml chloramphenicol.

**Plasmid and strain construction.** For a detailed description of the plasmids, strains, and oligonucleotides used in this study, refer to Table 18. All constructs were sequenced to ensure fidelity.

To construct plasmids for in-frame deletions, approximately 900 bp of flanking DNA on either side of the gene and several codons at the beginning and end of the gene were amplified via overlap extension PCR and cloned into pRL278 (Cai & Wolk, 1990) as a BamHI-SacI fragment using restriction sites introduced on the primers.

To construct plasmids for replacement of chromosomal alleles with a C-terminal gfpuv-tagged variant, approximately 900 bp of DNA downstream of the stop codon were amplified via PCR and cloned into pSCR569 (Risser, Wong & Meeks, 2012), as an SpeI-SacI fragment using restriction sites introduced on the primers. The coding region and approximately 900 bp of DNA upstream of the start codon were then amplified via PCR using and cloned into this plasmid as a BamHI-SmaI fragment using restriction sites introduced on the primers.

To construct a mobilisable shuttle vector containing Npun_R6513-gfp expressed from the petE promoter, the coding region of Npun_R6513 was amplified via PCR and subsequently cloned into pDDR155 (Risser, Chew & Meeks, 2014) as a BamHI-SmaI fragment, replacing the hmpA coding region, using restriction sites introduced on the primers.

Gene deletion was performed as previously described (Risser & Meeks, 2013), with N. *punctiforme* cultures supplemented with 4 mM sucralose to inhibit hormogonium development and enhance conjugation efficiency (Splitt & Risser, 2016; Khayatan *et al.*, 2017). To construct UOP203, UOP204, UOP205 and UOP206, plasmids pDDR518, pDDR527, pDDR517 and pDDR526, respectively, were introduced into wild type *N. punctiforme* ATCC29133.

**Immunoblot analysis.** Preparation of *N. punctiforme* cell material, protein extraction, and detection of GFPuv by immunoblot analysis were performed as previously described (Cho *et al.*, 2017).

**Microscopy.** Fluorescence microscopy was performed using an EVOS M5000 fluorescence microscope (Life Technologies) equipped with a 63x objective lens. Excitation and emission were as follows: EVOS™ light cube, Nrw 405 (AMEP4857: excitation 390+/-18 nm, emission 525+/-50 nm) for GFPuv and EVOS™ Light Cube, RFP (AMEP4652: excitation 531+/-40 nm, emission 593+/-40 nm) for cellular autofluorescence.

**Table 18. Strains, Plasmids and Primers used for *N. punctiforme* Strain Construction.**

| Strain Name | Description | Source |
|---|---|---|
| *N. punctiforme* ATCC29133 | Wild-type | ATCC |
| UOP203 | ΔNpun_R6514-6513 | This study |
| UOP204 | Npun_R6513-GFP | This study |
| UOP205 | ΔNpun_R6512 | This study |
| UOP206 | Npun_R6512-GFP | This study |

| Plasmid Name | Description | Primers Used to Construct Plasmid |
|---|---|---|
| pDDR517 | Suicide vector for in-frame deletion of Npun_R6512 | 1-4 |
| pDDR518 | Suicide vector for in-frame deletion of Npun_R6514-Npun_R6513 | 5-8 |
| pDDR526 | Suicide vector for replacement of chromosomal allele of Npun_R6512 with Npun_R6512-*gfp* | 4, 9-11 |
| pDDR527 | Suicide vector for replacement of chromosomal allele of Npun_R6513 with Npun_R6513-*gfp* | 8, 12-14 |
| pDDR552 | Shuttle vector expressing Npun_R6513-*gfp* from the *petE* promoter | 13, 15 |

| Primer Name | Sequence | Primer Number |
|---|---|---|
| NpR6512-5'-F | atataggatccATTTGCGTTGCTAGGCTTG | 1 |
| NpR6512-5'-R | gttgtttatttatcactCTGTTGTTGCATAGTTCTCG | 2 |
| NpR6512-3'-F | ctatgcaacaacagAGTGATAAATAAACAACAAGATACTG | 3 |
| NpR6512-3'-R | atatagagctcCCGCAAATACATATTGGTCAC | 4 |
| NpR6514-5'-F | atataggatccCGTCTCTCTTTAATAGATGTATTTC | 5 |
| NpR6514-5'-R | gctatagtaagcAGATGTCATCGGTATCCACTC | 6 |
| NpR6514-6513-3'-F | cgatgacatctGCTTACTATAGCTAATAACAG | 7 |
| NpR6513-3'-R | atatagagctcCCTATTACCATCAAGAATTGC | 8 |
| NpR6512-gfp-5'-F | atataggatccGGTGGTATTGGTTGGTTGTTAG | 9 |
| NpR6512-gfp-5'-R | atatacccgggATTTATCACTCAAAATTGTGTAAGCATC | 10 |
| NpR6512-gfp-3'-F | atataactagtACAACAAGATACTGGACTTATTTAATTAAG | 11 |
| NpR6513-gfp-5'-F | atataggatccACTCAAGCAAGAACGATTTCTG | 12 |
| NpR6513-gfp-5'-R | atatacccgggAGCTATAGTAAGCTAATAAATTGC | 13 |
| NpR6513-gfp-3'-F | atataactagtCAGTTTATTACTCTCATTCTTAGATAG | 14 |
| NpR6513-BamHI-F | ATATAGGATCCATGGTGAATCAAGTAGCAAC | 15 |